NON-LINEAR FINITE ELEMENT DYNAMIC ANALYSIS OF THE EFFECT OF COMPACTION ON UNDERGROUND CONDUITS

by

ANUPONG KARARAM

Presented to the Faculty of the Graduate School of

The University of Texas at Arlington in Partial Fulfillment

of the Requirements for the Degree of

DOCTOR OF PHILOSOPHY

THE UNIVERSITY OF TEXAS AT ARLINGTON

December 2009

ACKNOWLEDGEMENTS

I would like to express my sincere gratitude to Dr. Ali Abolmaali, the author's supervising professor, for his continual help and guidance throughout this study. The valuable suggestions made by the members of the supervising committee including Dr. Anand J. Puppala, Dr. John H. Matthys, Dr. Pranesh Aswath, and Dr. Sahadat Hossain are most appreciated and gratefully acknowledged.

My gratitude goes to Joe Lundy, Joe Zicaro, Josh Beakley, and Kim Spahn for providing invaluable input in understanding the pipe behavior, in general. I especially wish to thank the American Concrete Pipe Association, National Science Foundation, and Department of Civil and Environmental Engineering of the University of Texas at Arlington for their financial assistance throughout this study.

Finally, I thank my parents, and brothers for their support from my country, Thailand. I also extend my appreciation to my friends here, in USA, without whom the completion of this dissertation was not possible.

October 14, 2009

ABSTRACT

NON-LINEAR FINITE ELEMENT DYNAMIC ANALYSIS

OF THE EFFECT OF COMPACTION ON

UNDERGROUND CONDUITS

Anupong Kararam, Ph.D.

The University of Texas at Arlington, 2009

Supervising Professor: Ali Abolmaali

Construction loads are an important but often overlooked factor in underground pipe design and installation. Common compaction equipments used in pipeline construction can be a major contributor to pipe damage. To reduce load concentrations in excess of the design loads, construction equipment should be kept at a safe distance above the pipe location.

This study investigates the behavior of a reinforced concrete pipeline system under a compaction process. The full-scale experimental test was conducted using a Type-2 standard trench installations soil and minimum compaction requirement. Using a compaction machine “hoe pack” and including the weight of a backhoe, a maximum dynamic compaction force was applied to the entire area of the pipe-soil installation system. Induced pressure and deformation to the pipe wall were measured via load cells

and strain gauges respectively. Damage to the pipeline was also monitored by an inspection camera installed inside the pipeline. The test results showed the pipeline system was damaged due to the compaction force when only the first 6-in (15-cm) layer of backfill soil above the pipe's crown was completed. The most critical compaction location is at the joint of the pipeline system. Compaction here led to crack and fracture in the pipe wall. Thus, the test results ensured the effect of a heavy compaction force on the failure of the pipeline system during the construction process.

The finite element (FEM) model was developed based on the three-edge bearing experimental test known as "D-Load test." To verify the finite element (FEM) algorithm, the D-Load tests were conducted on eight full-scale reinforced concrete pipes with 18-in. (46-cm), 36-in. (91-cm), and 54-in. (1.37-m) diameters manufactured per the ASTM C76-08. The experimental tests closely exhibit the FEM results both when comparing load-deformation and crack initiation and propagation. Further, the significance of crack width in pipe stiffness characteristics is discussed. Complete three-dimensional (3-D) models of the "D-Load" test conducted on the reinforced concrete pipes is simulated by using FEM method. The simulation will predict the test up to failure by scaled dynamic analysis and discrete crack model. The crack model uses the constitutive material law for concrete coupled with tension stiffening algorithm. Also, the failure modes observed for different pipe diameters are documented and reported.

Consequently, a parametric study of a pipeline under the compaction process in trench installation was conducted to specify the minimum backfill depth above pipes before compacted. The 3-D FEM modeled two spans of a concrete pipe and surrounding

soils. The concrete brittle cracking criterion was applied for the post-failure behavior of a pipe model. In the surrounding soil zone, the Mohr-Coulomb criterion was used for the material property. A surface-to-surface contact property was employed in the interface between each two regions of a pipe and surrounding soils which employs a nonlinear incremental solution algorithm. The compaction force composed of a static weight of backhoe and a dynamic force from hoe pack applied simultaneously. All standard pipe sizes used in this parametric study are 24-in. (61-cm), 36-in. (91-cm), 48-in. (1.22-m), and 54-in. (1.37-m) diameters. The interesting parameters include the geometry related, material properties, and loading locations. This study shows the effect of backfill height on the stress reduction for each pipe size. At the most critical region on a pipeline, a minimum backfill soil cover above a pipe is defined.

TABLE OF CONTENTS

LIST OF ILLUSTRATIONS

LIST OF TABLES

CHAPTER 1

INTRODUCTION AND LITERATURE REVIEW

1.1 Introduction

In underground pipe work there are various factors effecting pipe-soil structure interaction either during or after construction. Many researchers have studied loading conditions on pipe-soil systems with varied covering depths. Both static earth load and dynamic live load have been studied experimentally and theoretically. During construction, the compaction process is the major issue in transferring large impacting forces to the pipe structure. Hansen et al. (1997) provided a report of a proven link between the premature cracking of small diameter (less than 36 in. or 90 cm) concrete stormwater pipes and construction loading. The major causes of pipe cracking were most likely related to trench backfilling and compaction method. Trench compaction and road construction equipment are often found to induce loads far greater than the typical service load for which the pipes were designed. Common compaction equipment used in pipeline construction is the wacker packer, trench roller, and excavator compaction wheel. Such construction equipment can be a major contributor to pipe cracking. The design and selection of a pipe class must consider the construction loadings.

By the 1980's, vibratory compactors were connected to the arms of an excavator such as a backhoe and used for compacting material in a trench without requiring a man

to enter the trench. The invention related to a plate-type vibratory compactor (Dresher, 1971) which permits the direction-reversing feature of a self-propelled vibratory compactor. The improved construction method also led to the invention of a hydraulically operated vibratory soil compactor adapted for use with a backhoe (St. Louis, 1980). Thus, most standard specifications include minimum cover requirements as a safe distance for construction equipment live loads (Poucher et al., 1976; and Pacific Northwest Concrete Pipe Association, 1993). The effects of heavy construction equipment passing over concrete pipes are also considered in the Concrete Pipe Installation Manual (American Concrete Pipe Association, 2007) to avoid load concentrations in excess of the design loads. These regulations require adequate protection against ongoing heavy equipment and require a temporary earth fill to be completed prior to the passing of equipment.

This research mainly focuses on the effect of a vibratory force produced by a heavy compaction device during the construction process of a concrete pipe embedded in shallow soils. A full scale experimental test included the trench installation of a pipeline. Every 6-in. (15-cm) increment of backfill soil layers was compacted. The instrumentation on the concrete pipes included earth pressure cells to investigate the induced pressure on pipe wall and strain gauges to evaluate pipe's deformation, respectively. Also, an inspection camera was used to observe the occurrence of failure on the buried pipe.

The further study of post-failure behavior of the concrete pipe involved the full scale D-Load test. A pipe specimen was set up in the three-edge bearing (TEB) machine

composed of two supports and a load bearing strip. With this test, the crack sizes, crack propagations, and failure modes on a pipe under the increased crushing force were determined. The instrumentation included a linear variable displacement transducer (LVDT) for measuring the deformation in both vertical and horizontal directions of a pipe cross-section. Load increments were gradually applied by the TEB machine at the controlled rate until the service strength and the ultimate strength were reached. The results were also used to verify the concrete brittle cracking property in the finite element (FEM) modeling.

The FEM model of pipe-soil installation was created to simulate and predict the behavior of a buried pipeline subjected to the effects of the compaction process. For the post-failure behavior of concrete under cracking, tension stiffening defines the presence of reinforcement in the concrete used for the brittle cracking model. Mohr-Coulomb plasticity model was used for analysis applications in the surrounding soil zone. According to the experimental test, the vibratory force from hoe pack and the static weight from backhoe were simulated for the applied load in a model. The scaled mass matrix was used for each increment within the dynamic analysis step to increase computational efficiency. Consequently, a parametric study was accomplished with several interesting variables: pipe sizes, backfill soil depths, side-fill soil materials, and loading locations.

1.2 Construction Induced Stress

The construction load from the compaction machine is applied to the pipe as a non-uniformly distributed external pressure. The pipe derives its support from

distributed external earth pressure around the lower portion of its circumference. The pressure distribution, transferred via the surrounding soil, significantly influences the pipe's stiffness. The applied earth pressure has a normal component and a traction component, resulting from friction between soil and concrete. As shown in Figure 1.1, the combined effects of moment (M) and thrust (N) at the sections of maximum flexural stress produce the tension on the inside of the pipe and compression on the outside of the pipe at crown and invert. In contrary, at springline, the tension and compression occur on the outside and inside of the pipe, respectively.

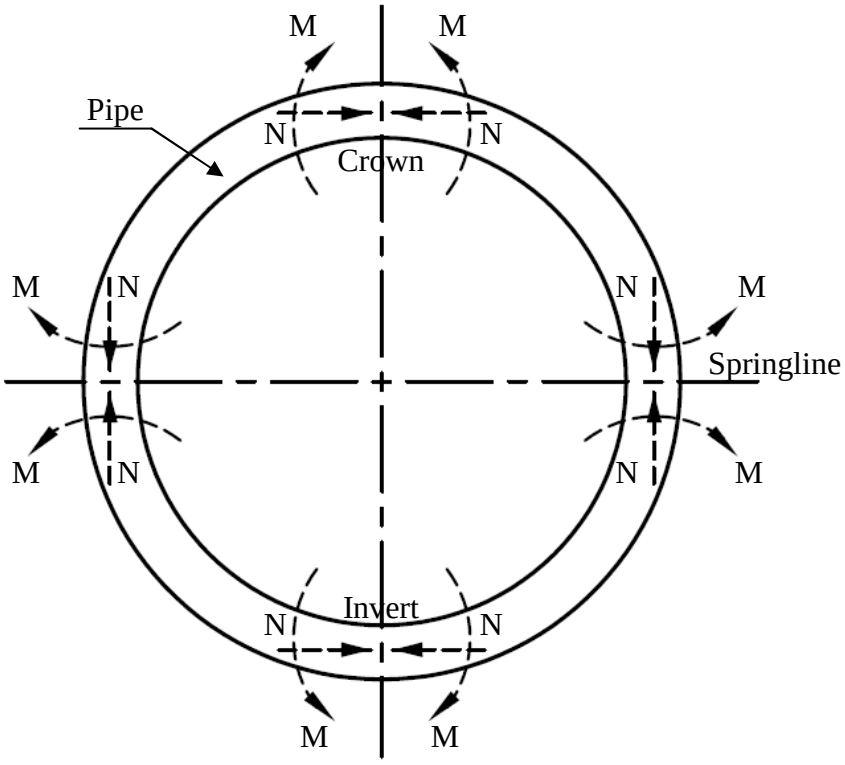

Figure 1.1 Moment and thrust induced on a buried pipe.

1.3 Pipe Design Methods

Marston (1930) developed theory of earth loads on a buried pipe, using experiments and field data conducted over 20 years. Marston also advanced the characteristic force diagram representing the earth pressures induced on a buried pipe. Spangler (1933) developed three bedding configurations and the bedding factor. The objective of Spangler's research was to determine the supporting strength of buried rigid pipe when subjected to the earth load predicted by Marston's theories of earth loads on projecting culverts. Based on Marston and Spangler's theory (1930, 1933), Olander (1950) presented the bulb-shaped distribution of earth pressures and the analysis of stress around a buried concrete pipe. Marston and Spangler's research is the basis of the currently used "Indirect Design" method.

The indirect design method emphasizes on the comparison of the structural strength of the pipe from the three-edge bearing (TEB) test to the field supporting strength of a buried pipe. The method uses the 0.01-in. (0.25-mm) crack criterion developed in a TEB test to evaluate the supporting strength of reinforced concrete pipe. For circular pipes, ASTM C 655 (2007) defines the TEB ultimate load and an observed 0.01-in. (0.25-mm) crack width in terms of D-Loads multiplied by a strength factor. ASTM C 76 (2008) contains tables for steel reinforcement requirement corresponding to the specified classes of reinforced concrete pipe based on test data. In 1983, the indirect design method was included in a new section of the AASHTO M 170 (2005) and M 242 (2005).

Therefore, the TEB method is widely used for testing of strength and cracks occurred in reinforced concrete pipes. Sizes of the crack on buried pipes have become a concerned topic for many researchers due to the exposure of the reinforcing steel. As the tensile strength of concrete is exceeded, cracks will form as the tensile load is transferred to the steel. Consequently, the 0.01-in. (0.25-mm) crack criteria has been used and accepted as a conservative design for reinforced concrete pipe (American Concrete Pipe Association, 2001).

Due to the developments of the knowledge of soil properties, as well as advancements in structural analysis techniques, the design practice of concrete pipes has been significantly improved. In 1970, American Concrete Pipe Association (ACPA) began a long range research program on the interaction of buried concrete pipe and soil (American Concrete Pipe Association, 2001). The research program on soil-structure interaction was conducted by researchers at Northwestern University. Included were full-scale tests at the Ohio Transportation Research Center. As a result, new standard installation types were recommended, which differ considerably from those originally developed by Marston and Spangler (1930, 1933). Consecutively, four new standard installations, Heger earth pressure distribution, and the “Direct Design Method” were incorporated in an American Society of Civil Engineers (ASCE) standard, 1994.

The direct design method is a limit state design procedure of reinforced concrete pipe that requires the determination of total load on the pipe and the distribution of earth pressure around the pipe. The direct design procedures consider the effects of the distribution of loads on a buried pipe by making assumptions on the variation of earth

pressure around the pipe circumference. The required strength of the concrete pipe is determined from the effects of bending moment, thrust, and shear forces. The physical properties of a concrete pipe and reinforcement are evaluated using the procedures based on the strength and crack width limits.

1.4 Performed Theoretical and Experimental Studies

Two types of pipe-soil installation, trench and embankment, are widely used in the construction field. Trench installations are used in relatively narrow excavations with the pipeline covered with earth backfill extending to the original ground surface. For embankment installations, the pipe is installed with the top of the pipe projecting above the surface of the natural ground and backfill material is placed in layers above the natural ground. After installation, the concrete pipe and the enveloping soil become a composite unit. The amount of load carried by the pipe is dependent on the soil stiffness around the pipe. The general characteristics of the loads, consisting of pipe weight and earth load, exert a distribution of earth pressure around the pipe.

The supporting strength of the buried pipe has been investigated to provide the distribution of the vertical reaction around the lower exterior surface of the pipe and reduce stress concentrations within the pipe wall. Marston suggested the use of sand bearings over a 90-degree arc for the test of the supporting strength of pipe. Furthermore, Marston et al. (1917) focused on the supporting strength of pipe as it is affected by bedding conditions. Schlick (1920) performed the pipe-laying tests under several bedding conditions.

Since 1970, the theoretical and experimental performance of pipe-soil interaction system have been continuously studied and developed. Improvements to well-established design criteria required more precise analysis techniques and systematic testing approaches. Full-scale test results were used to evaluate and validate theoretical studies. Parmelee (1973) studied buried concrete pipes under imposed loading. The project consisted of field installations and a comprehensive FEM program. For the field tests, pipe sections were instrumented with strain gauges, fittings for taking diameter and chord measurements, and surface pressure meters. Stress cells were installed in the soil at various locations in the vicinity of the pipe. Field data and laboratory tests under controlled load conditions were used to verify the nonlinear mechanical properties for both concrete and soil in the plane strain computer FEM model. The digital computers and FEM have been applied to a mathematical model for analyzing the behavior of a concrete pipe buried in soil mass. Krizek and McQuade (1978) incorporated the principles of pipe-soil interaction in the calculated analysis results for eight different field installations.

Webb et al. (1996) performed full-scale tests at the University of Massachusetts at Amherst to evaluate the behavior of pipe-soil interaction during backfilling. The installation practices involved the use of compaction devices. This study indicated that the rammer compactor produced greater backfill density than the vibratory plate compactor, and it produced higher residual lateral soil stresses that contribute to better overall pipe performance during backfilling. Zoladz et al. (1996) conducted the laboratory testing of the pipe-soil interactions under the backfilling process. Test

variables included were pipe types, trench conditions, backfill materials, compaction methods, haunch effort, and bedding conditions. They found that wider trench produced the greater upward deflections during sidefill compaction. The rammer compactor was the most effective means of achieving high backfill density and stiffness, forcing backfill into the haunch zone, and developing lateral stresses at the sides of the pipe. The coarser-grained backfill material achieved suitable soil unit weight and stiffness with less compactive energy than the finer-grained material. The haunching effort provided pipe support in the lower haunch zone. Furthermore, Webb et al. (1998) applied controlled low strength material as backfill part of a study for installation procedures. The controlled low strength material provided excellent support for the pipe in especially hard to reach areas.

The instrumentation and data measurement are also significant procedures for the field study. McGrath et al. (1999) devised an extensive instrumentation plan to monitor buried pipe behavior, soil behavior, and pipe-soil interaction during backfilling. Measurements of pipe shape, pipe strains, pipe-soil interface pressures, soil density, soil stresses, and soil strains were collected. McGrath et al. (2000) conducted full-scale field tests to evaluate the pipe-soil interactions that take place as pipes were buried and backfilled. Tests included two types of backfill soil, the compaction levels, three trench widths, and varying haunching effort. They found that compaction of backfill in the region from the springline to 45 to 60 degrees below the springline has a significant positive effect in mitigating poor bedding and haunching condition. Also, the use of soft bedding is effective in reducing invert pressures on the pipe. Talesnick (2005) studied

on the design and test of a soil contact pressure sensor. Based on the null method, the calibration and validation of a sensor showed a good response. In field tests, the sensor is generally used to measure the development of contact pressures on boundaries of buried structures.

1.5 FEM Computer Programs for Pipe-Soil System

Because of the complexity of the soil-structure interaction system, the theory of continuum mechanics, “Finite Element Method”, in conjunction with an electronic computer was considered. Several unified computer programs for the pipe-soil interaction analysis and design have been developed. CANDE (Culvert Analysis and Design) was first introduced by Katona et al. (1976) under the sponsorship of Federal Highway Administration. CANDE operates either in a design or an analysis mode and offers a choice of three solution levels ranging from an elasticity solution to a general FEM solution. After 2000, researchers utilized the CANDE program in a wide range of the pipe-soil interaction analysis. McGrath (2003) completed the two-dimensional embankment installation FEM model using CANDE. The specified version was CANDEcad which used the CANDE program for calculations, but adds an Autocad based pre- and post-processor. Maher (2005) created the FE model for the parametric study of factors effecting on buried reinforced concrete pipes. The computer program CANDE was used as the two-dimensional plane strain model considering nonlinear soil performance.

A computerized direct design method for buried concrete pipe named SPIDA (Soil-Pipe Interaction Design and Analysis) was presented (Heger et al., 1985). The

soil-structure interaction FEM system for embankment and trench installations were described. Also, the new reinforced concrete design methods developed for shear, radial tension, and cracked section were summarized. SPIDA is the culmination of over 20 years of research and testing to develop improved methods for determining earth loads and pressure distributions on buried concrete pipe. McGrath and Kurdziel (1991) provided the method for reinforced concrete pipe design using the program SPIDA. PIPECAR (Pipe Culvert Analysis and Reinforcing design) is a Federal Highway Administration-sponsored microcomputer program that sizes reinforcing based on the assumed loads and soil pressure distributions. The computer program, SIDD (Standard Installation Direct Design), is a further development of PIPECAR that incorporates more sophisticated pressure distributions based on the results of research with SPIDA that represent standard installations.

1.6 Installation Techniques

The pipe embedment consists of the soil that is placed under and around the pipe immediately above the bedding. It includes the sidefill and the initial cover. The sidefill soils adjacent to the pipe provide beneficial lateral support. The most critical region of embedment is the haunch fill, extending under the pipe from the springline down to the top of the bedding. If the soil in this region is highly compacted over similarly compacted bedding under the two outer one-thirds of the pipe outside diameter, the pipe installation will achieve a beneficial distribution of earth support (American Concrete Pipe Association, 2001).

1.6.1 Trench Installation

Figure 1.2 shows the concept of trench installation. The pipe is located completely below the natural ground surface and the backfill over the pipe is placed between vertical walls of pre-existing soil extending to the surface. Trench installations are made in relatively narrow excavations and the pipeline covered with earth backfill which extends to the original ground surface. Sewers, drains and water mains are usually constructed in trenches. The shallow trench installation is the installation technique used in this research.

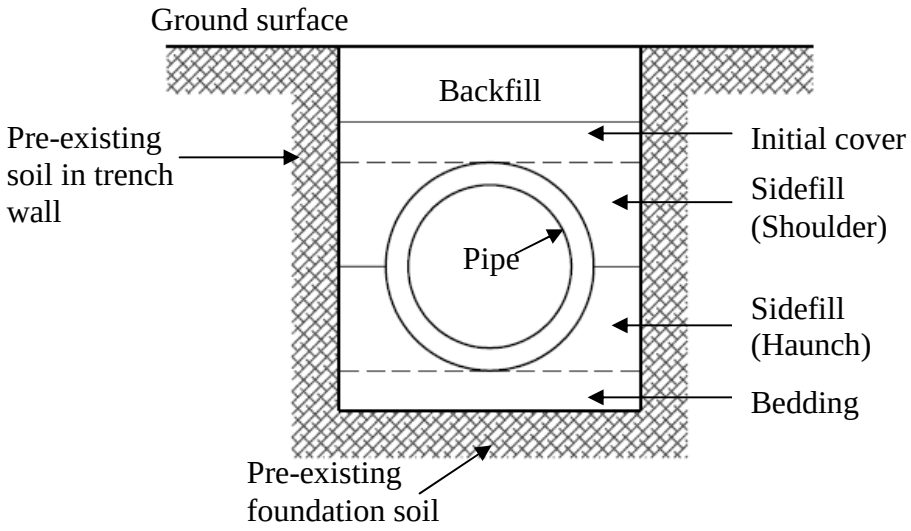

Figure 1.2 Typical details of trench installation.

1.6.2 Embankment Installation

Figures 1.3 through 1.5 show the concept of embankment installation. The pipe is placed in layers above the natural ground. Highway and railroad culverts are typically

installed under fills or embankments. The backfill soil over the pipe is the principal source of load on the pipe. The unit weight of this soil is a function of the soil type and compaction. Generally, increasing compaction of backfill over the pipe results in increased load on the pipe for both trench and embankment installations. However, the load on the pipe is also influenced by the soil beyond the embedment adjacent to the pipe. There are three types of embankment installation:

- Positive projection in sub-trench: pipe is initially installed as positive projection. When the embankment fill has been placed to an elevation of at least one pipe diameter over the proposed top of the pipe, a trench is excavated over the pipe and backfilled with a more compressible material, simulating a negative projection installation. (Figure 1.3)
- Negative projection in sub-trench: pipe is installed in relatively shallow trenches of such depth that the top of the pipe is below the level of the natural ground surface or compacted fill, and the covered with earth backfill to a height appreciably greater than the distance from the natural ground surface or original compacted fill surface to the top of the pipe. (Figure 1.4)
- Positive projection: pipe is installed with the top of the pipe projecting above the surface of the natural ground, or compacted fill, and then covered with earth backfill soil. This type also includes pipe installed in extremely wide trenches. (Figure 1.5)

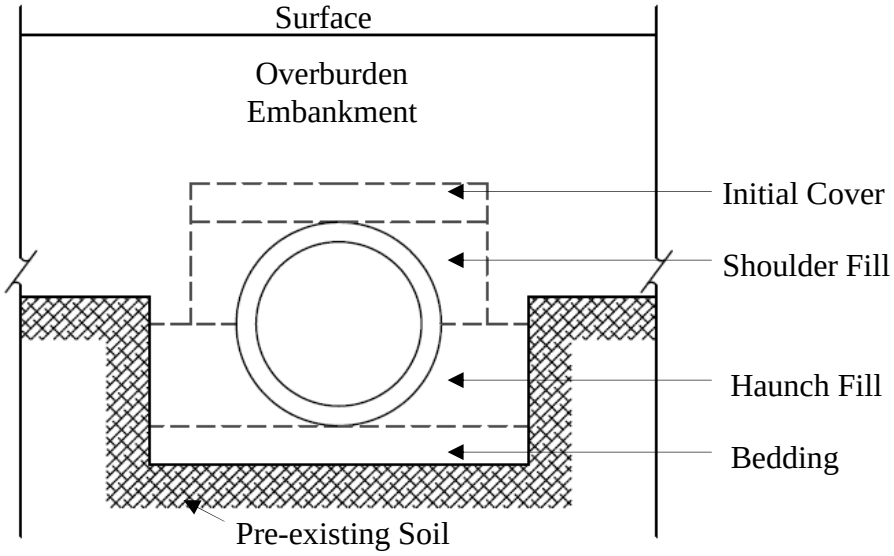

Figure 1.3 Embankment installation with partial height trench (positive projection).

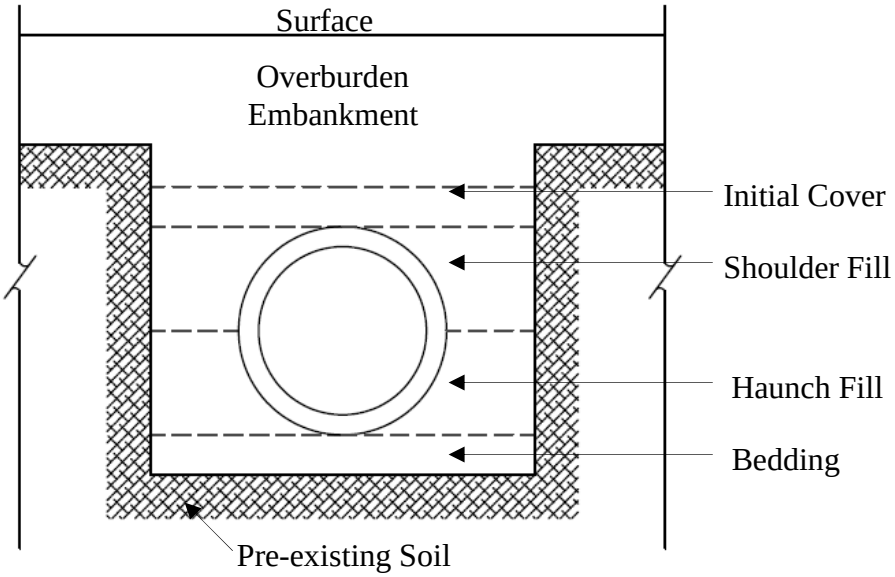

Figure 1.4 Embankment installation with partial height trench (negative projection).

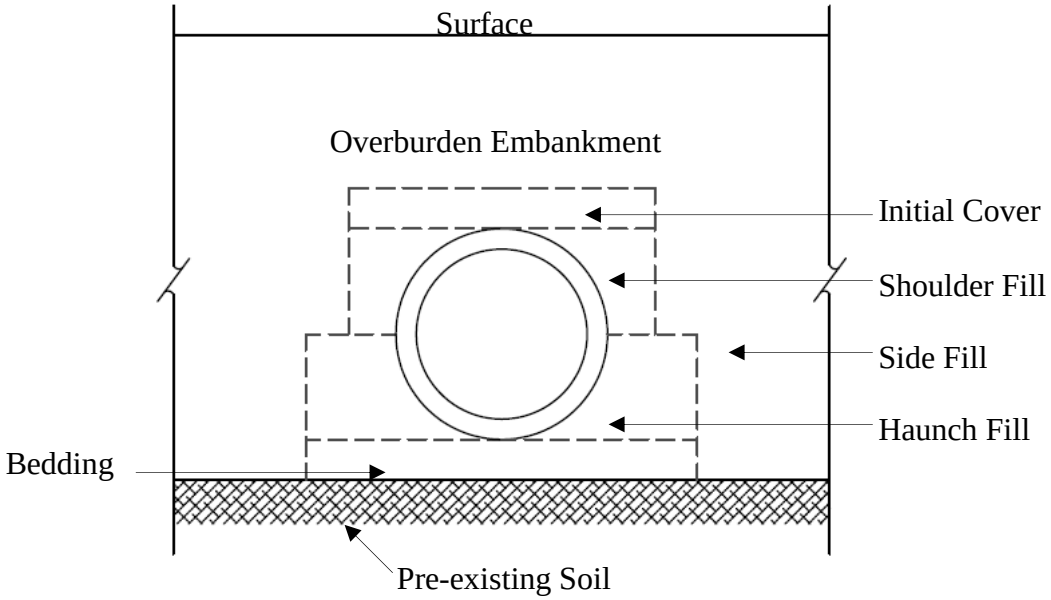

Figure 1.5 Embankment installation (positive projection).

1.7 Bedding and Foundation

Bedding is the placed or natural soil immediately below or adjacent to the bottom of the pipe that is in place before the pipe is positioned in the installation. It may consist of a flat configuration of natural in-situ soil, or natural soil that is loosened, or natural soil that is shaped to the profile of the bottom of the pipe for some portion of the bottom circumference defined as the bedding angle. In installations of higher quality, it often includes a placed soil to provide a cushion and foundation below the pipe, usually with a flat surface configuration, but sometimes shaped to the profile of the bottom of the pipe over the bedding angle. The ideal bedding consists of a relatively loose soil cushion over the central third of the pipe diameter and a very firm compacted bedding below a well compacted haunch fill over each outer third of the pipe diameter. This

concentrates support of the pipe and earth loads away from the central portion of the pipe, reducing critical bending and shear stress resultants in the invert region.

In trench installations, soil beyond the embedment at the sides of the pipe is the in-situ soil of the trench wall. The location with respect to the outside of the pipe wall and the stiffness of this natural soil affects the load on the pipe. As this soil becomes stiffer and closer to the pipe, the load on the pipe decreases. This is because a portion of the backfill soil weight is supported by shear forces at the interface between placed backfill and in-situ trench wall.

Increasing compaction of the backfill over the pipe in a trench installation increases the unit weight of the soil above the pipe and thus tends to increase the load on the pipe. However, increased compaction of trench backfill is beneficial for reducing settlement of the trench fill relative to the in-situ soil trench walls and increasing the transfer of a portion of the trench backfill weight to the trench walls due to arching action.

In positive projecting embankment installations, the type and compaction of soil beyond the embankment at the sides of the pipe may influence the load on the pipe, since increased settlement in this region causes transfer of more load to the rigid pipe. In these installations, relatively rigid concrete pipe are normally stiffer than the sidefill. However, the magnitude of the additional load is significantly influenced by the level of compaction of the backfill in the region above the top of the pipe relative to the level of compaction of sidefill, in the region adjacent to the pipe. The backfill in the region above the top of the pipe acts as a “shear beam” supported by the elastic spring stiffness

of the sidefill soil and the pipe plus its bedding. The load on the pipe is minimized when the sidefill soil is stiffer than the backfill above the top of the pipe and is increased when the sidefill soil is not as stiff as the backfill above the pipe.

1.8 Soil Characterization

Soil types are commonly classified by ASTM D 2487 (2005) or by AASHTO M 145 (2005). Descriptions and notation for classification of the principal soil types are given. These classifications of soil types apply to both natural (pre-existing) soils and to placed soils. However, constructed soil characterization for structural purposes also depends on the level of compaction for a given placed soil type. This is related to the density achieved by compaction (densification) following placement of the soil. Various quantitative measures of compaction level or soil density are used in geotechnical engineering practice. Placed or constructed soil properties, as used in the soil-structure interaction procedures are related to compaction levels represented by the commonly specified “Standard Proctor” compaction reference test and “Modified Proctor” compaction reference test. The former is defined in ASTM D 698 (2005) and AASHTO T 99 (2005). The latter is defined in ASTM D 1557 (2005), and AASHTO T 180 (2005). The level of compaction is specified as the ratio of required field dry unit weight to the maximum dry unit weight (at optimum moisture content) in the reference test, expressed as a percent.

The Modified Proctor reference test uses a greater compaction effort than the Standard Proctor reference test. Thus, a particular compaction level achieved in the field represents a lower percentage of Modified Proctor than of Standard Proctor densities.

For example, if a granular soil is compacted to 90 percent of Standard Proctor density, it may be at 85 percent of Modified Proctor density. Equivalent soil classifications are given in Table 1.1.

Table 1.1 Equivalent ASTM and AASHTO Soil Classifications

Basic Soil Type	ASTM D 2487	AASHTO M 145
SW (Gravelly sand, Sn)	SW, SP, GW, GP sands and gravels with 12% or less fines	A1, A3
ML (Sandy silt, Si)	GM, SM, ML also GC and SC with less than 20% passing a No. 200 sieve	A-2-4, A-2-5, A-4
CL (Silty clay, Cl)	CL, MH, GC, SC also GC and SC with more than 20% passing a No. 200 sieve	A-2-6, A-2-7, A-5, A-6

In Table 1.1, the soil classification listed in parentheses is the type that was tested to develop the constrained soil modulus values. The correlations to other soil types are approximate.

Soil properties for use in soil-structure interaction analysis are most accurate when obtained by testing the specific soils and compaction levels that are to be specified for a particular pipe-soil installation design. Properties for each soil category have been evaluated by testing a representative soil in each category. The soil shear strength and stiffness that is obtained by a given compaction level in terms of percent Standard Proctor dry density (or percent Modified Proctor dry density), varies significantly with soil type. Of the three standard soil types described in the previous

section, gravelly sand soils have the largest shear strength and stiffness at a given compaction level while silty clays have the least.

1.9 Goals, Objectives, and Contributions

The main objective of this research is to provide an in-depth understanding of the effect of compaction process on a buried concrete pipeline and the significance of backfill soil depth to dissipate the compaction force so that the safe covering distance from the compaction machine are identified.

To accomplish this objective, both experimental and analytical works are used. Figure 1.6 shows a flow chart that summarizes the work procedures to achieve the goals and objectives. For the full scale pipe-soil compaction, an experimental test was performed using typical standards of trench installation. As indicated by the experimental compaction test results, inadequacy of backfill soil layers above the pipeline causes the cracking and failure occurred on pipe during the compaction process. The full-scale experimental D-Load test provides the means to evaluate the cracking behavior of concrete pipes. The experimental test results of three different pipe sizes were compared with the FEM analysis. The exact value of tension stiffening used for a concrete brittle cracking model was verified.

The contribution of this research is to provide the minimum depth of backfill soil layers above a buried pipe such that the effect of compaction forces on pipe's damage is diminished. The FEM model of pipe-soil compaction was created for the parametric study of a pipeline compaction under various variables including pipe sizes, backfill depths, side-fill materials, and loading locations.

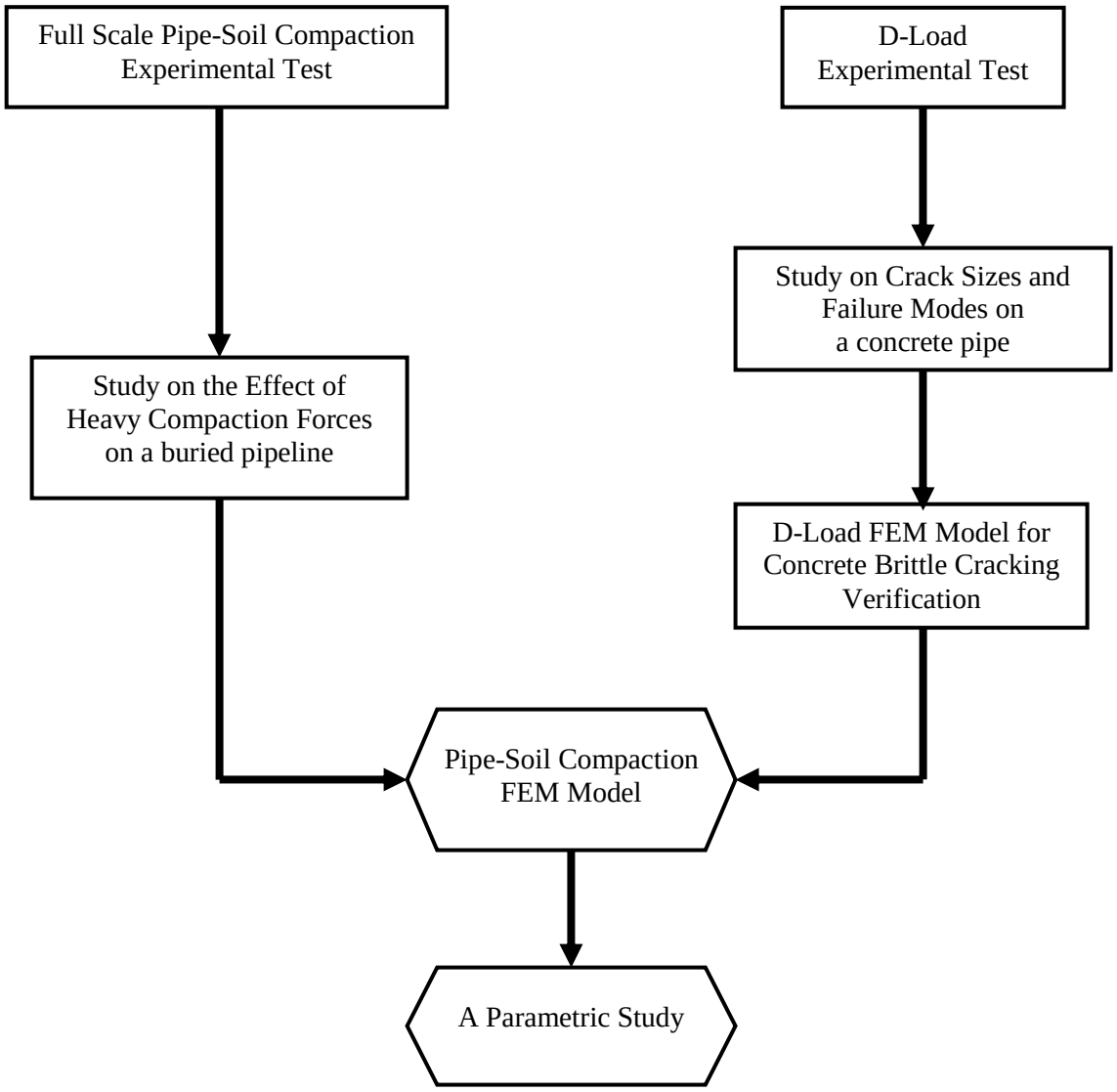

Figure 1.6 Summary of the procedure to accomplish the goal of the study.

CHAPTER 2

EXPERIMENTAL TEST STUDY

2.1 Test Description

The major goal of this study is experimental verification of the effect of large compaction forces on reinforced concrete (RC) pipeline systems. This full scale experimental testing involves the process of Type-2 trench installation for the RC pipeline system as shown in Figure 2.1. The 24-in. (61-cm) diameter pipes with concrete strength of 4,000 psi (27.60 MPa) were used for the pipe specimens. Two 8-ft (2.44-m) spans were considered as pipe specimen# 1 and specimen# 2. The 4-ft (1.22-m) spans were considered as supports. The compaction effort was applied for every increment of backfill soil layer of 6 in. (15 cm). The states of the compaction were divided into “sidefill compaction (SC)” and “backfill compaction (BC)” which will be explained in the experimental test procedures.

To fully understand the cracking behavior of reinforced concrete pipe, D-Load tests were conducted. The results were also used to verify the concrete property, “tension stiffening,” for the FEM model. A TEB machine was designed to apply a crushing force upon the pipe specimen in a plane through the vertical axis extending along the length of the specimen. The pipe specimen was supported on a lower bearing of two longitudinal strips and the load applied through an upper bearing (Figure 2.2). The test set-up was provided by the Hanson Pipe and Precast Products.

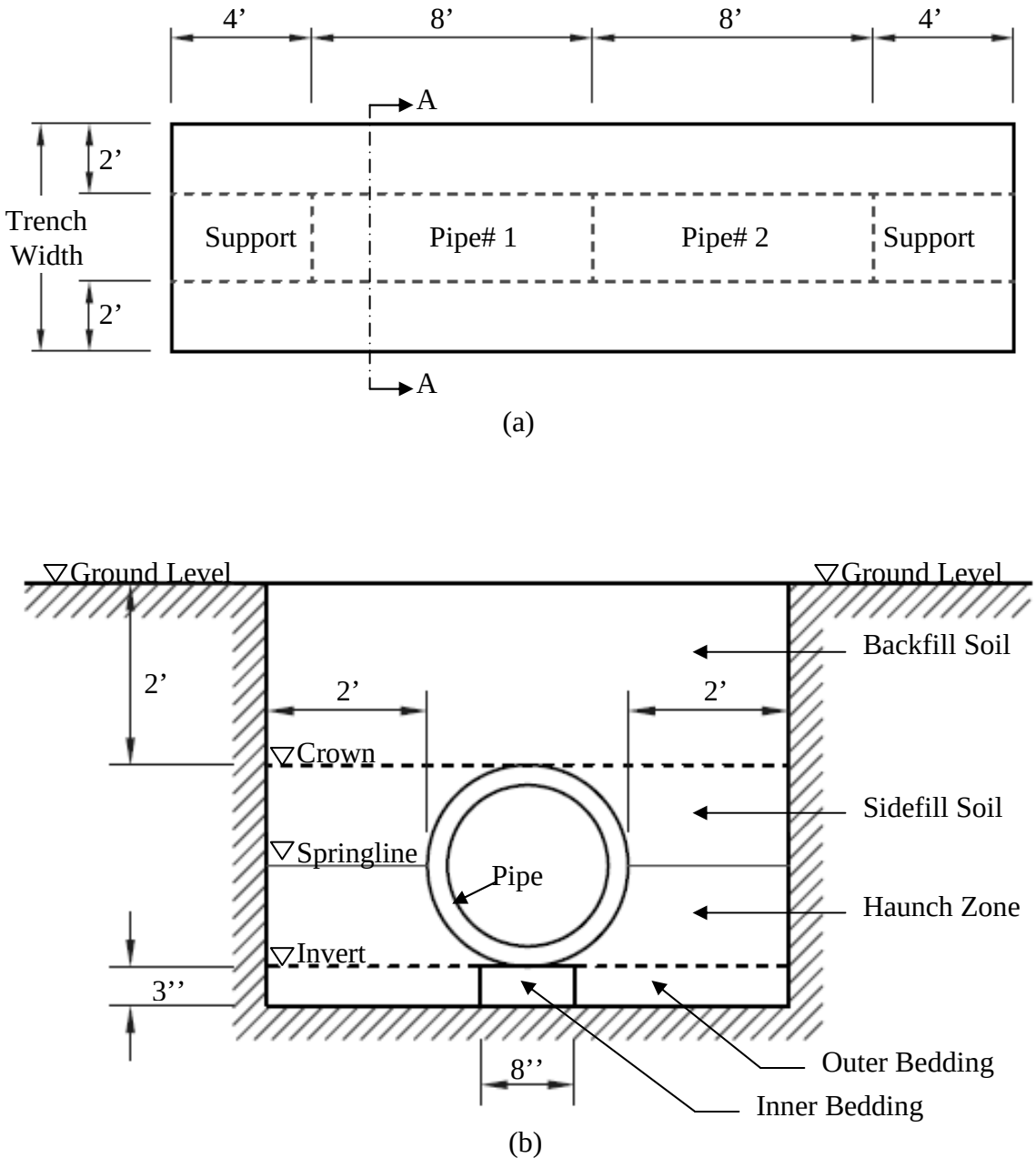

Figure 2.1 Typical details of experimental type-2 trench installation;
(a) plan view and (b) section A – A.

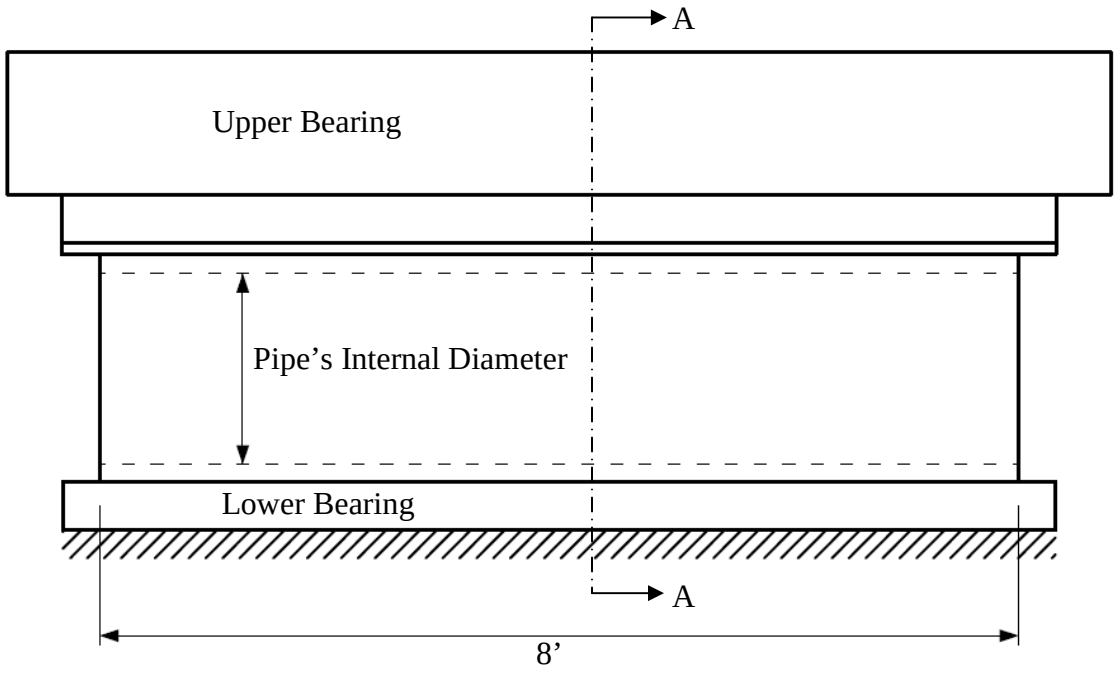

(a)

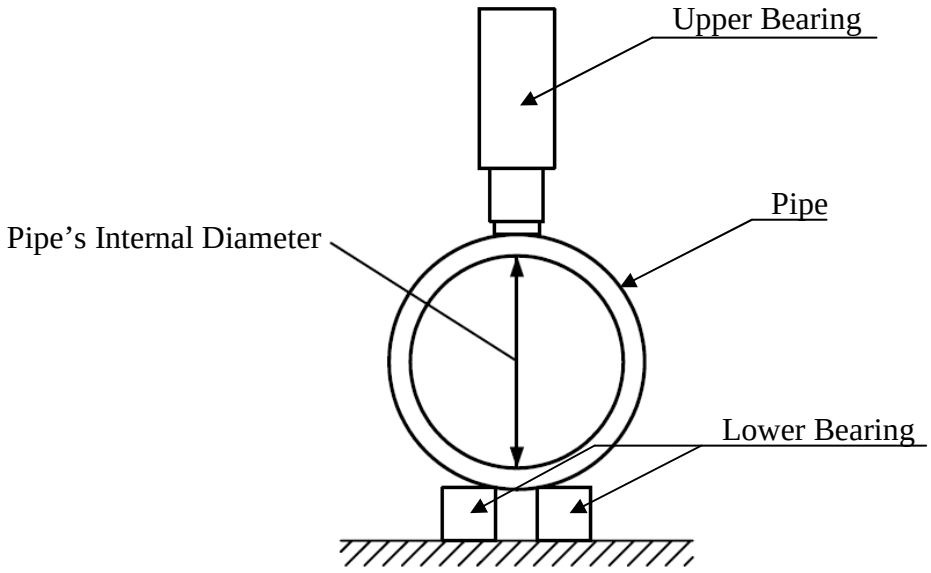

(b)

Figure 2.2 Typical details of D-Load experimental test;
(a) longitudinal view and (b) section A – A.

Eight D-Load test cases composed of two sets of the pipe diameter of 18 in. (46 cm), 36 in. (91 cm), and 54 in. (1.37 m) with concrete strength of 4,000 psi (27.60 MPa) and two sets of the pipe diameter of 54 in. (1.37 m) with concrete strength of 6,000 psi (41.37 MPa) as shown in Table 2.1. The experimental tests were corresponding to the design requirement for class III and class V reinforced concrete pipe in ASTM C 76 (2008).

Table 2.1 Total Cases for the D-Load Experimental Test

Pipe Internal Diameter	Number of Testing Specimens	
	Class III, Wall B f'_c = 4,000 psi (27.60 MPa)	Class V, Wall C f'_c = 6,000 psi (41.37 MPa)
18 in. (46 cm)	2	-
36 in. (91 cm)	2	-
54 in. (1.37 m)	2	2

The TEB bearing strength could be expressed in terms of "D–Load," with units of pounds per linear foot per foot of inside diameter (D_i):

$$D - Load = \frac{TEB\ Load}{D_i} \tag{2.1}$$

For reinforced concrete pipes, the required TEB service load was defined in terms of the D–Load to produce a 0.01–in (0.25–mm) crack, "$D_{.01}$." With the safety factor of 1.5 (against flexural cracking at service load), the required ultimate D–Load was "$D_{ult} = 1.5D_{.01}$." In this study, TEB strength for both service load condition and ultimate strength was reached.

2.2 Instrumentation and Test Setup

2.2.1 Reinforced Concrete Pipe Preparations

The reinforced concrete pipe preparation process composed of strain gauge and concrete casting (Figure 2.3). Strain gauges were attached to steel reinforcement in the radial direction. To protect the erosion of strain gauges from the concrete casting process, epoxy was used to strengthen the strain gauge attachment. All positions of attached strain gauges will be demonstrated in the test setup section. After finished strain gauge work, steel cages were brought to the concrete dry casting process.

2.2.2 Instrumentations used in the Test Programs

To evaluate the behavior of the buried pipeline system, the measurements of induced pressure on the pipe wall, deformation of the pipe's cross section, and failure behavior are considered. Induced pressure and deformation were measured by earth pressure cells and strain gauges, respectively. Also, an inspection camera was installed inside the 4-ft (1.22-m) span of the pipe. All acquired information was processed via data acquisition methods. In case of TEB test, linear variable displacement transducers (LVDT) were installed inside the pipe specimen to record the deformations of cross section horizontal and vertical. Feeler gauge was used to measure the crack width. Samples of the instrumentations used in the test programs are also shown in Figure 2.4.

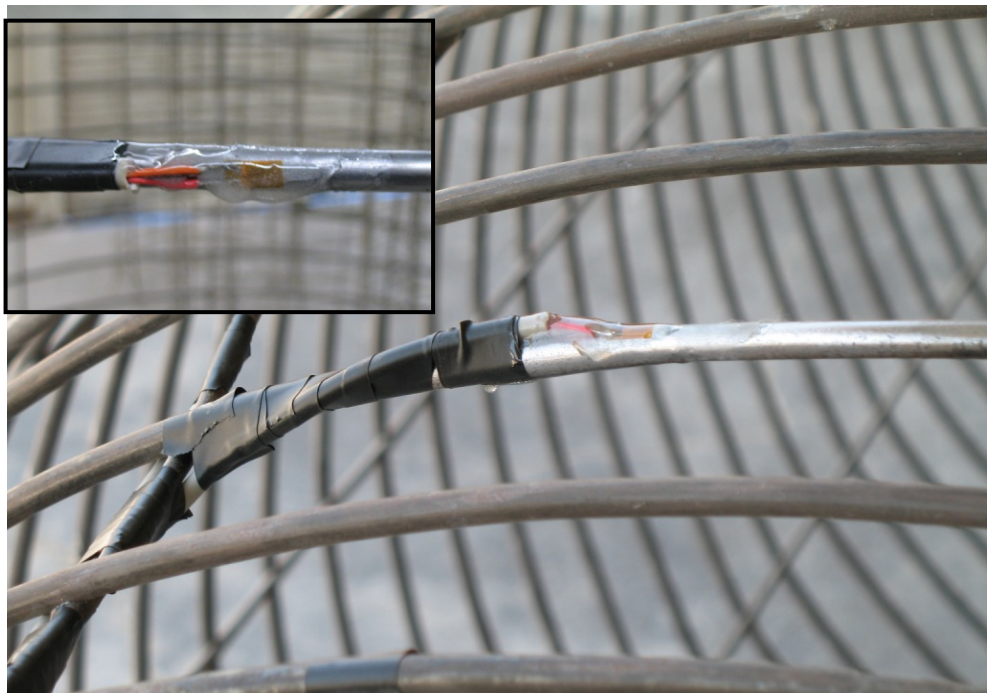

(a)

(b)

Figure 2.3 Reinforced concrete pipe preparations; (a) strain gauge installation and (b) dry casting process.

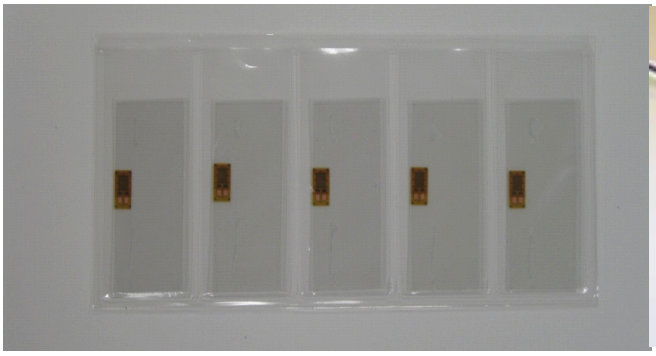

(a)

(b)

(c)

(d)

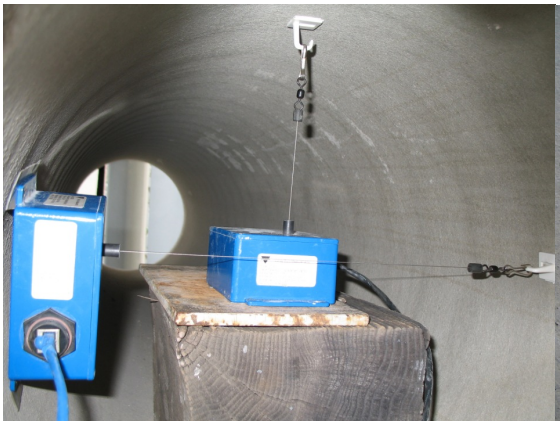

(e)

(f)

Figure 2.4 Instrumentations used in the test programs; (a) strain gauges, (b) earth pressure cell, (c) data logger, (d) inspection camera, (e) LVDTs, (f) feeler gauge.

2.2.3 Test Setup for the Pipeline Compaction Test

Before the installation process, earth pressure cells were installed on the pipeline system at four different locations as shown in Figure 2.5. At the middle span of Pipe# 1, two earth pressure cells were installed at the pipe's crown and springline. At the joint of the pipeline system, two earth pressure cells were installed at the pipe's crown on both Pipe# 1 and Pipe# 2. Each pipe specimen composed of six strain gauges, installed at the crown, springline, and invert at the middle span and joint section, as shown in Figure 2.5(b).

2.2.4 Test Setup for the D-Load Test

For D-Load test, the displacement of pipe's cross section and deformation of steel reinforcement were measured by LVDTs and strain gauges, respectively. The schematic setup details of an 8-ft (2.44-m) span pipe specimen for the D-Load test are shown in Figure 2.6. Two LVDTs were installed inside the pipe in both vertical and horizontal directions at the middle span. Also, three strain gauges were installed at crown, springline, and invert at the middle span and end span as shown in Figure 2.6(b).

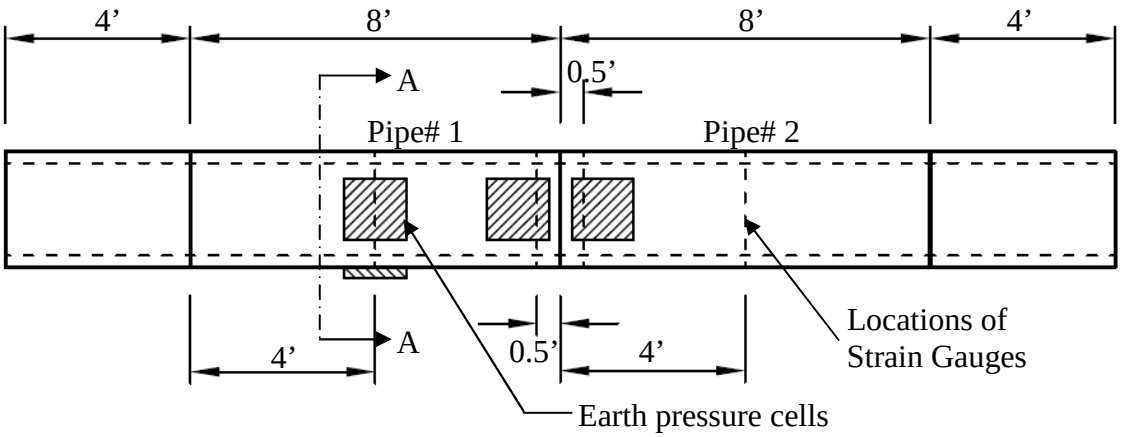

(a)

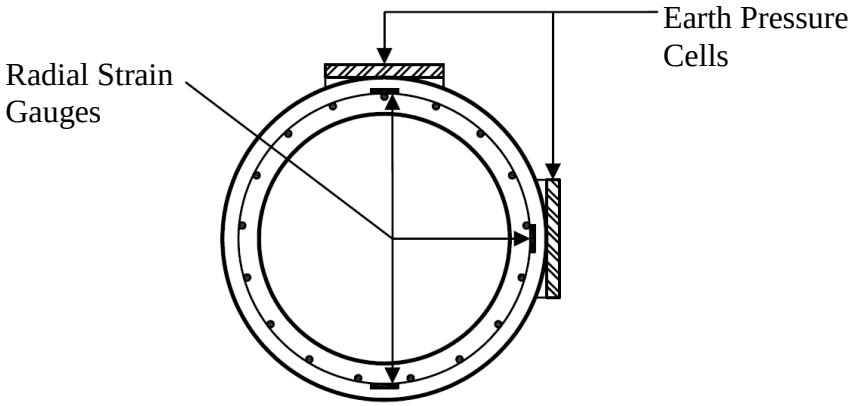

(b)

(c)

Figure 2.5 Typical test setup details for pipeline system; (a) plan view, (b) section A – A, (c) Pipe# 1 with earth pressure cells.

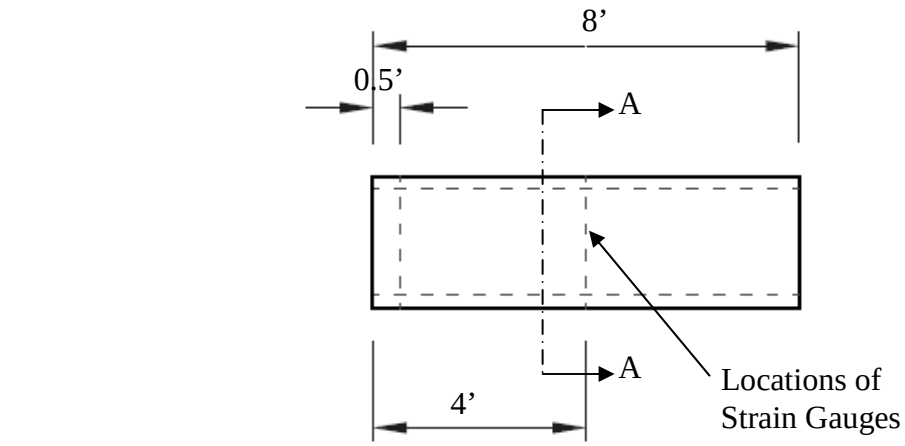

(a)

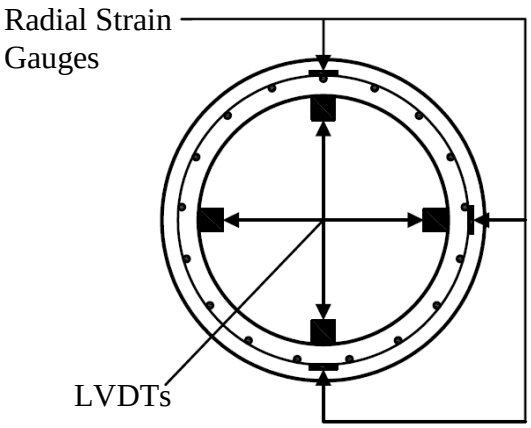

(b)

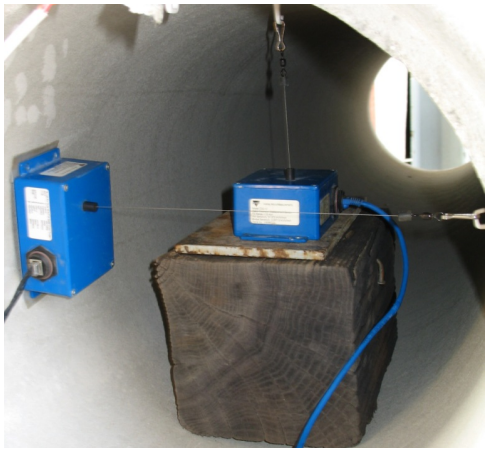

(c)

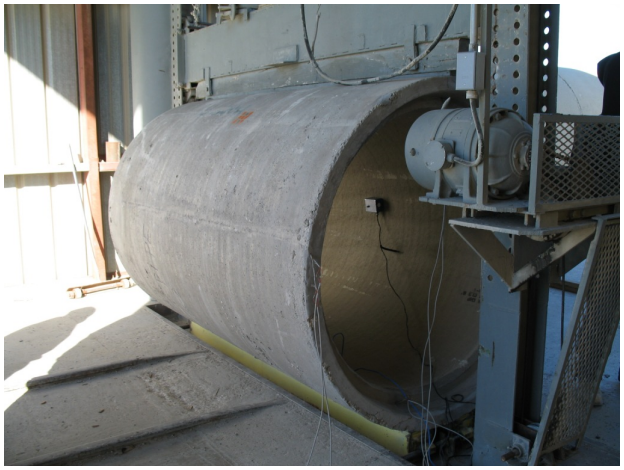

(d)

Figure 2.6 Typical test setup details for D-Load tests; (a) plan view, (b) section A – A, (c) installed LVDTs, (d) pipe set up in TEB machine.

2.3 Experimental Pipeline Compaction Test and Results

2.3.1 Pipeline Compaction Testing Processes

The trench excavation consisted of the trench dimensioning and soil removal as shown in Figures 2.7 and 2.8, respectively. The dimensions of trench were made in conformity with the Type-2 trench installation for the RC pipeline system as shown in Figure 2.1. Excavation's depth was measured in its original position by taking the difference between the ground surface at the time the trench was excavated and that after the excavation was completed. By using a backhoe, the soil removed in making the excavation will be used for the backfilling process.

After the excavation was completed, the inner bedding zone was first filled with uncompacted soil for entire length of the pipeline's position as shown in Figure 2.9. The corresponding dimensions are shown in Figure 2.1. A supporting pipe with an installed inspection camera was placed at the first end of the pipeline system as shown in Figure 2.10. Consequently, pipe specimen# 1 and pipe specimen# 2 were installed and connected with an elastomeric seal at the joint as shown in Figure 2.11. After finishing the pipeline installation as shown in Figure 2.12, which consisted of two pipe specimens and two supporting pipes at each end, all cables for the inspection camera, earth pressure cells, and strain gauges were run through the inside of the pipeline to connect to the data logger system located next to the trench installation area.

Figure 2.7 Trench dimensioning.

Figure 2.8 Accomplished trench excavation.

Figure 2.9 Bedding zone preparation.

Figure 2.10 an installed inspection camera at a supporting pipe.

Figure 2.11 Sealing work at the pipe joint.

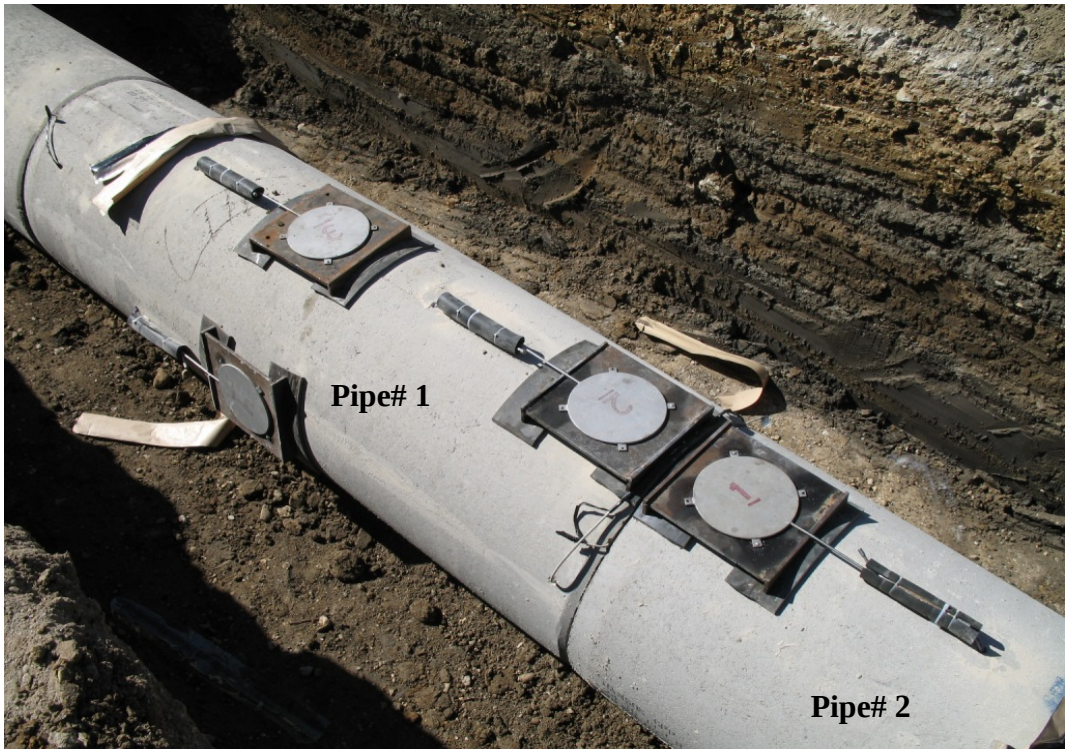

Figure 2.12 Accomplished pipeline in the trench.

To study the effect of the compacting force, the compaction process was applied for every increment of 6-in. (15-cm) backfilling soil layer. Each layer of backfilling soil was filled with a coarse-grained material and was compacted to 90% of Standard Proctor Density, measured by a nuclear gauge (model# MC-1DR-P) as shown in Figure 2.13. No subsequent layers were placed until the specified compaction level was obtained for the previous layer. The states of the compaction were divided into “side-fill compaction (SC)” and “backfill compaction (BC)”.

In the SC state, the haunch and side-fill zones were compacted by the backhoe’s bucket tamping as shown in Figure 2.14(a). The SC state was performed until the pipe’s crown level was reached. Figure 2.14(b) shows the measurement of soil compaction and height of backfilling soil layer referred to the pipe’s crown level.

Figure 2.13 Nuclear gauge for determining soil density and moisture content (model# MC-1DR-P).

(a)

(b)

Figure 2.14 Side-fill Compaction (SC) state; (a) compaction process and (b) soil compaction and level measurement.

In the BC state, the compaction forces composed of a vibratory force from hoe pack and the weight of backhoe itself. As shown in Figure 2.15, the hoe pack model# HC920 used in the experimental test has an impulse force of 16,000 lbf (71 kN) and delivers 2,200 cycles per minute. The compaction force is transferred to soil via a 28-in. (71-cm) by 40-in. (102-cm) plate. The BC process centered on the heavy compaction of backfill soil layers above the pipe's crown level. Figure 2.16(a) shows the first 6-in. (15-cm) backfilling soil above the pipe's crown level. The backfill soil was thoroughly compacted for the entire area of trench installation as shown in Figure 2.16(b). The compaction process was applied for every increment of 6-in. (15-cm) backfilling soil layer. The pipe's failure was monitored by the inspection camera installed inside a supporting pipe. When the pipe's failure occurred, the BC process was completely stopped so the failure mode on a pipeline could be investigated.

(a) (b)

Figure 2.15 Hoe pack (model# HC920) used in the experimental test;
(a) before installed and (b) installed to backhoe's arm.

(a)

(b)

Figure 2.16 Backfill Compaction (BC) state; (a) backfilling soil above the pipe's crown level and (b) compaction process.

2.3.2 Nomenclature used in Pipeline Compaction Test Results

To examine the behavior of the pipeline, various positions of loading and deformation were investigated. The interesting locations at the crown, invert, and springline were monitored at the middle-span and joint of the pipeline. The results were recorded in both SC and BC states. Time periods corresponding to the compactor locations were explained in Figure 2.17. The following nomenclature was used to identify each test specimen:

AAA_BBB_XXX,

where:

AAA – Positions on the pipe wall for each cross-section, composed of

INV – Invert

CRN – Crown

SPL – Springline

BBB – Positions respect to the span of the pipeline (see Figure 2.5(a)), composed of

MS1 – Middle span of pipe# 1

MS2 – Middle span of pipe# 2

JT1 – Joint of pipe# 1

JT2 – Joint of pipe# 2

XXX – Steps of the compaction process, divided into

SC – Side-fill compaction state

BC – Backfill compaction state

For instances;

- INV_MS1_SC defines the location at invert, middle span of pipe# 1, in the side-fill compaction state.
- CRN_MS2_SC defines the location at crown, middle span of pipe# 2, in the side-fill compaction state.
- SPL_JT1_BC defines the location at springline, joint of pipe# 1, in the backfill compaction state.

The following sections show the interesting results for the critical positions on a pipeline. All compaction experimental test results are provided in Appendix A.

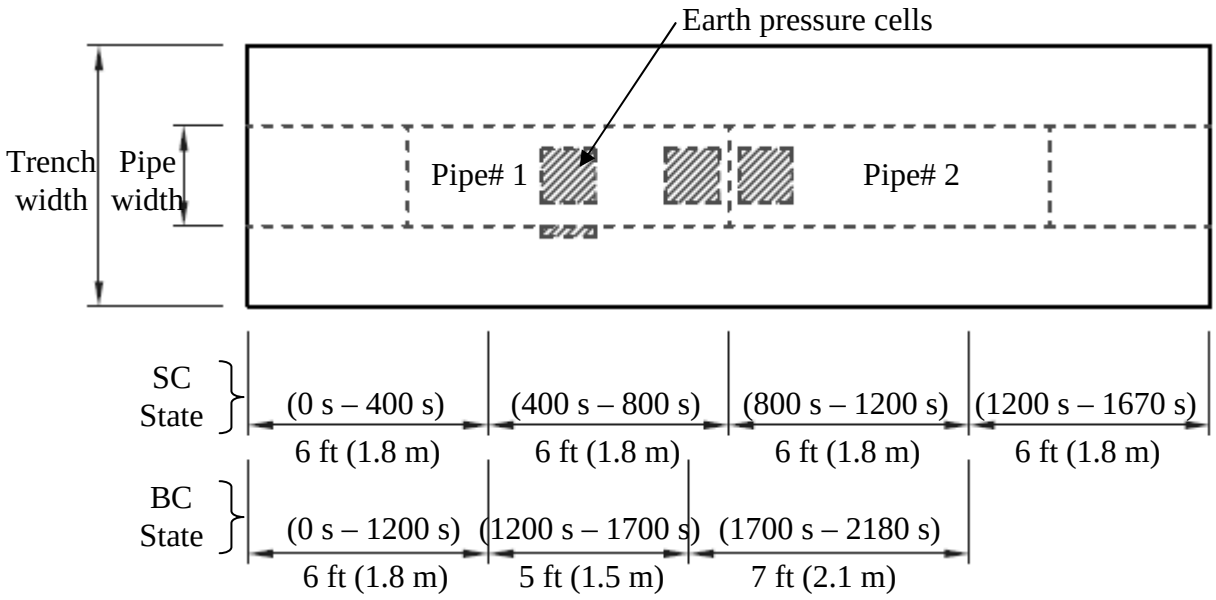

Figure 2.17 Time periods corresponding to compaction states (plan view).

2.3.3 Maximum Pressures Induced on the Pipe Wall in the SC state

In the SC state (Figures 2.18), the maximum pressures on the pipe at crown and springline were 1.8 psi (12.41 kPa) and 7 psi (48.27 kPa), respectively. Both values occurred at the mid-span of the Pipe# 1. Consequently, the induced pressures at the pipe's springline were 4 times higher than those at the pipe's crown.

2.3.4 Maximum Pressures Induced on the Pipe Wall in the BC state

During the BC state (Figures 2.19), the results show that at the same location (middle span of the Pipe# 1 in this case), the maximum pressures induced at the pipe's crown were 9 times higher than those at the pipe's springline, which were 38.71 psi (266.90 kPa) versus 4.45 psi (30.68 kPa), respectively. Also, the maximum pressures induced at the joint of the pipeline were 1.4 times higher than those at the middle span of Pipe# 1, which were 52.96 psi (365.15 kPa) versus 38.71 psi (266.90 kPa), respectively. Consequently, the highest pressures which were transferred at the pipe's crown by the hoe pack occurred at the joint of the pipeline.

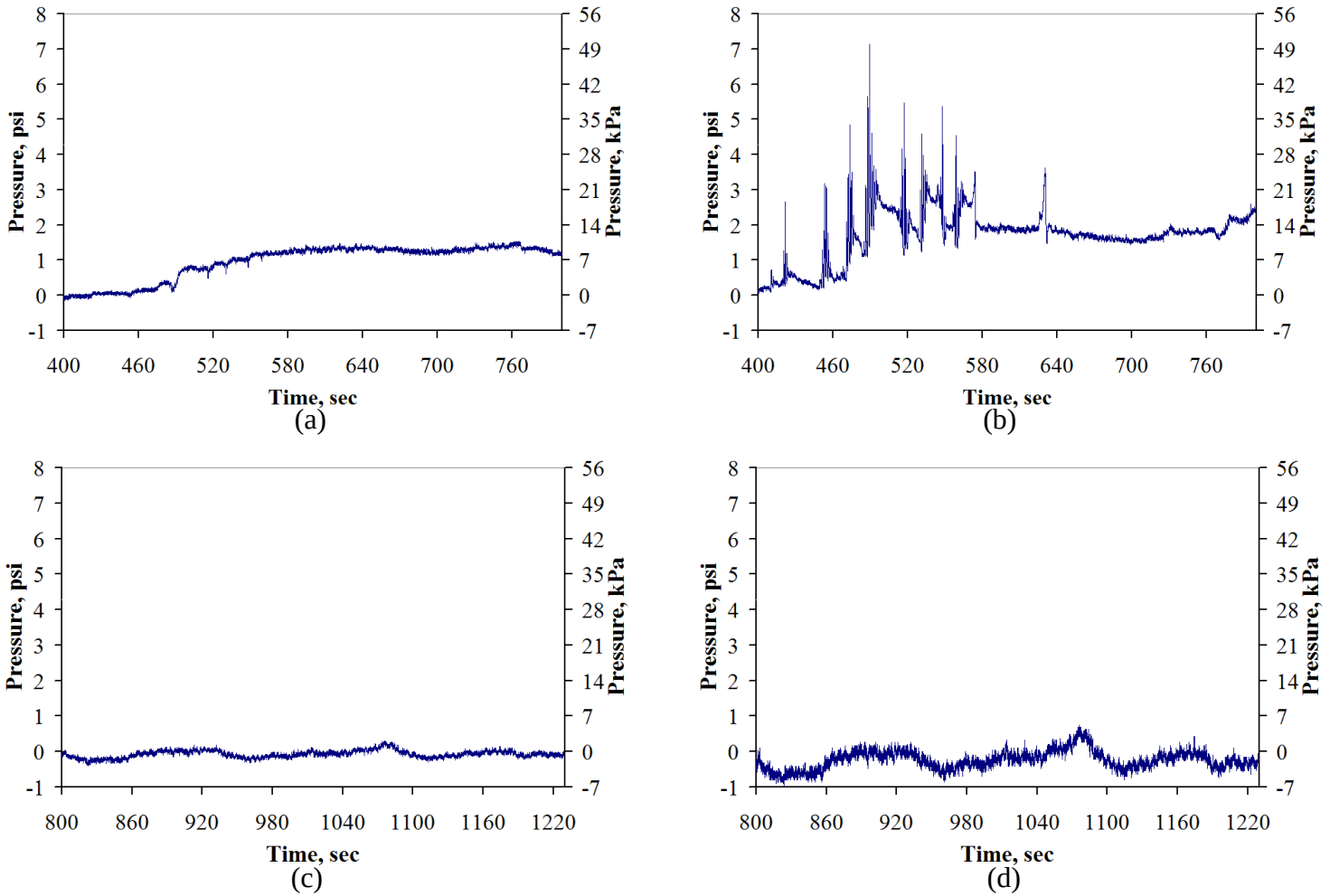

Figure 2.18 Different locations of pressure results in the SC state; (a) CRN_MS1_SC, (b) SPL_MS1_SC, (c) CRN_JT1_SC, (d) CRN_JT2_SC.

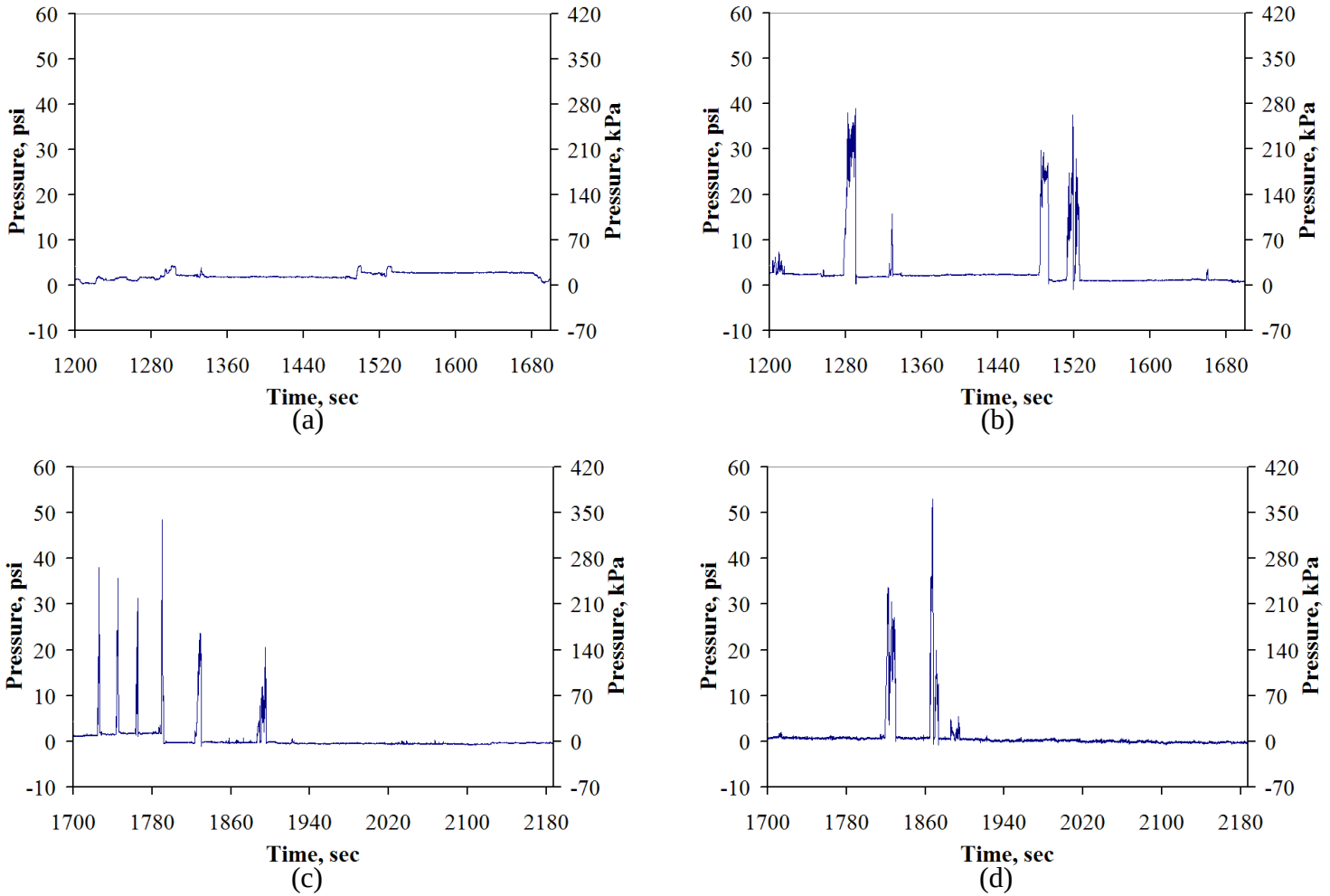

Figure 2.19 Different locations of pressure results in the BC state; (a) CRN_MS1_BC, (b) SPL_MS1_BC, (c) CRN_JT1_BC, (d) CRN_JT2_BC.

2.3.5 Deformation of the Steel Cage in the SC state

The deformation results were measured by the strain gauges attached to steel cage in the RC pipes. Three strain gauges at CRN_MS1, INV_MS1, and CRN_JT2 were damaged during the concrete casting process. The deformation of the steel cage was more obvious at the crown and springline than that at the invert. Figure 2.20(a) shows the maximum strain of 20×10^{-6} in./in. occurred at crown, mid-span of Pipe# 1. Figure 2.20(b) shows the second maximum strain of 15×10^{-6} in./in. occurred at springline, joint of Pipe# 1. In this SC state, the deformations of steel cage were small when compared with those in the BC state. This is because the compaction force was applied at the side-fill soil zone and then transferred to a pipeline.

2.3.6 Deformation of the Steel Cage in the BC state

During the BC state, the compaction force was applied at the backfill soil zone through the location of a pipeline and produced high deformation on the steel cage in the pipe wall. As shown in Figure 2.20(c) the maximum strain at crown, mid-span of Pipe# 1 was $16{,}776 \times 10^{-6}$ in./in. The strain at the pipe's springline was the second highest from the strain at the pipe's crown. As shown in Figure 2.20(d), the maximum strain at springline, joint of the Pipe# 1 was 50×10^{-6} in./in. In this case, the maximum strain at crown was 336 times higher than that at springline because the compaction was applied above the pipe at the backfill soil layer.

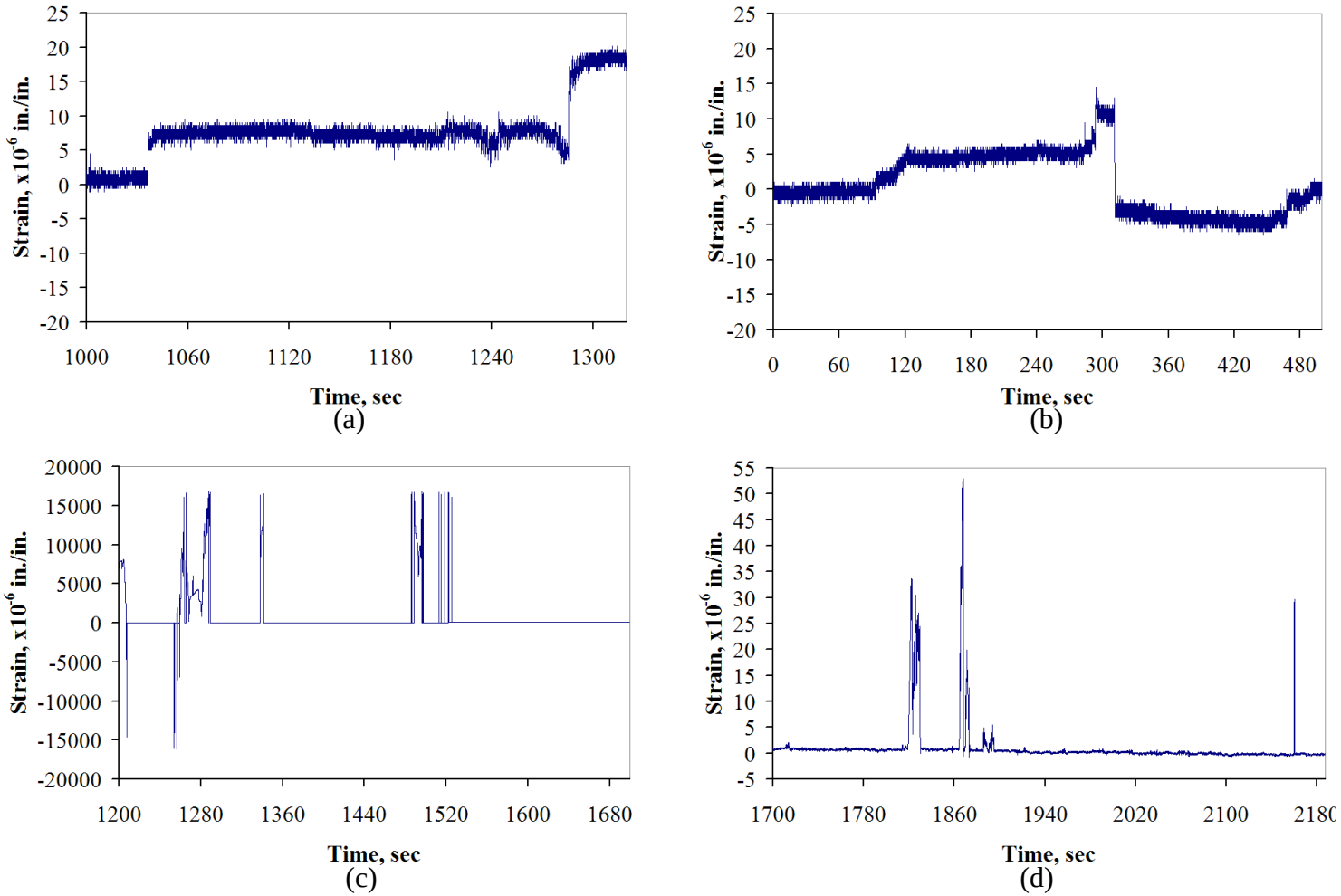

Figure 2.20 Different locations of strain results in SC and BC states; (a) CRN_MS1_SC, (b) SPL_JT1_SC, (c) CRN_MS1_BC, (d) SPL_JT1_BC.

2.3.7 Failure Observation

During the BC state, the damage on the pipeline occurred at the same locations of the highest induced pressure and deformation. The occurrence of damage was monitored by the inspection camera inside a supporting pipe. This occurred at the pipe's crown, at joint when the first layer of 6-in (15-cm) height backfill soil was covered above the pipe's crown level. Then, the backfill soil was removed so that the damage on pipe can be thoroughly investigated. There were two types of damage from the observation: fracture and crack line as shown in Figure 2.21. The fracture resulted in the deterioration and a hole on the pipe's wall. The dimension of fracture was 3.50 in. (8.89 cm) by 1.50 in. (3.81 cm). The crack line was produced continually from the fracture and caused an opening of the concrete covering the steel reinforcement. Crack lines propagated at the pipe joint from the crown to the region above the springline level as shown in Figure 2.21(b). There was no occurrence of the longitudinal crack along the pipe length. Also, no damage occurred at pipe's springline and invert. This section emphasized the deficiency of backfill soil cover above the pipeline under the compaction process.

(a)

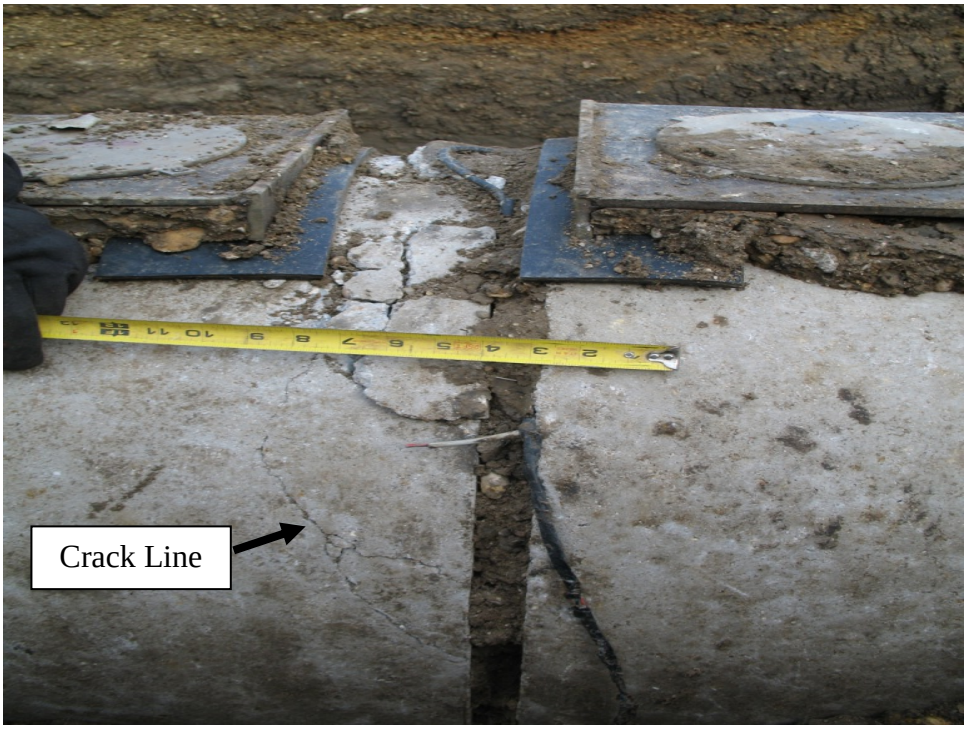

(b)

Figure 2.21 Failure at joint of pipeline; (a) fracture and (b) cracklines.

2.4 Experimental Pipeline D-Load Test and Results

2.4.1 D-Load Testing Processes

To verify the FEM algorithm, the TEB tests known as “D-Load tests” were conducted on eight full-scale reinforced concrete pipes with 18-in. (46-cm), 36-in. (91-cm), and 54-in. (1.37-m) diameters manufactured per the ASTM C 76 (2008). The compared results between FEM and experimental tests were accomplished for load-deformation, crack initiation, and crack propagation. Further, the significance of crack width in pipe stiffness was discussed.

The standard TEB testing machine follows ASTM C 497 (2007). A pipe specimen was uniformly placed on the two bearing strips. When the adjustment of pipe’s position was completed, the upper bearing strip was firmly placed on the top (crown) of the pipe as shown in Figure 2.22. The LVDTs were installed inside the pipe for both vertical and horizontal directions. All cable works for the LVDTs and strain gauges were connected to the data logger as shown in Figure 2.23.

In order to observe the behavior of cracks on the pipe, load increments were gradually applied at the rate of 3,000 lbf/linear foot (44 kN/linear meter) of pipe per minute. This rate of loading, controlled by the TEB machine (Figure 2.24(a)), was continuous until the service strength and the ultimate strength were reached. Using a feeler gauge (Figure 2.24(b)), the opening crack sizes were measured corresponding to the magnitudes of the applied load. Displacement and strain results were recorded by the data logger.

(a)

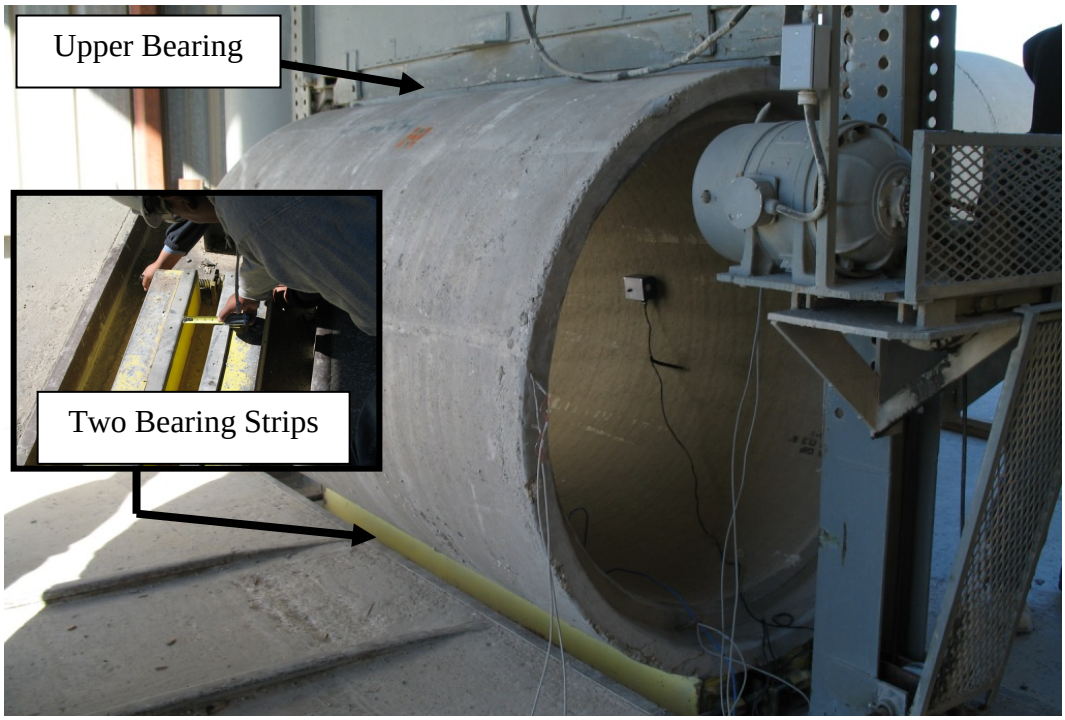

(b)

Figure 2.22 Positioning and alignment; (a) pipe conveyance and (b) instrumented pipe in TEB machine.

(a)

(b)

Figure 2.23 Instrument set up; (a) LVDTs in vertical and horizontal directions and (b) data logger and cable connection.

(a)

(b)

Figure 2.24 Load control and crack observation; (a) loading rate control and (b) crack size measurement.

2.4.2 Nomenclature used in D-Load Test Results

To fully understand the cracking behavior and failure modes of concrete pipe, experimental D-Load tests were conducted on three different pipe sizes corresponding to the design requirement for classes III and V reinforced concrete pipe as specified in ASTM C 76 (2008). The nomenclature was used to identify the D-Load test specimens. For instances; "P18_III(B)_1" stands for an 18-in. (46-cm) pipe, class III wall B, Specimen# 1. "P54_V(C)_2" stands for a 54-in. (1.37-m) pipe, class V wall C, Specimen# 2.

Under the TEB load, positive moments that produce tension in the inner surface of the pipe wall and compression in the outer surface of the pipe wall occur at crown and invert. In contrary, negative moments that produce compression in the inner surface of the pipe wall and tension in the outer surface of the pipe wall occur at springline as shown in Figure 2.25.

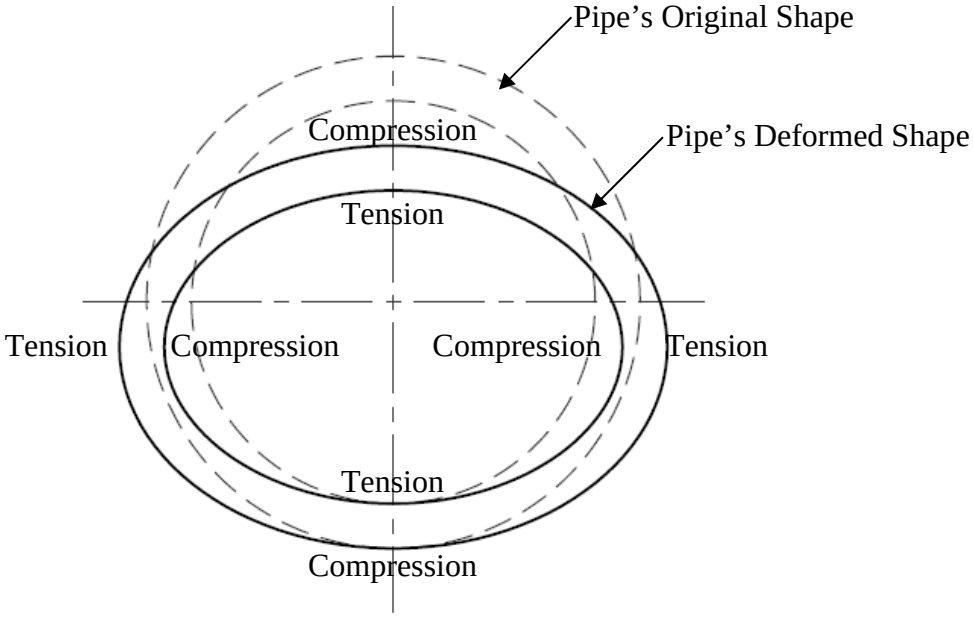

Figure 2.25 Deformation of a pipe cross-section.

2.4.3 D-Load Testing Results

Table 2.2 shows the D-Load experimental results of test loads at the state of 0.01–in. (0.25-mm) crack "$P_{.01}$" and the state of ultimate strength "P_{ult}" for all sizes of pipe specimens. Different sizes and classes of reinforced concrete pipe express the different load capacity results. For the 54-in. (1.37-m) pipe, there is the variation in strength between Specimen# 1 and Specimen# 2 because of the occurrence of shear crack which will be explained in the failure mode (Section 2.4.4). According to the ASTM C 76 (2008), the D-Load is expressed by test load per linear foot per foot of diameter. For an instance of Specimen# P18_III(B)_1; $D_{.01} = \frac{P_{.01}}{L \times D_i} = \frac{23{,}125\ lbf}{8\ ft \times 1.5\ ft} =$ 1,927 lbf / ft-length / ft-diameter. All experimental D-Load results at the 0.01–in. (0.25-mm) crack "$D_{.01}$" and the state of ultimate strength "D_{ult}" are also calculated and shown in Table 2.3.

Table 2.2 Experimental Test Load Results

Specimen#	$P_{.01}$, lbf (kN)	P_{ult}, lbf (kN)	P_{ult} / $P_{.01}$
P18_III(B)_1	23,125 (103)	34,910 (155)	1.51
P18_III(B)_2	17,244 (77)	37,677 (168)	2.19
P36_III(B)_1	44,655 (199)	75,722 (337)	1.70
P36_III(B)_2	38,956 (173)	65,229 (290)	1.67
P54_V(C)_1	81,278 (362)	127,210 (566)	1.57
P54_V(C)_2	69,291 (308)	85,620 (379)	1.24
P54_III(C)_1	51,493 (229)	105,688 (470)	2.05
P54_III(C)_2	48,260 (215)	105,607 (469)	2.20

Table 2.3 Experimental D-Load Results

Specimen#	$D_{.01}$, lbf / ft-length / ft-diameter	D_{ult}, lbf / ft-length / ft-diameter	D_{ult} / $D_{.01}$
P18_III(B)_1	1,927	2,909	1.51
P18_III(B)_2	1,437	3,140	2.19
P36_III(B)_1	1,861	3,155	1.70
P36_III(B)_2	1,623	2,718	1.67
P54_V(C)_1	2,258	3,534	1.57
P54_V(C)_2	1,925	2,378	1.24
P54_III(C)_1	1,443	2,936	2.05
P54_III(C)_2	1,341	2,934	2.20

2.4.4 Failure Modes

The failure modes recorded were flexural for 18-in. (46-cm) and 36-in. (91-cm) diameter and shear for 54-in. (1.37-m) diameter. For all testing pipe sizes, the longitudinal cracks started at invert, crown and springline, respectively. For flexural type failure, the crack pattern started at invert and crown. Cracks initiated from internal surface of the pipe wall (tension zone) and propagated outward in the radial direction to external surface of the pipe wall (compression zone). At springline, cracks initiated from external surface of the pipe wall (tension zone) and propagated inward in the radial direction to internal surface of the pipe wall (compression zone).

As shown in Figure 2.26 for P18_III(B), a single opening crack occurring at a location of invert, crown and springline is pronounced. Figure 2.27(a) shows the crack behavior in P36_III(B) was similar to the case of P18_III(B), but three additional crack lines propagated at the crown location. Also, Figures 2.27(b) and 2.27(c) show a single opening crack in P36_III(B) at invert and springline, respectively.

In the case of P54_V(C), the types of failure cracks observed were different from smaller pipes. Due to a large diameter pipe, the wall thickness is relatively thick and the reinforcing system takes the form of double cages. When the double cages became inadequate under the increased loading, additional shear and diagonal tension were encountered as shown in Figures 2.28(a) and 2.28(b). Thus, the mode of failure recorded for these pipes was shear. Typically, the stirrups, tied to the inner and outer cages, resist diagonal stress and prevent slabbing at the inner wall. Slabbing is a radial tension failure wherein the inside cage tends to flatten out at the invert and crown sections whereupon the cage pulls away from the pipe wall (Concrete Pipe Information, 1976; and Buttner, 1985). This behavior leads to a pattern of shear crack on the pipe wall. Moreover, multiple cracks which composed of five lines of longitudinal cracks formed along the springline of the 54-in. (1.37-m) pipes. These multiple cracks also distributed above and below the location of pipe's springline as shown in Figure 2.28(c).

(a) (b)

(c)

Figure 2.26 Cracks on P18_III(B); (a) crown, (b) invert, (c) springline.

(a) (b)

(c)

Figure 2.27 Cracks on P36_III(B); (a) crown, (b) invert, (c) springline.

(a) (b)

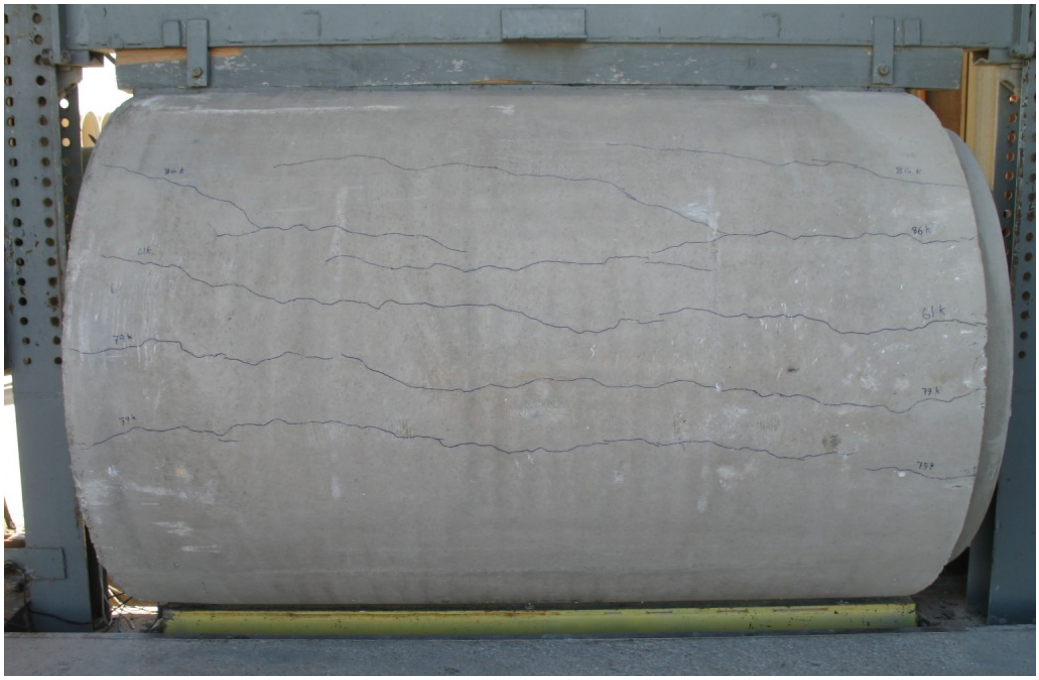

(c)

Figure 2.28 Cracks on P54_V(C); (a) crown, (b) invert, (c) springline.

2.4.5 Different crack sizes with load increments

As the applied load increased, the number and size of cracks increased. Various crack sizes were measured corresponding to the increasing loads. Thus, the evaluation of the crack sizes with the strength capacity of pipe specimens can be explained via the load-deformation curves. The deformation of pipe's cross section was measured in both vertical and horizontal directions. Also, all test load results at the 0.01-in. (0.25-mm) crack and at the ultimate capacity were corresponding to those in the Table 2.2.

For the 18-in. (46-cm) pipe, the load-deformation curves were shown in Figures 2.29 and 2.30 for P18_III(B)_1 and P18_III(B)_2, respectively. The deformations of a pipe's cross section were recorded until the 0.01-in. (0.25-mm) crack occurred at invert. The loads at the 0.01-in. (0.25-mm) crack were 23,125 lbf (103 kN) for P18_III(B)_1 and 17,244 lbf (77 kN) for P18_III(B)_2. After this point, the LVDTs were removed from the 18-in. (46-cm) pipe specimens and no further deformation data were recorded. However, the ultimate loads at failure were 34,910 lbf (155 kN) for P18_III(B)_1 and 37,677 lbf (168 kN) for P18_III(B)_2.

For the 36-in. (91-cm) pipe, the initiation of crack at invert was recorded from the hair line crack size until the failure crack size. The results indicate that after the occurrence of 0.01-in. (0.25-mm) crack at the invert, the pipe was capable to support more loads without failure. Figure 2.31 shows the load-deformation of P36_III(B)_1. As the applied load reached 75,722 lbf (337 kN), a pipe failed with the crack size of 0.03-in. (0.75-mm) width. The ultimate load was 1.7 times higher than the load at the 0.01-in. (0.25-mm) crack. Figure 2.32 shows the load-deformation of P36_III(B)_2. As

the applied load reached 65,229 lbf (290 kN), a pipe failed with the crack size of 0.05-in. (1.25-mm) width. The ultimate load was 1.67 times higher than the load at the 0.01-in. (0.25-mm) crack.

In the case of the 54-in. (1.37-m) pipe, crack behaviors included the shear crack (slabbing) and the multiple cracks. The results are explained in the load-deformation curves together with the related tables. Figure 2.33 and Table 2.4 show the results of P54_V(C)_1. The 0.01-in. (0.25-mm) crack, occurring at the load of 81,278 lbf (362 kN), initiated at invert and had no effect on the pipe strength. At crown, the 0.01-in. (0.25-mm) crack occurred when the load reached 95,176 lbf (423 kN). After the load exceeded 95,176 lbf (423 kN), there was no change in the sizes of opening cracks which remained 0.01 in. (0.25 mm) and 0.016 in. (0.40 mm) at crown and invert, respectively. But, the shear cracks initiated at these locations. Shear cracks separated the pipe wall through the thickness so that they caused the failure at the load of 127,210 lbf (566 kN). The load at shear crack is 1.2 times of the load at the 0.01-in. (0.25-mm) crack while the load at failure is 1.6 times of the load at 0.01-in. (0.25-mm) crack.

Figure 2.34 and Table 2.5 show the results of P54_V(C)_2. The 0.01-in. (0.25-mm) crack at invert and crown initiated at the applied load of 69,291 lbf (308 kN). Beyond the applied load of 78,920 lbf (351 kN), there was no change in sizes of opening cracks which remained 0.01 in. (0.25 mm) at invert and crown, but the shear cracks initiated at these locations. Shear cracks caused the failure at the load of 85,620 lbf (381 kN). The load at shear crack is 1.14 times of the load at 0.01-in. (0.25-mm) crack while the load at failure is 1.2 times of the load at 0.01-in. (0.25-mm) crack.

Figure 2.35 and Table 2.6 show the results of P54_III(C)_1. The 0.01-in. (0.25-mm) crack initiated at the invert and crown when the applied load reached 51,493 lbf (229 kN). The shear crack started when the load reached 79,436 lbf (353 kN) and propagated until a pipe failed at the load of 105,688 lbf (470 kN). The load at shear crack is 1.54 times of the load at 0.01-in. (0.25-mm) crack while the load at failure is 2.05 times of the load at 0.01-in. (0.25-mm) crack.

Figure 2.36 and Table 2.7 show the results of P54_III(C)_2. The 0.01-in. (0.25-mm) crack initiated at the invert and crown when the applied load reached 48,260 lbf (215 kN). The pipe's strength was changed, but it was still capable to support the applied load. The shear crack initiated when the load reached 83,348 lbf (371 kN) and propagated until a pipe failed at the load of 105,607 lbf (470 kN). The load at shear crack is 1.7 times of the load at 0.01-in. (0.25-mm) crack while the load at failure is 2.2 times of the load at 0.01-in. (0.25-mm) crack.

At the springline of the 54-in. (1.37-m) pipe, for both class-V and class-III, the longitudinal crack sizes were hair lines, but the total amount of hair line cracks increased considerably. At failure, there were five crack lines for a class-V pipe and four crack lines for a class-III pipe. Compared to the 18-in. (46-cm) and 36-in. (91-cm) pipes, cracks at the springline of 54-in. (1.37-m) pipe indicate that the larger pipe size has larger load-transferred surface areas so that cracks are able to propagate and distribute over these regions in the forms of the multiple crack.

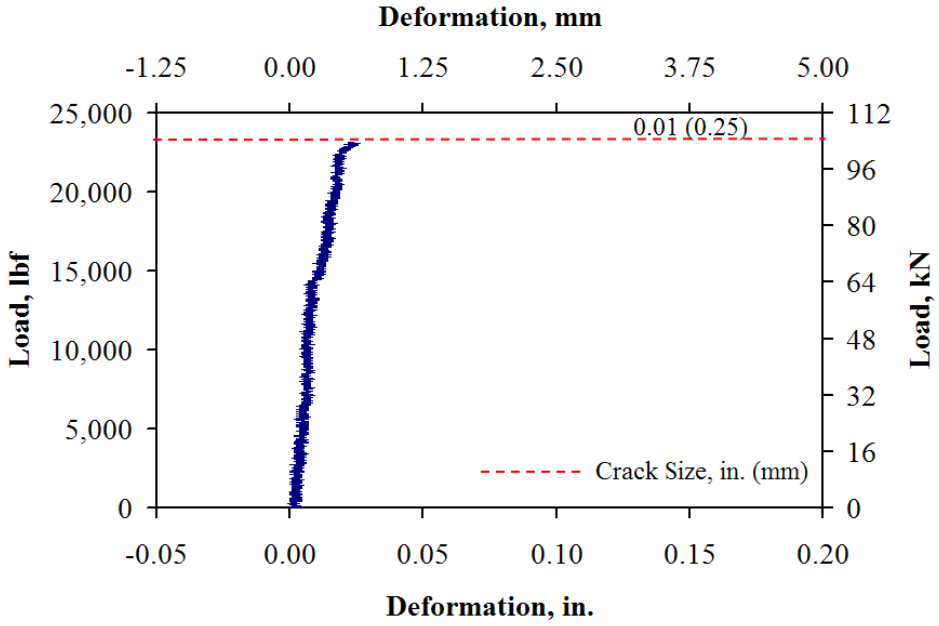

(a)

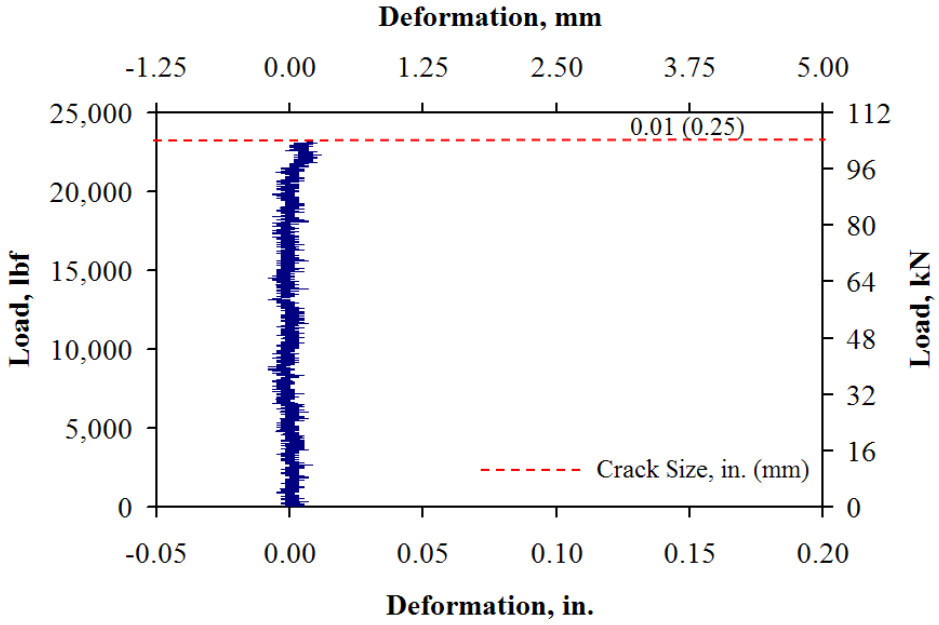

(b)

Figure 2.29 Load versus deformation results at mid span of P18_III(B)_1;
(a) vertical deformation of pipe's cross section and
(b) horizontal deformation of pipe's cross section.

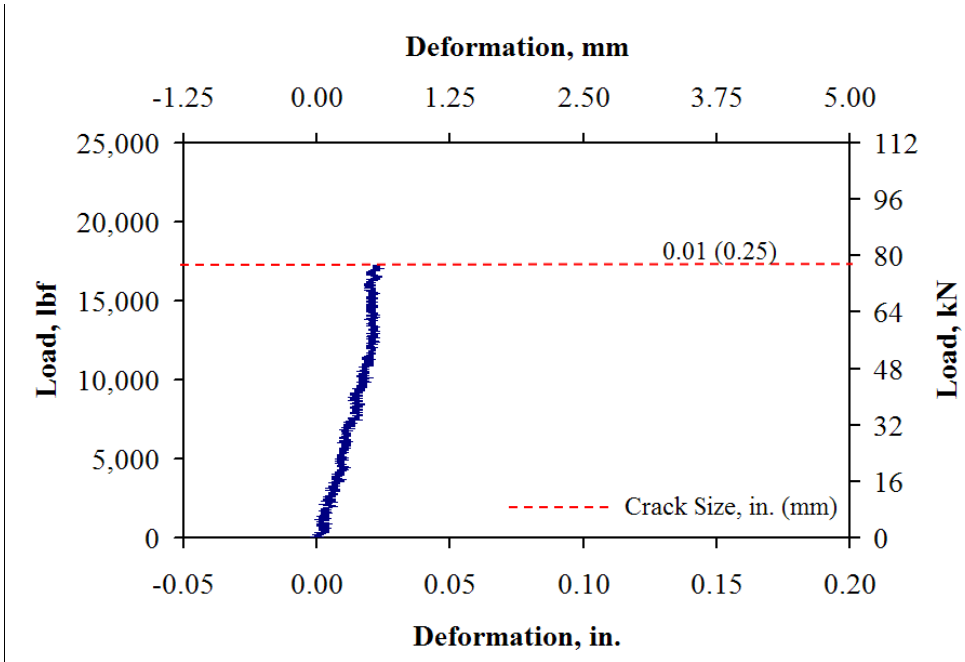

(a)

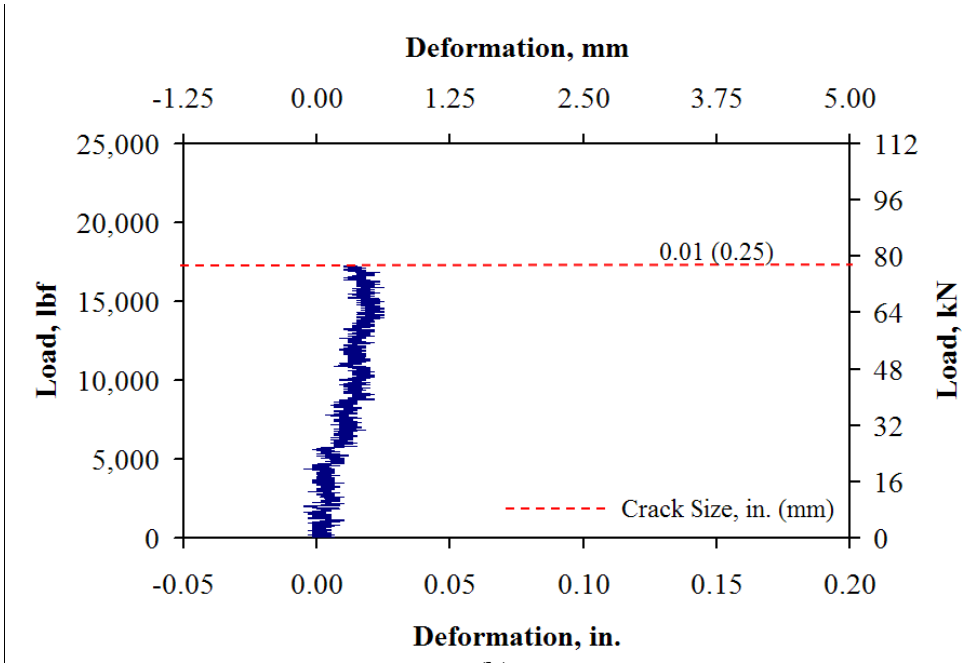

(b)

Figure 2.30 Load versus deformation results at mid span of P18_III(B)_2;
(a) vertical deformation of pipe's cross section and
(b) horizontal deformation of pipe's cross section.

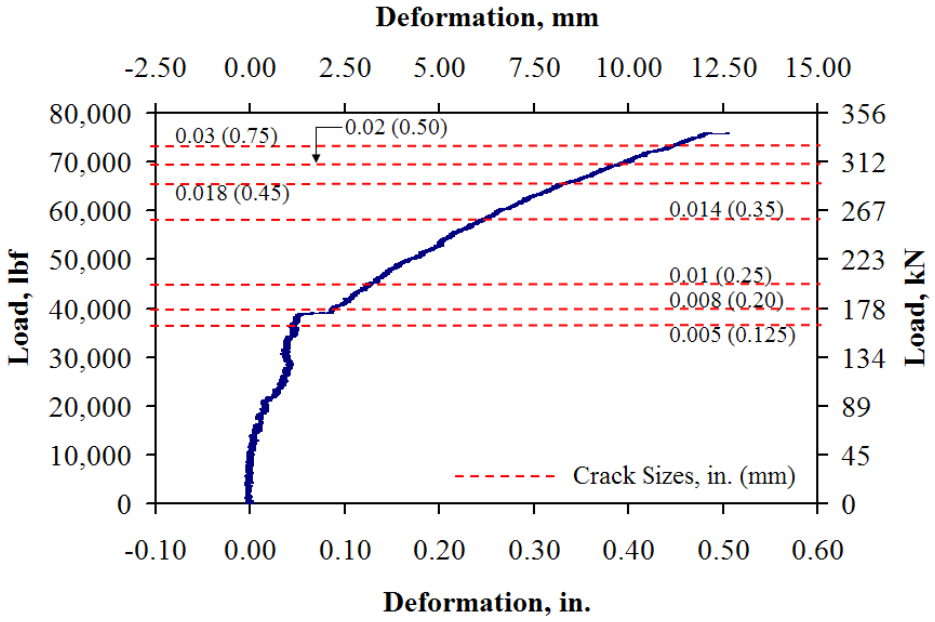

(a)

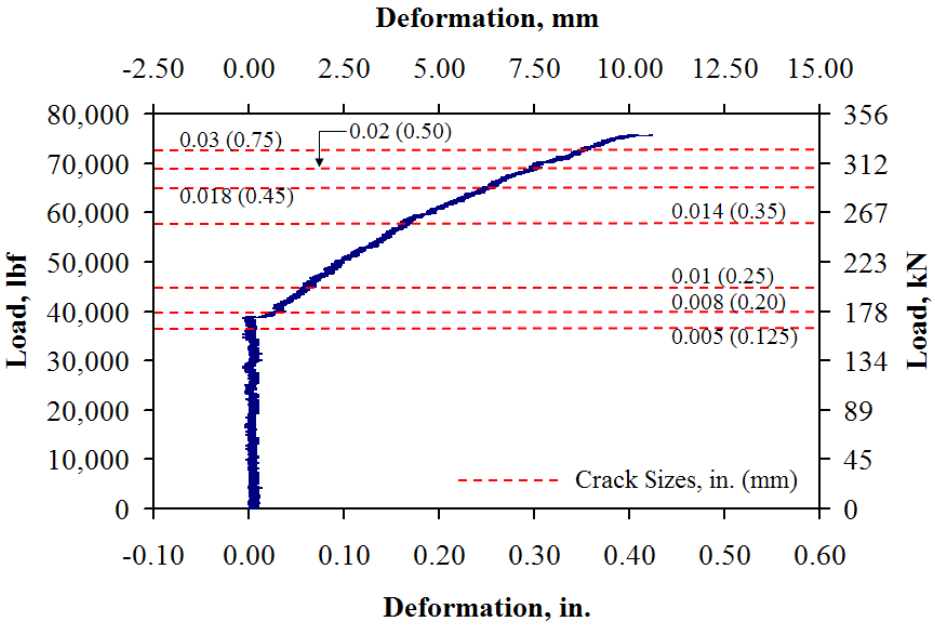

(b)

Figure 2.31 Load versus deformation results at mid span of P36_III(B)_1;
(a) vertical deformation of pipe's cross section and
(b) horizontal deformation of pipe's cross section.

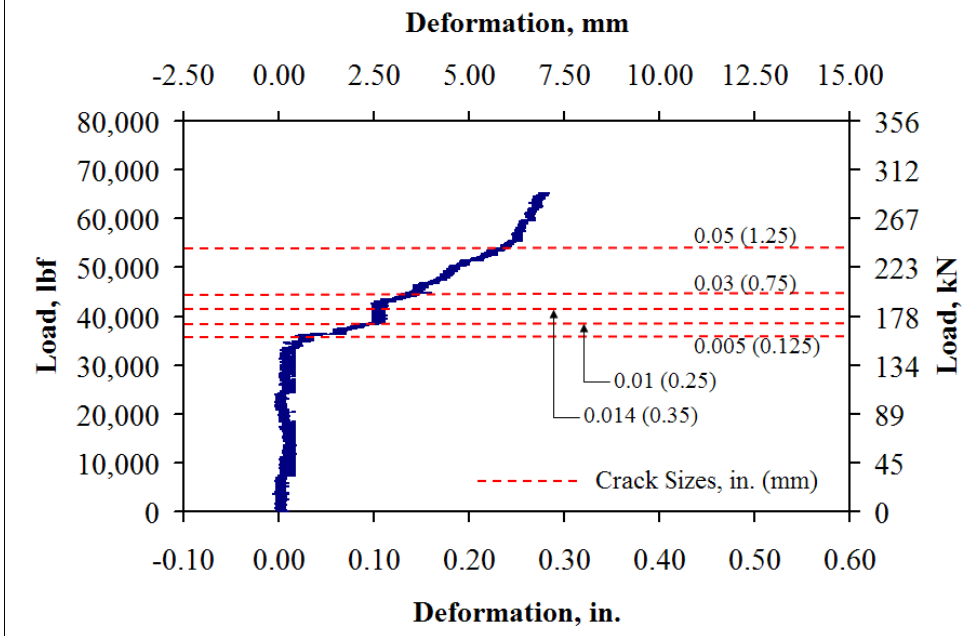

(a)

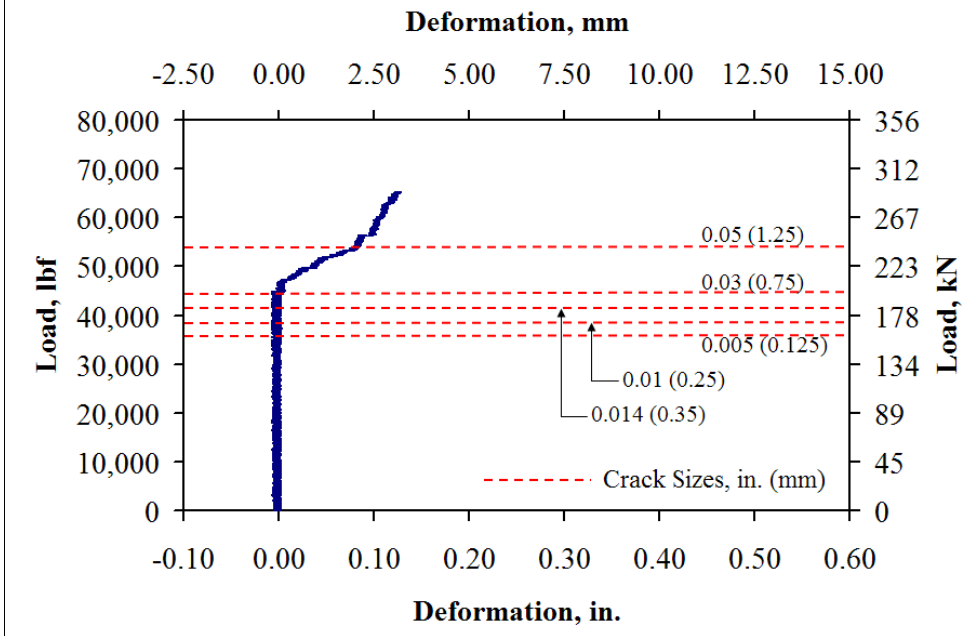

(b)

Figure 2.32 Load versus deformation results at mid span of P36_III(B)_2;
(a) vertical deformation of pipe's cross section and
(b) horizontal deformation of pipe's cross section.

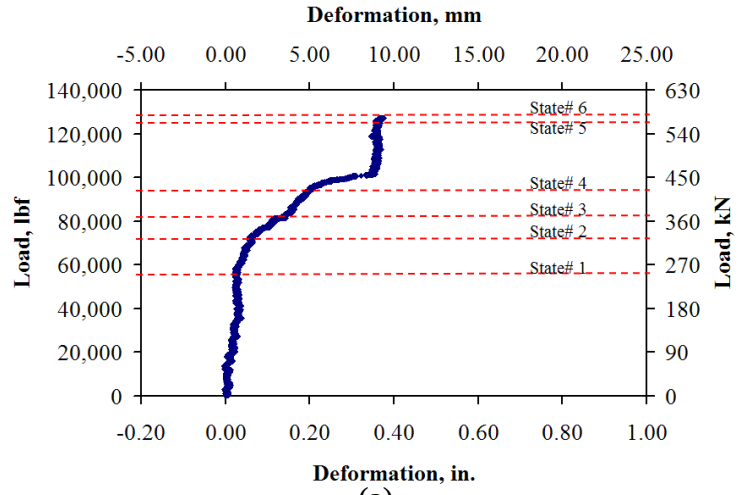

(a)

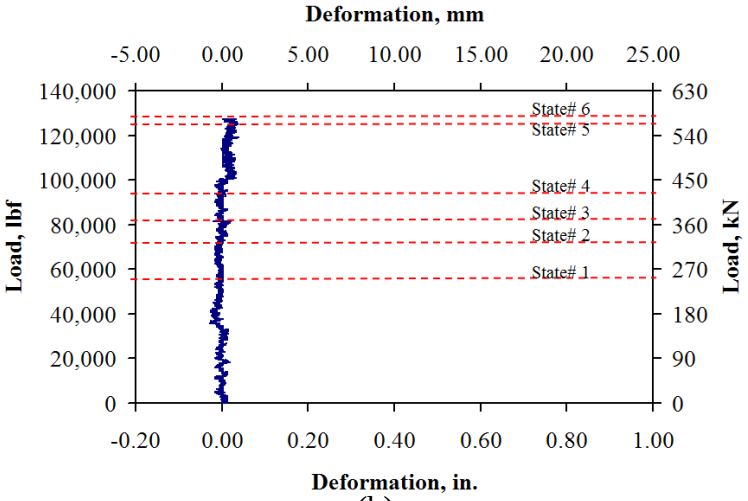

(b)

Figure 2.33 Load versus deformation results at mid span of P54_V(C)_1;
(a) vertical deformation of pipe's cross section and
(b) horizontal deformation of pipe's cross section.

Table 2.4 Crack Behaviors at Each State in Figure 2.33

State#	Load, lbf (kN)	Crack Sizes, in. (mm), and Patterns		
		Crown	Invert	Springline
1	57,505 (256)	1 x Hair Line	1 x Hair Line	-
2	73,000 (325)	1 x Hair Line	2 x Hair Lines	-
3	81,278 (362)	2 x 0.005 (0.125)	2 x 0.01 (0.25)	1 x Hair Line
4	95,176 (423)	2 x 0.01 (0.25), and Shear Crack	2 x 0.016 (0.40), and Shear Crack	3 x Hair Lines
5	126,000 (560)	2 x 0.01 (0.25), and Shear Crack	2 x 0.016 (0.40), and Shear Crack	5 x Hair Lines
6	127,210 (566)	2 x 0.01 (0.25), and Shear Crack	2 x 0.016 (0.40), and Shear Crack	5 x Hair Lines

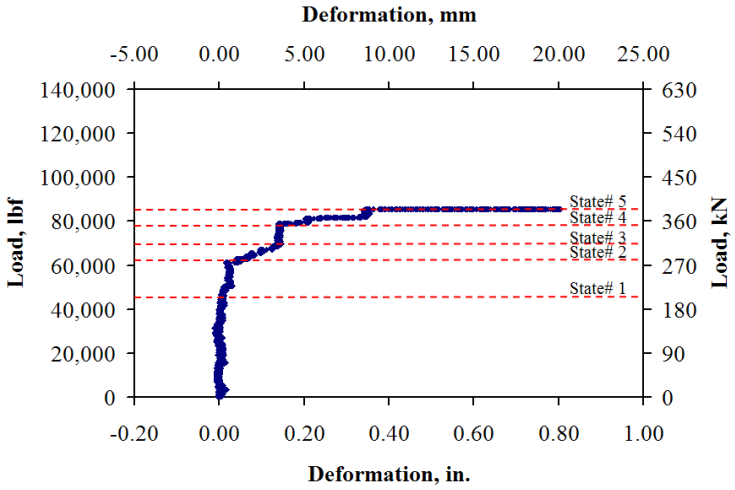

(a)

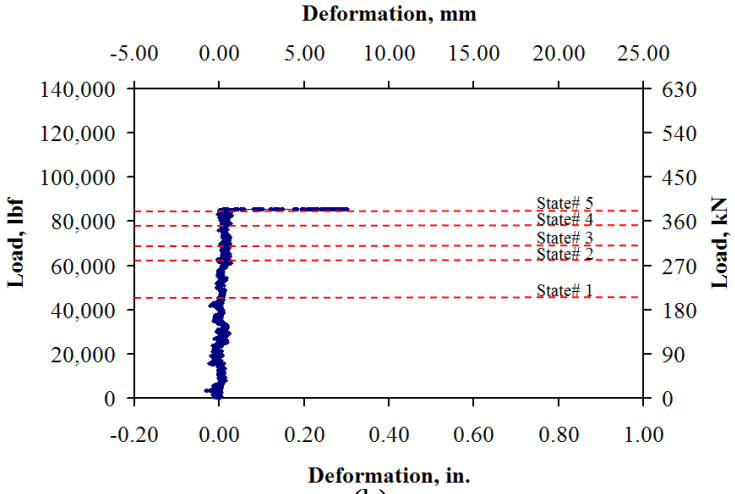

(b)

Figure 2.34 Load versus deformation results at mid span of P54_V(C)_2;
(a) vertical deformation of pipe's cross section and
(b) horizontal deformation of pipe's cross section.

Table 2.5 Crack Behaviors at Each State in Figure 2.34

State#	Load, lbf (kN)	Crack Sizes, in. (mm), and Patterns		
		Crown	Invert	Springline
1	46,200 (206)	1 x Hair Line	1 x Hair Line	-
2	61,500 (274)	1 x Hair Line	2 x Hair Lines	1 x Hair Line
3	69,291 (308)	2 x 0.01 (0.25)	2 x 0.01 (0.25)	1 x Hair Line
4	78,920 (351)	2 x 0.01 (0.25), and Shear Crack	2 x 0.01 (0.25), and Shear Crack	3 x Hair Lines
5	85,620 (381)	2 x 0.01 (0.25), and Shear Crack	2 x 0.01 (0.25), and Shear Crack	6 x Hair Lines

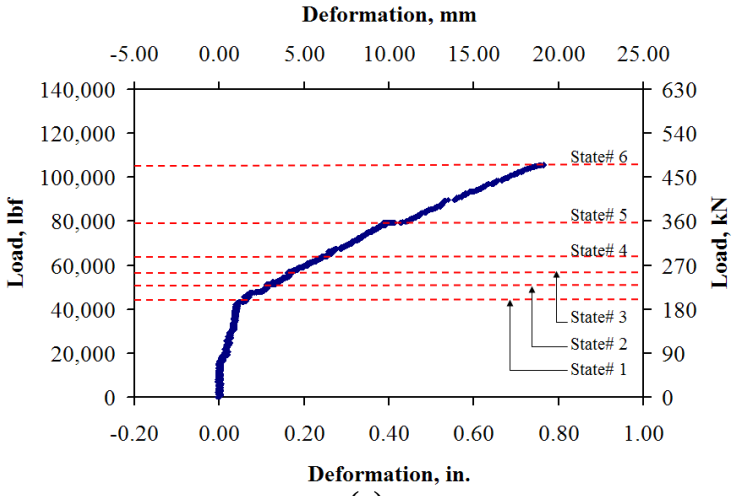

(a)

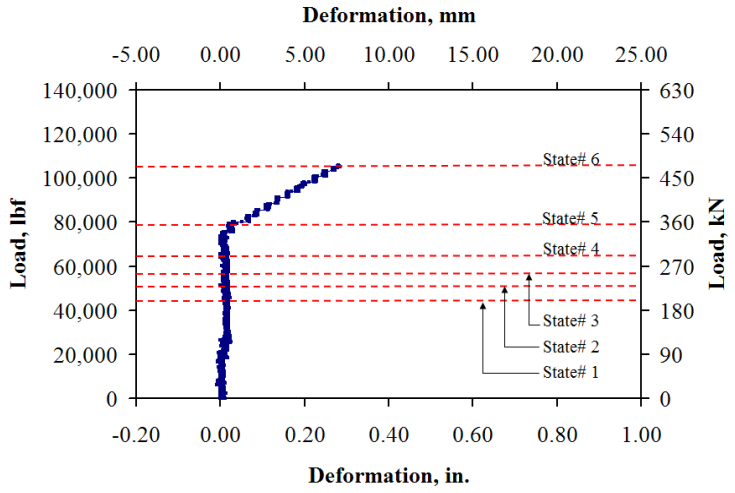

(b)

Figure 2.35 Load versus deformation results at mid span of P54_III(C)_1;
(a) vertical deformation of pipe's cross section and
(b) horizontal deformation of pipe's cross section.

Table 2.6 Crack Behaviors at Each State in Figure 2.35

State#	Load, lbf (kN)	Crack Sizes, in. (mm), and Patterns		
		Crown	Invert	Springline
1	45,743 (204)	1 x Hair Line	1 x Hair Line	-
2	51,493 (229)	1 x 0.01 (0.25)	1 x 0.01 (0.25)	1 x Hair Line
3	56,889 (253)	1 x 0.016 (0.40)	1 x 0.014 (0.35)	1 x Hair Line
4	65,487 (291)	1 x 0.024 (0.60)	1 x 0.028 (0.70)	2 x Hair Lines
5	79,436 (353)	1 x 0.045 (1.125), and Shear Crack	1 x 0.05 (1.25), and Shear Crack	3 x Hair Lines
6	105,688 (470)	1 x 0.045 (1.125), and Shear Crack	1 x 0.05 (1.25), and Shear Crack	5 x Hair Lines

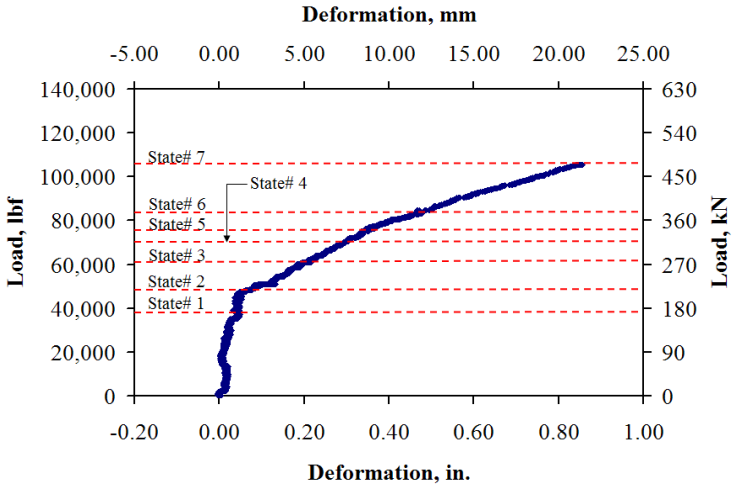

(a)

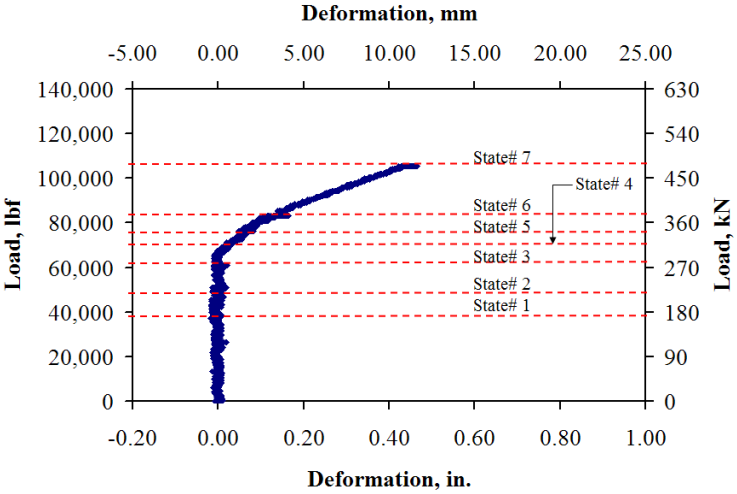

(b)

Figure 2.36 Load versus deformation results at mid span of P54_III(C)_2;
(a) vertical deformation of pipe's cross section and
(b) horizontal deformation of pipe's cross section.

Table 2.7 Crack Behaviors at Each State in Figure 2.36

State#	Load, lbf (kN)	Crack Sizes, in. (mm), and Patterns		
		Crown	Invert	Springline
1	39,000 (174)	1 x Hair Line	1 x Hair Line	-
2	48,260 (215)	1 x 0.01 (0.25)	1 x 0.01 (0.25)	1 x Hair Line
3	61,018 (271)	1 x 0.01 (0.25)	1 x 0.02 (0.50)	2 x Hair Lines
4	71,900 (320)	1 x 0.02 (0.50)	1 x 0.024 (0.60)	2 x Hair Lines
5	76,460 (340)	1 x 0.02 (0.50)	1 x 0.03 (0.75)	3 x Hair Lines
6	83,348 (371)	1 x 0.02 (0.50), and Shear Crack	1 x 0.03 (0.75), and Shear Crack	4 x Hair Lines
7	105,607 (470)	1 x 0.02 (0.50), and Shear Crack	1 x 0.03 (0.75), and Shear Crack	4 x Hair Lines

CHAPTER 3

FINITE ELEMENT MODEL CRACK VERIFICATION

3.1 Introduction

A FEM program was used; ABAQUS version 6.8-2, to simulate the three-dimensional models of D-Load test. Material properties adopted herein were based on the experimental measurement. In the concrete pipe section, the concrete brittle cracking was applied for the plasticity behavior and used for the predicted crack patterns. To simulate the post failure behavior of concrete under cracking, tension stiffening defines the presence of reinforcement in the concrete used for the brittle cracking model. The scaled mass matrix is used for each increment within the dynamic analysis step to increase computational efficiency. With regard to the element type, the optimum mesh was conformed to the geometry of the part instance. The models included 3-D brick solid (C3D8R) element having geometric and material non-linearity. The interaction areas were modeled by using node-to-surface contact elements.

3.2 Element Types

All elements used in ABAQUS relate numerical integration to allow complete generality in material behavior. A composite layered section can be specified with different materials. Each cross-section of the element can be integrated numerically, so that nonlinear response can be tracked precisely. To create the model, the combination

of elements can be used with the complete geometric modeling capability. In this study, two types of elements: solid element and thick shell element were used.

Solid elements used are the standard volume elements which include several regions of different materials. For the complex contact conditions, the first-order hexahedral (brick) elements, C3D8R, were chosen for the accuracy of stress/displacement results as shown in Figure 3.1. Five aspects of an element characterize its behaviors including with family, degrees of freedom, number of nodes, formulation, and integration (ABAQUS, 2008). The first letter shows the family of elements belonged. The degrees of freedom are the translations and rotations at each node. For the first-order elements, nodes are located only at their corners. An element's formulation refers to the mathematical theory used to define the element's behavior. Using Gaussian quadrature for most elements, ABAQUS evaluates the material response at each integration point in each element. In the Lagrangian, the element deforms with the material. The numerical techniques are used to integrate various quantities over the volume of each element. In this model, the C3D8R elements were applied to the parts modeled for TEB machine, and concrete pipes. Reduced integration was applied to decrease running time, especially in three dimensional models.

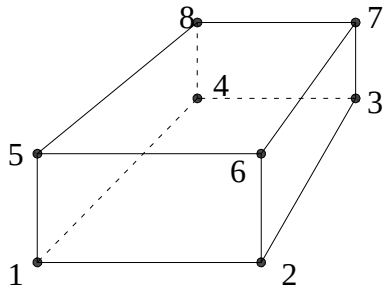

Figure 3.1 The 8-noded linear brick, reduced integration "C3D8R"
(Re: ABAQUS version 6.8-2, 2008).

3.3 Typical FEM Model

The typical FEM model of the D-Load test (Figure 3.2) shows the components and elements in each part of the model. The TEB machine model composed of upper bearing beam and lower bearing support. Considered from the convergence of the FEM results, the element types were selected properly for each region.

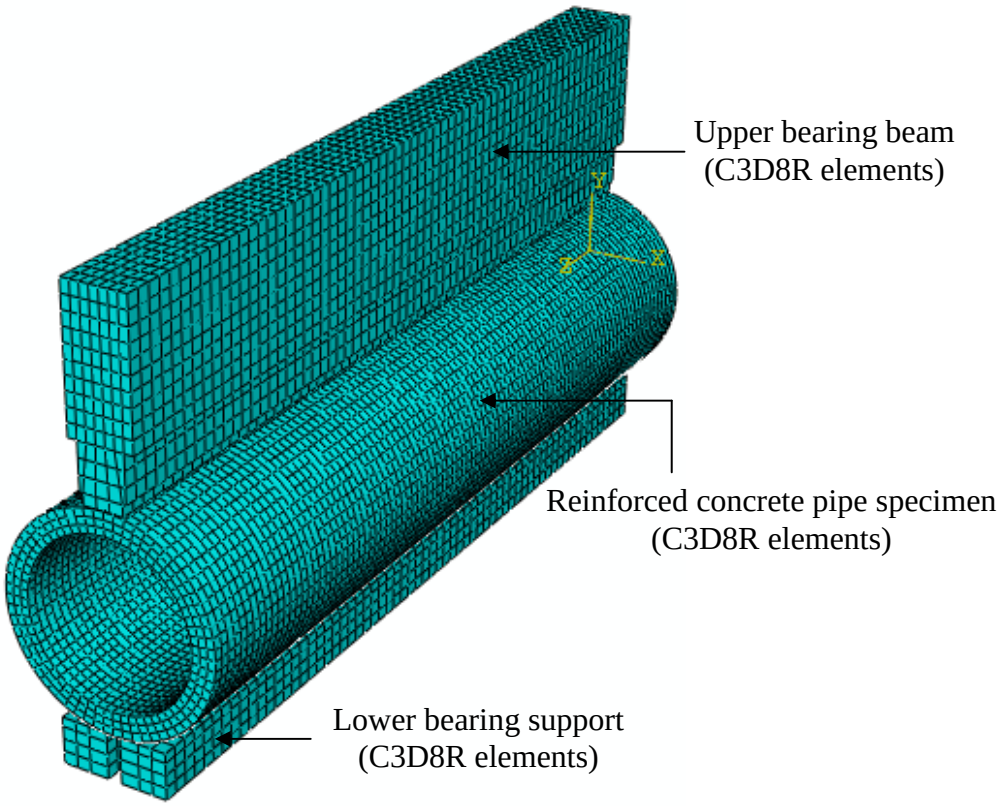

Figure 3.2 Typical FEM model for the D-Load test.

Each element of FEM model composes of a set of nodal points located at the corners or end points. Thus, nodes define the geometry of element and degrees of freedom. The total numbers of nodes and elements for the FEM model of D-Load test depend on the size of pipe specimen as shown in Table 3.1.

Table 3.1 Total Numbers of Nodes and Elements for the D-Load Test Model

Pipe Internal Diameter	Nodes	Elements	Degrees of Freedom
18 in. (46 cm)	108,953	89,128	653,718
36 in. (91 cm)	150,316	127,064	901,896
54 in. (1.37 m)	163,878	143,074	983,268

3.4 Material Properties and Behaviors

The material library in ABAQUS provides comprehensive coverage of linear and nonlinear behaviors. The use of numerical integration in the elements, including numerical integration across the cross-sections of shells and bricks, provides the flexibility to analyze the most complex composite structures.

3.4.1 Concrete Pipe Section

Obtained from the laboratory testing data, linear-elastic behaviors of concrete pipe were modeled with a density of 150 pcf (2,520 kg/m^3) and Poisson's ratio of 0.2. The compressive strength of 4,000 psi (27.6 MPa) and Young's Modulus of 3,605 ksi (24.8 MPa) were used for the class III reinforced concrete pipe. The compressive strength of 6,000 psi (41.4 MPa) and Young's Modulus of 4,415 ksi (30.4 MPa) were used for the class V reinforced concrete pipe. The plasticity properties, brittle crack, tension stiffening, shear retention, and failure ratio, were calibrated from the experimental test results.

3.4.2 Brittle Cracking Model

The brittle cracking model in Abaqus/Explicit is most accurate in applications where the brittle behavior is dominated by tensile cracking and it is adequate to assume that the material is linear in compression. Brittle failure criterion is available to allow the removal of elements from a mesh. Corresponding to the design assumptions (ACI Committee 318, 2008), the tensile stress in the extreme tension fiber of a plain concrete beam test specimen at the load that produces rupture when tested in accordance with third-point loading (ASTM C 78, 2008) or center-point loading (ASTM C 293, 2008) is defined as the modulus of rupture:

$$f_r = 7.5\sqrt{f_c'}\,, \tag{3.1}$$

where

f_r is the modulus of rupture of concrete, psi,

f_c' is the specified compressive strength of concrete, psi.

In the FEM analysis, f_r was considered as a concrete cracking tensile strength, f_t, for the concrete brittle cracking criterion.

3.4.3 Brittle Failure Criterion

When one, two, or all three local direct cracking strain components at a material point reach the failure strain, the material fails and all the stress components are set to zero. If all of the material points in an element fail, the element is removed from the mesh.

In a monotonically loaded structure whose failure mechanism is expected to be dominated by a single tensile macro-fracture, it is reasonable to use the brittle failure criterion to remove elements. It is possible to use the brittle failure criterion in brittle cracking elements for which rebar are also defined. Thus, the brittle failure criterion was applied to the modeling of reinforced concrete pipes in this study. When such elements fail according to the brittle failure criterion, the brittle cracking contribution to the element stress carrying capacity is removed but the rebar contribution to the element stress carrying capacity is not removed.

3.4.4 Tension Stiffening

The postfailure behavior for the strain across cracks was modeled with tension stiffening. The strain-softening behavior was defined as postfailure stress in a function of strain across the crack by means of a postfailure stress-strain relation. The values given for tension stiffening are very important aspect of simulations using the brittle cracking model. The post-cracking tensile response is highly dependent on the reinforcement present in the concrete. The approximation of tension stiffening depends on the density of reinforcement, the bond between the rebar and the concrete, the size of concrete aggregate, and the mesh generation. From Figure 3.3, after failure, the strain-softening reduces the stress linearly to zero at a total strain of about 10 times the strain at failure which is 10^{-4} for standard concrete (ABAQUS, 2008). This parameter was also calibrated with the D-Load test data.

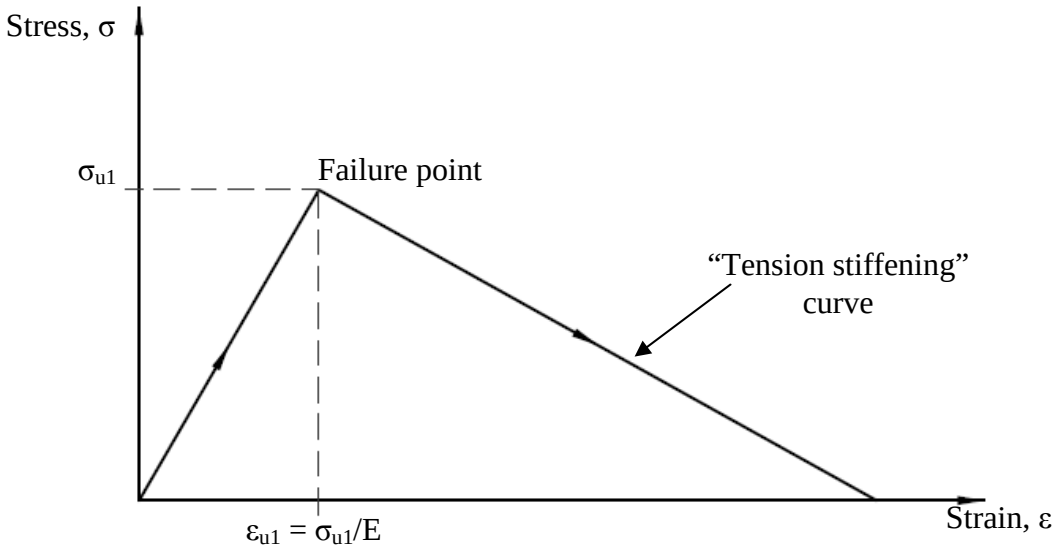

Figure 3.3 Tension stiffening model (Re: ABAQUS version 6.8-2, 2008)

3.4.5 Shear Retention

As concrete cracks, its shear stiffness is diminished. By ABAQUS program, this behavior was simulated by the reduction in the shear modulus as a function of the opening strain across the crack. The new shear stiffness has been degraded by the presence of the crack.

The modulus for shearing of the crack was defined as ρG, where G is the elastic shear modulus of the uncracked concrete and ρ is a multiplying factor. The shear retention model assumed that the shear stiffness of open cracks reduces linearly to zero as the crack opening increases:

$$\rho = (1 - \varepsilon/\varepsilon_{max}) \qquad \text{for } \varepsilon < \varepsilon_{max} \qquad (3.2)$$

$$\rho = 0 \qquad \text{for } \varepsilon > \varepsilon_{max,} \qquad (3.3)$$

where

ε is the direct strain across the crack,

ε_{max} is a user-defined value.

3.4.6 Failure Ratio

Failure ratio was used to define the shape of the failure surface for a concrete model. To define the failure surface for a concrete model, four failure ratios were specified:

- The ratio of the ultimate biaxial compressive stress to the ultimate uniaxial compressive stress.
- The absolute value of the ratio of the uniaxial tensile stress at failure to the ultimate uniaxial compressive stress.
- The ratio of the magnitude of a principal component of plastic strain at ultimate stress in biaxial compression to the plastic strain at ultimate stress in uniaxial compression.
- The ratio of the tensile principal stress at cracking, in plane stress, when the other principal stress is at the ultimate compressive value, to the tensile cracking stress under uniaxial tension.

Four values of failure ratios (mentioned above) used in the FEM model were 1.16, 0.09, 1.28, and 0.333 respectively.

3.4.7 Steel Reinforcement Section

With the rebar behavior as the steel reinforcement in concrete, the steel section properties included the Young's Modulus of 29,000 ksi (200,000 MPa) and Poisson's ratio of 0.3. The intensity of steel reinforcement (area per linear foot of pipe wall) was

specified by the design requirement (ASTM C 76, 2008), depending on the class of reinforced concrete pipes.

3.4.8 Hyperelastic Behavior for Elastomeric Materials

Hard rubber sections were modeled using hyperelastic material, which is isotropic and nonlinear. These sections were applied at the load strip and supports of the TEB model. Elastomeric materials exhibited instantaneous elastic response up to large strains. Due to finite-strain applications, the geometric nonlinearity was accounted during the analysis steps.

The mechanical behavior of rubberlike materials was expressed in terms of a strain energy potential:

$$U = U(F), \text{ such that } S = \frac{\partial U(F)}{\partial F}, \tag{3.4}$$

where S is a stress measure and F is a measure of deformation. Because the material was initially isotropic, the strain energy potential in terms of the strain invariants $\bar{I}_1, \bar{I}_2,$ and J_{el} is

$$U = U(\bar{I}_1, \bar{I}_2, J_{el}), \tag{3.5}$$

where $\bar{I}_1$ and $\bar{I}_2$ are the first and second deviatoric strain invariants. J_{el} is the volume ratio, a measure of volumetric strain.

3.5 Load and Boundary Condition

The load and boundary condition steps were precisely simulated from the experimental test. For the three-edge bearing test FEM model as shown in Figure 3.4, the load was applied through the upper bearing beam. The roller support in vertical direction was applied at each side of the upper bearing beam such that the load transferred to the pipe's crown without eccentricity. The translational degree of freedom was constrained at the bottom of two parallel longitudinal strips.

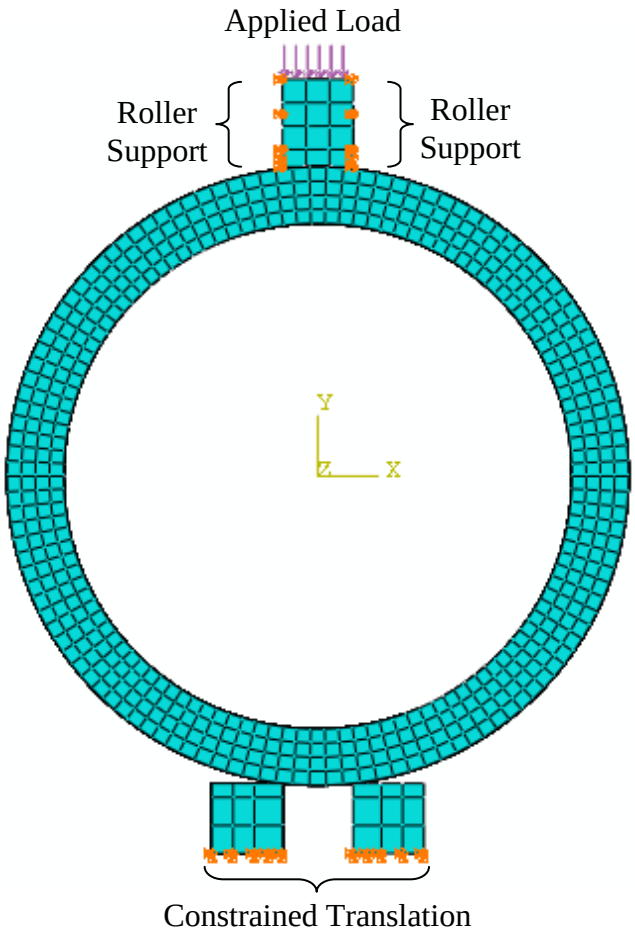

Figure 3.4 Load and boundary condition for the D-Load FEM model.

3.6 Typical Results for D-Load FEM Model

Analysis results were provided by the visualization module in ABAQUS. The graphical display of FEM models and results obtains information from the output database. The visualization module represented the values as customized colored bands on the model. A contour plot displayed the values of stress at a specified step and frame.

3.6.1 Extraction of the FEM Results

The stress and displacement at each point in the model were obtained by interpolating the unique nodal technique, using the averaging criteria defined in the result options dialog box. With this technique, the output results were extracted from the active steps/frames. The positions of unique nodes were selected from the node labels in the FEM model.

3.6.2 Typical FEM Stress Results

As shown in Figure 3.5, the applied load produced a compressive stress above the neutral axis (external section) of the pipe wall. Below the neutral axis (internal section) of the pipe wall, the applied load produced a tensile stress. Along the neutral axis, the internal stress changed from compression to tension. These stress patterns at the pipe wall were similar for the crown and invert, but opposite to those at springline.

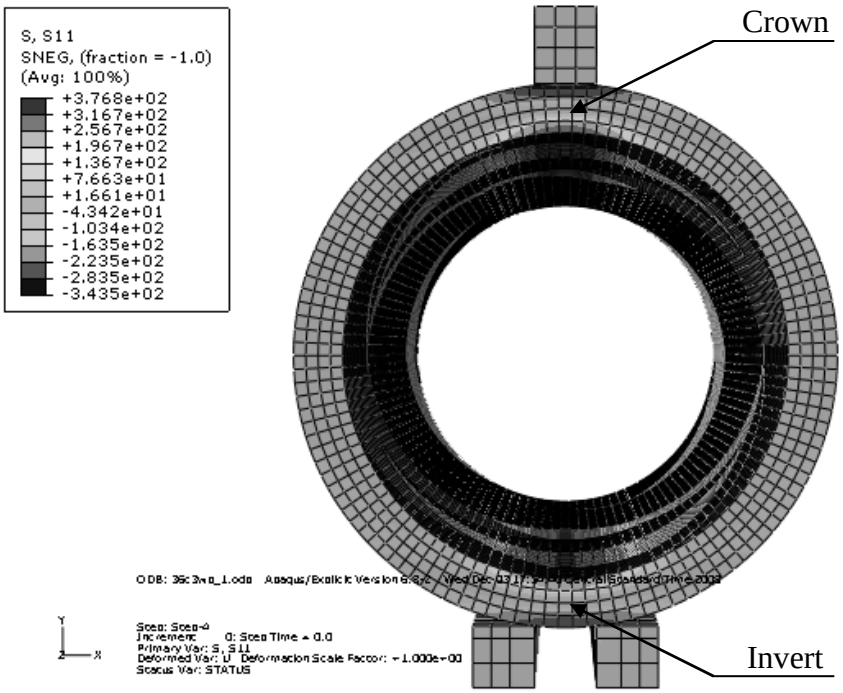

(a)

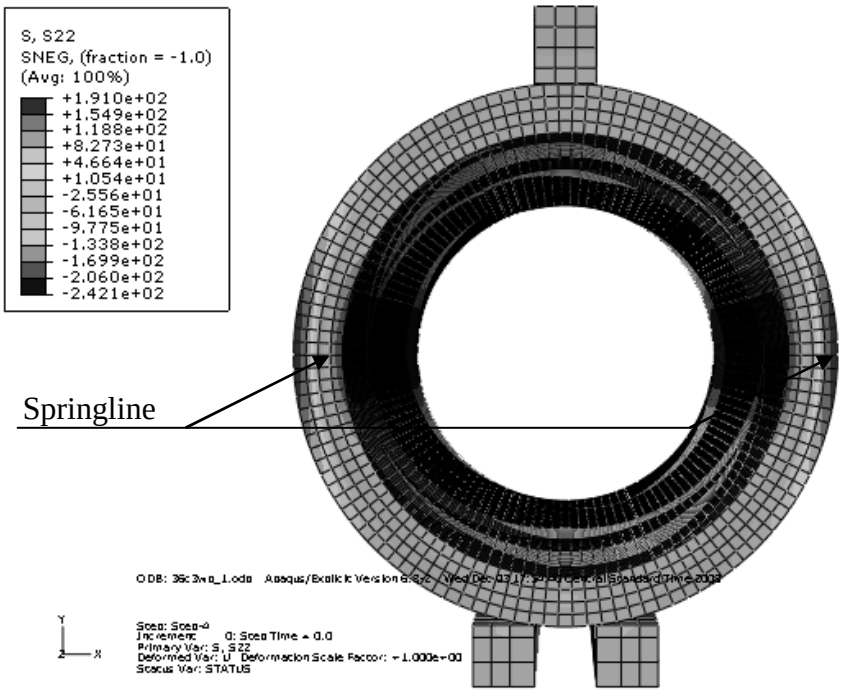

(b)

Figure 3.5 Typical FEM stress results; (a) stress S11 at crown and invert and (b) stress S22 at springline.

3.6.3 Typical FEM Deformation Results

The deformation shape of a pipe cross section is shown in Figure 3.6. The FEM results showed the loss of circular shape of the pipe's cross-section which was deformed symmetrically about the vertical centerline. The decrease in pipe's vertical diameter and the increase in pipe's horizontal diameter caused a pipe's cross-section to become the oval shape.

3.6.4 Typical FEM Crack Results

The brittle model in ABAQUS showed the visualized opening crack results. The resulting material was brittle in tension. As a result of the vertical and horizontal deformation of a pipe's cross-section, the cracks were located at the pipe's invert, crown, and springline as shown in Figure 3.7. For the invert and crown, the longitudinal cracks began at the internal surface (tension zone) of the pipe wall and propagated outwardly in a radial direction to the external surface (compression zone). For the springline, the longitudinal cracks started at the external surface (tension zone) of the pipe wall and propagated inwardly in a radial direction to the internal surface (compression zone). Moreover, in case of the 54-in. (1.37-m) pipe, there was the occurrence of multiple longitudinal cracks at the springline.

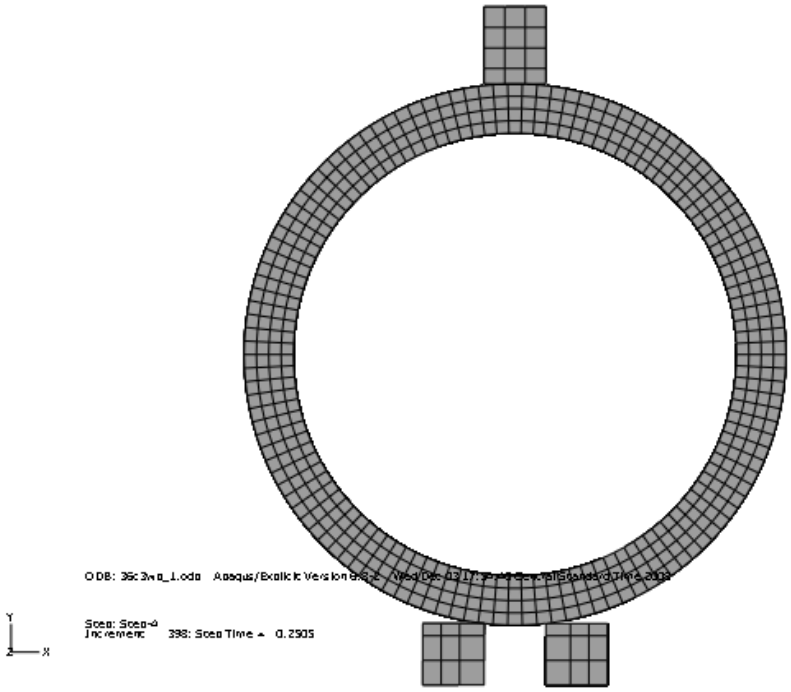

(a)

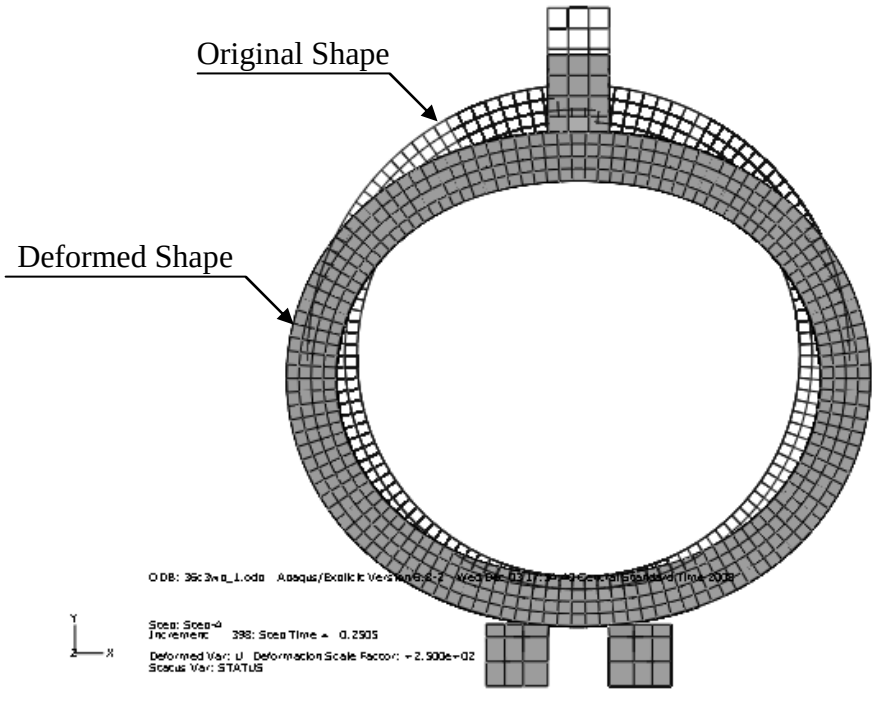

(b)

Figure 3.6 Typical FEM deformation results (magnified scale = 250 times); (a) original shape before loaded and (b) deformed shape after loaded.

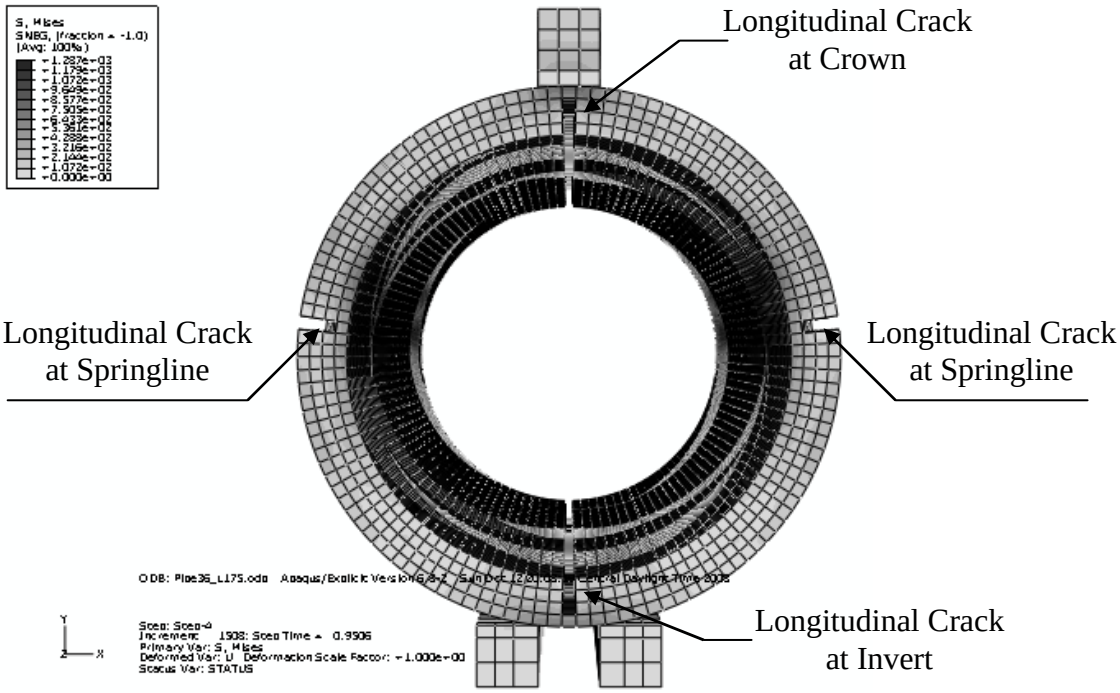

(a)

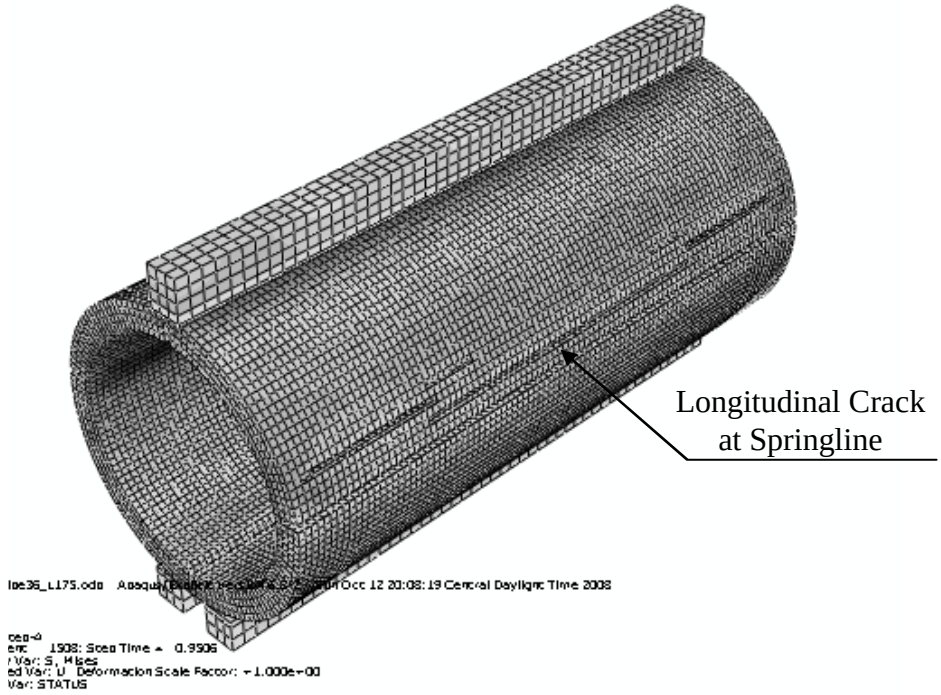

(b)

Figure 3.7 Typical FEM crack results; (a) X – Y plane view
and (b) isometric view.

3.7 FEM Results Compared with Experimental Test Results

The results of the developed FEM analysis were compared with the experimental results in forms of load-deformation curves. The results included 36-in. (91-cm) and 54-in. (1.37-m) pipes. The case of an 18-in. (46-cm) pipe was not considered in this section due to the removal of LVDTs during the test such that no deformation data were recorded beyond the state of 0.01-in. (0.25-mm) crack.

With the applied post-failure property of concrete, “tension stiffening”, the FEM showed an excellent agreement with the compared experimental results as shown in Figures 3.8 and 3.9. By the FEM results, the crack propagation was provided but not included with the measured crack size. Figure 3.8 shows the FEM results for a 36-in. (91-cm) diameter pipe specimen. The tested specimen# 1 and specimen# 2 were defined as Test# 1 and Test# 2, respectively. From FEM results, the first crack at invert occurred at the applied load of 44,160 lbf (196 kN). Figures 3.9 shows the results for 54-in. (1.37-m) diameter pipe specimen. The first crack at invert occurred at the applied load of 70,000 lbf (311 kN).

The graphical displays of FEM cracking results compared with experimental investigations were illustrated in this section. At the ultimate load, FEM results introduced the failure mode for each pipe size. For the 18-in. (46-cm) and 36-in. (91-cm) pipes, the opening crack occurred at invert, crown, and springline as shown in Figures 3.10 and 3.11. In the case of 54-in. (1.37-m) pipe, the crack patterns revealed shear cracks occurred at crown and invert as shown in Figures 3.12(a) and 3.12(b),

respectively. Additionally, at springline, there appeared multiple cracks propagated in a large region as shown in Figure 3.12(c).

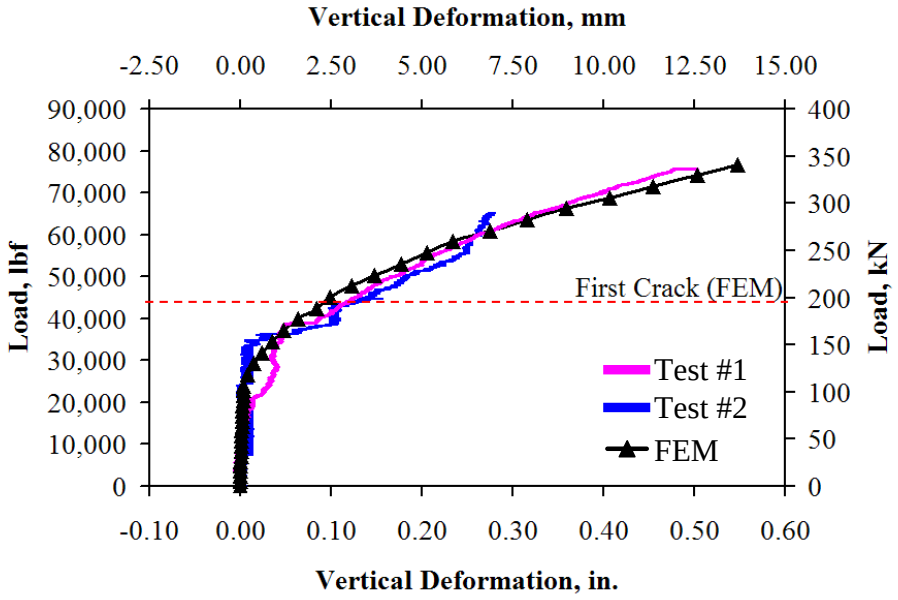

(a)

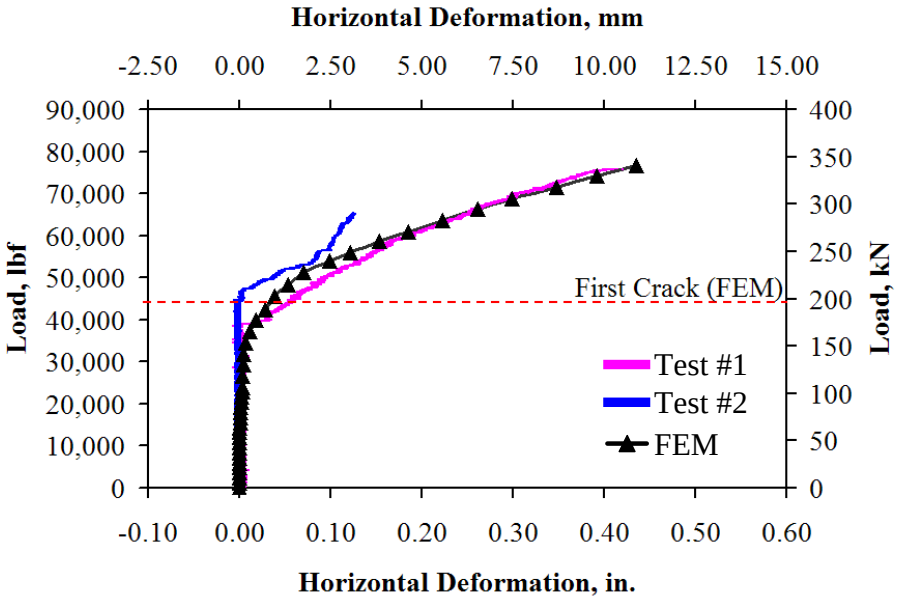

(b)

Figure 3.8 FEM versus experimental results of the 36-in. (91-cm) pipe specimen;
(a) vertical deformation of a pipe's cross section and
(b) horizontal deformation of a pipe's cross section.

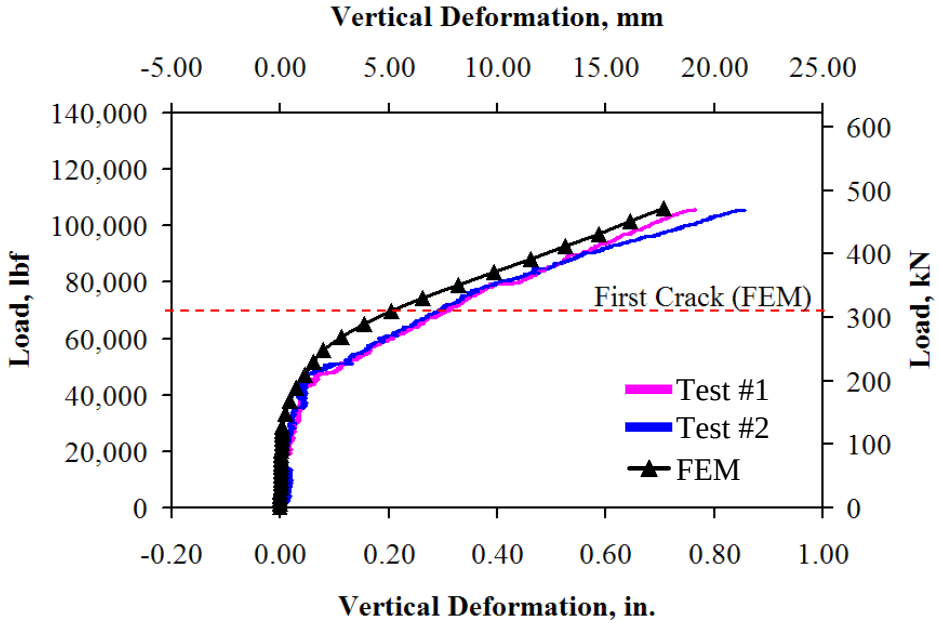

(a)

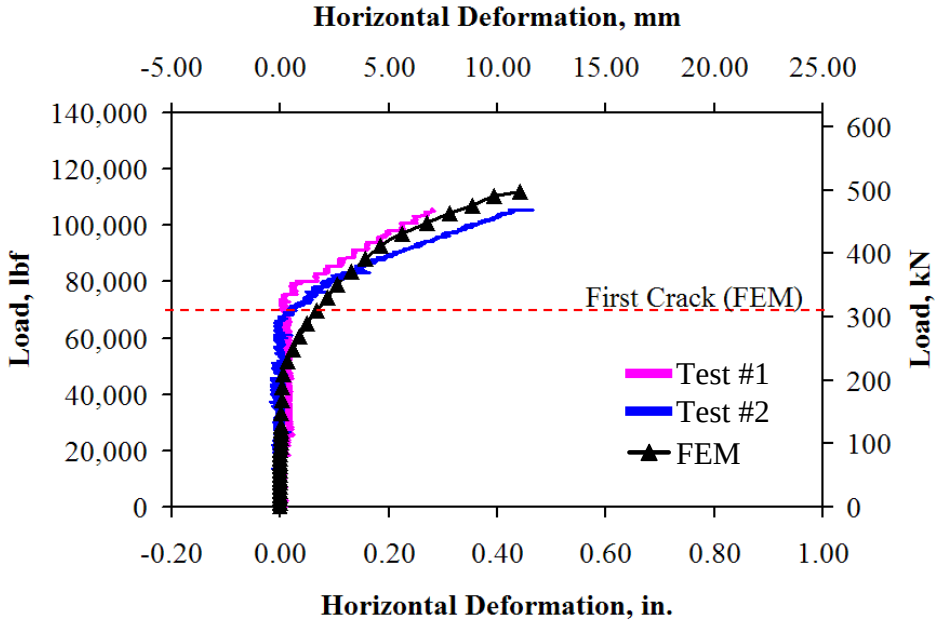

(b)

Figure 3.9 FEM versus experimental results of the 54-in. (1.37-m) pipe specimen;
(a) vertical deformation of a pipe's cross section and
(b) horizontal deformation of a pipe's cross section.

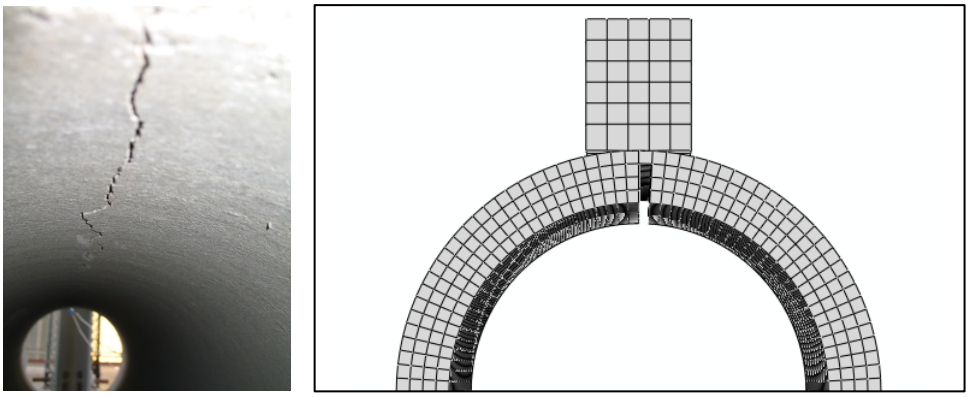

(a)

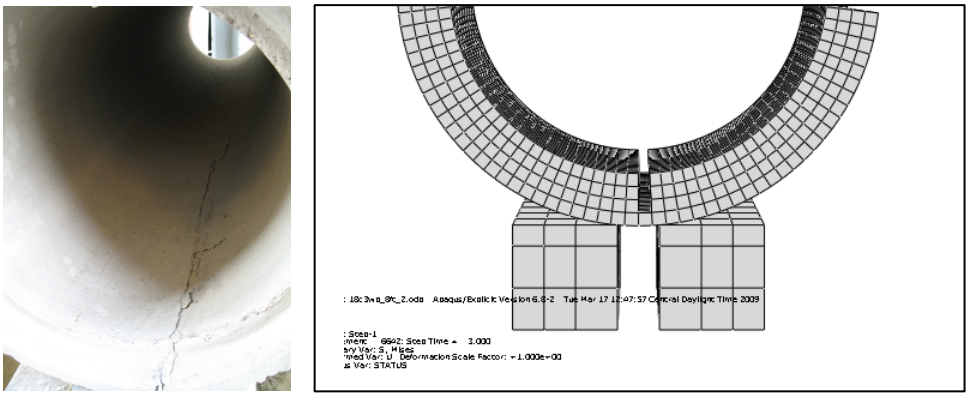

(b)

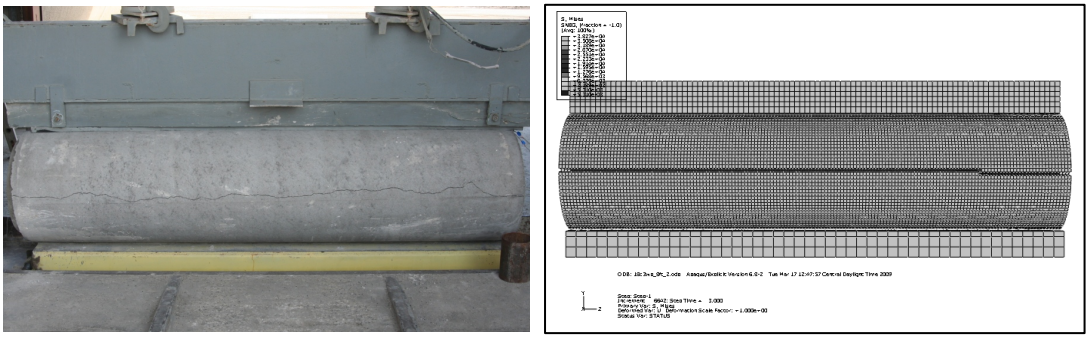

(c)

Figure 3.10 Comparison of experimental results and a FEM model of the crack results on the 18-in. (46-cm) pipe specimen; (a) crown, (b) invert, (c) springline.

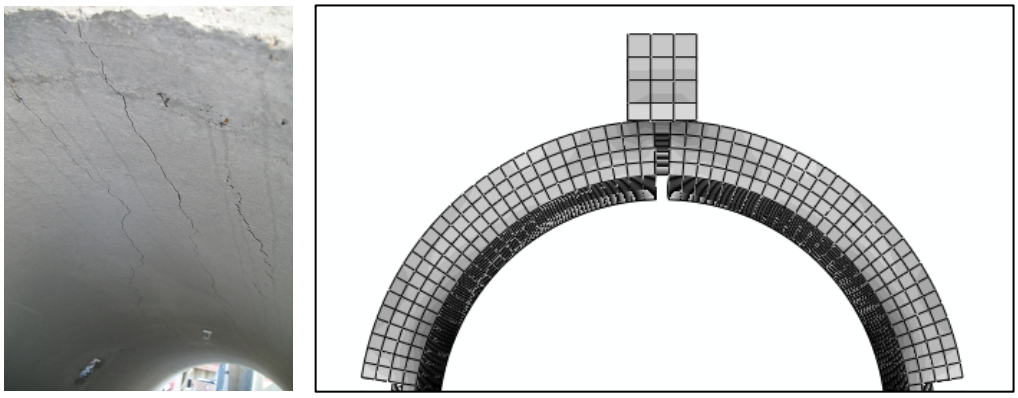

(a)

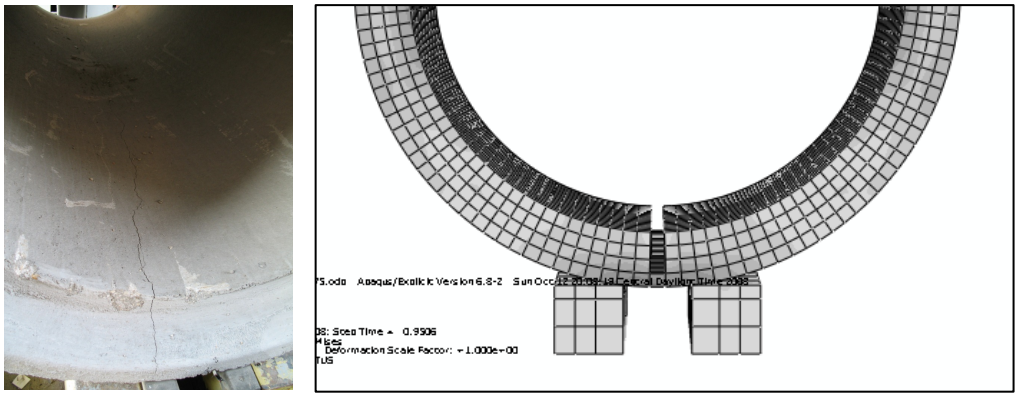

(b)

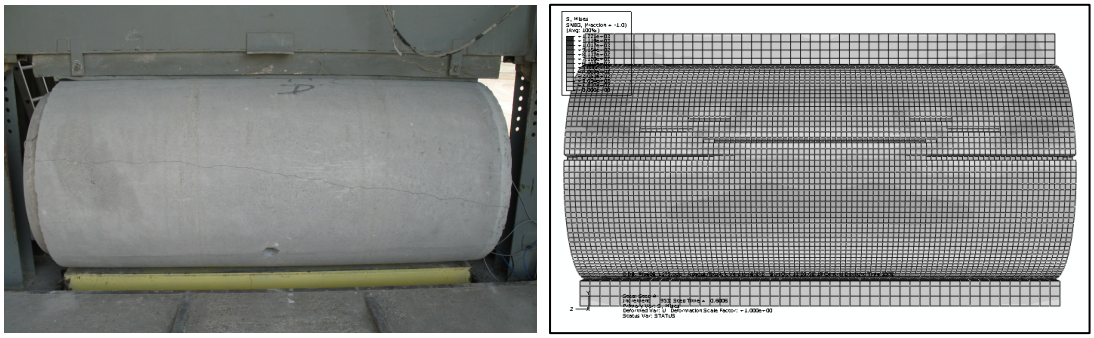

(c)

Figure 3.11 Comparison of experimental results and a FEM model of the crack results on the 36-in. (91-cm) pipe specimen; (a) crown, (b) invert, (c) springline.

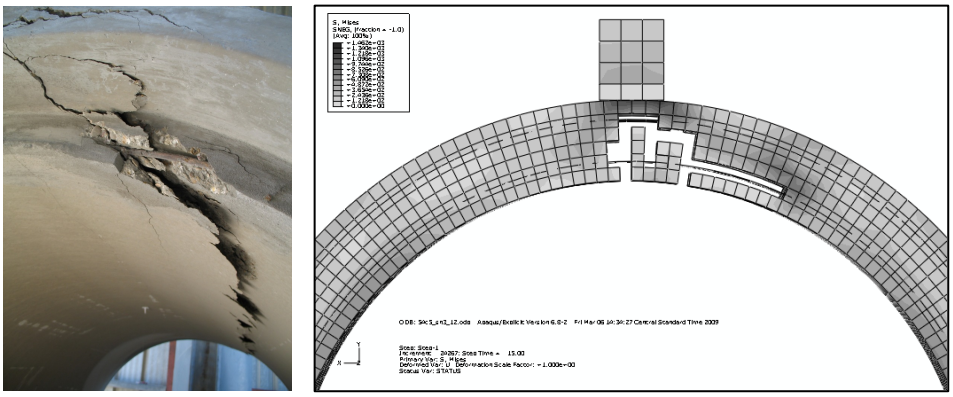

(a)

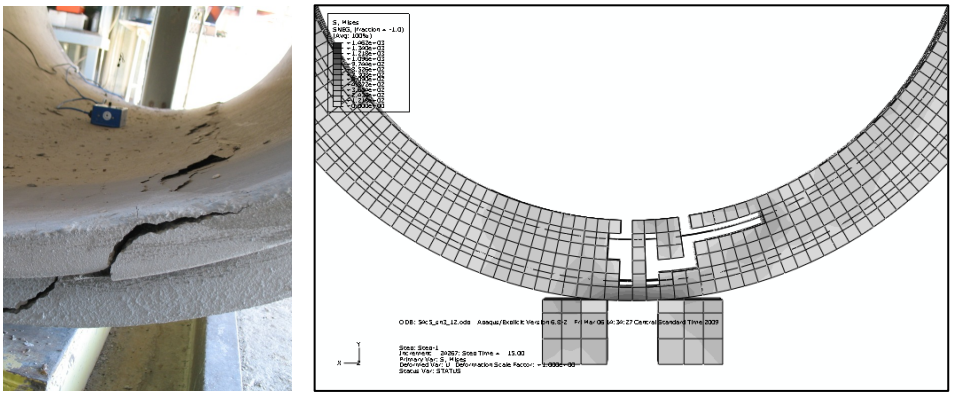

(b)

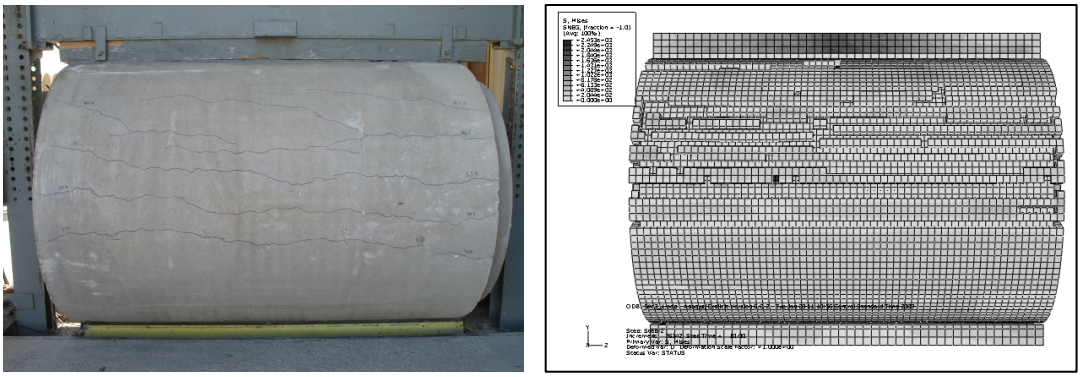

(c)

Figure 3.12 Comparison of experimental results and a FEM model of the crack results on the 54-in. (1.37-m) pipe specimen; (a) crown, (b) invert, (c) springline.

CHAPTER 4

FINITE ELEMENT COMPACTION MODELING OF PIPE-SOIL TRENCH INSTALLATION

4.1 Introduction

In this chapter, the pipe-soil compaction was modeled using a computer program, ABAQUS version 6.8-2 to simulate a pipeline in trench installation under the compaction process. The concrete brittle cracking criterion was properly applied for the post-failure property of a concrete pipe FEM model as verified by the D-Load study in Chapter 3. The geometric dimensions of the models are presented in Figure 4.1. The models included 3-D brick solid (C3D8R) and 3-D triangular solid (C3D6) elements having geometric and material non-linearity. The optimum mesh with regard to element type was selected by the convergence of analysis results. The pipe-soil interface, modeled by using node-to-surface method, allowed the stress transferred between contacting surfaces. The surrounding soil model was partitioned into specific zones so that the related properties were distinguished. The Mohr-Coulomb plasticity model was used for analysis applications in the surrounding soil zone. The pipe-soil compaction FEM model was created such that several interesting parameters can be varied and investigated. Consequently, the complete model will be used for a parametric study in Chapter 5.

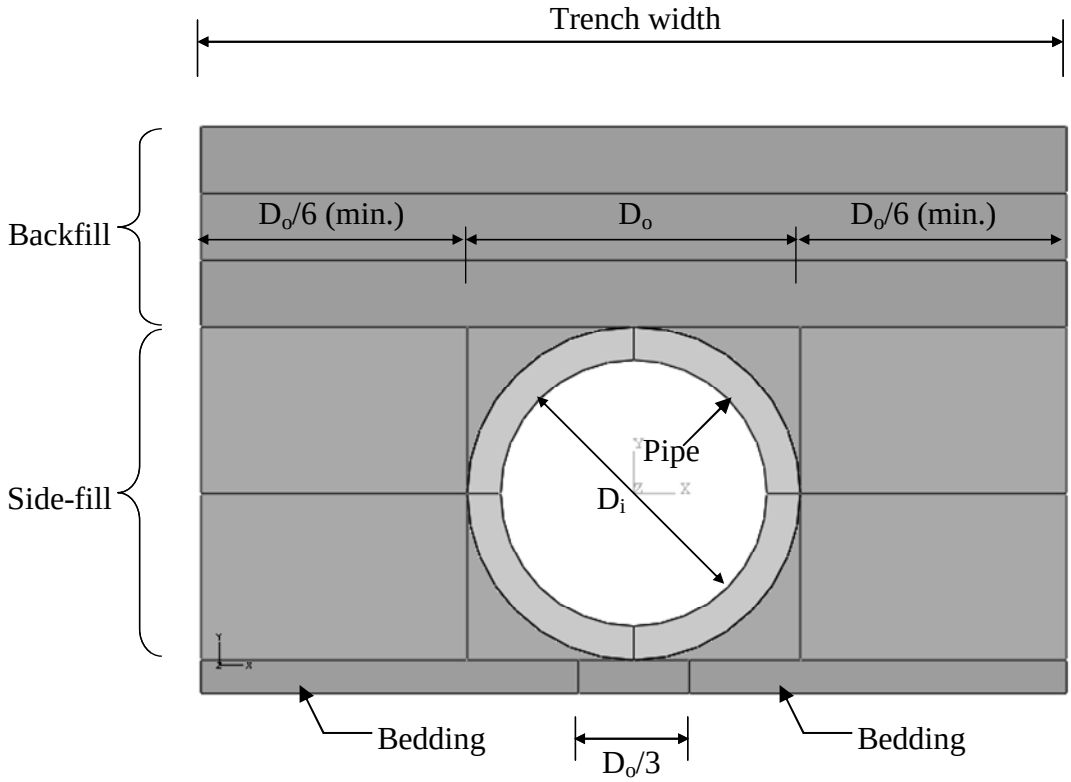

Figure 4.1 Geometric dimensions of a trench installation FEM model.

4.2 Typical FEM Model

The model contains two main parts: pipeline and surrounding soils. All element types included the first-order hexahedral element (C3D8R) and triangular prism element (C3D6) as shown in Figure 4.2.

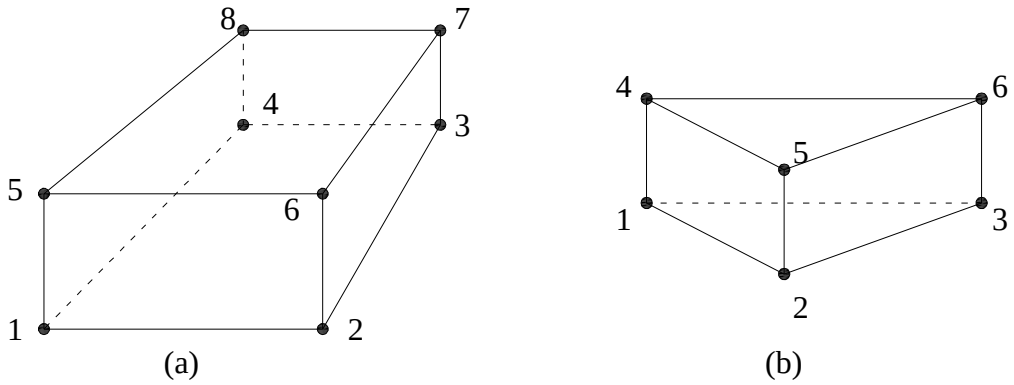

Figure 4.2 Element types used in the pipe-soil compaction model;
(a) 8-noded linear brick "C3D8R" and (b) 6-noded triangular prism "C3D6"
(Re: ABAQUS version 6.8-2, 2008).

4.2.1 Pipeline Model

The pipeline model (Figure 4.3) was created as two spans of an 8-ft (2.44-m) reinforced concrete pipe section are laid and connected together. At the pipe's joint, tongue and groove configurations were also simulated. The structured meshing technique was applied using the hexagonal element shape. The C3D8R element was used for the concrete pipe section.

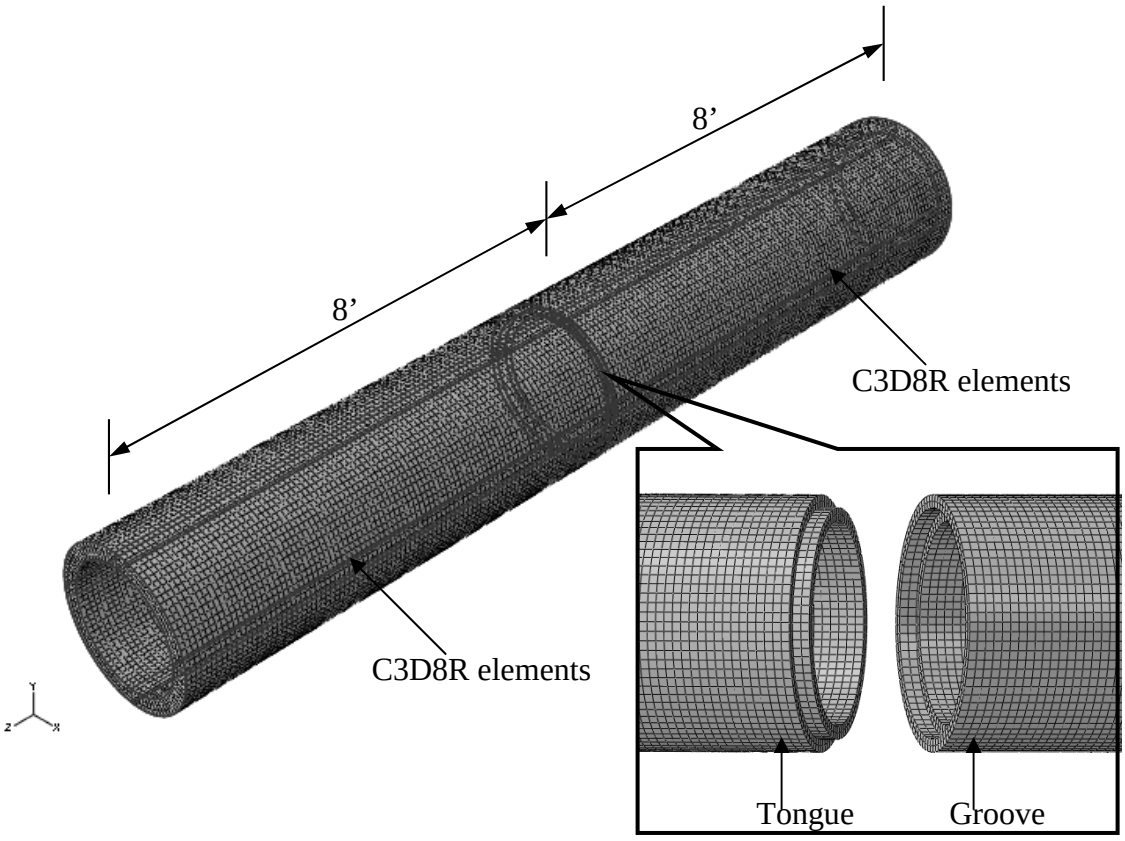

Figure 4.3 FEM model of RC pipeline.

4.2.2 Surrounding Soil Model

The surrounding soil model was partitioned into specific regions: bedding, sidefill, and backfill soils as shown in Figure 4.1. For the mesh generation (Figure 4.4),

the swept meshing technique was applied using the hex-dominated element shape. This technique primarily used hexahedral elements, but allowed some triangular prisms in transition regions. The C3D8R element was applied to the rectangular-shape region and the C3D6 element was applied to the small curved-shape region.

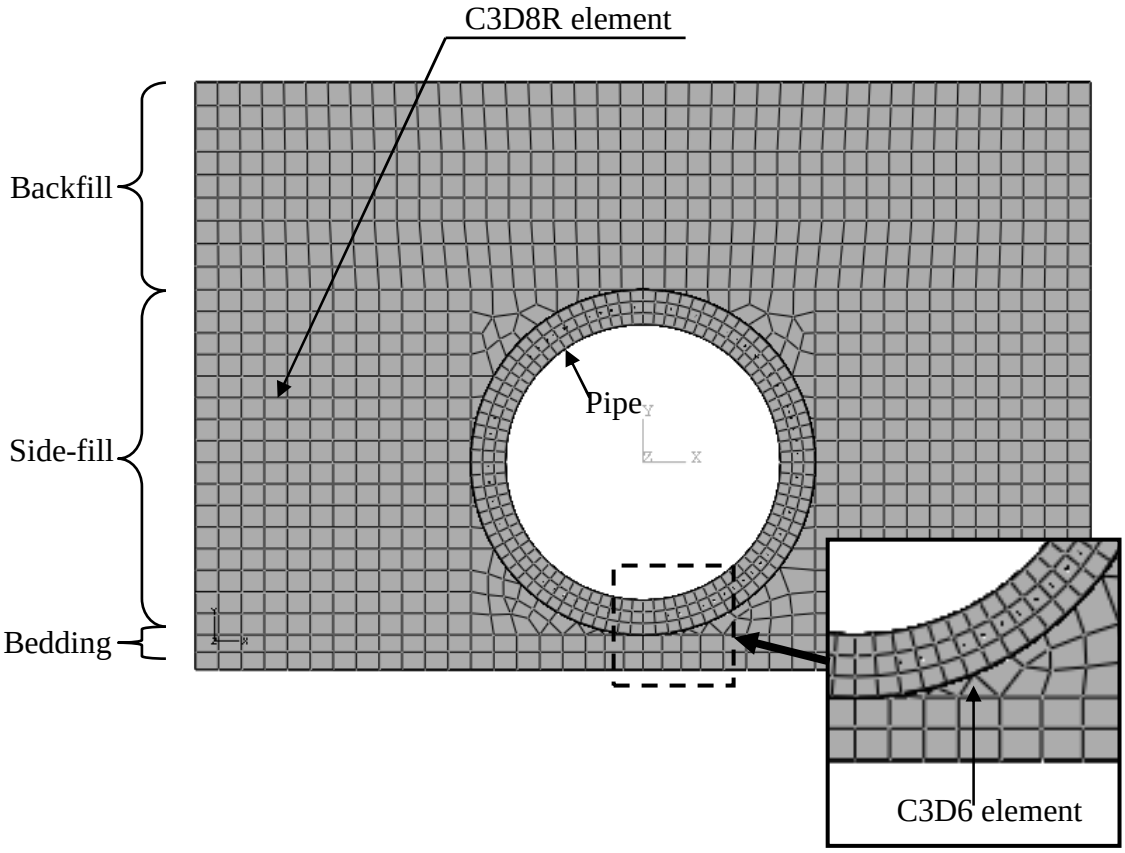

Figure 4.4 FEM model of pipe-soil interaction (trench installation).

4.2.3 Nodes and Elements

Total nodes and elements for the FEM pipe-soil interaction model depend on the pipe sizes, reinforcement and backfill heights. The bigger size of pipe, the more nodes and elements required. Total numbers of nodes and elements are shown in Table 4.1.

Table 4.1 Total Numbers of Nodes and Elements for the Compaction Model

Pipe Internal Diameter	Backfill Height	Nodes	Elements	Degrees of Freedom
24 in. (61 cm)	6 in. (15 cm)	146,228	123,016	877,368
	12 in. (31 cm)	154,060	130,063	924,360
	18 in. (46 cm)	163,916	139,546	983,496
	24 in. (61 cm)	173,684	148,942	1,042,104
36 in. (91 cm)	6 in. (15 cm)	184,170	153,528	1,105,020
	12 in. (31 cm)	187,030	156,216	1,122,180
	18 in. (46 cm)	192,295	161,272	1,153,770
	24 in. (61 cm)	197,690	166,456	1,186,140
48 in. (1.22 m)	6 in. (15 cm)	193,004	165,229	1,158,024
	12 in. (31 cm)	199,916	171,844	1,199,496
	18 in. (46 cm)	206,700	178,396	1,240,200
	24 in. (61 cm)	213,484	184,948	1,280,904
54 in. (1.37 m)	6 in. (15 cm)	224,269	195,952	1,345,614
	12 in. (31 cm)	226,523	198,112	1,359,138
	18 in. (46 cm)	231,129	202,528	1,386,774
	24 in. (61 cm)	233,432	204,736	1,400,592

4.3 Material Properties and Behaviors

The material manager in ABAQUS was used to define the material properties of the section, and associate these properties with the section assignment. For the section with combined properties, such as surrounding soil zones, the partition cell was created to divide the corresponding regions.

4.3.1 Pipeline Section

For the pipeline model (Figure 4.3), the brittle cracking criterion in ABAQUS was applied for the concrete behavior beyond the elastic range. To define the brittle cracking behavior, concrete properties were applied in conjunction with tension stiffening, shear retention, and failure ratios as described in chapter 3. The

homogeneous solid section was used for the concrete section property associated with the solid elements.

The steel reinforcement was also defined in the concrete pipe section by means of tension stiffening property in ABAQUS. As mentioned in Chapter 3, after cracking, concrete continued to carry tensile stress between cracks by the transfer of forces from the tensile reinforcement to the concrete through bond. This contribution of the tensile concrete is known as tension stiffening and it affects the pipe's stiffness after cracking. The tension stiffening was defined as the strain at ultimate is 10 times the strain at failure.

4.3.2 Surrounding Soil Section

The Mohr-Coulomb plasticity model was used for analysis applications in the surrounding soil zone. The model used the classical Mohr-Coulomb yield criterion: a straight line in the meridional plane and an irregular hexagonal section in the deviatoric plane (Figure 4.5). Soil properties (Selig, 1990) used in the FEM model are shown in Chapter 5.

The Mohr-Coulomb model is based on the maximum and minimum principal stresses at failure. The failure occurs when the shear stress on any point reaches a value that depends linearly on the normal stress in the same plane. The failure line is the straight line that touches these Mohr's circles (Figure 4.6).

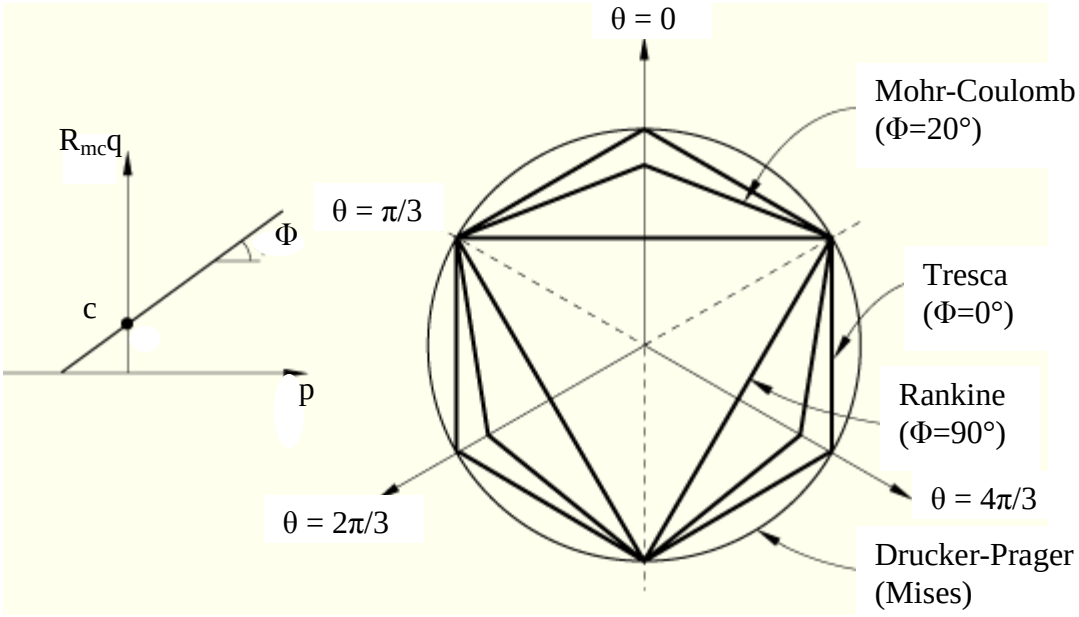

Figure 4.5 Mohr-Coulomb yield surfaces in meridional and deviatoric planes (Re: ABAQUS version 6.8-2, 2008).

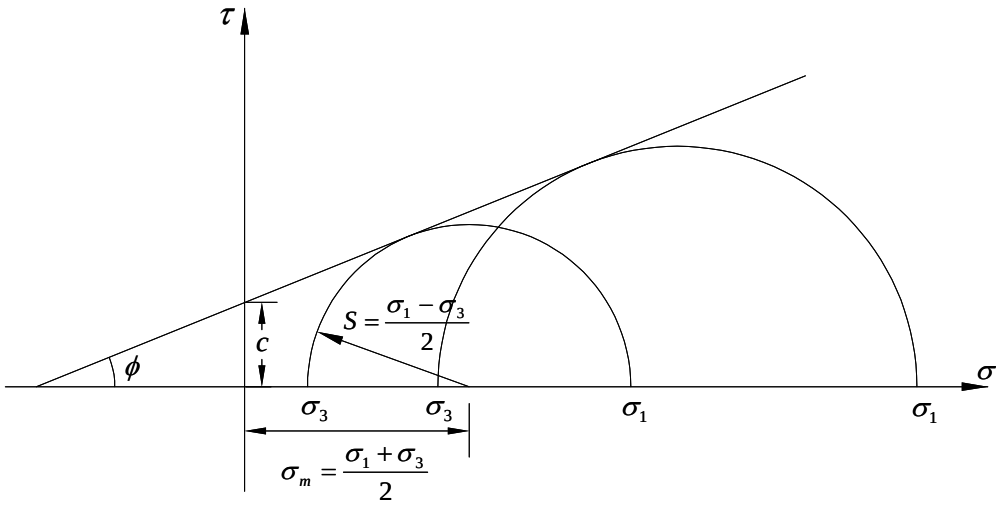

Figure 4.6 Mohr-Coulomb failure model (Re: ABAQUS version 6.8-2, 2008).

Therefore, the Mohr-Coulomb model is defined by

$$\tau = c + \sigma \tan\phi\,, \tag{4.1}$$

where c is the cohesive strength, and ϕ is the friction angle.

For the maximum shear stress, S, and average stress, σ_m, they are defined as:

$$S = \frac{1}{2}(\sigma_1 - \sigma_3) \tag{4.2}$$

$$\sigma_m = \frac{1}{2}(\sigma_1 + \sigma_3), \tag{4.3}$$

where σ_1 and σ_3 are the maximum and minimum principal stresses respectively.

4.4 Explicit Dynamic Analysis

The explicit dynamic analysis performs a large number of small time increments. The use of small increments is advantageous because it allows the solution to proceed without iterations and without tangent stiffness matrices. It also simplifies the treatment of contact conditions and uses a large-deformation theory (ABAQUS, 2008). Thus, the explicit dynamic method is appropriate for the FEM model of pipe-soil compaction which composes of small meshing elements, increasing dynamic forces, and complex pipe-soil interaction surfaces.

An explicit central-difference time integration rule is used so that each increment is relatively reduced. The explicit central-difference operator satisfies the dynamic equilibrium equations at the beginning of the increment, t, the accelerations calculated at time t are used to advance the velocity solution to time $t + \Delta t/2$ and the displacement solution to time $t + \Delta t$. The method is, therefore, computationally attractive for problems where the total dynamic response time.

The explicit dynamics analysis procedure is based upon the implementation of an explicit integration rule together with the use of diagonal ("lumped") element mass

matrices. The equations of motion for the body are integrated using the explicit central-difference integration rule:

$$u^N_{\left(i+\frac{1}{2}\right)} = u^N_{\left(i-\frac{1}{2}\right)} + \frac{\Delta t_{(i+1)} + \Delta t_{(i)}}{2} u^N_{(i)} \tag{4.4}$$

$$u^N_{(i+1)} = u^N_{(i)} + \Delta t_{(i+1)} u^N_{\left(i+\frac{1}{2}\right)}, \tag{4.5}$$

where

u^N is a degree of freedom (a displacement or rotation component),

i is the increment number in an explicit dynamic step.

The use of diagonal element mass matrices leads to the computational efficiency because the accelerations at the beginning of the increment are computed by

$$u^N_{(i)} = \left(M^{NJ}\right)^{-1}\left(P^J_{(i)} - I^J_{(i)}\right), \tag{4.6}$$

where

M^{NJ} is the mass matrix,

P^J is the applied load vector,

I^J is the internal force vector.

A lumped mass matrix is used because the vector multiplication of the mass inverse by the inertial force requires only n operations, where n is the number of degrees of freedom in the model. The explicit procedure requires no iterations and no tangent stiffness matrix. The internal force vector, I^J, is assembled from contributions from the individual elements such that a global stiffness matrix need not be formed.

4.4.1 Nodal Mass and Inertia

The explicit integration scheme in ABAQUS/Explicit requires nodal mass or inertia to exist at all activated degrees of freedom unless constraints are applied using boundary conditions. A nonzero nodal mass must exist unless all activated translational degrees of freedom are constrained and nonzero rotary inertia must exist unless all activated rotational degrees of freedom are constrained. When degrees of freedom at a node are activated by elements with a nonzero mass density (e.g., solid, beam) or mass and inertia elements, a nonzero nodal mass or inertia occurs naturally from the assemblage of lumped mass contributions.

4.4.2 Estimating the Stable Time Increment

In general, the actual stable time increment chosen by ABAQUS/Explicit will be less than this estimate by a factor between $1/\sqrt{2}$ and 1 in a 2-D model and between $1/\sqrt{3}$ and 1 in a 3-D model. The time increment chosen by ABAQUS/Explicit also accounts for any stiffness behavior in a model associated with penalty contact.

The computer time involved in running a simulation using explicit time integration with a given mesh is proportional to the time period of the event. The time increment based on the element-by-element stability estimate can be rewritten (ignoring damping) in the form

$$\Delta t \le \min\left(L_c \sqrt{\frac{\rho}{\lambda + 2\mu}} \right), \tag{4.7}$$

where

L_c is a characteristic length associated with an element,

ρ is the density of the material in the element,

λ and μ are the effective Lamé constants for the material in the element.

The number of increments, n, required is $n = T/\Delta t$ if Δt remains constant, where T is the time period of the event being simulated. Even the element-by-element approximation of Δt will not remain constant in general, since element distortion will change L_c and nonlinear material response will change the effective Lamé constants. But the assumption is sufficiently accurate for the purposes of this discussion. Thus,

$$n \approx T_{\max}\left(\frac{1}{L_c}\sqrt{\frac{\lambda + 2\mu}{\rho}}\right). \tag{4.8}$$

4.4.3 Mass Scaling

Artificially increasing the material density, ρ, by a factor f^2 reduces n to n/f. This concept (ABAQUS, 2008), called "mass scaling," reduces the ratio of the event time to the time for wave propagation across an element while leaving the event time fixed. The rate-dependent behavior is included in the analysis. Mass scaling has exactly the same effect on inertia forces as speeding up the time of simulation. It is often used for computational efficiency in dynamic analyses that contain a few very small elements that control the stable time increment.

Since the mass density influences the stability limit, under some circumstances scaling the mass density can potentially increase the efficiency of an analysis. For example, due to the complex discretization of many models, there are regions containing very small or poorly shaped elements that control the stability limit. These controlling elements are often few in numbers and may exist in localized areas. By

increasing the mass of only these controlling elements, the stability limit can be increased significantly, while the effect on the overall dynamic behavior of the model may be negligible.

In the pipe-soil compaction model, there composed of many regions containing very small elements and complex interaction. Mass scaling was used for the process of scaling the element's mass simulations to adjust the time step. Fixed mass scaling factor was applied to all elements in the model at beginning of the analysis steps.

4.5 Load and Boundary Condition

The dynamic forces from HC 920 hydraulic-compactor machine (hoe pack) including with the weight of backhoe were used in the FEM compaction model. The HC 920 has an impulse force of 16,000 lbf (71 kN) and delivers 2,200 cycles per minute. With a 28-in. (0.7-m) by 40-in. (1-m) plate, the impulse force was applied in a form of force per unit area: $\frac{16{,}000}{28 \times 40}$ = 14.3 psi (98.5 kN/m^2), as shown in Figure 4.7. Moreover, the load from backhoe's weight itself was simulated as ramp condition as shown in Figure 4.8.

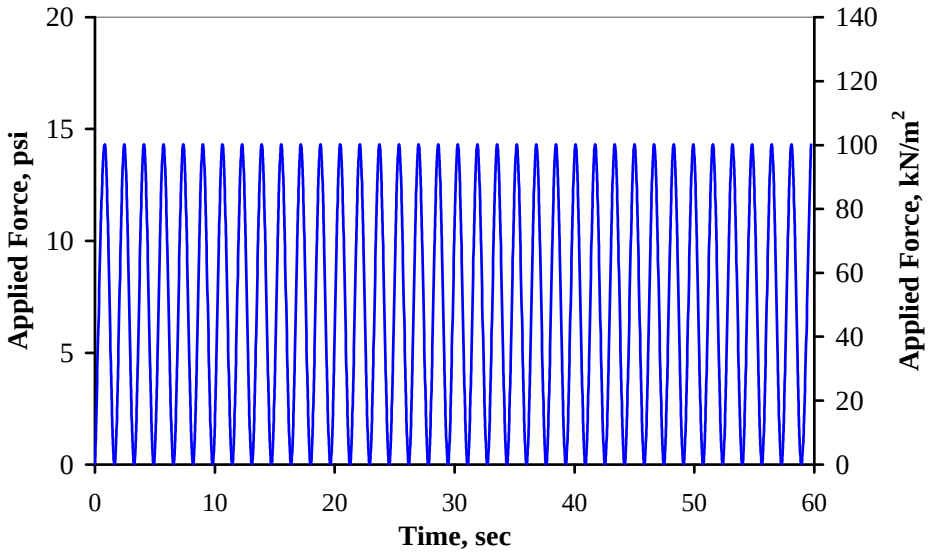

Figure 4.7 Simulated dynamic forces from hoe pack.

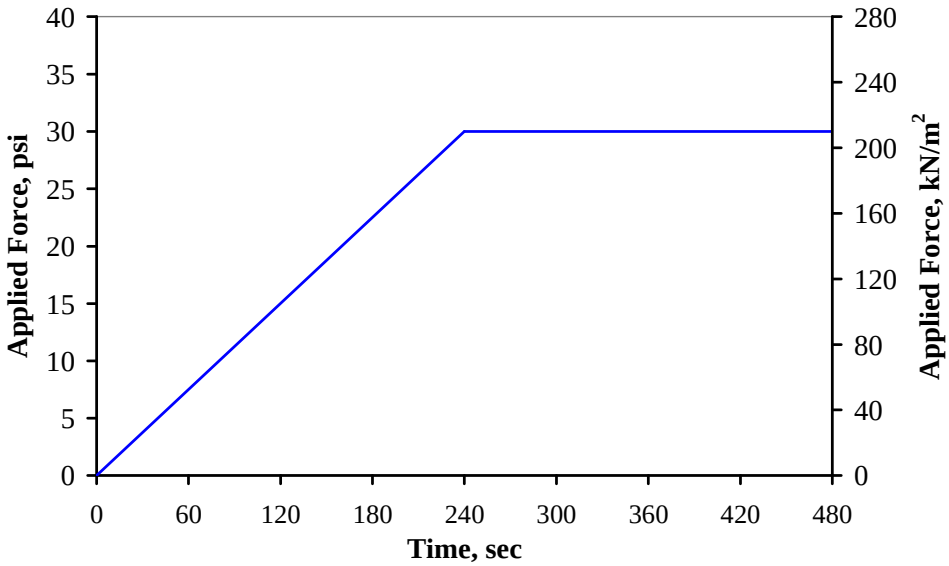

Figure 4.8 Simulated forces from backhoe's weight.

The compaction forces were applied to the backfill soil zone above the pipeline as shown in Figure 4.9. The loading area was corresponding to the dimension of a compacting plate of hoe pack. The applied compaction forces were also varied for four

different locations to investigate the most critical region on the pipeline system. The total load cases will be explained in the parametric study in chapter 5.

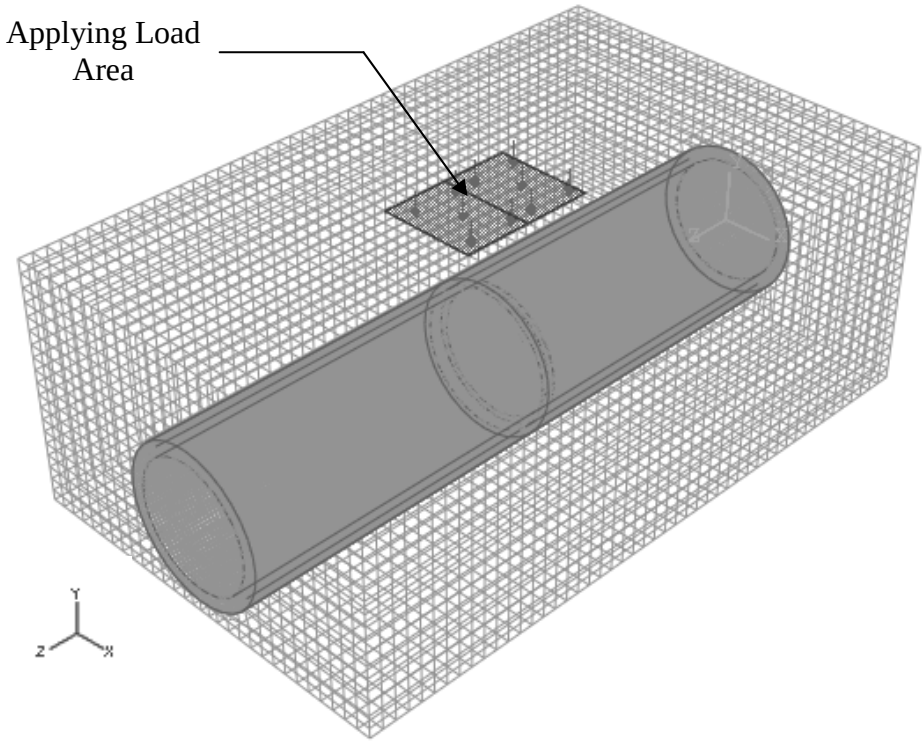

Figure 4.9 Typical load application for pipe-soil FEM model.

The boundary conditions were used to simulate the actual constraints that represent the effect of the surrounding soil in the trench installation. As shown in Figure 4.10, the roller support in vertical direction was applied at all four sides of a trench wall. The translation degree of freedom was constrained at the bottom of the bedding zone. In this case, every node above the bottom of the bedding zone can be freely displaced downward in vertical direction (Y-direction).

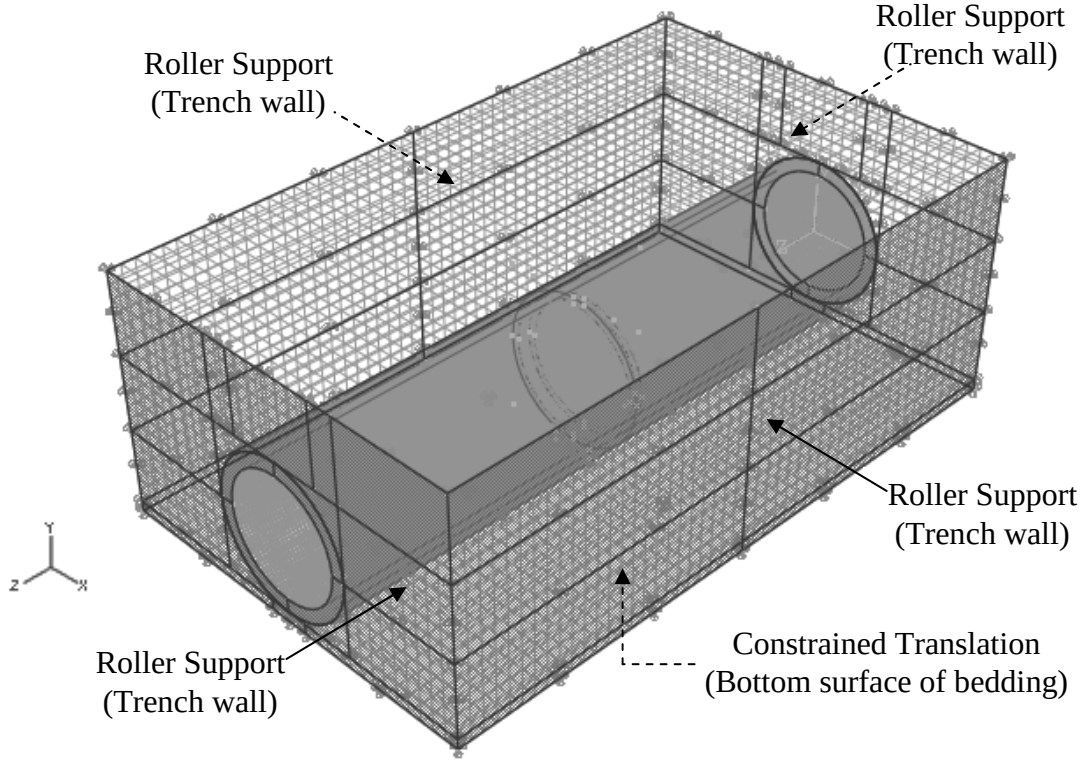

Figure 4.10 Boundary conditions for pipe-soil FEM model.

4.6 Typical Results for FEM Model

With the visualization module, the output results for pipe-soil FEM model were shown by stress components, spatial displacement, and crack behavior. The graphical display expressed the stress intensity by discrete bands of the colored contour. At the interesting position, the set of specific nodes was created as a tabular form to plot the stress and displacement curve. The display group manager in ABAQUS allowed selecting separate parts of the model to show the behavior in each region. The crack propagation was also observed by the graphical display at each step/frame.

4.6.1 Typical FEM Stress Results

The dynamic forces were applied through the backfill soil above the pipe and induced the stresses on pipe's wall. Figure 4.11 shows the stress transferring in backfill soil layers. As shown in Figure 4.12, the stress results on pipe's wall were indicated as S11 and S22. According to the coordinate axis, S11 described the stress results at crown and invert. S22 described the stress results at springline. At crown and invert, a compressive stress occurred at the external section of pipe's wall and a tensile stress occurred at the internal section of the pipe's wall. In contrary, at springline, a compressive stress occurred at the internal section of pipe's wall and a tensile stress occurred at the external section of the pipe's wall.

4.6.2 Typical FEM Deformation Results

Pipe's cross section was compressed vertically and extended horizontally. The values can be observed by the change in vertical and horizontal diameters. Depending on the properties of sidefill zone, the deformation shape was shown in Figure 4.13. As properties of two sidefill zones were identical, pipe deformed symmetrically about the vertical centerline. In contrast, difference in properties of two sidefill zones affected the symmetrical deformation.

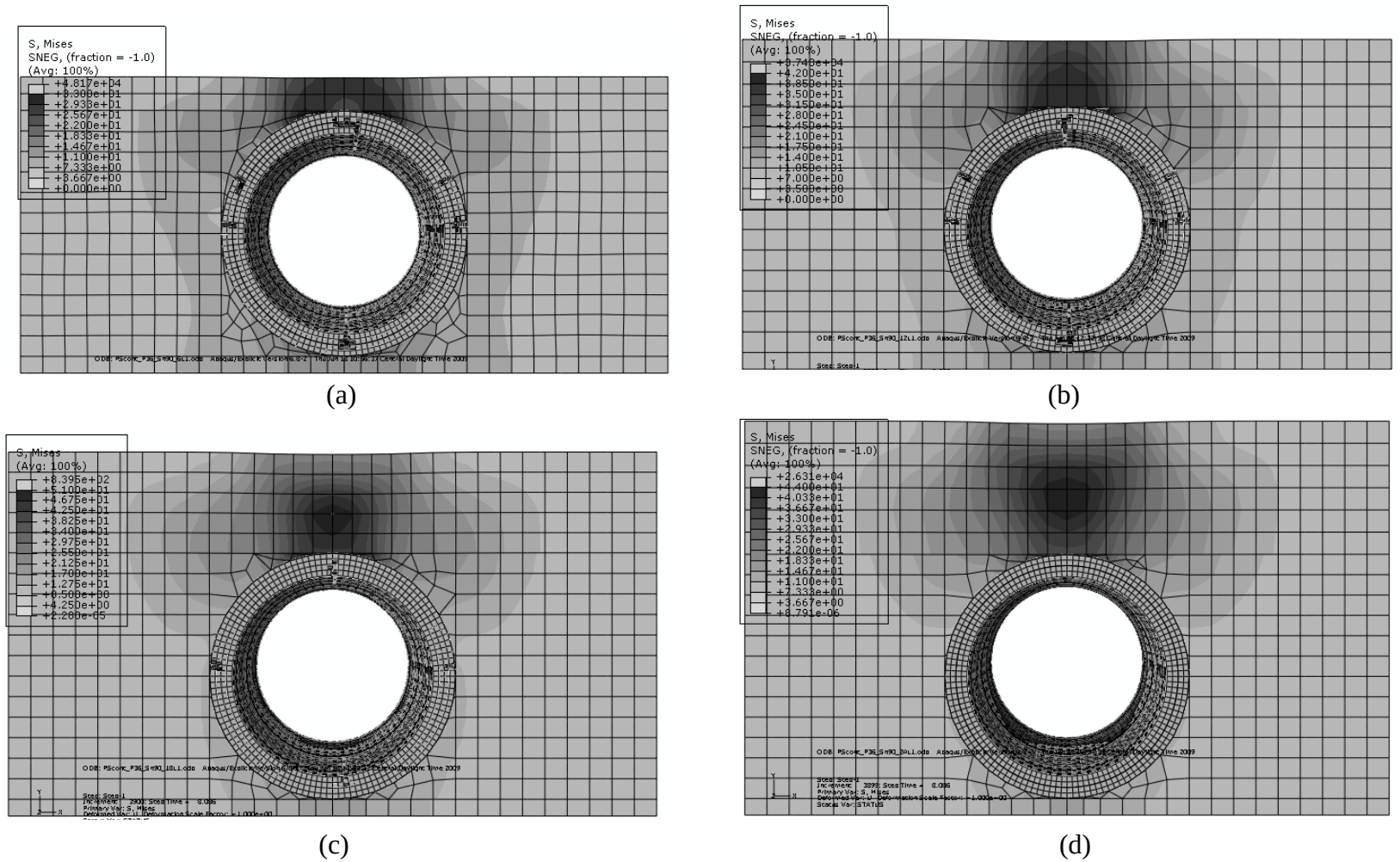

Figure 4.11 Typical stresses transferring in the backfill soil layers;
(a) 6-in. (15-cm) backfill soil, (b) 12-in. (31-cm) backfill soil,
(c) 18-in. (46-cm) backfill soil, (d) 24-in. (61-cm) backfill soil.

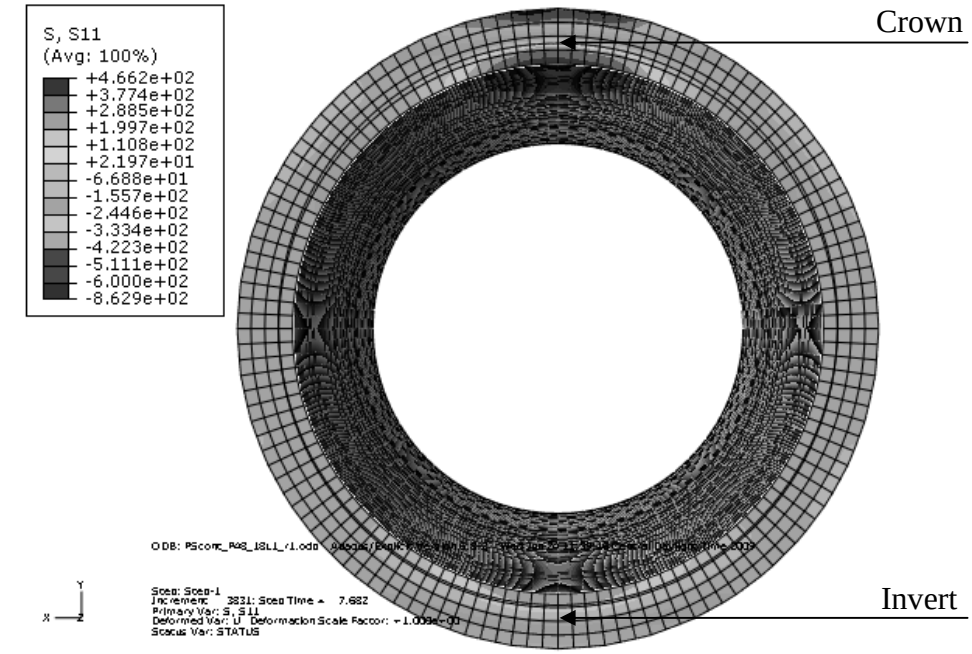

(a)

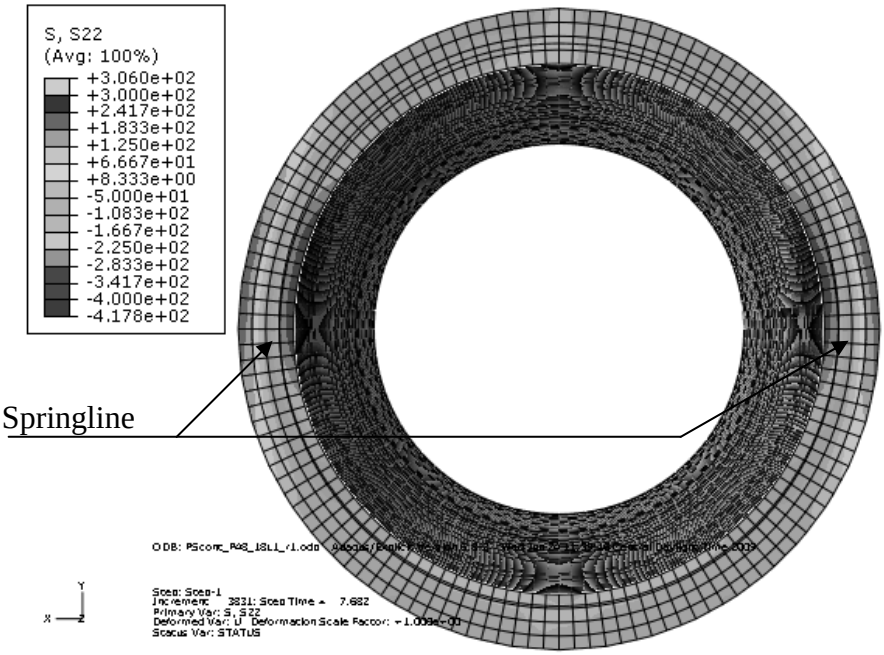

(b)

Figure 4.12 Typical FEM stress results on pipe;
(a) stress S11 at crown and invert and (b) stress S22 at springline.

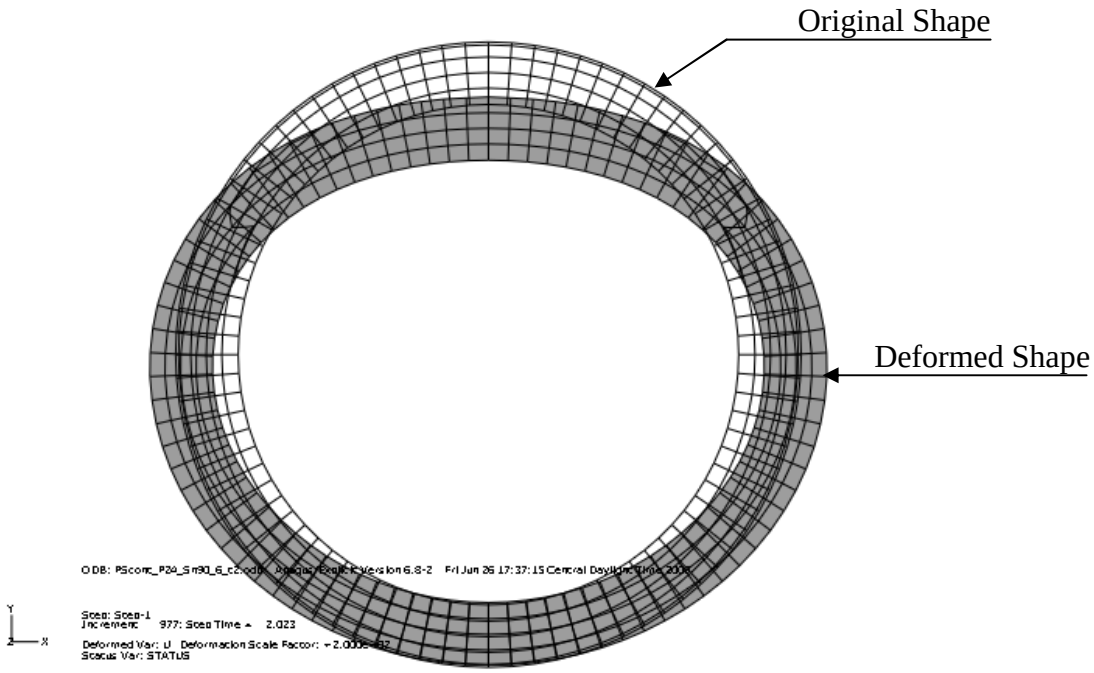

(a)

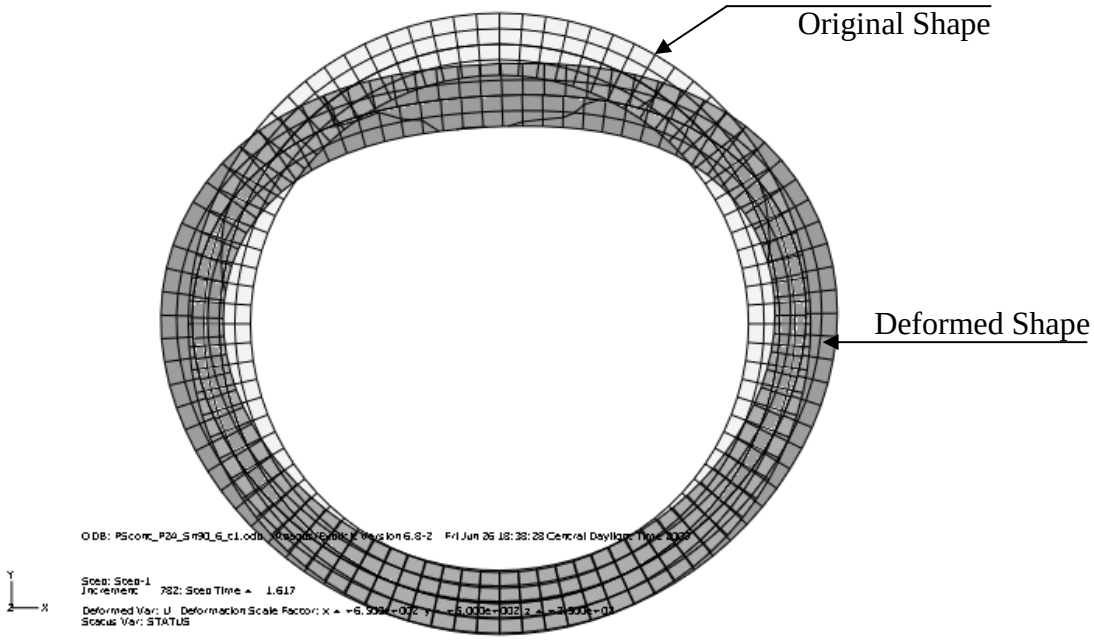

(b)

Figure 4.13 Typical FEM deformation results (magnified scale = 250 times); (a) identical side-fill zones and (b) different sidefill zones.

4.6.3 Typical FEM Crack Results

As the concrete brittle property in ABAQUS was applied, the element in FEM pipe-soil model was automatically removed when its failure strength in tension was reached. This behavior precisely simulated the crack propagation on the buried concrete pipe's wall. However, the actual sizes of crack width can not be verified through the FEM results due to the element size corresponding to the analytical run time. The length and shape of crack are provided. In this model, typical longitudinal cracks started at crown, invert, and springline respectively. Cracks firstly occurred at tension surface and then propagated to the compression surface as shown in Figure 4.14. Moreover, the circumferential crack occurred at the joint of pipeline system for the case of a 24-in. (61-cm) pipe with the backfill height of 6 in. (15 cm) as shown in Figure 4.15.

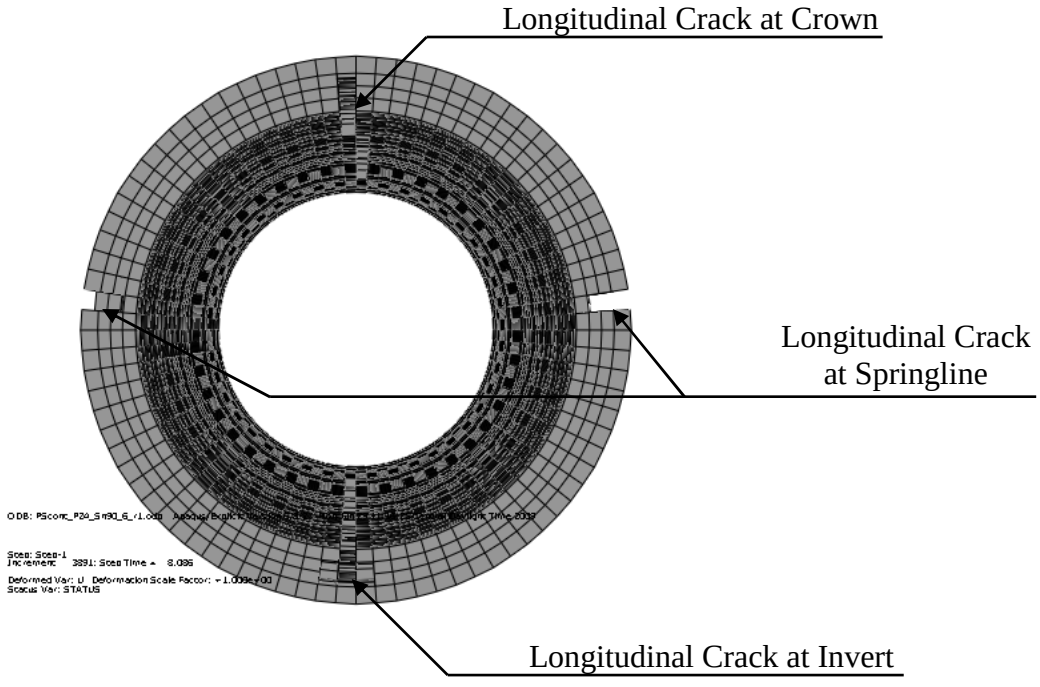

Figure 4.14 Typical FEM crack results in cross-sectional view.

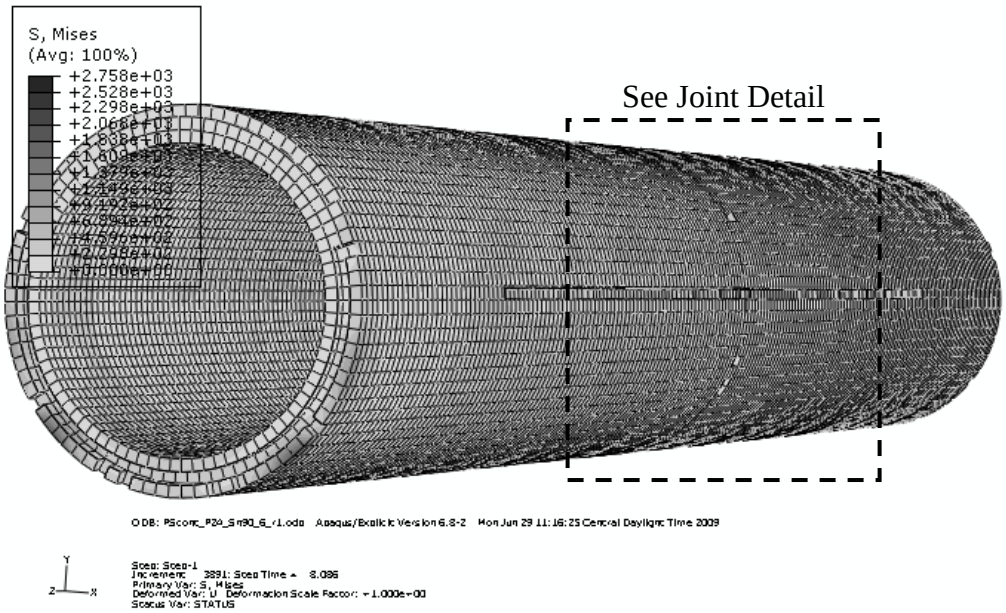

(a)

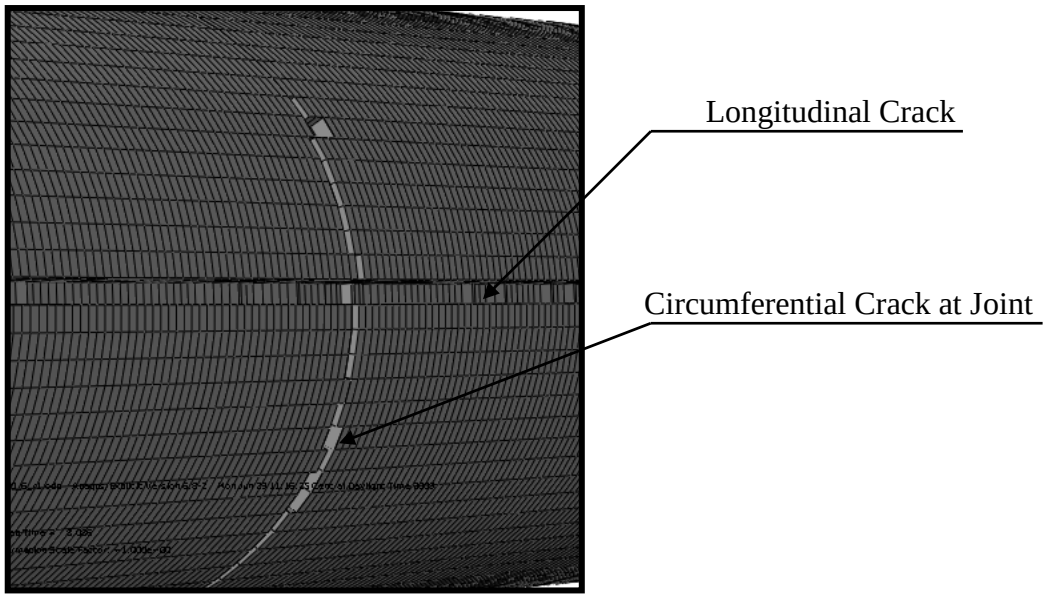

(b)

Figure 4.15 Typical FEM crack results in longitudinal view;
(a) cracking on a 2-span pipeline model and (b) joint detail.

CHAPTER 5

PARAMETRIC STUDY

5.1 Introduction

Parametric studies of pipe-soil compaction model execute the analysis with different sets of input parameters as shown in Table 5.1. In this parametric study, the executions composed of 128 analysis cases which conduct to the effects of the compaction force on the underground pipeline. The main objective is to specify the minimum backfill soil covered above the pipe such that there is no damage occurred on the pipeline during the compaction process. The interesting parameters included with the pipe sizes, backfill heights, side-fill materials, and loading locations on the RC pipeline compaction process. For all analysis cases, bedding thickness was 3 in. (7.62 cm). Also, Sn90 was applied for bedding and backfill soil materials.

5.2 Details of Reinforced Concrete Pipe

Different pipe sizes were studied for investigating the various behaviors of induced stresses, deformations, and cracking patterns on the pipe wall. Four different sizes composed of 24-in. (61-cm), 36-in. (91-cm), 48-in. (1.22-m), and 54-in. (1.37-m) diameters as shown in Table 5.2. The concrete strength, wall thickness, and reinforcement details were corresponding to the design requirement (ACPA, 2007).

Table 5.1 Total 128 Cases in Parametric Study

Pipe Diameter	Backfill Height	Side-fill Material	Loading Locations
24 in. (61 cm)	6 in. (15 cm) 12 in. (31 cm) 18 in. (46 cm) 24 in. (61 cm)	Sn90/Sn90 Sn90/Si85	L1 L2 L3 L4
36 in. (91 cm)	6 in. (15 cm) 12 in. (31 cm) 18 in. (46 cm) 24 in. (61 cm)	Sn90/Sn90 Sn90/Si85	L1 L2 L3 L4
48 in. (1.22 m)	6 in. (15 cm) 12 in. (31 cm) 18 in. (46 cm) 24 in. (61 cm)	Sn90/Sn90 Sn90/Si85	L1 L2 L3 L4
54 in. (1.37 m)	6 in. (15 cm) 12 in. (31 cm) 18 in. (46 cm) 24 in. (61 cm)	Sn90/Sn90 Sn90/Si85	L1 L2 L3 L4

Table 5.2 Reinforced Concrete Pipe Properties

Pipe Diameter	Class/ Wall	Wall Thickness	Concrete Strength	Reinforcement, $in.^2$ / linear ft of pipe wall	
				Inner Cage	Outer Cage
24 in. (61 cm)	III/B	3 in. (7.62 cm)	4,000 psi (28 MPa)	0.07	-
	III/C	$3\frac{3}{4}$ in. (9.38 cm)	4,000 psi (28 MPa)	0.07	-
36 in. (91 cm)	III/B	4 in. (10 cm)	4,000 psi (28 MPa)	0.17	-
	III/C	$4\frac{3}{4}$ in. (12 cm)	4,000 psi (28 MPa)	0.08	-
48 in. (1.22 m)	III/B	5 in. (13 cm)	4,000 psi (28 MPa)	0.24	0.14
	III/C	$5\frac{3}{4}$ in. (15 cm)	4,000 psi (28 MPa)	0.16	0.10
54 in. (1.37 m)	V/B	$5\frac{1}{2}$ in. (14 cm)	6,000 psi (41 MPa)	0.82	0.49
	V/C	$6\frac{1}{4}$ in. (16 cm)	6,000 psi (41 MPa)	0.58	0.35

5.3 Backfill Soil Zone

Backfill height was increased from 6 in. (15 cm) to 24 in. (61 cm) above the pipe's crown level as shown in Figure 5.1. Compaction forces were applied at every increment of the backfill soil layers. The 6-in. (15-cm) backfill height simulated the most critical case of the pipe compaction when the backfill covering was deficient. Backfill height was then increased until there was no cracking occurred on a buried pipe under the applied compaction force. Material properties for backfill soil for all analysis cases were Sn90, gravelly sand at 90% of standard proctor density (ASTM D 698, 2005; and AASHTO T 99, 2005). The properties of Sn90 are described as follows: soil unit weight = 135 lb/ft^3 (2,163 kg/m^3), Young's modulus = 1,300 psi (9 MPa), Poisson's ratio = 0.35, cohesion yield stress = 0.145 psi (1 kPa), friction angle = 42 degree, and dilation angle = 12 degree (Selig, 1990).

5.4 Side-fill Soil Zone

Side-fill soil was separated into two cases when both sides were identical and uneven properties. The first case simulated a good control of sidefill compaction as shown in Figure 5.2(a), while another case simulated the lack of controlled sidefill compaction in the construction as shown in Figure 5.2(b). Materials used for sidefill soil zone were Sn90, gravelly sand at 90% of standard proctor density, and Si85, sandy silt at 85% of standard proctor density (ASTM D 698, 2005; and AASHTO T 99, 2005). For Sn90, properties compose of soil unit weight = 135 lb/ft^3 (2,163 kg/m^3), Young's modulus = 1,300 psi (9 MPa), Poisson's ratio = 0.35, cohesion yield stress = 0.145 psi (1 kPa), friction angle = 42 degrees, and dilation angle = 12 degrees. For Si85,

properties compose of soil unit weight = 114 lb/ft^3 (1,826 kg/m^3), Young's modulus = 360 psi (2.5 MPa), Poisson's ratio = 0.37, cohesion yield stress = 0.145 psi (1 kPa), friction angle = 30 degrees, and dilation angle = 0 degree (Selig, 1990).

5.5 Loading Locations

The effect of compacting locations on the behavior of a buried pipeline was evaluated. To indicate the most critical zone in the compaction process, the dynamic force was applied at four different locations: L1, L2, L3, and L4 as shown in Figure 5.3. L1 simulated the compaction at the pipeline's joint. L2 simulated the compaction at the pipe's edge. Consequently, L3 simulated the compaction at a pipe's middle span. Finally, L4 simulated the compaction on the side of pipe's middle span. The total magnitude of applied force (Chapter 4) was identical for all analysis cases. Also, all loading locations were applied during every increment of 6-in. (15-cm) backfill soil layer in order to investigate the effect of backfill height on the reduction of compacting force.

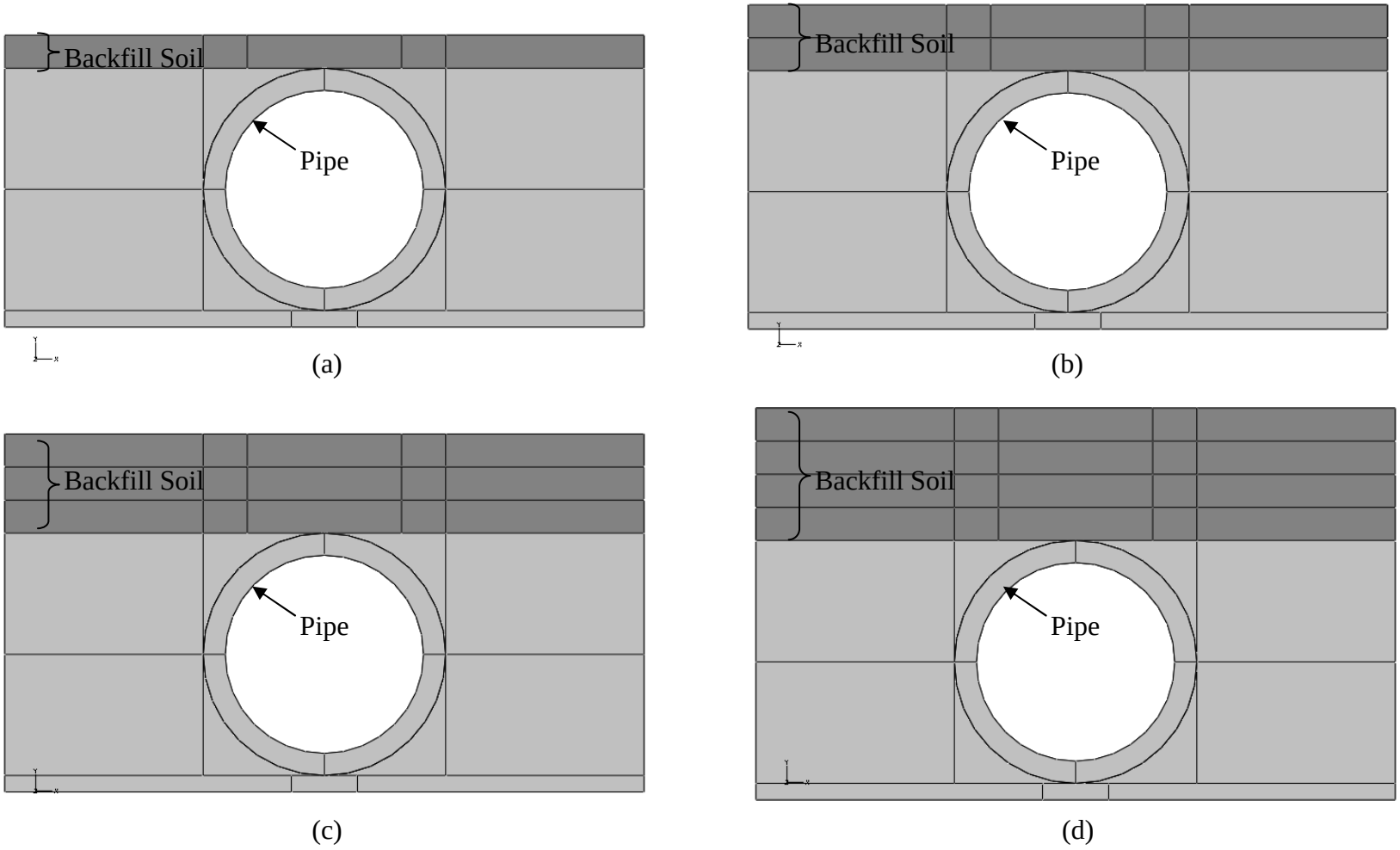

Figure 5.1 Increment of backfill soil layers; (a) 6-in. (15-cm) backfill height, (b) 12-in. (31-cm) backfill height, (c) 18-in. (46-cm) backfill height, (d) 24-in. (61-cm) backfill height.

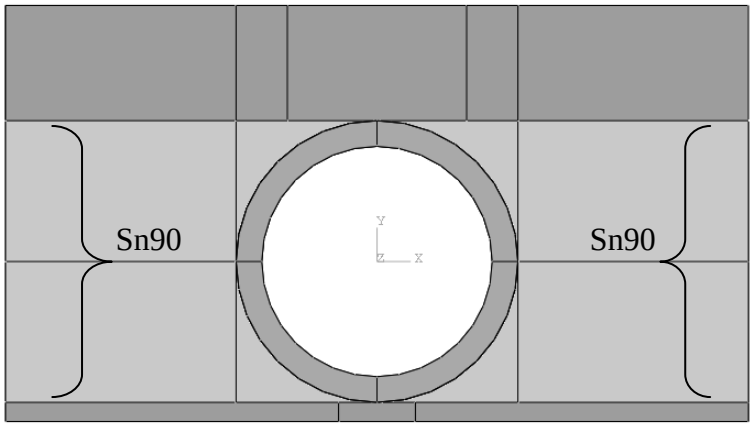

(a)

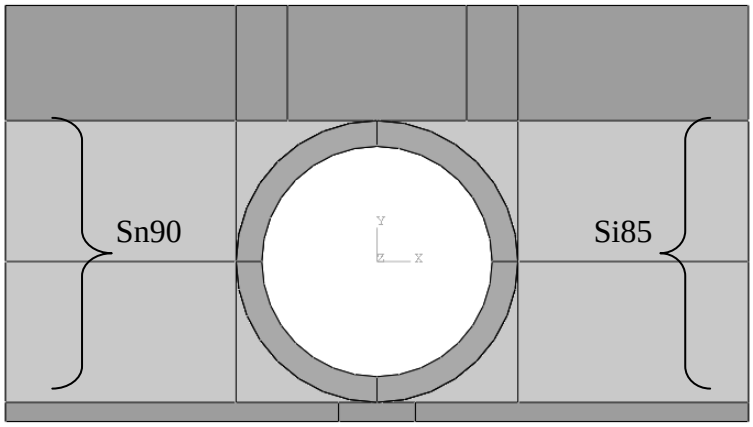

(b)

Figure 5.2 Side-fill soil applications; (a) identical side-fill (Sn90/Sn90) and (b) different side-fill (Sn90/Si85).

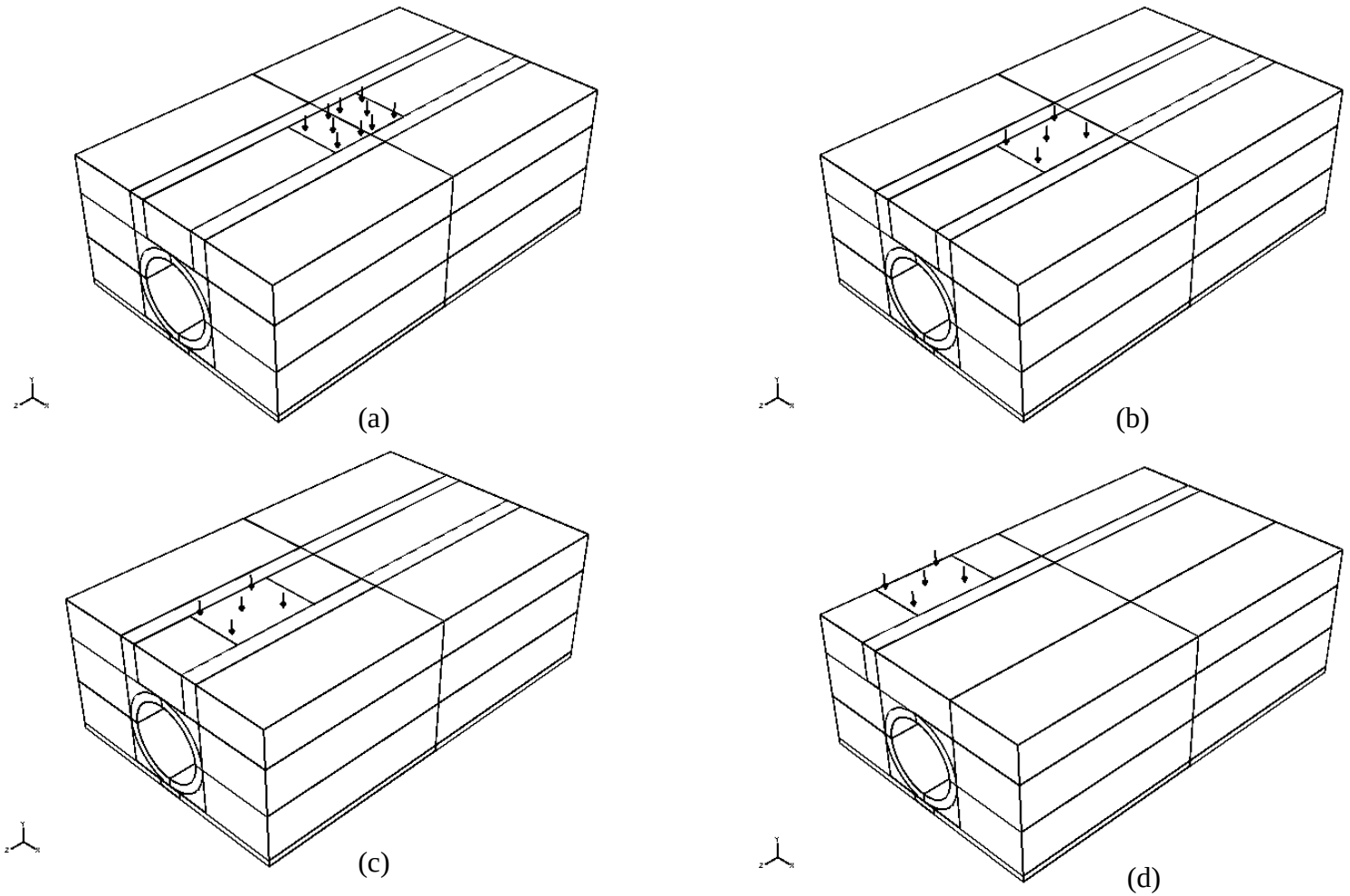

Figure 5.3 Four different locations of applied force; (a) location L1, (b) location L2, (c) location L3, (d) location L4.

5.6 Discussion on Parametric Study

The parametric study results described the influence of backfill heights on the stresses induced on the pipe wall, the deformations occurred, and the crack propagation. The results were shown in forms of the deformation versus backfill height, stress versus deformation, and decrease in tensile stresses for different pipe sizes, as shown in Figures B.1 through B.20.

5.6.1 Deformation versus Backfill Height

As shown in Figures B.1 through B.8, the results show that, for all pipe sizes, the increase in backfill height decreases the deformation of pipe's cross section in both vertical and horizontal directions. The most critical location of loading is at L2 (compaction at joint of pipeline) and the least critical location of loading is at L4 (compaction at side of pipeline).

The application of lower compacted soil on one side of the sidefill (Sn90/Si85) yields higher pipe's deformation than identically controlled compaction of the sidefill (Sn90/Sn90). For an example of 24-in. (61-cm) pipe with 6-in. (15-cm) backfill height under the L2 loading location, the vertical deformation is 0.38 in. (9.65 mm) for Sn90/Sn90 while the vertical deformation becomes 0.48 in. (12.19 mm) for Sn90/Si85 as shown in Figure B.1 (a). Also, for the horizontal deformation, the result values are 0.25 in. (6.35 mm) for Sn90/Sn90 and 0.32 in. (8.13 mm) for Sn90/Si85, respectively as shown in Figure B.1 (b).

Moreover, the effect of backfill height on pipe's deformations becomes minimized as pipe size increases. The results of decrease in pipe's deformation with the

increase in backfill height under L2 loading location, Sn90/Sn90 sidefill soil for all pipe sizes are shown in Table 5.3, corresponding to Figures B.1, B.3, B.5, and B.7. The results of decrease in pipe's deformation with the increase in backfill height under L2 loading location, Sn90/Sn90 sidefill soil for all pipe sizes are shown in Table 5.4, corresponding to Figures B.2, B.4, B.6, and B.8.

Table 5.3 Decrease in Effect of Backfill Height with Larger Pipe Sizes under Sn90/Sn90 Side-fill Condition

Pipe Diameter	**Increase in Backfill Soil Layers**	**Decrease in Deformations**	
		Vertical	**Horizontal**
24 in. (61 cm)	6 in. (15 cm) to 24 in. (61 cm)	92 %	87 %
36 in. (91 cm)	6 in. (15 cm) to 24 in. (61 cm)	91 %	85 %
48 in. (1.22 m)	6 in. (15 cm) to 24 in. (61 cm)	63 %	56 %
54 in. (1.37 m)	6 in. (15 cm) to 24 in. (61 cm)	47 %	46 %

Table 5.4 Decrease in Effect of Backfill Height with Larger Pipe Sizes under Sn90/Si85 Side-fill Condition

Pipe Diameter	**Increase in Backfill Soil Layers**	**Decrease in Deformations**	
		Vertical	**Horizontal**
24 in. (61 cm)	6 in. (15 cm) to 24 in. (61 cm)	93 %	90 %
36 in. (91 cm)	6 in. (15 cm) to 24 in. (61 cm)	91 %	90 %
48 in. (1.22 m)	6 in. (15 cm) to 24 in. (61 cm)	69 %	65 %
54 in. (1.37 m)	6 in. (15 cm) to 24 in. (61 cm)	58 %	54 %

5.6.2 Stress versus Deformation

Figures B.9 through B.20 show the stress-deformation curve at the most critical location of loading, L2, on the pipeline. The results included all tensile and compressive stresses at crown, invert, and springline with the increasing backfill heights of 6 in. (15 cm), 12 in. (31 cm), 18 in. (46 cm), and 24 in. (61 cm) above the pipe's crown. The

vertical deformation of pipe cross section was considered. Under compacting force, the use of 6-in. (15-cm) backfill height yielded the most critical condition, while the 24 in. (61 cm) backfill height conducted the safest condition. The higher the backfill soil, the more alleviation in the effect of compacting force, and the less crack occurred on the pipe wall. When the cracking tensile stress, $f_t = 7.5\sqrt{f_c'}$, was reached, the first crack initiated. For the 24-in. (61-cm) pipe, 36-in. (91-cm) pipe, and 48-in. (1.22-m) pipe, $f_t = 7.5\sqrt{f_c'}$ = 474 psi (3.3 MPa). For the 54-in. (1.37-m) pipe, $f_t = 7.5\sqrt{f_c'}$ = 581 psi (4 MPa). Cracks propagated at crown, invert, and springline respectively.

In the 24-in. (61-cm) pipe, cracking at crown occurred when the vertical deformation was 0.013 in. (0.33 mm) as shown in Figure B.9. Cracking at invert occurred when the vertical deformation was 0.018 in. (0.45 mm) as shown in Figure B.10. Cracking at springline occurred when the vertical deformation was 0.02 in. (0.5 mm) as shown in Figure B.11. All cracks occurred with the use of 6-in. (15-cm) up to 18-in. (46-cm) backfill height. However, there was no sign of cracking at all locations of crown, invert, and springline when backfill height was 24 in. (61 cm) above the pipe's crown.

In the 36-in. (91-cm), cracks occurred at crown and invert only. There was no crack happened at springline. Cracking at crown occurred when the vertical deformation was 0.02 in. (0.5 mm) as shown in Figure B.12. Cracking at invert occurred when the vertical deformation was 0.03 in. (0.75 mm) as shown in Figure B.13. Also, there was no crack occurred for the case of 24-in. (61-cm) backfill height above the pipe's crown.

In the 48-in. (1.22-m), Cracking at crown occurred when the vertical deformation was 0.029 in. (0.73 mm) as shown in Figure B.15. Cracking at invert occurred when the vertical deformation was 0.043 in. (1.08 mm) as shown in Figure B.16. Under the 12-in. (31-cm) backfill height, cracking occurred at crown only. There was no crack at invert and springline. Then, under the 24-in. (61-cm) backfill height, there was no crack occurred at any locations on the 48-in. (1.22-m) pipe.

In the case of 54-in. (1.37-m) pipe, under the compacting force, there was no crack appeared on the pipe wall for all backfill heights from 6 in. (15 cm) to 24 in. (61 cm). As shown in Figures B.18 through B.20, at all locations of crown, invert, and springline, induced tensile stresses on the pipe wall did not reach the cracking tensile stress $f_t = 7.5\sqrt{f_c'}$ = 581 psi (4 MPa).

5.6.3 Effect of Backfill Height on Decreased Tensile Stresses for Different Pipe Sizes

According to the most critical region, the discussion centers on the tensile stresses at pipe's crown. The highest tensile stresses at each backfill height were plotted for all pipe sizes. In this case, for the 24-in. (61-cm) pipe, 36-in. (91-cm) pipe, and 48-in. (1.22-m) pipe, maximum tensile stresses reached the cracking stress for all backfill heights, except for the 24-in. (61-cm) backfill height. However, there was no crack occurred for the 54-in. (1.37-m) pipe and the maximum tensile stress was below the cracking stress. Figure 5.4 shows the effect of backfill height on the change in tensile stress reduction for different pipe sizes. Backfill height has the greatest effect on the reduction of tensile stresses for the 24-in. (61-cm) pipe and it has the smallest effect for

the 54-in. (1.37-m) pipe. The bigger pipe size, the less effect of backfill height involves in the stress reduction.

However, in the case of the 36-in. (91-cm) pipe, the results show the small effect of backfill height on the stress reduction. Although the backfill height of 24 in. (61 cm) was used, the maximum tensile stress on the 36-in. (91-cm) pipe was still high as close as the cracking stress level. This aspect led to the consideration of the ratio between pipe's internal diameter (D) and wall thickness (T), called the "D/T ratio", as well as the density of reinforcement. The higher value of the D/T ratio indicates the lower stiffness of a pipe because when a pipe is increased in diameter, the wall thickness must have a proportional depth. As shown in Table 5.5, the D/T ratio of a 36-in. (91-cm) pipe is the second highest next to that of a 48-in. (1.22-m) pipe. But, a 36-in. (91-cm) pipe composes of only one layer of a steel reinforcement which is much lighter if compared with double-layer reinforcement in a 48-in. (1.22-m) pipe. Thus, a 36-in. (91-cm) pipe is the weakest pipe in this FEM study and the maximum tensile stresses induced on the pipe wall are also high even modeled under the 24-in. (61-cm) backfill height.

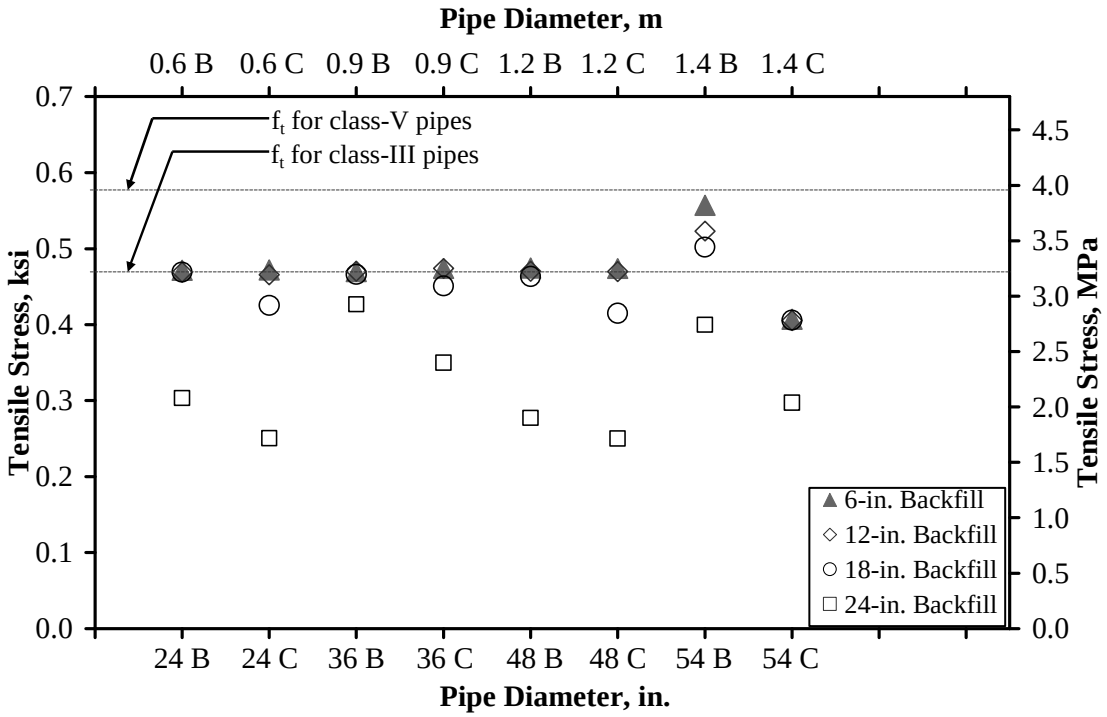

Figure 5.4 Tensile stresses at crown for different pipe sizes under increased backfill heights.

Table 5.5 Pipe's D/T Ratio and Reinforcement Density

Pipe Diameter, D	Class/ Wall	Wall Thickness, T	D/T Ratio	Reinforcement, in.^{2} / linear ft of pipe wall	
				Inner Cage	Outer Cage
24 in. (61 cm)	III/B	3 in. (7.62 cm)	8	0.07	-
	III/C	$3\frac{3}{4}$ in. (9.38 cm)	6.4	0.07	-
36 in. (91 cm)	III/B	4 in. (10 cm)	9	0.17	-
	III/C	$4\frac{3}{4}$ in. (12 cm)	7.58	0.08	-
48 in. (1.22 m)	III/B	5 in. (13 cm)	9.6	0.24	0.14
	III/C	$5\frac{3}{4}$ in. (15 cm)	8.35	0.16	0.10
54 in. (1.37 m)	V/B	$5\frac{1}{2}$ in. (14 cm)	9.81	0.51	0.31
	V/C	$6\frac{1}{4}$ in. (16 cm)	8.64	0.58	0.35

CHAPTER 6

SUMMARY, CONCLUSIONS, AND RECOMMENDATIONS

6.1 Summary

The behavior of concrete pipe was investigated experimentally and analytically. The overall work included the D-Load test and pipe compaction under the heavy machine. Properties of all pipe specimens: concrete strength, wall thickness, and reinforcement details were corresponding to the Concrete Pipe Design Requirement ASTM C76 – 08.

Firstly, a full-scale pipeline installation test was performed. The 24-in. (61-cm) diameter pipes were installed in the Type-B trench installation, defined by the Concrete Pipe Technology Handbook. Two spans of interesting pipe specimens were equipped with instruments: strain gauges, earth pressure cells and inspection camera so that the test data were recorded during the test. The investigation was made for both sidefill (lateral sides of pipe) compaction and backfill (above pipe) compaction. According to the real construction, compaction forces were applied at every increment of 6-in. (15-cm) layer of backfilling soil. In the sidefill compaction state, lateral soil at both sides of pipeline was compacted using the backhoe's bucket tamping. In the backfill compaction state, backfill soil above the pipeline was compacted using hoe pack including the weight of backhoe. Experimental test results included the induced pressure on the pipe

wall, strain results, and the failure mode. Also, the most critical region of pipeline under the compaction process was revealed.

However, the results from an experimental pipeline compaction test could not be perfectly obtained and verified with the analytical method due to many disturbing variables as pipes were buried underground and interacted by the surrounding soil. This concern led to the study of concrete pipes under crushing force, called “D-Load” test. In this controlled-situation test, a pipe specimen was set up in the standard three-edge bearing (TEB) machine, specified by the ASTM C 497. There was no surrounding soil related. TEB machine provided two lower strips as pipe’s supports and upper bearing to apply crushing force to a pipe at center line through the pipe’s length. Test specimen sizes included 18-in. (46-cm), 36-in. (91-cm), and 54-in. (1.37-m) diameter pipes. The instrumentations included strain gauges and linear variable displacement transducers to measure the strain and pipe’s deformation. The applied load steps were controlled by using the TEB machine. For each pipe size, the results showed the crack widths, crack patterns, and failure modes corresponding to the load-deformation curves so that the pipe behaviors were could be continuously investigated. Not only were the results used for understanding concrete pipe behaviors, but also to verify the analytical model using the finite element (FEM) analysis.

Thereafter, the three-dimensional (3-D) FEM models of the D-Load test were created using computer program, ABAQUS version 6.8-2. The 8-noded brick element was used with the mesh convergence to model a pipe tested in the TEB machine. All pipe sizes were the same as those in the experimental tests. The TEB machine model

was composed of two support strips and upper bearing strip. Contact regions were modeled as hard contact. During the dynamic analysis, applied loads were simulated as increment steps and mass scaling was considered to increase the analytical efficiency. The property of concrete brittle criteria was applied to the pipe section so that the postfailure behavior of concrete was defined. With this concept, the tension stiffening played a major role introducing strain across the crack on concrete. Consequently, the value of strain at ultimate by strain at cracking was verified using compared results from the experimental D-Load tests.

Finally, a parametric study was conducted to predict the effect of dynamic compaction forces on the buried pipeline under the trench installation. The 3-D FEM model composed of two spans of a concrete pipe and surrounding soils. All standard pipe sizes included 24-in. (61-cm), 36-in. (91-cm), 48-in. (1.22-m), and 54-in. (1.37-m) diameter pipes. The concrete pipe properties followed the Concrete Pipe Design Requirement ASTM C76 – 08. Based on the maximum and minimum principal stresses at failure, the Mohr-Coulomb criterion was used to assign the properties of surrounding soil models. The elements used were 8-noded brick for the concrete pipe and surrounding soil sections. Also, 6-noded triangular prism was used to fit the small curved regions between pipe and soil. At the interfaces between the pipe-soil regions, all surfaces were in contact and transmitted shear as well as normal forces across their interfaces. The converged mesh generation was obtained using energy based convergence criteria. In the dynamic analysis step, the magnitude and vibration of applied forces were simulated from the hoe pack including with the back hoe’s weight.

The scaled mass matrix was used for each increment within the dynamic analysis step to increase computational efficiency. A parametric study results showed the effect of backfill height on the stress and deformation reduction when varying the pipe sizes, soil material, and loading locations.

The related variables used in a parametric study included the effects of geometry, material, and loading location. The geometric related variables of concrete pipe were evaluated by using four standard sizes of concrete pipe: 24-in. (61-cm), 36-in. (91-cm), 48-in. (1.22-m), and 54-in. (1.37-m) diameter pipes. Also, geometric related variables of surrounding soil were centered on the backfill soil heights, increased from 6 in. (15 cm) to 24 in. (61 cm). The material related variables simulated the compaction control at the sidefill soil zone. Materials involved the gravelly sand (Sn90) and sandy silt (Si85). Two cases of sidefill compaction were defined as Sn90/Sn90 and Sn90/Si85. The Sn90/Sn90 case indicated the perfectly controlled compaction on both sides. The Sn90/Si85 case indicated the lack in controlled compaction for each side. The loading location related variables simulated four different locations of dynamic forces applied on buried pipeline to observe the most critical region under compaction. Four locations included the pipe's joint, pipe's edge next to the joint, pipe's middle span, and sidefill compaction. All four loading locations were modeled at every 6-in. (15-cm) increment of backfill soil.

6.2 Conclusions

The conclusion of this study proposes in the following forefront:

- The sidefill compaction process does not cause the pipeline's failure. In this process, the vertical compaction force is laterally transferred by the surrounding soil (sidefill zone) to the lateral side of a pipeline. The total impacting force, recorded by the earth pressure cell at pipe's springline, is much less than that recorded by the earth pressure cell at pipe's crown from the backfill compaction process.

- The backfill compaction is a crucial process causing the failure on pipeline. This is because the vertical compaction force is directly transferred to the pipe at crown. Depending on the depth of backfill cover above the pipe, the compaction force can be alleviated. However, in this study, the compaction force is applied to every 6-in. (15-cm) increment of a backfill soil layer. Thus, the failure occurs during the compaction of pipeline under the first backfill depth.

- The effect of applied compaction force is predominant at the location of pipe's joint. This indicates the weakest position on a pipeline when performing the backfill compaction process. At the joint, two pipes are connected with tongue and groove parts and the thickness for each part is only a half of the thickness of a pipe wall. Thus, the stiffness at the pipe's joint is small, compared with the pipe's body.

- The FEM verification from D-Load tests shows an excellent agreement for the concrete brittle model. In forms of load-deformation curve, the compared FEM results with experimental test results demonstrate the compatibility in pipe's strength as well as the crack occurrence. The applied force advancing the first crack in the FEM model is

close to the applied force causing the 0.01-in. (0.25-mm) crack in the experimental test result.

- The insignificance of the 0.01-in. (0.25-mm) crack is affirmed. All pipe specimens can support more load after the occurrence of the 0.01-in. (0.25-mm) crack until failed at the ultimate load. The load at ultimate is approximately 1.8 times the load at the 0.01-in. (0.25-mm) crack.

- The crack sequence of occurrence initiates at crown (internal wall), invert (internal wall), and springline (external wall), respectively. This is showed by the pipe compaction FEM results for all sizes of pipe specimens. Because a pipe is subjected to applied compaction force from the top, pipe's crown is the first location to support the applied force. Then, it transfers to at the support location which is pipe's invert. After pipe deforms, the induced force in pipe's wall is transferred to springline. Moreover, cracking occurs at the tensile surface of pipe's wall and propagates to the compressive surface.

- Different pipe diameter exhibited different failure modes. In the 18-in. (46-cm) and 36-in. (91-cm) diameter pipes, the failure mode is flexural and pipes fail with the opening crack occurred at crown, invert, and springline. For the 54-in. (1.37-m) diameter pipe, the failure mode is shear and pipes fail with the shear crack occurred at crown and invert. Also, at the lateral side of a pipe, the multiple cracks occupy above and below the location of pipe's springline.

- Compaction of backfill height has greater effect on a small pipe size. Due to the compaction force, stress and deformation induced in small pipes are higher than those

induced in larger pipes. Moreover, small pipes are more sensitive to the backfill increment than larger pipes. In this case, the increase in backfill height remarkably decreases stress and deformation in small pipes. In contrast, the significance of backfill increment becomes vanished in larger pipes.

6.3 Recommendations

The appropriate compaction and geometry of surrounding soil are the important factors for a pipeline installation. The backfill compaction process in this study mainly focuses on the heavy compaction machine to simulate the most critical situation. The backfill soil covering above the pipe has major effects on the stress distribution in the pipe.

Before the compaction process is started, the minimum backfill height for the 24-in. (61-cm) diameter pipe shall be 24-in. (61-cm) height for wall-B and 18-in. (46-cm) height for wall-C. The minimum backfill height for the 36-in. (91-cm) diameter pipe shall be 24-in. (61-cm) height for both wall-B and wall-C. The minimum backfill height for the 48-in. (1.22-m) diameter pipe shall be 24-in. (61-cm) height for wall-B and 18-in. (46-cm) height for wall-C. The minimum backfill height for the 54-in. (1.37-m) diameter pipe shall be 12-in. (31-cm) height and 6-in. (15-cm) height for wall-B and wall-C, respectively.

The soil zones at lateral sides of a pipe also have significant effects on the stress and deformation of a buried pipeline. Pipe-soil system has more stiffness when both sides of lateral soil zones are well-compacted, because these zones provide the lateral

support for a pipe. Thus, the care should also be concerned for the material used and compaction level at the sidefill soil zones.

APPENDIX A

EXPERIMENTAL PIPE COMPACTION RESULTS

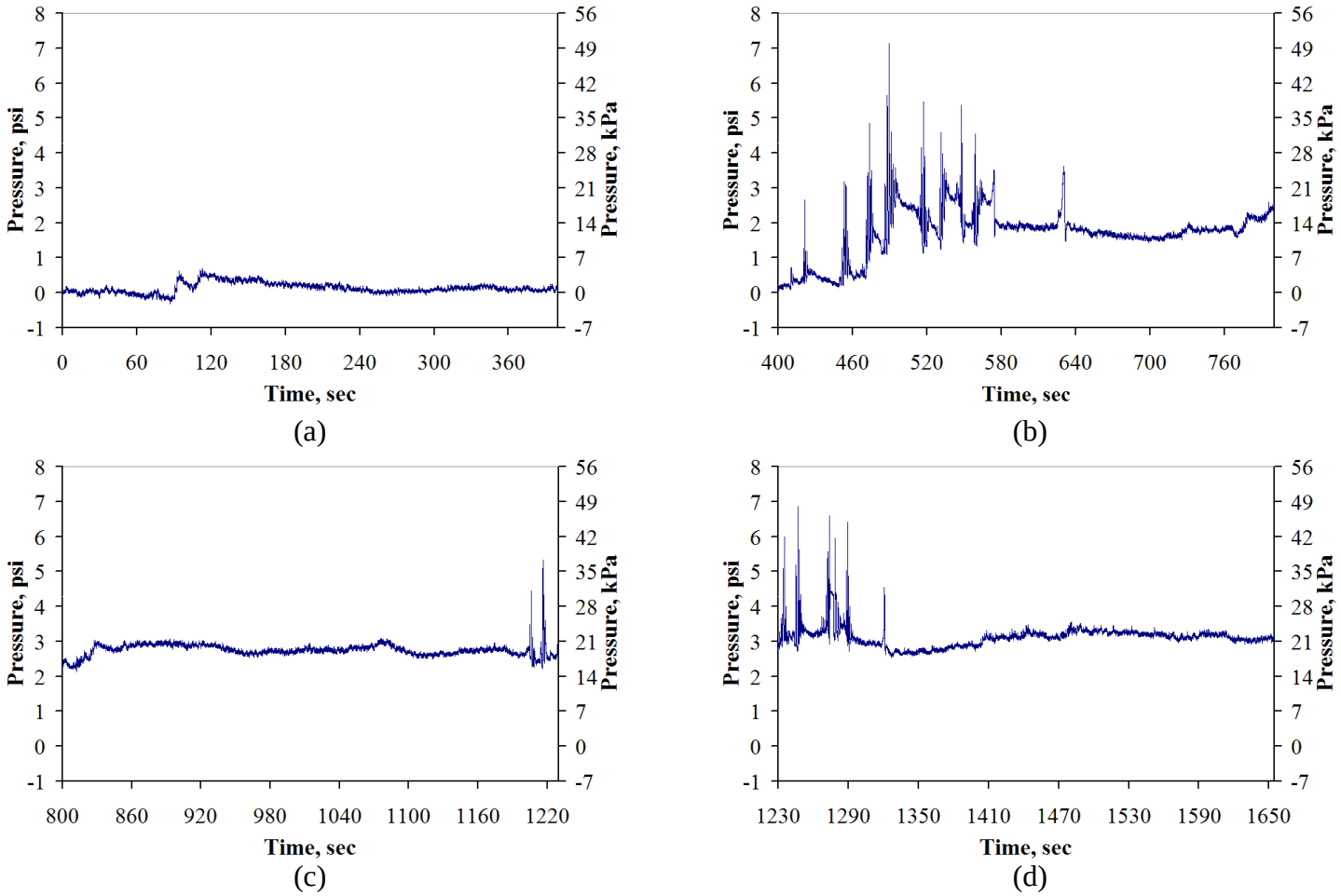

Figure A.1 Pressure results from earth pressure cell at SPL_MS1_SC;
(a) at 0 – 400 sec, (b) at 400 – 800 sec, (c) at 800 – 1230 sec, (d) at 1230 – 1654 sec.

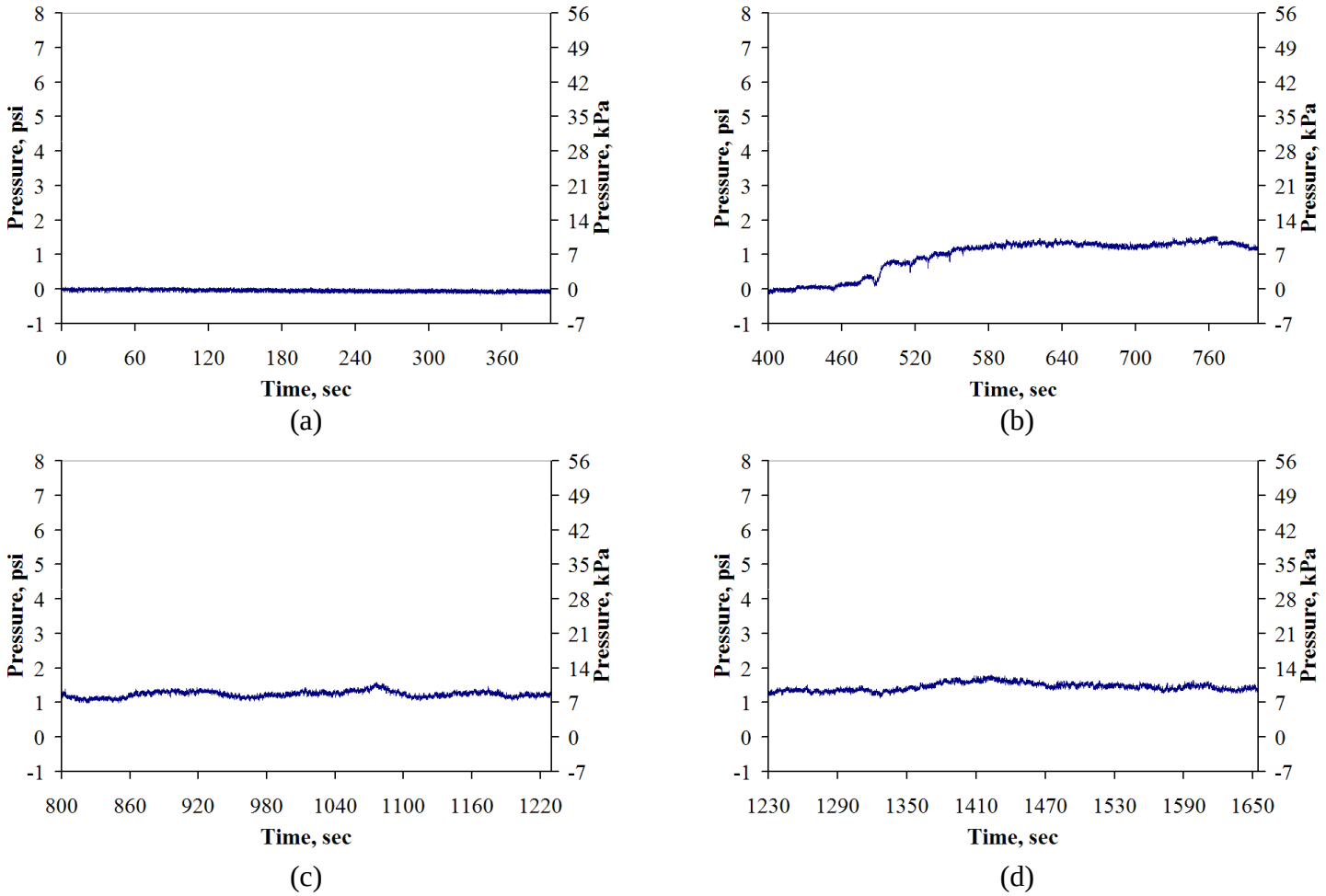

Figure A.2 Pressure results from earth pressure cell at CRN_MS1_SC;
(a) at 0 – 400 sec, (b) at 400 – 800 sec, (c) at 800 – 1230 sec, (d) at 1230 – 1654 sec.

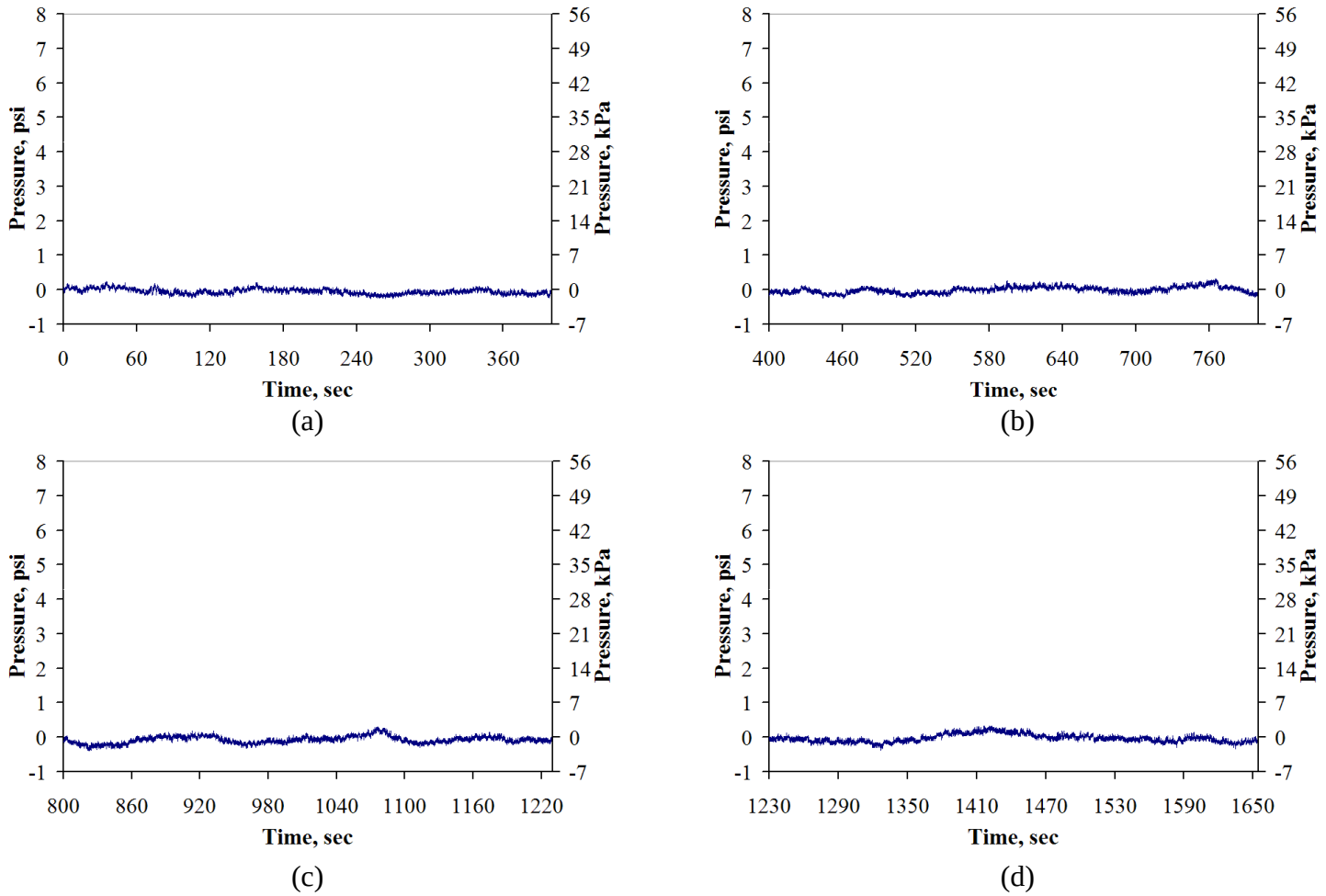

Figure A.3 Pressure results from earth pressure cell at CRN_JT1_SC;
(a) at 0 – 400 sec, (b) at 400 – 800 sec, (c) at 800 – 1230 sec, (d) at 1230 – 1654 sec.

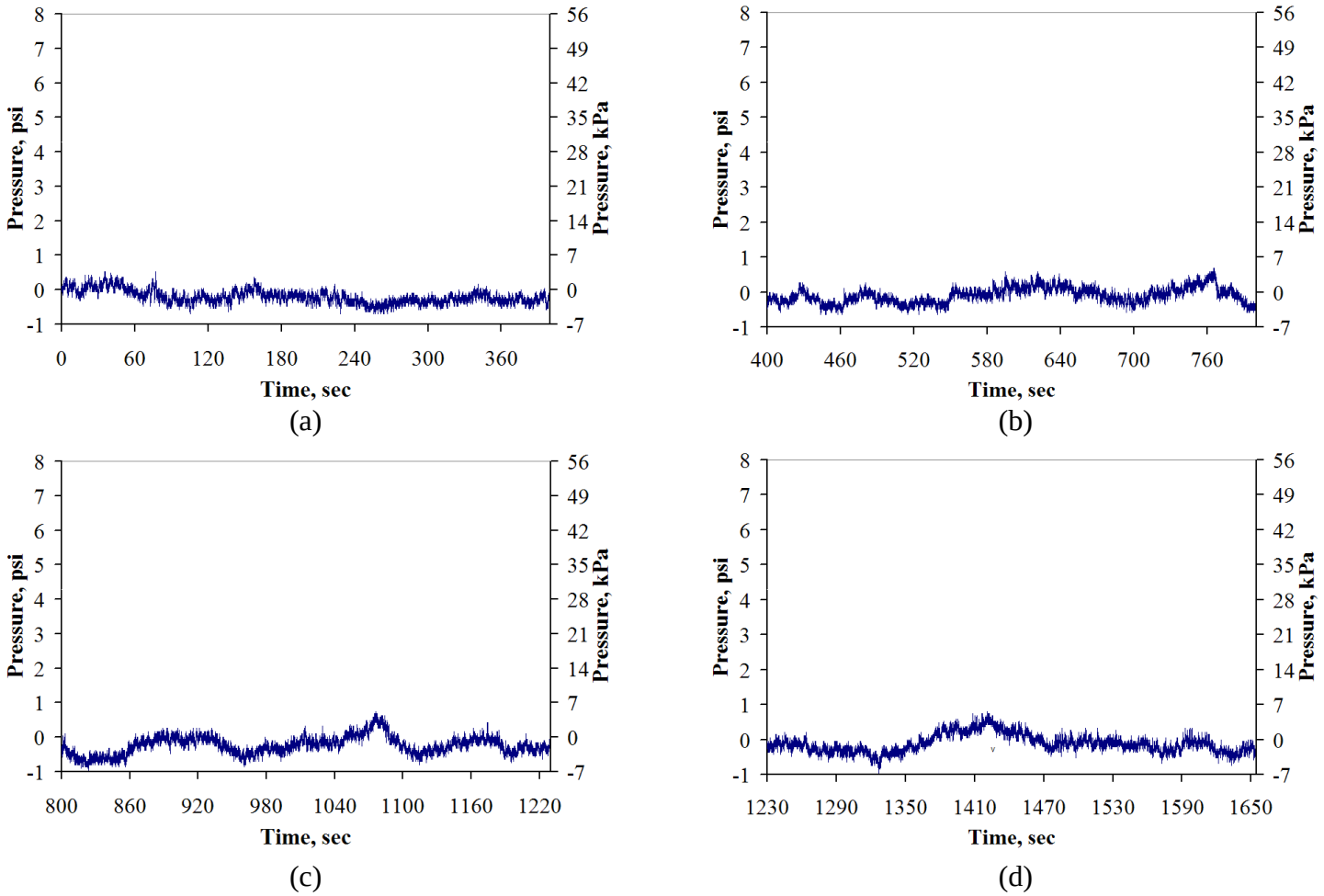

Figure A.4 Pressure results from earth pressure cell at CRN_JT2_SC;
(a) at 0 – 400 sec, (b) at 400 – 800 sec, (c) at 800 – 1230 sec, (d) at 1230 – 1654 sec.

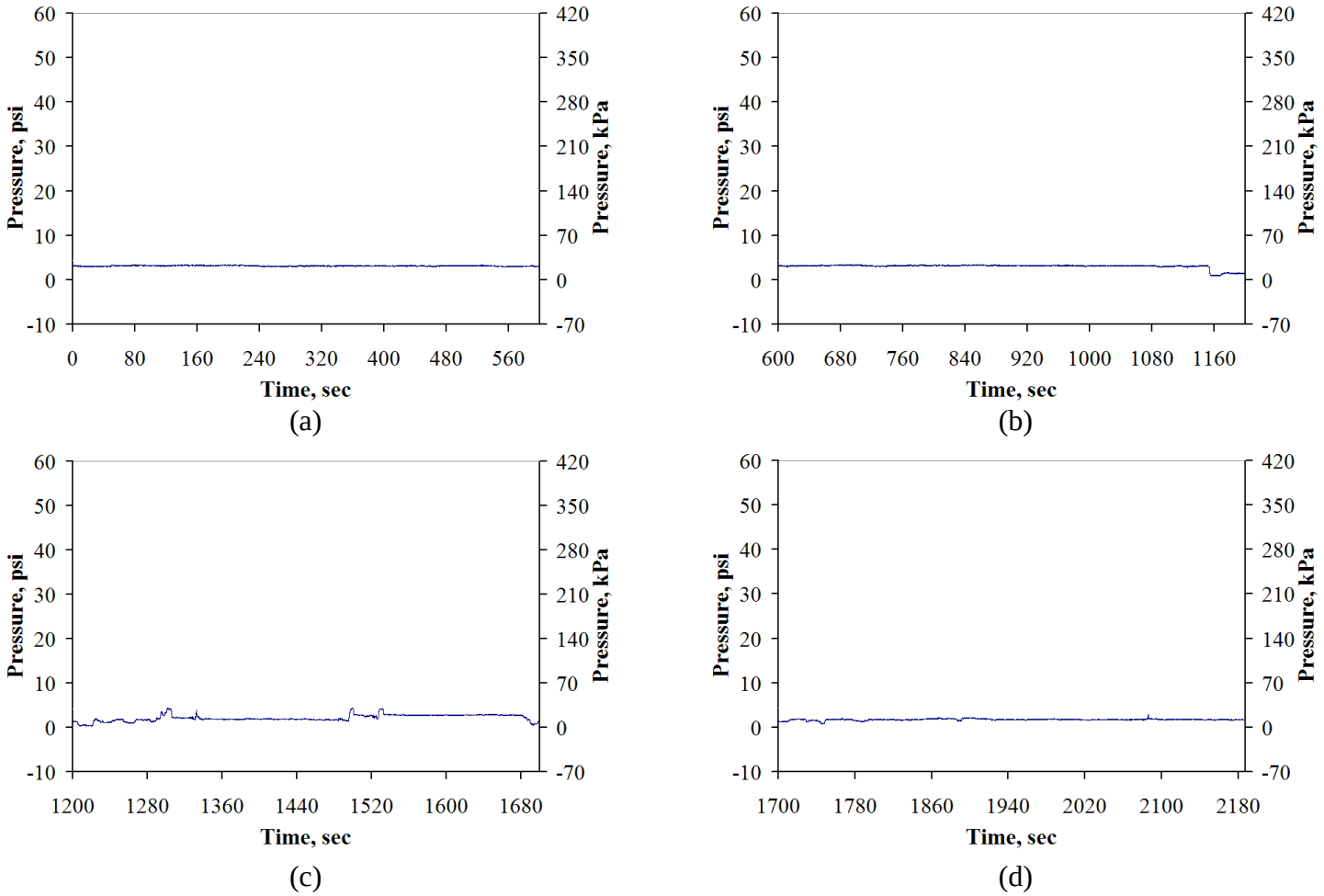

Figure A.5 Pressure results from earth pressure cell at SPL_MS1_BC;
(a) at 0 – 600 sec, (b) at 600 – 1200 sec, (c) at 1200 – 1700 sec, (d) at 1700 – 2187 sec.

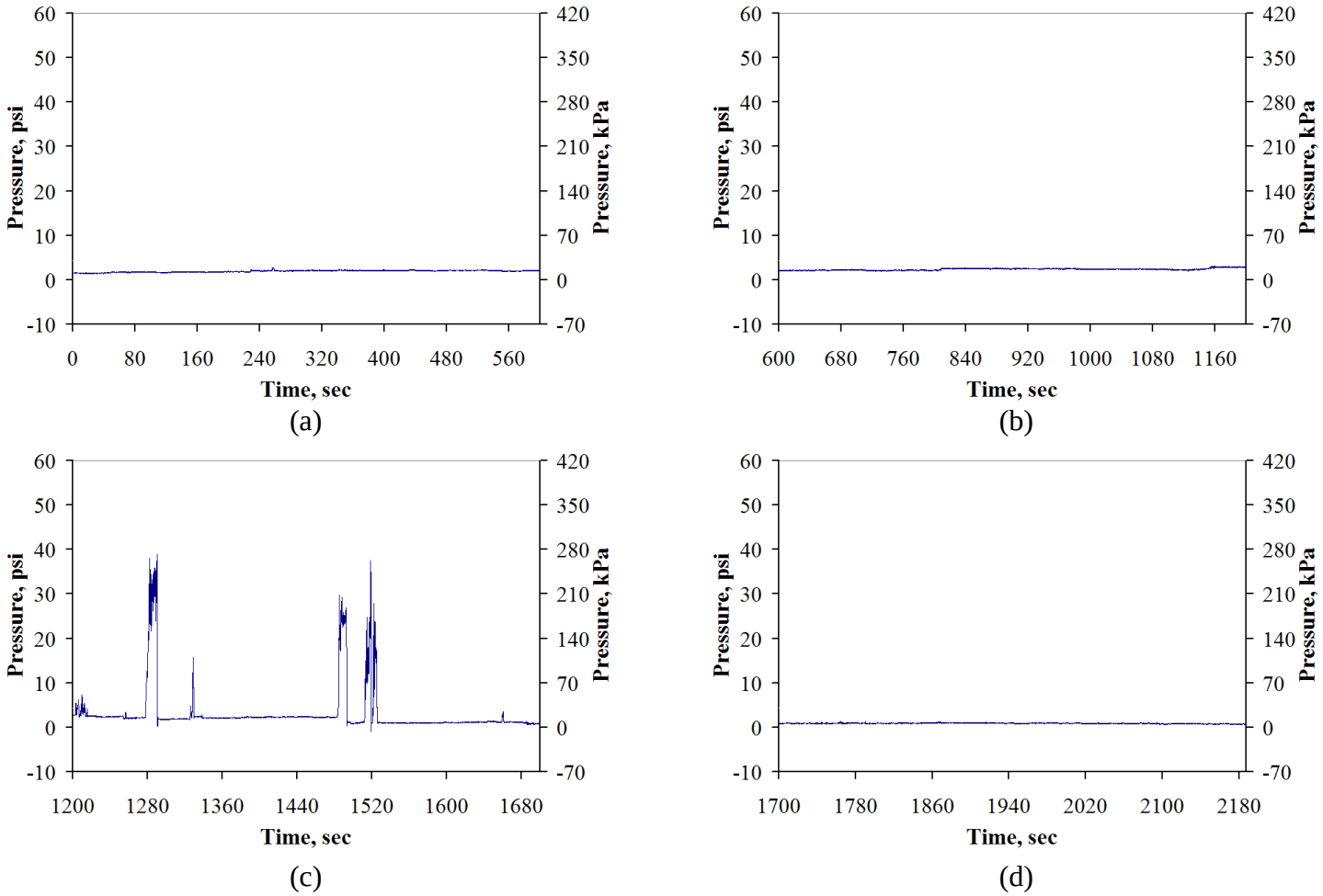

Figure A.6 Pressure results from earth pressure cell at CRN_MS1_BC;
(a) at 0 – 600 sec, (b) at 600 – 1200 sec, (c) at 1200 – 1700 sec, (d) at 1700 – 2187 sec.

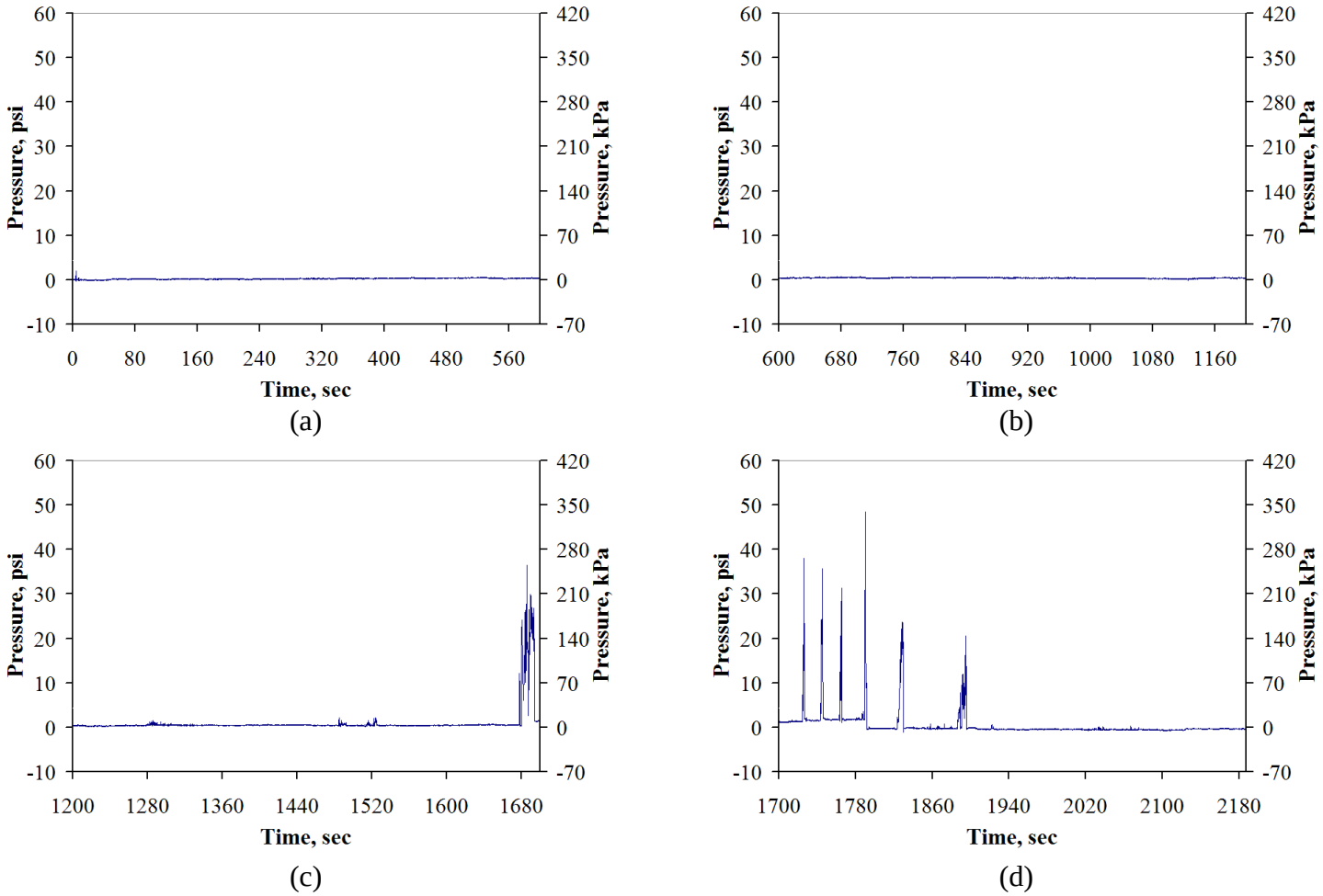

Figure A.7 Pressure results from earth pressure cell at CRN_JT1_BC;
(a) at 0 – 600 sec, (b) at 600 – 1200 sec, (c) at 1200 – 1700 sec, (d) at 1700 – 2187 sec.

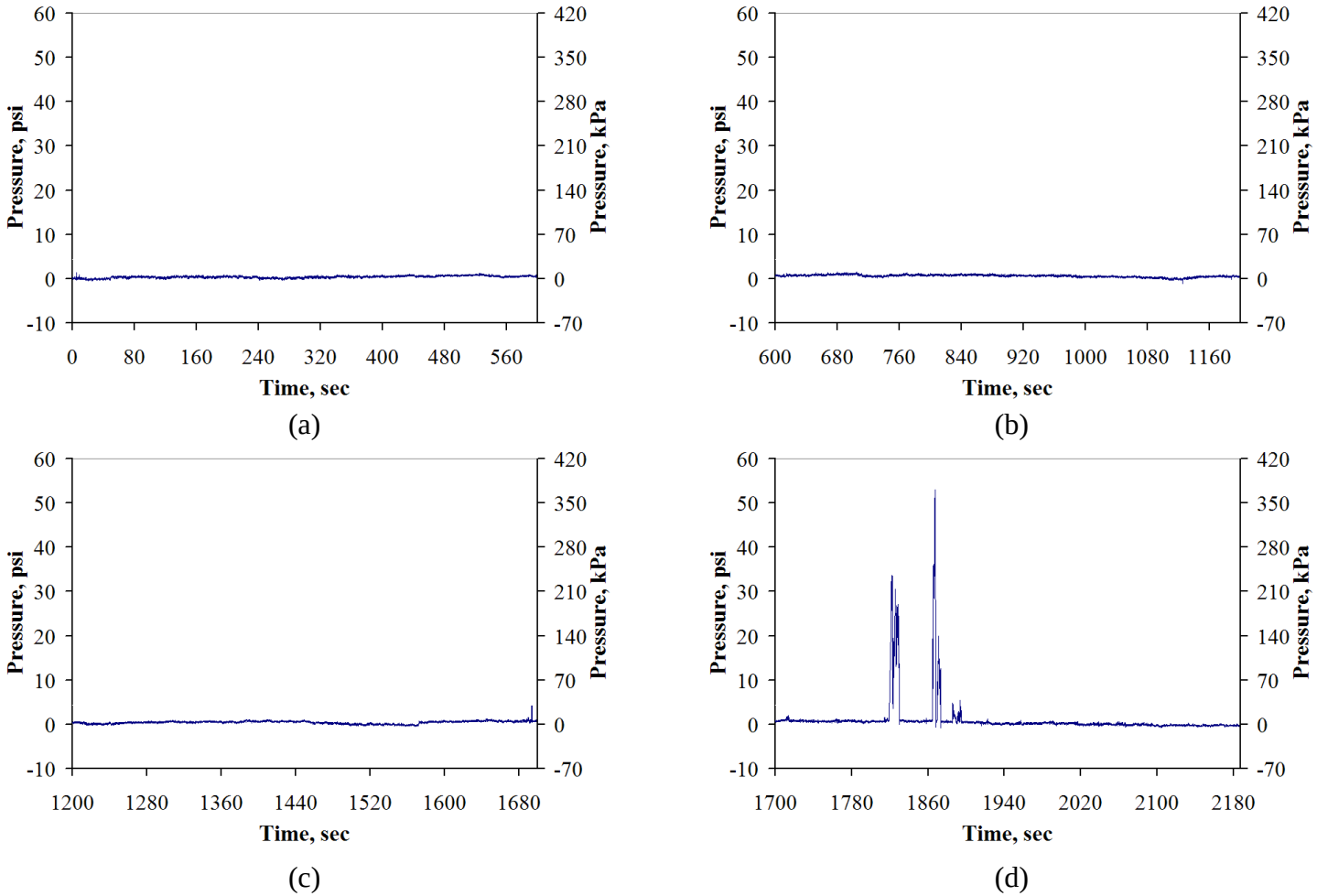

Figure A.8 Pressure results from earth pressure cell at CRN_JT2_BC;
(a) at 0 – 600 sec, (b) at 600 – 1200 sec, (c) at 1200 – 1700 sec, (d) at 1700 – 2187 sec.

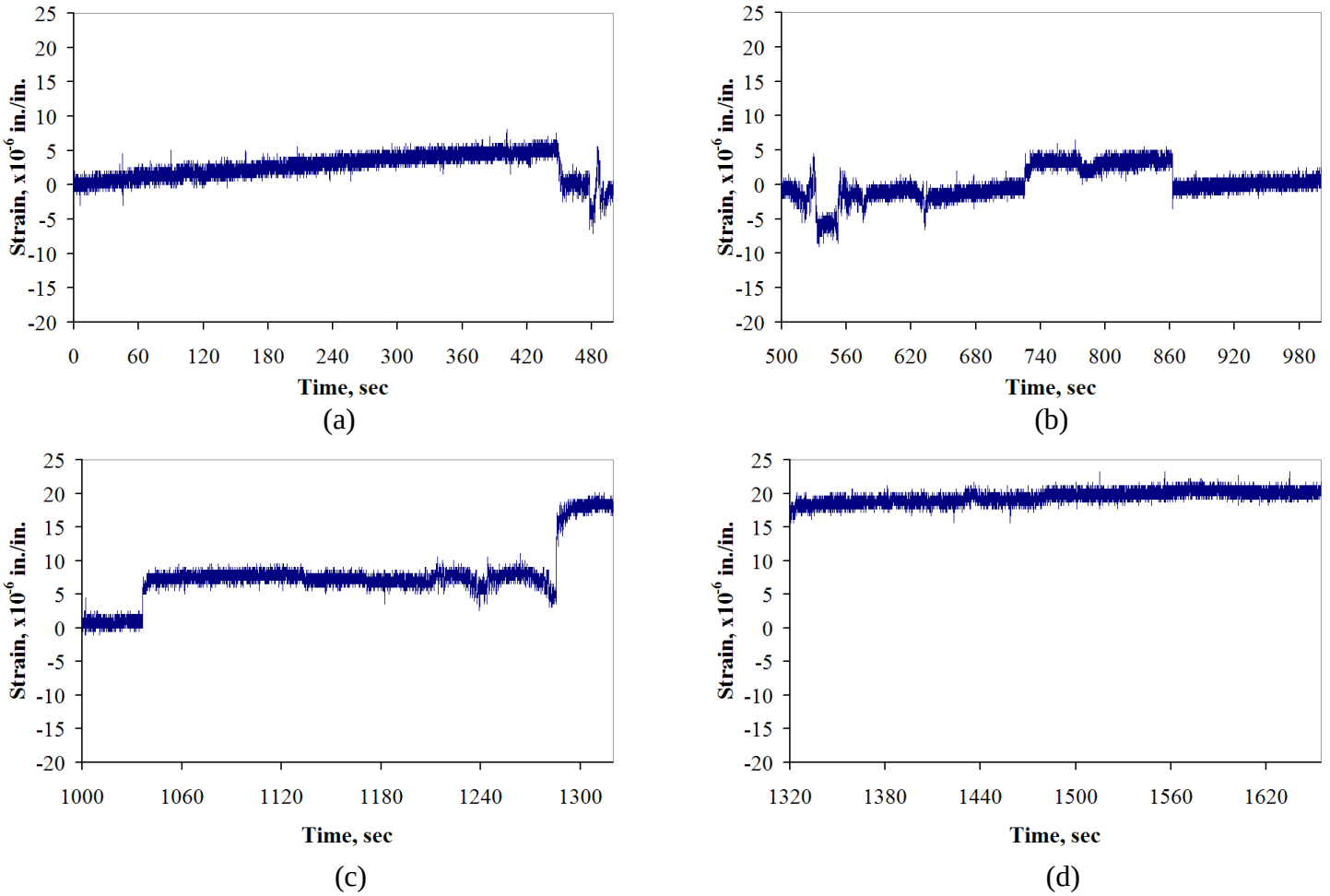

Figure A.9 Strain results at CRN_MS1_SC;
(a) at 0 – 500 sec, (b) at 500 – 1000 sec, (c) at 1000 – 1320 sec, (d) at 1320 – 1654 sec.

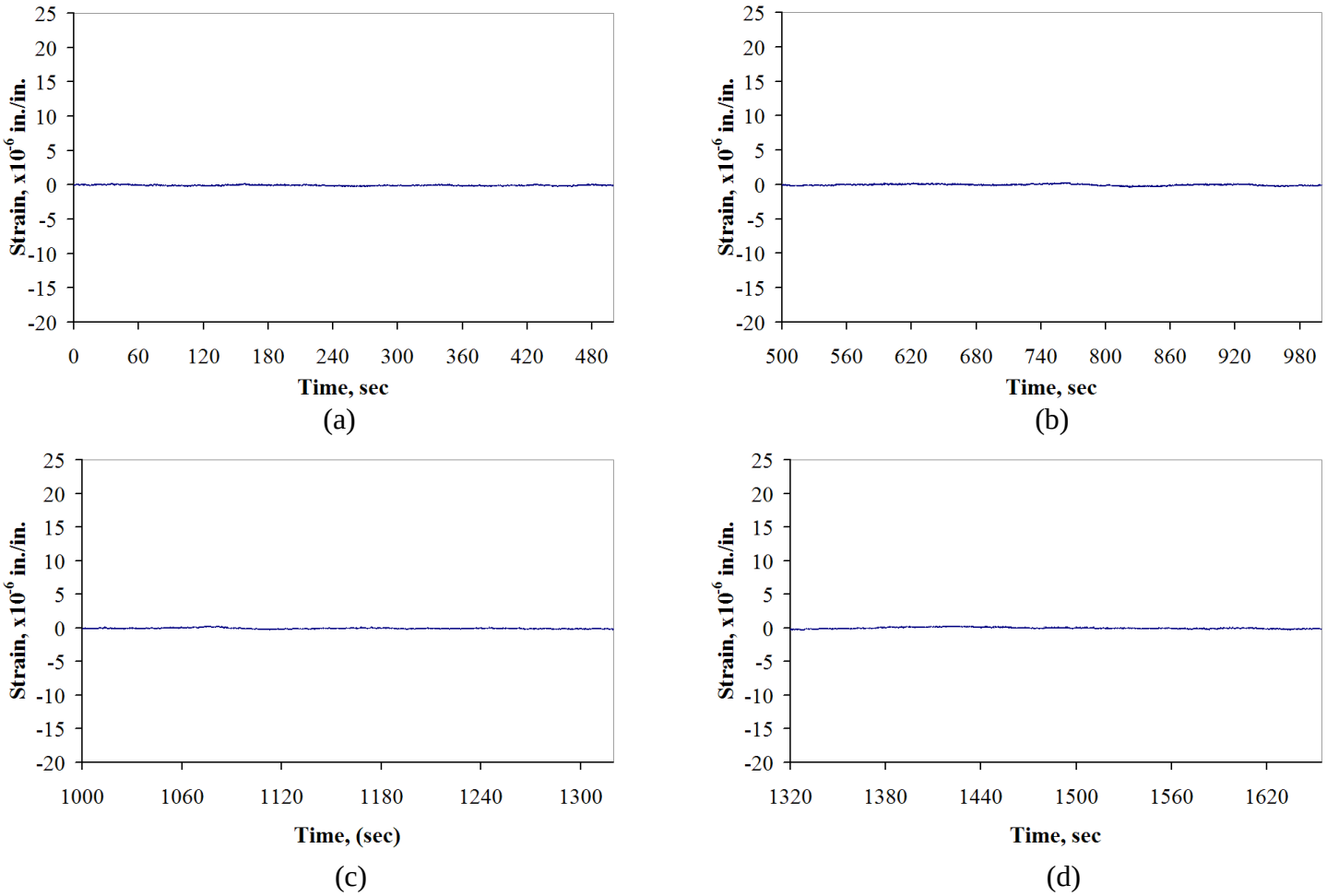

Figure A.10 Strain results at SPL_MS1_SC;
(a) at 0 – 500 sec, (b) at 500 – 1000 sec, (c) at 1000 – 1320 sec, (d) at 1320 – 1654 sec.

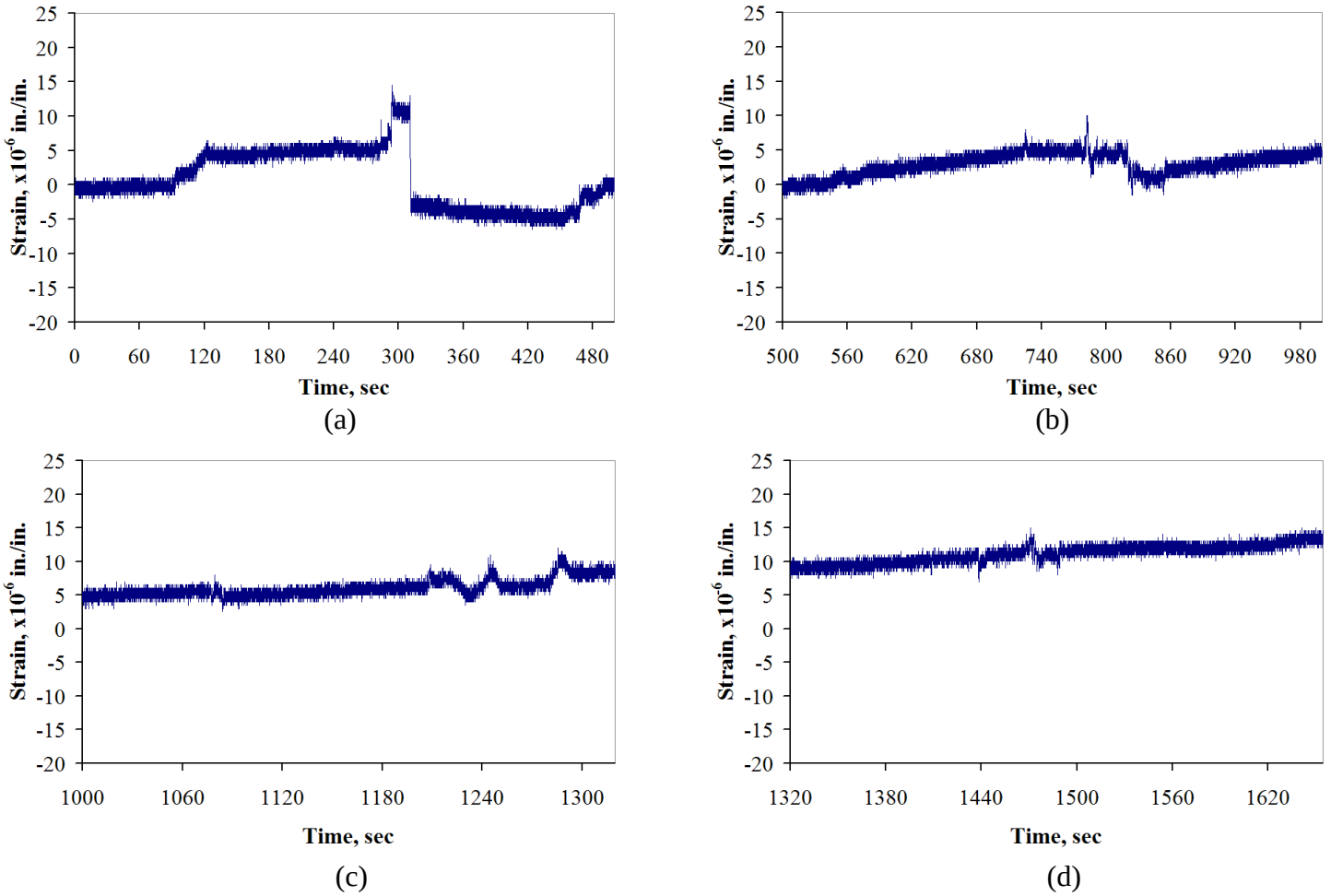

Figure A.11 Strain results at SPL_JT1_SC;
(a) at 0 – 500 sec, (b) at 500 – 1000 sec, (c) at 1000 – 1320 sec, (d) at 1320 – 1654 sec.

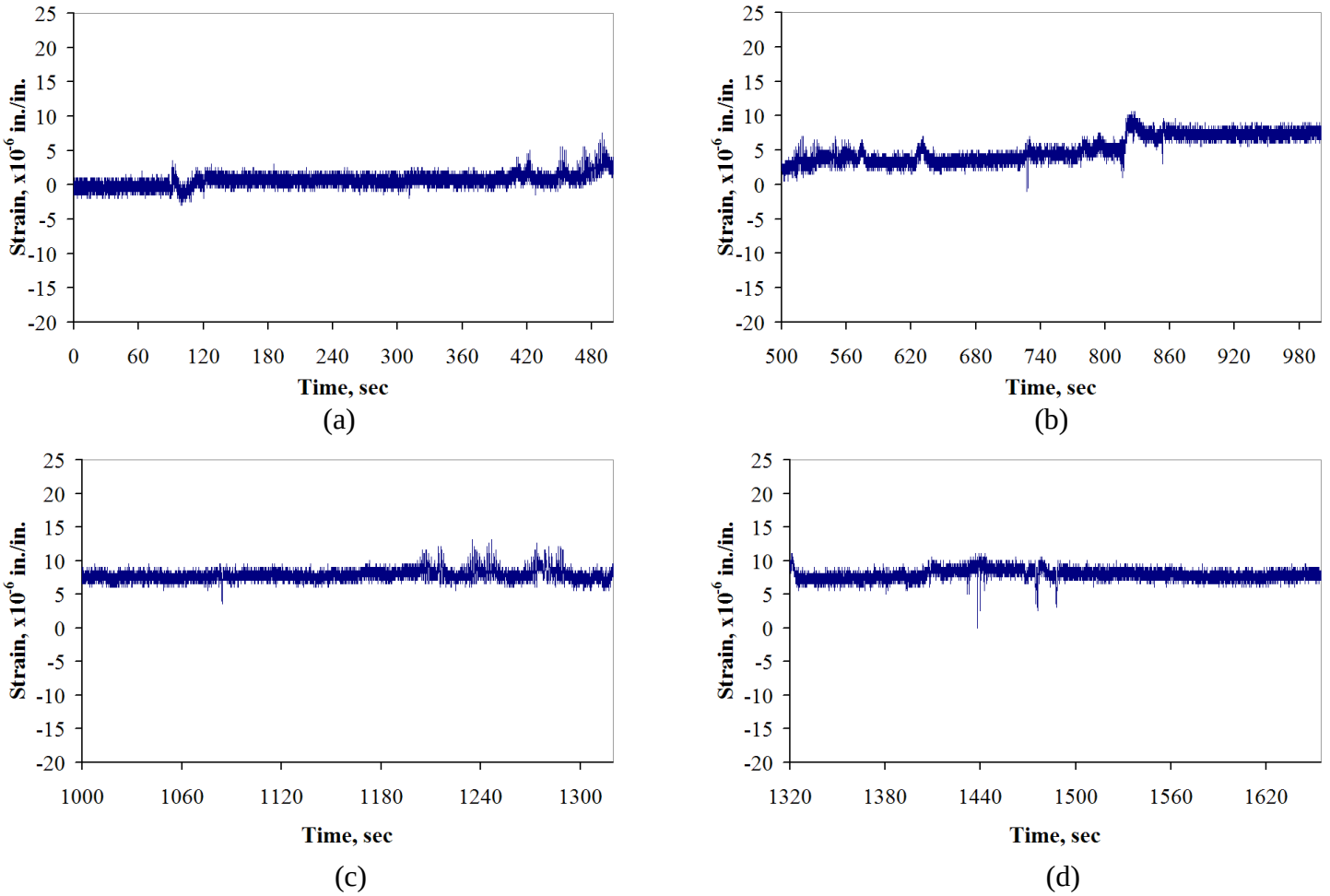

Figure A.12 Strain results at INV_JT1_SC;
(a) at 0 – 500 sec, (b) at 500 – 1000 sec, (c) at 1000 – 1320 sec, (d) at 1320 – 1654 sec.

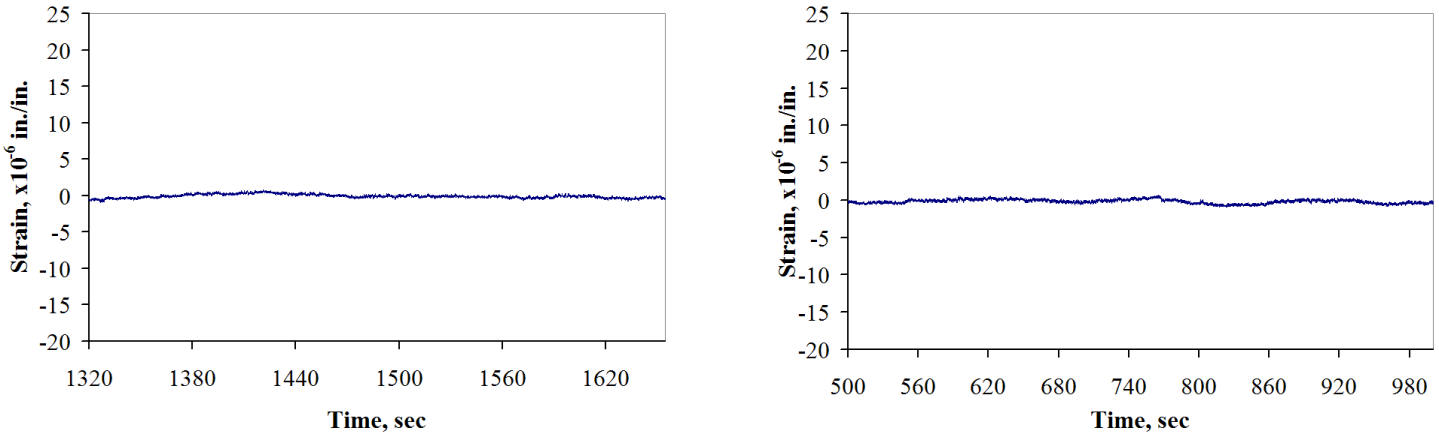

(a)

(b)

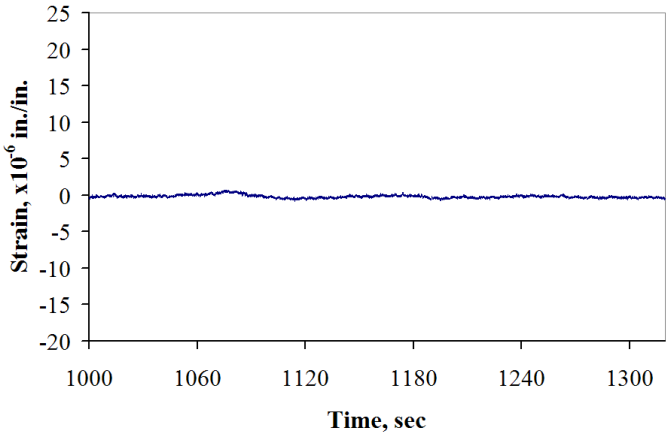

(c)

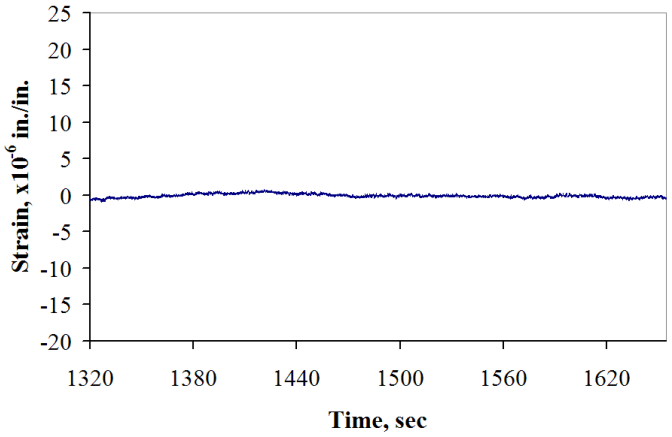

(d)

Figure A.13 Strain results at SPL_JT2_SC;
(a) at 0 – 500 sec, (b) at 500 – 1000 sec, (c) at 1000 – 1320 sec, (d) at 1320 – 1654 sec.

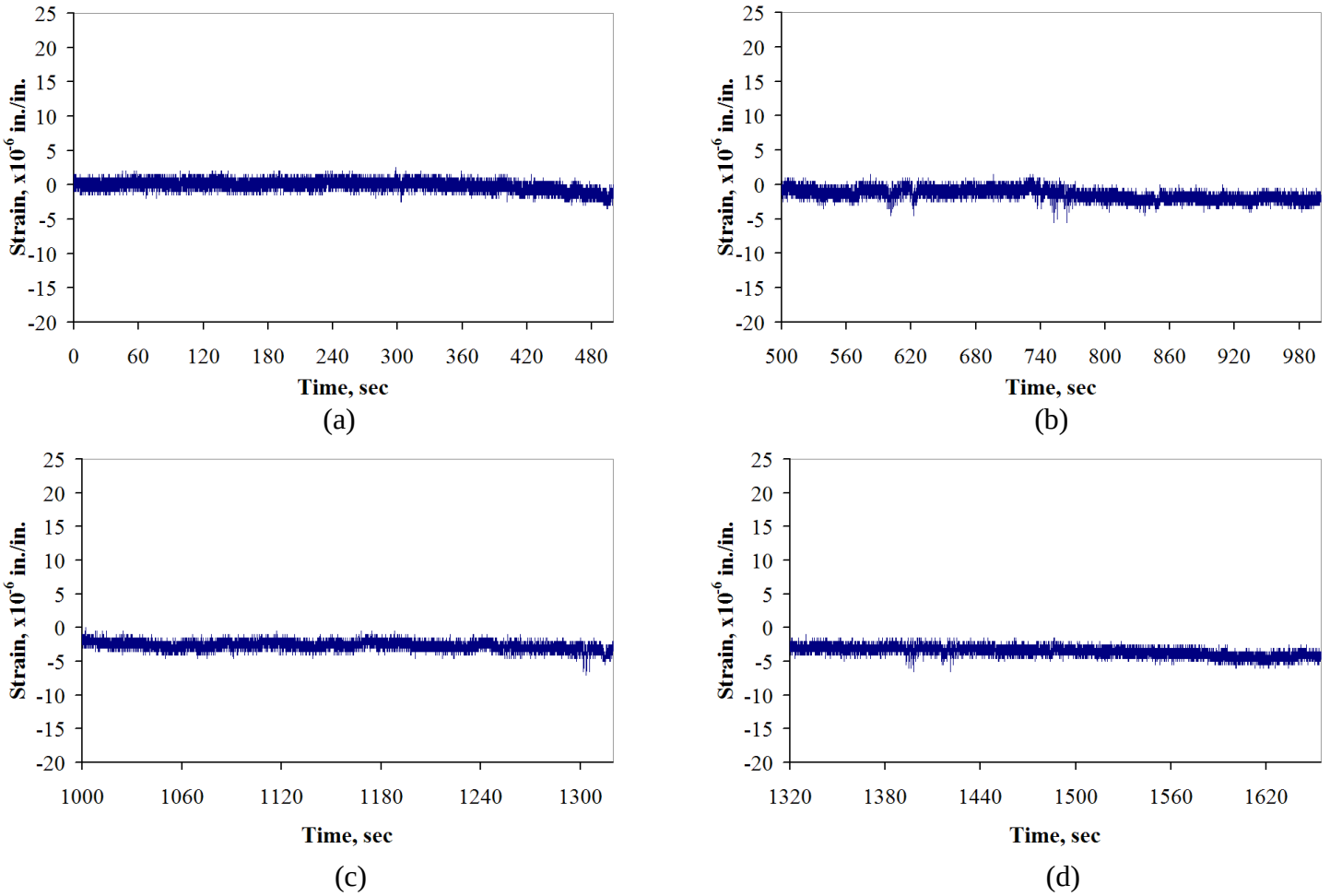

Figure A.14 Strain results at INV_JT2_SC;
(a) at 0 – 500 sec, (b) at 500 – 1000 sec, (c) at 1000 – 1320 sec, (d) at 1320 – 1654 sec.

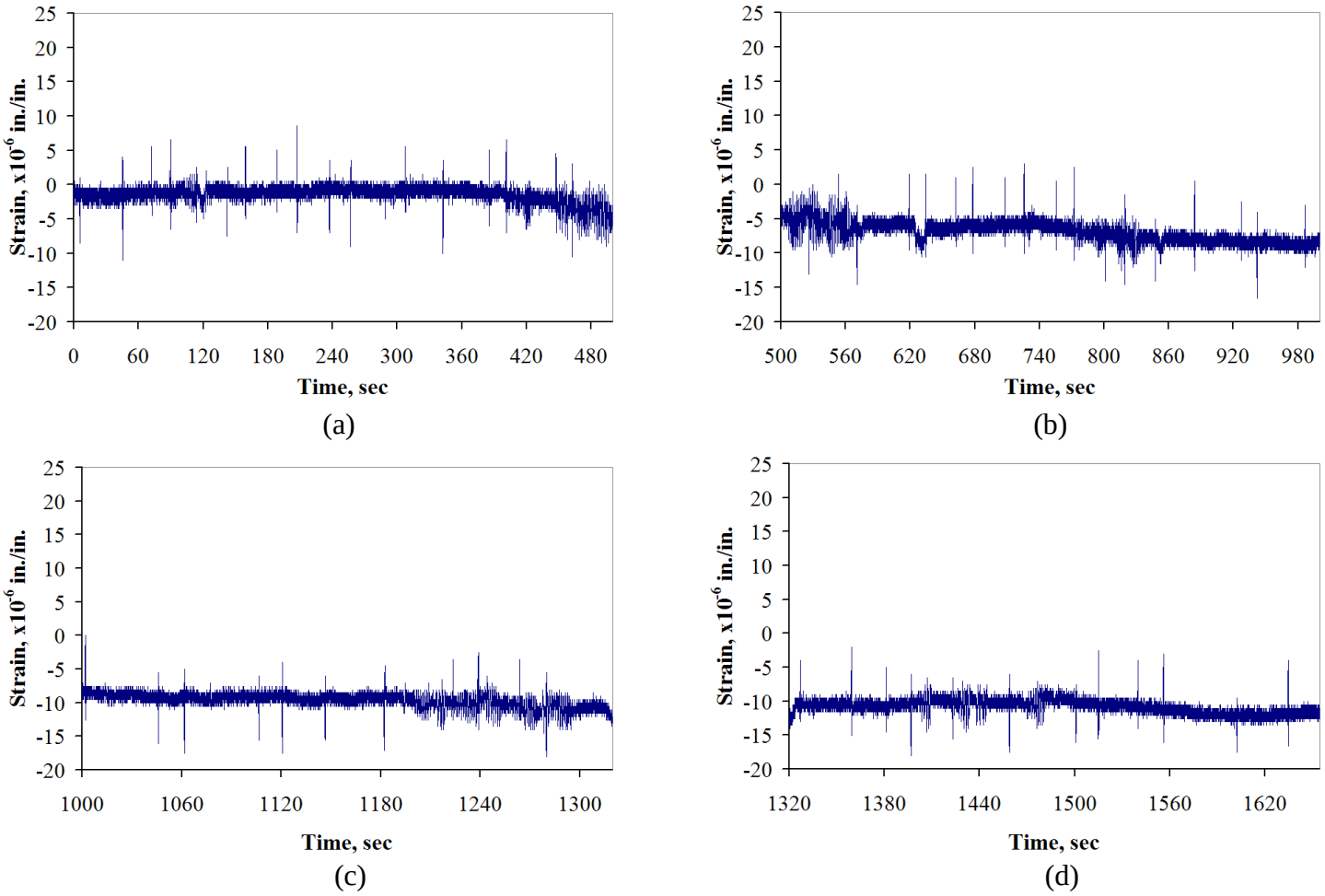

Figure A.15 Strain results at CRN_MS2_SC;
(a) at 0 – 500 sec, (b) at 500 – 1000 sec, (c) at 1000 – 1320 sec, (d) at 1320 – 1654 sec.

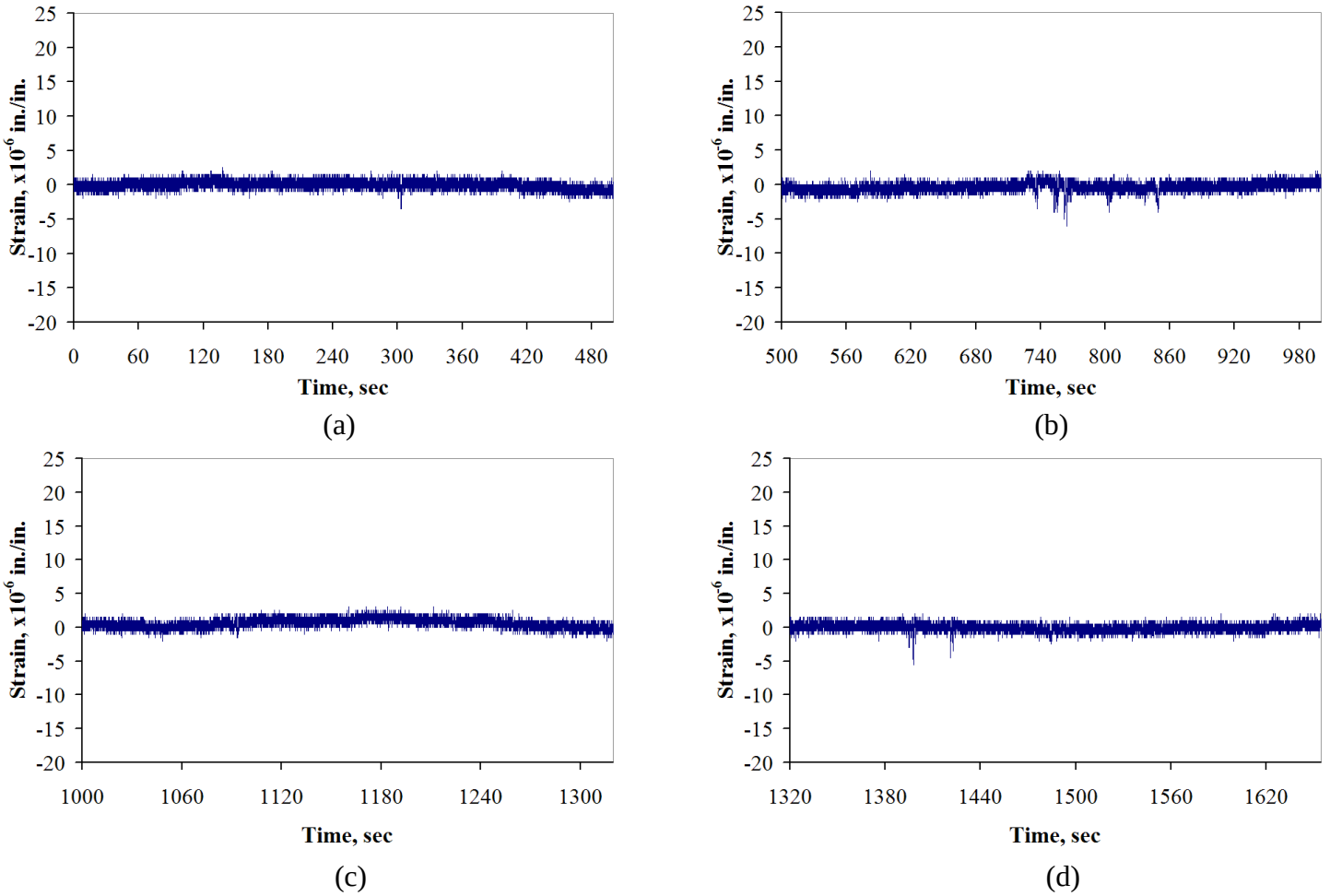

Figure A.16 Strain results at SPL_MS2_SC;
(a) at 0 – 500 sec, (b) at 500 – 1000 sec, (c) at 1000 – 1320 sec, (d) at 1320 – 1654 sec.

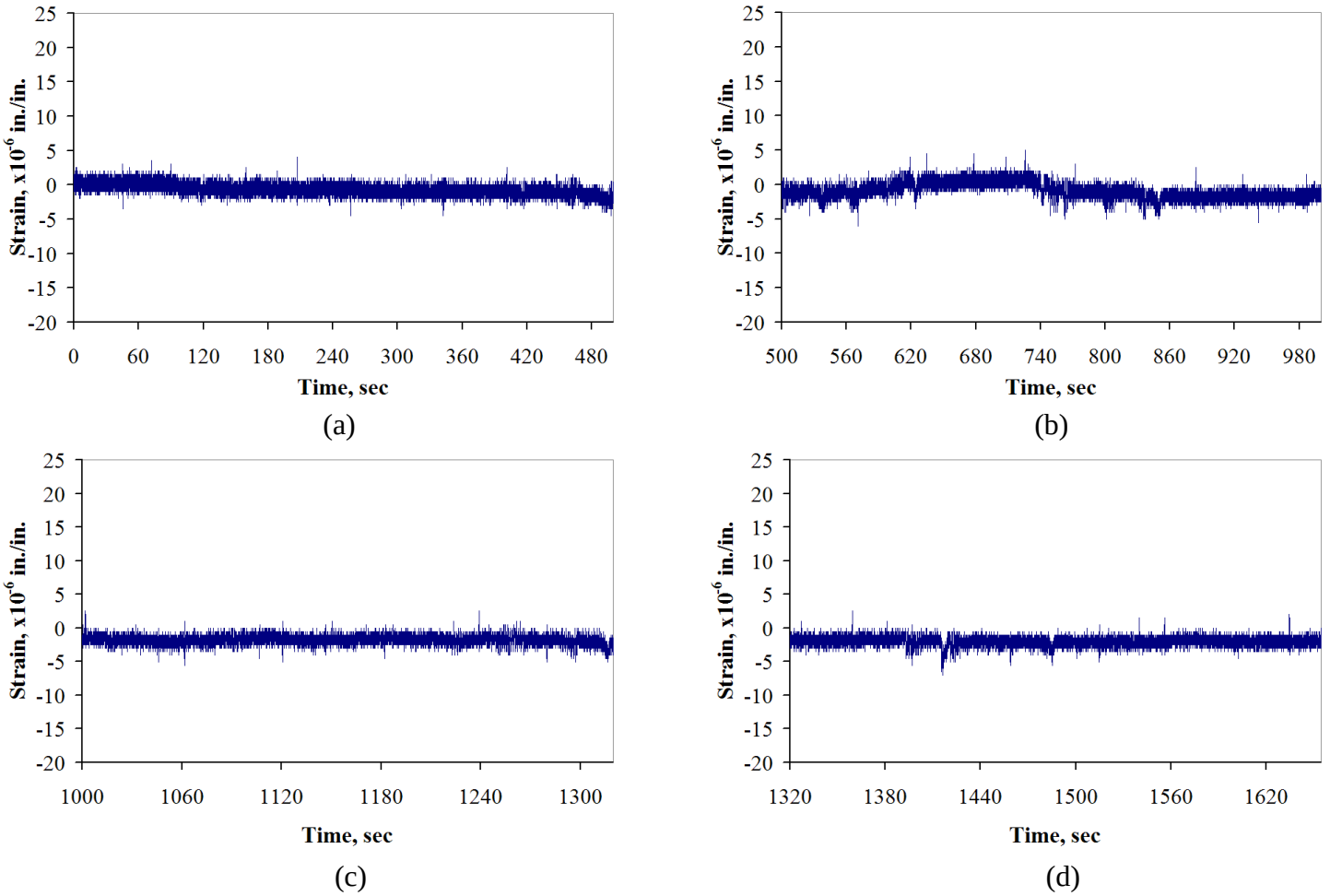

Figure A.17 Strain results at INV_MS2_SC;
(a) at 0 – 500 sec, (b) at 500 – 1000 sec, (c) at 1000 – 1320 sec, (d) at 1320 – 1654 sec.

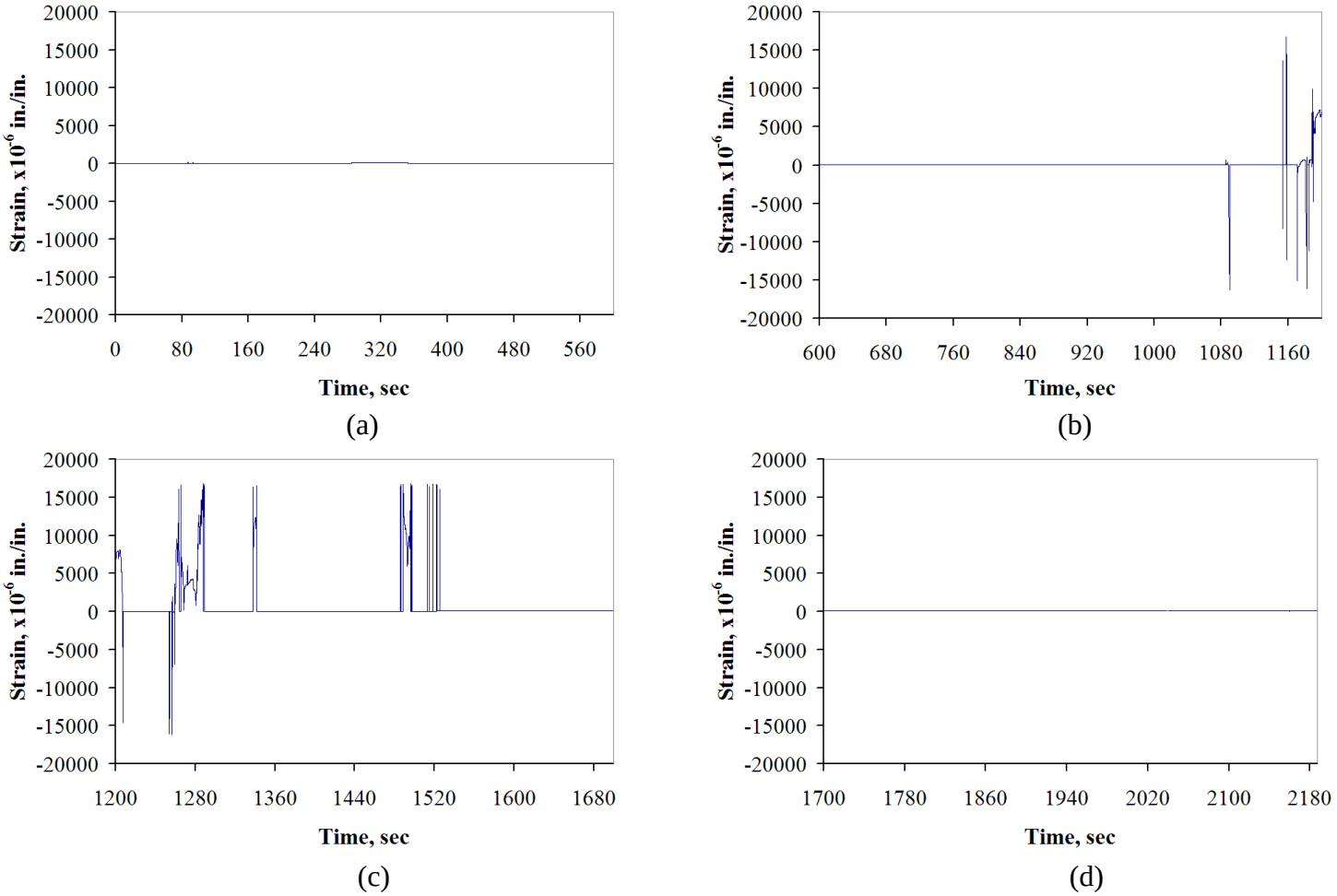

Figure A.18 Strain results at CRN_MS1_BC;
(a) at 0 – 600 sec, (b) at 600 – 1200 sec, (c) at 1200 – 1700 sec, (d) at 1700 – 2187 sec.

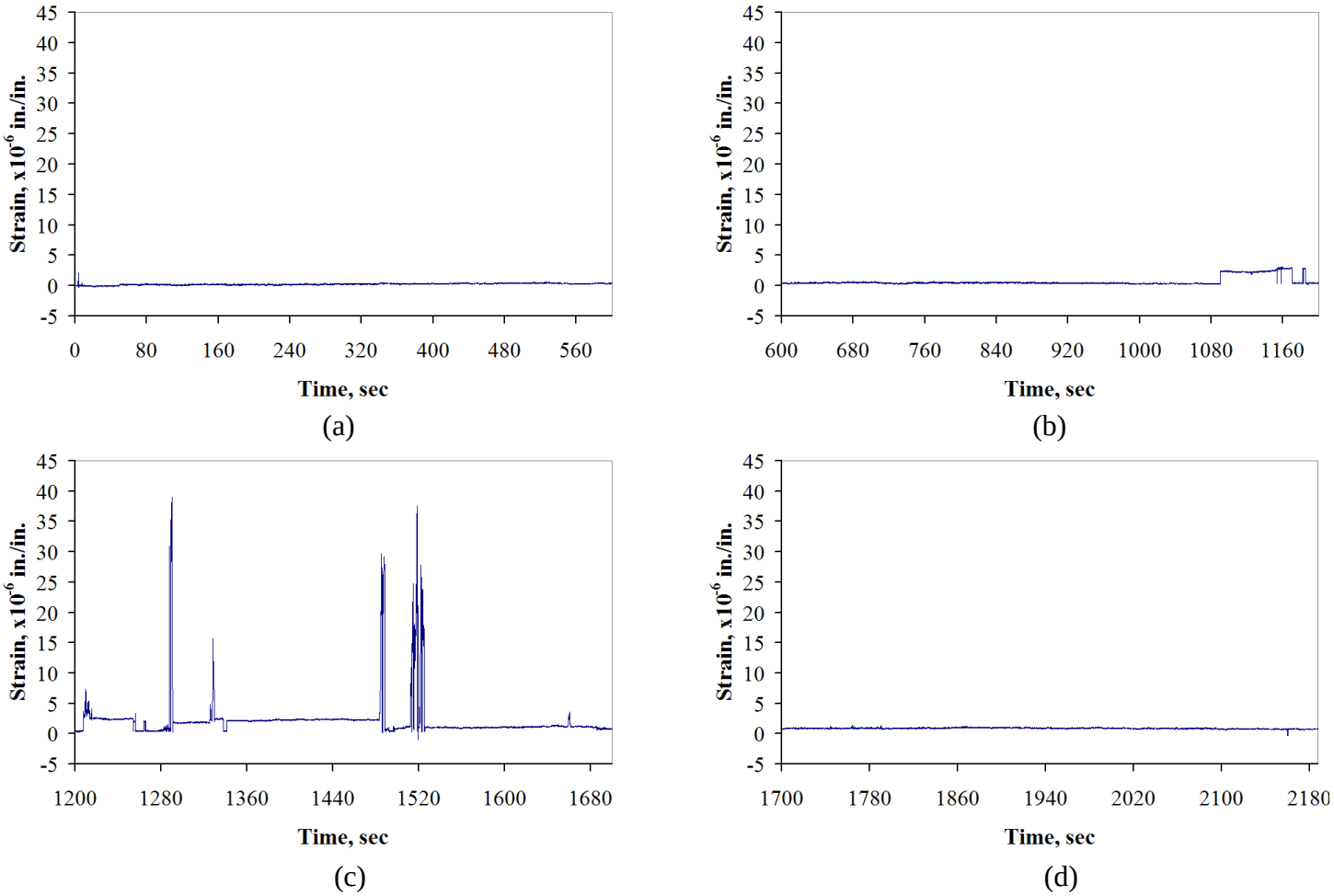

Figure A.19 Strain results at SPL_MS1_BC;
(a) at 0 – 600 sec, (b) at 600 – 1200 sec, (c) at 1200 – 1700 sec, (d) at 1700 – 2187 sec.

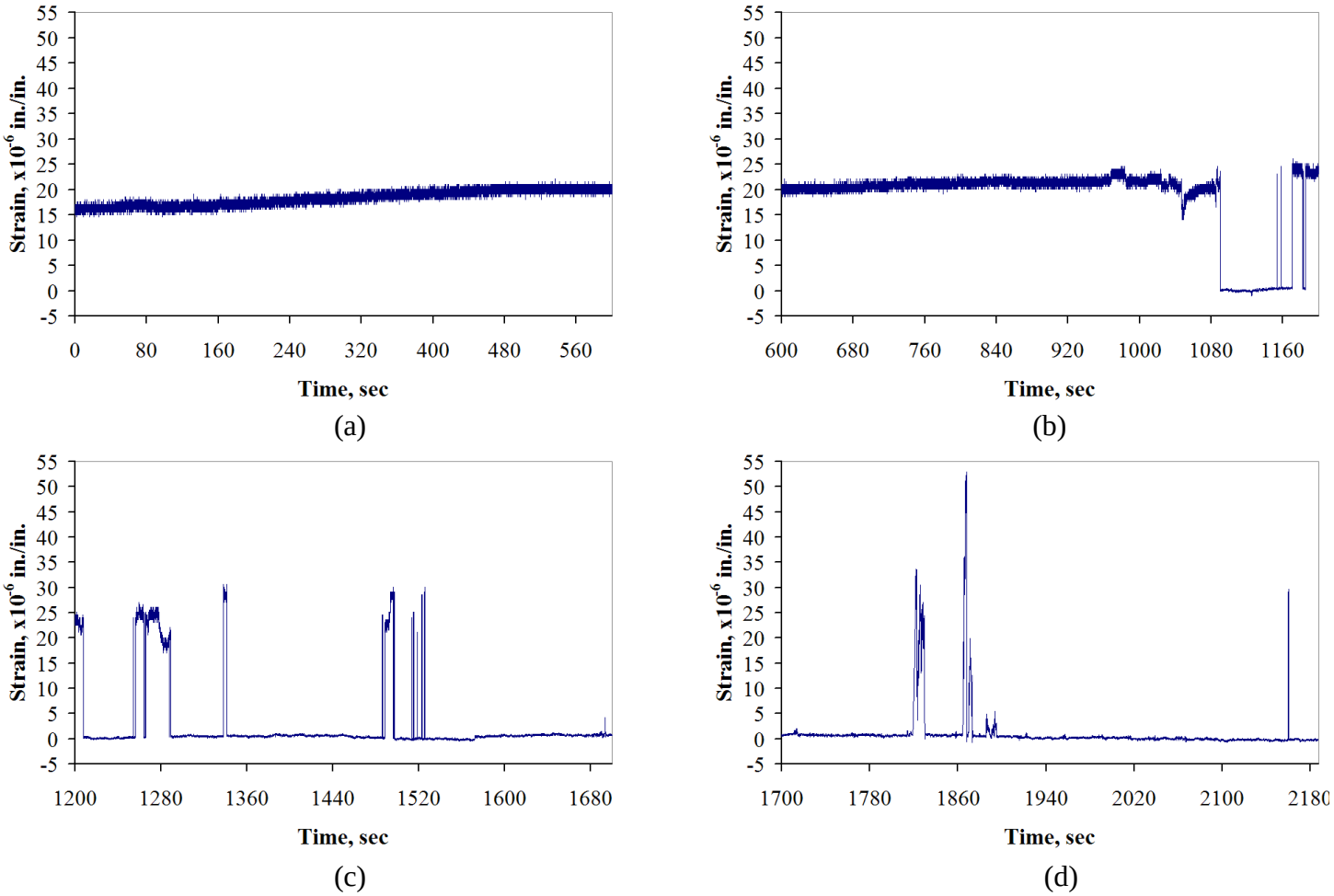

Figure A.20 Strain results at SPL_JT1_BC;
(a) at 0 – 600 sec, (b) at 600 – 1200 sec, (c) at 1200 – 1700 sec, (d) at 1700 – 2187 sec.

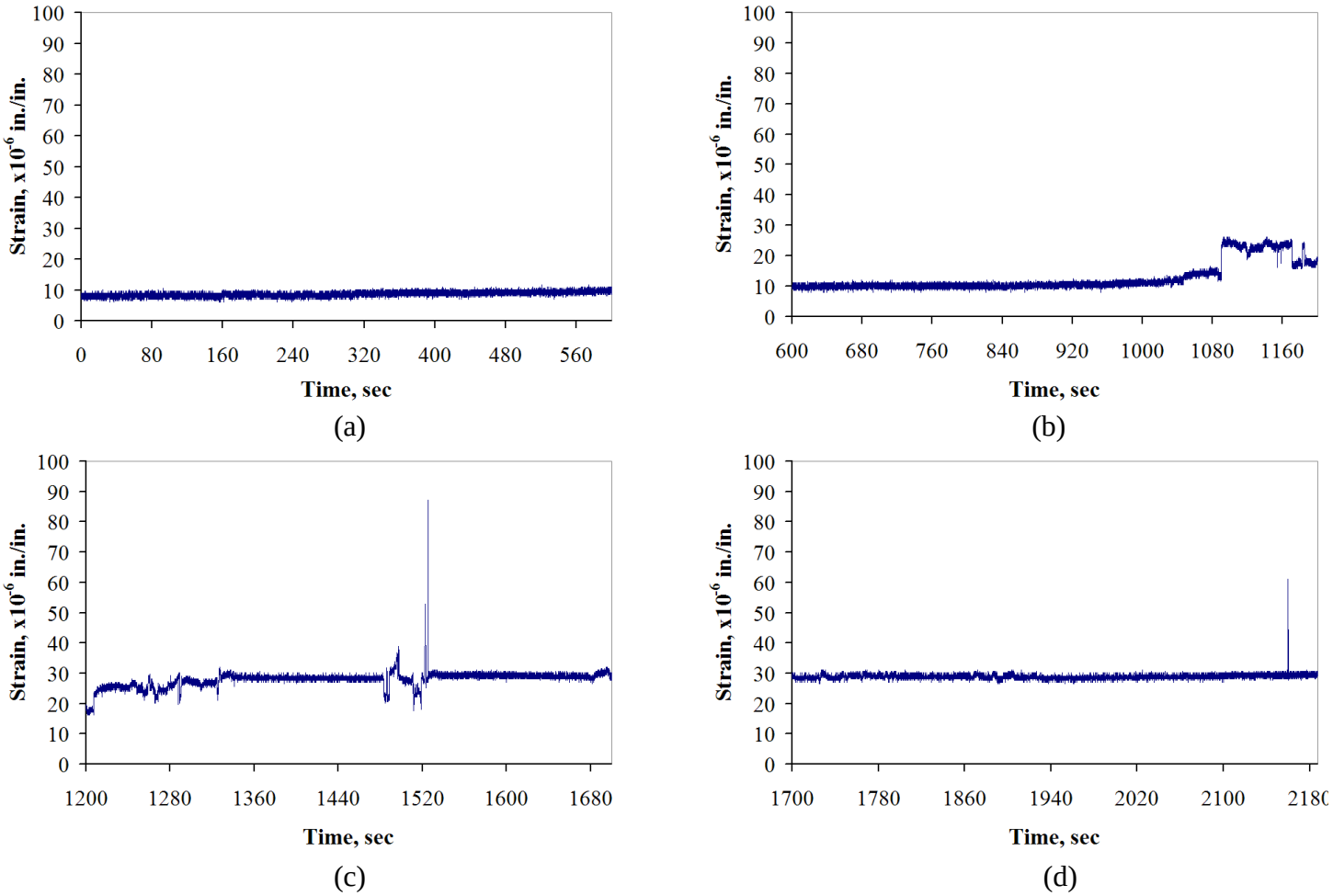

Figure A.21 Strain results at INV_JT1_BC;
(a) at 0 – 600 sec, (b) at 600 – 1200 sec, (c) at 1200 – 1700 sec, (d) at 1700 – 2187 sec.

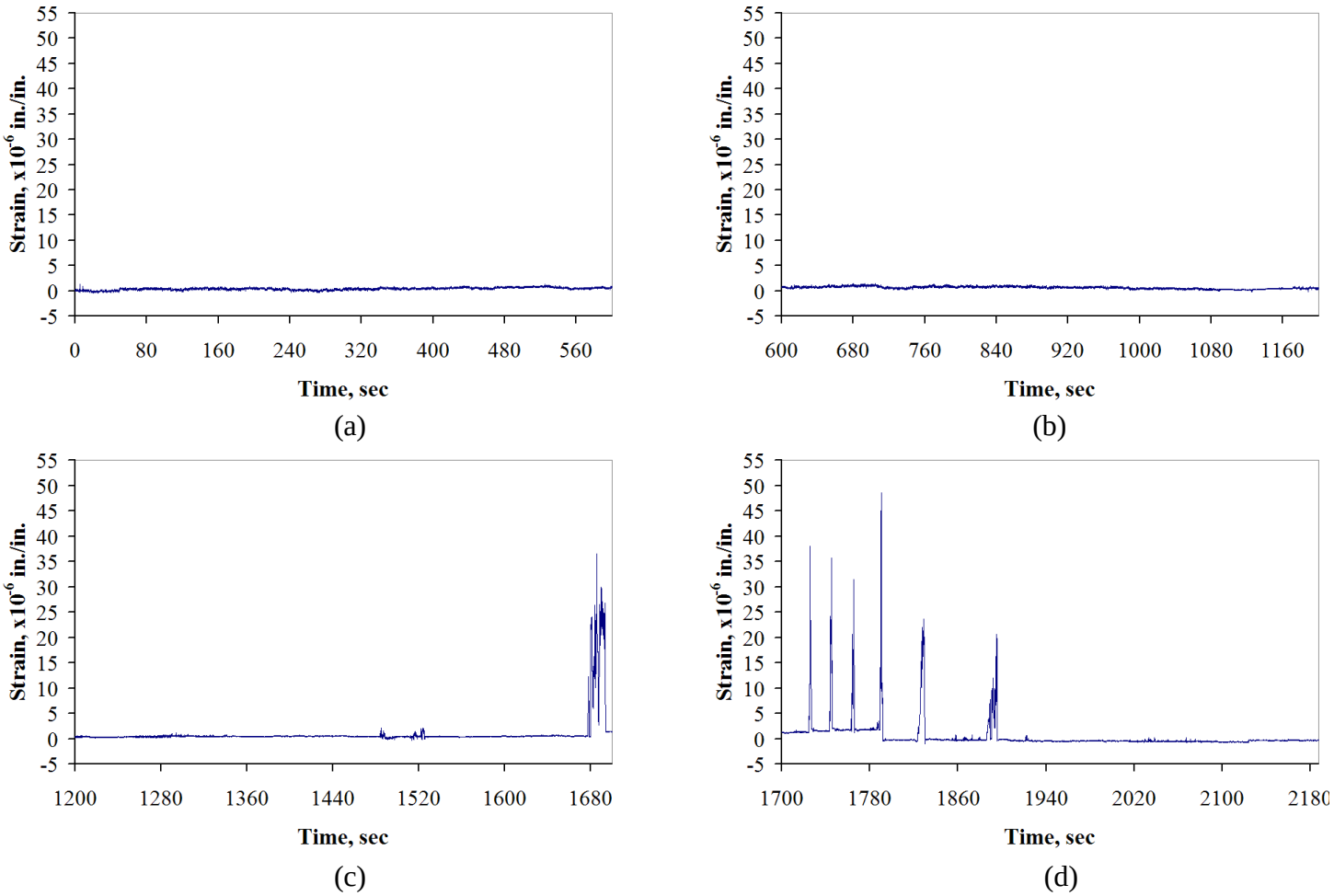

Figure A.22 Strain results at SPL_JT2_BC;
(a) at 0 – 600 sec, (b) at 600 – 1200 sec, (c) at 1200 – 1700 sec, (d) at 1700 – 2187 sec.

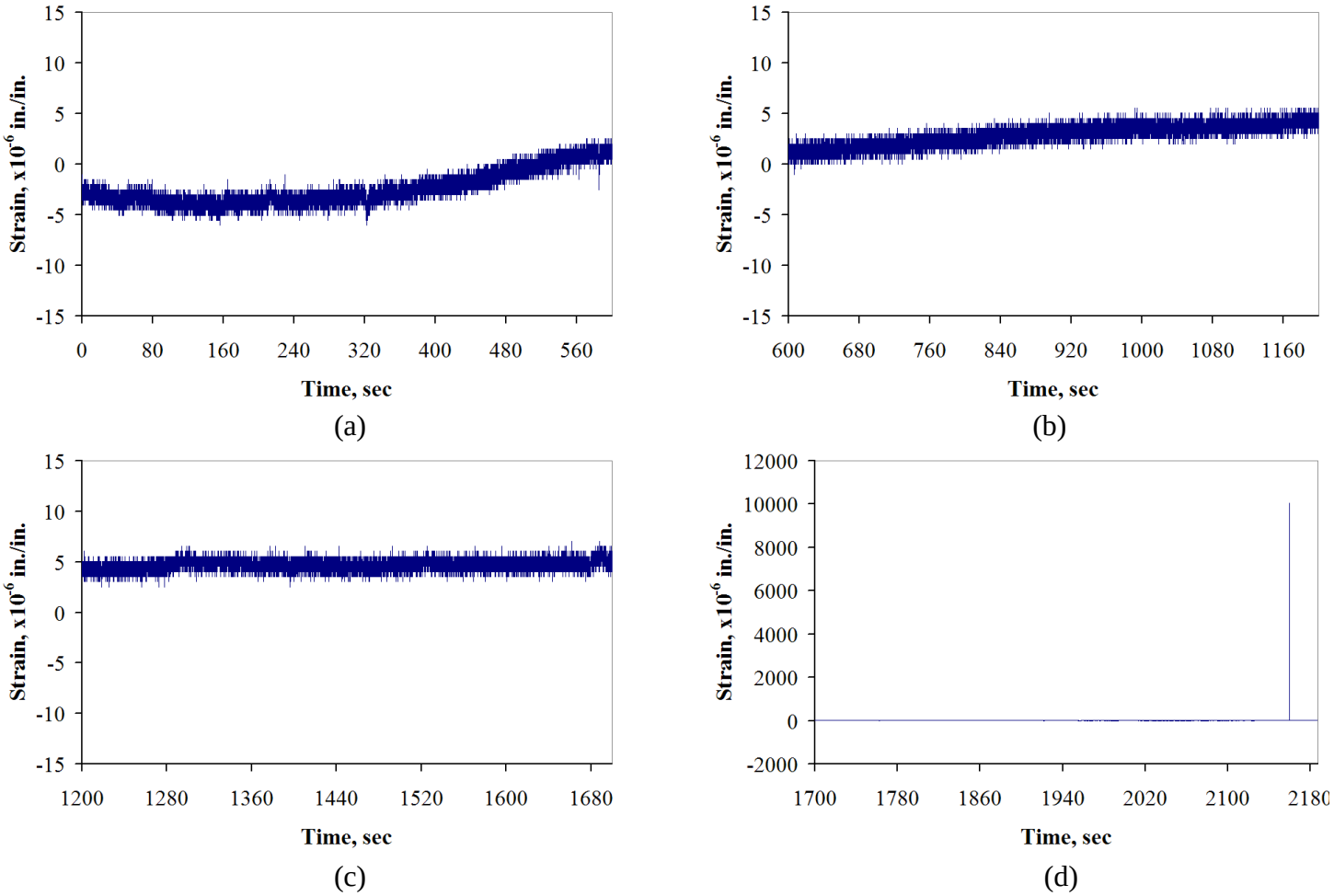

Figure A.23 Strain results at INV_JT2_BC;
(a) at 0 – 600 sec, (b) at 600 – 1200 sec, (c) at 1200 – 1700 sec, (d) at 1700 – 2187 sec.

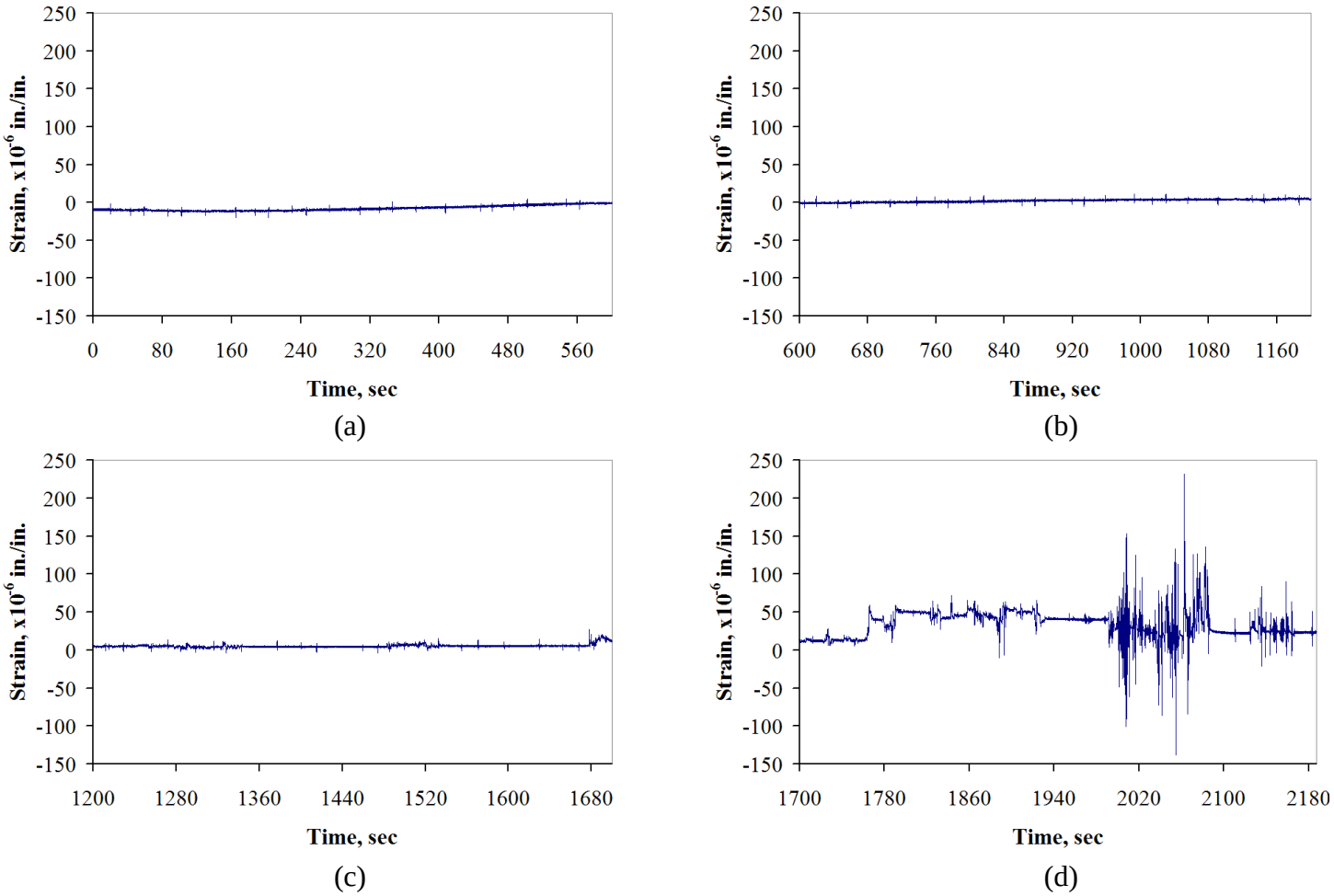

Figure A.24 Strain results at CRN_MS2_BC;
(a) at 0 – 600 sec, (b) at 600 – 1200 sec, (c) at 1200 – 1700 sec, (d) at 1700 – 2187 sec.

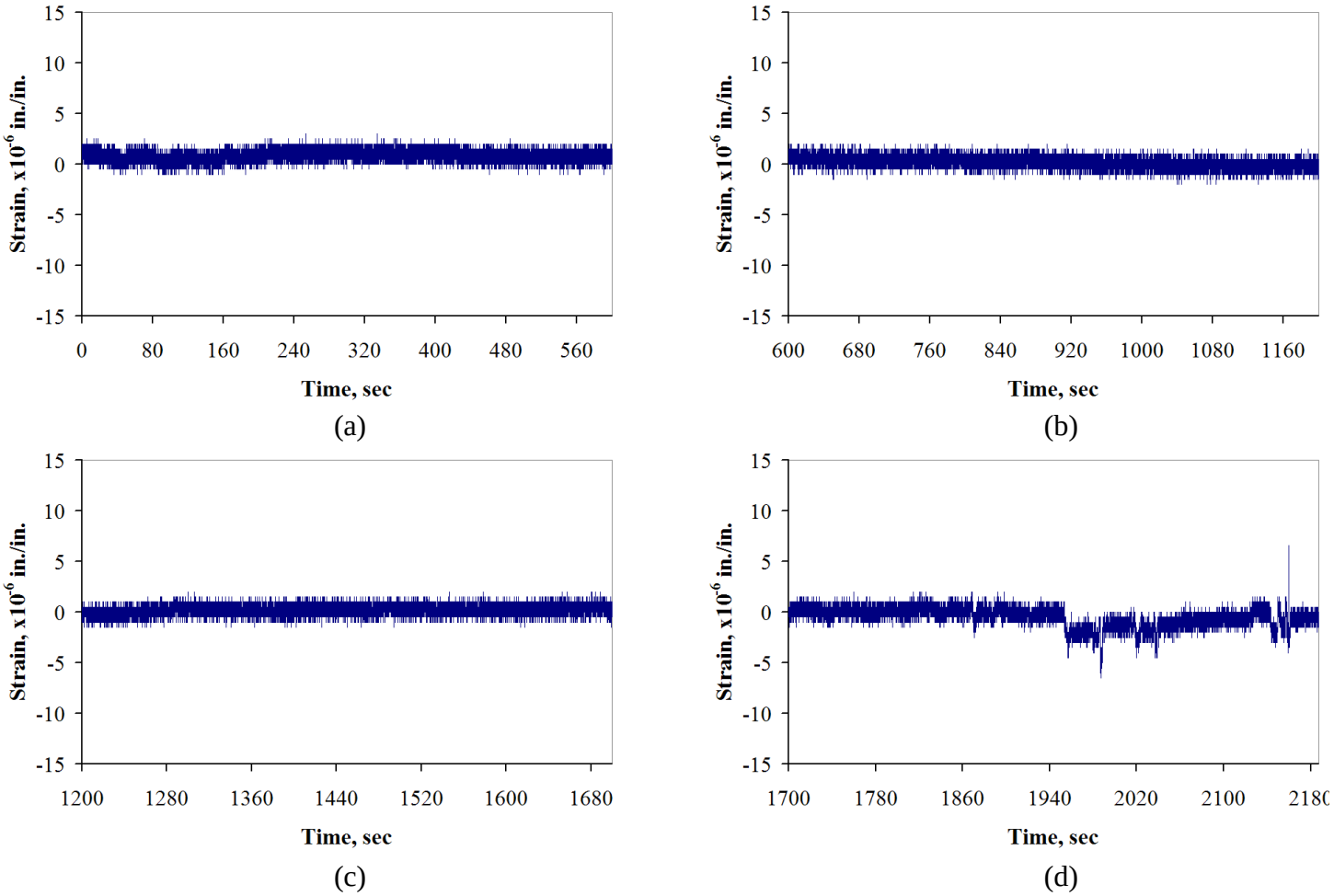

Figure A.25 Strain results at SPL_MS2_BC;
(a) at 0 – 600 sec, (b) at 600 – 1200 sec, (c) at 1200 – 1700 sec, (d) at 1700 – 2187 sec.

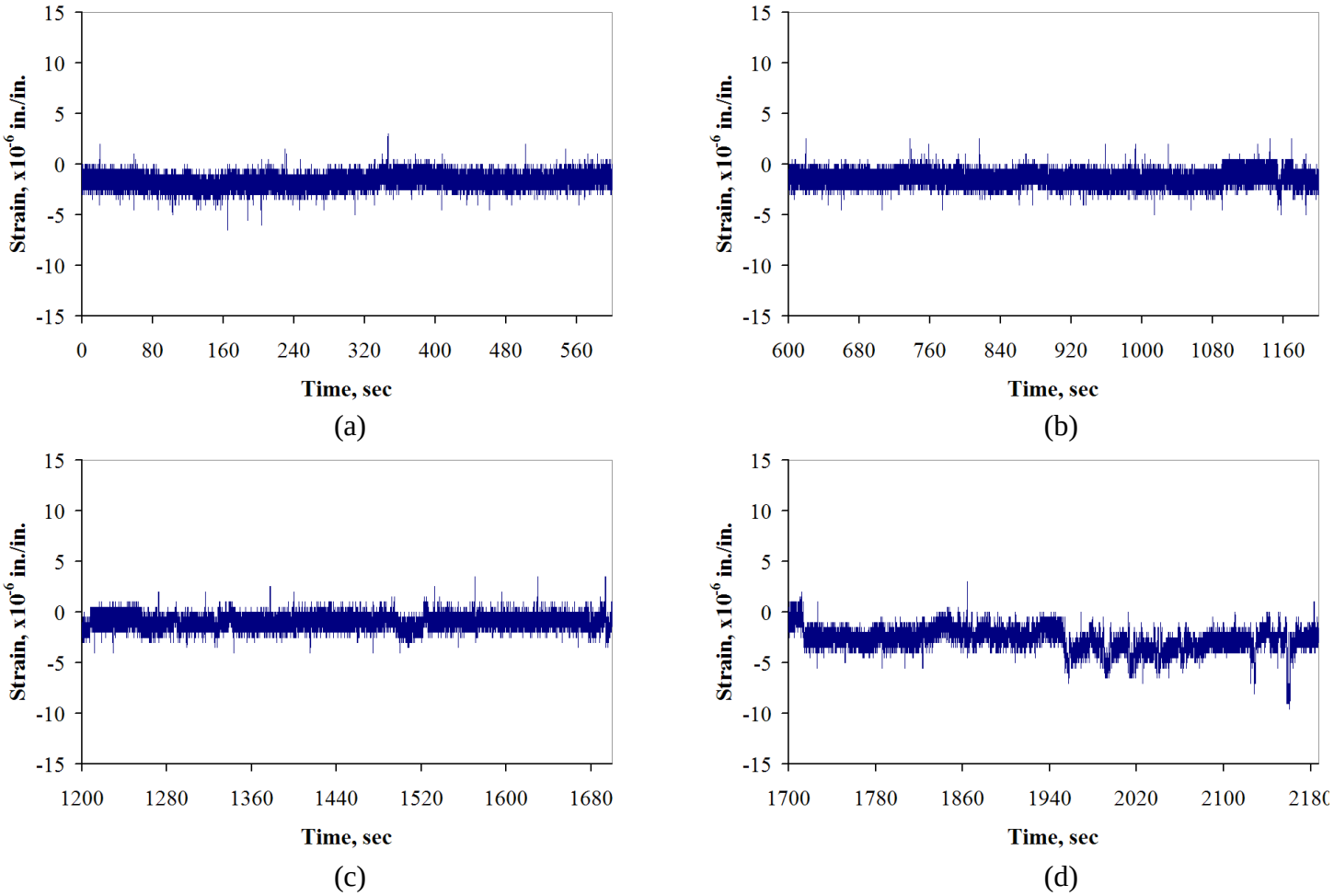

Figure A.26 Strain results at INV_MS2_BC;
(a) at 0 – 600 sec, (b) at 600 – 1200 sec, (c) at 1200 – 1700 sec, (d) at 1700 – 2187 sec.

APPENDIX B

PARAMETRIC STUDY RESULTS

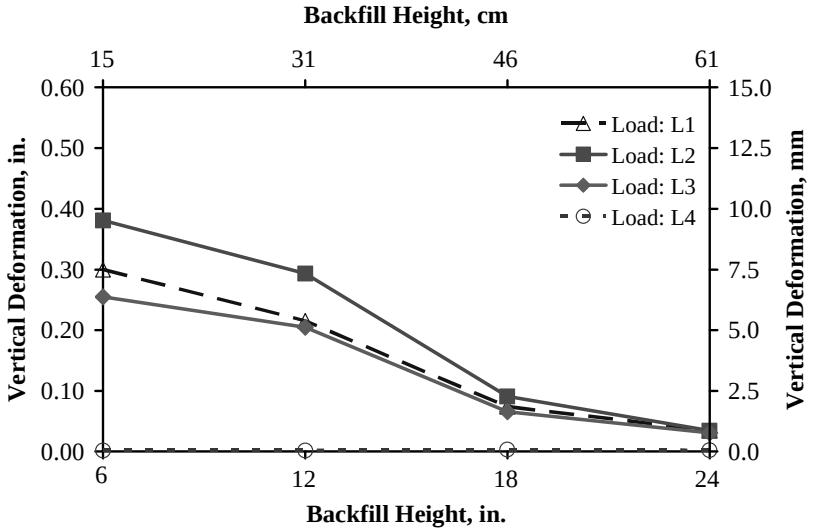

(a)

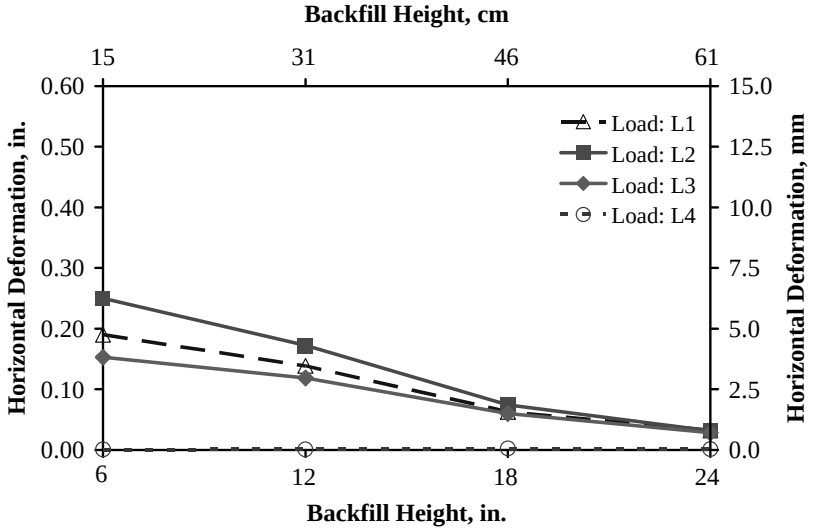

(b)

Figure B.1 Deformation versus backfill height FEM results for P24 under the side-fill Sn90/Sn90; (a) vertical deformation and (b) horizontal deformation.

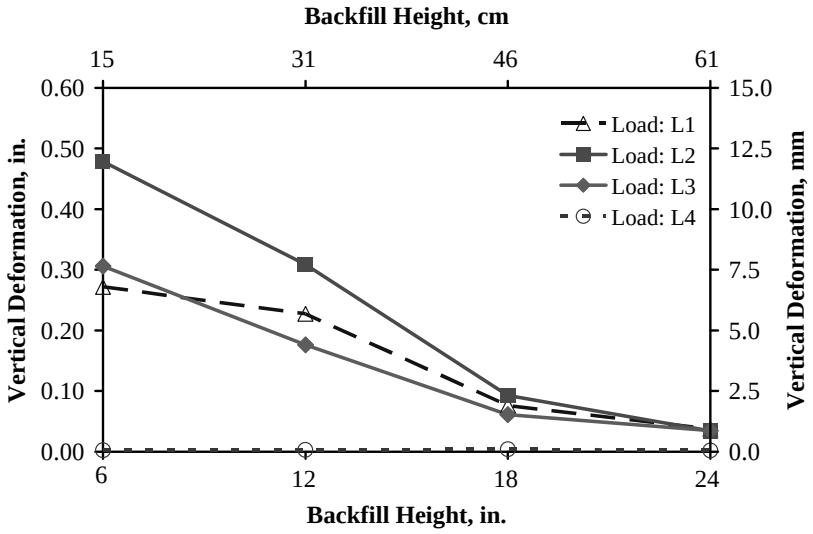

(a)

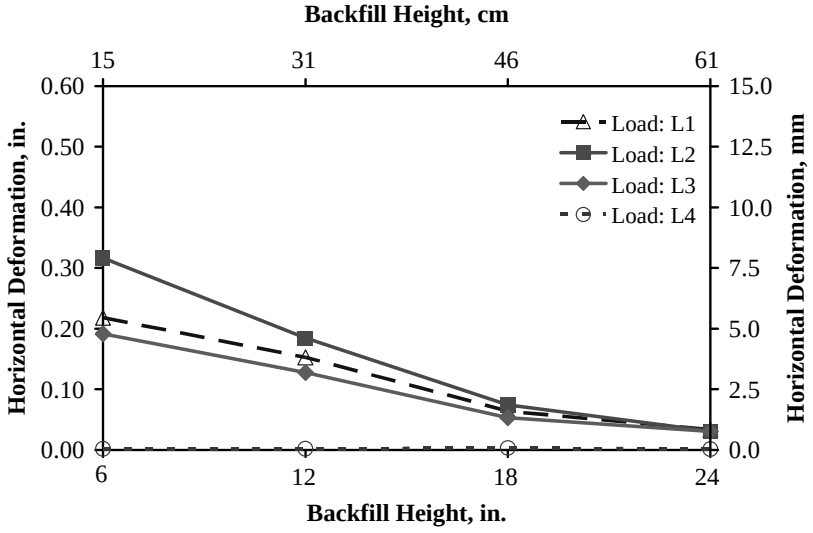

(b)

Figure B.2 Deformation versus backfill height FEM results for P24 under the side-fill Sn90/Si85; (a) vertical deformation and (b) horizontal deformation.

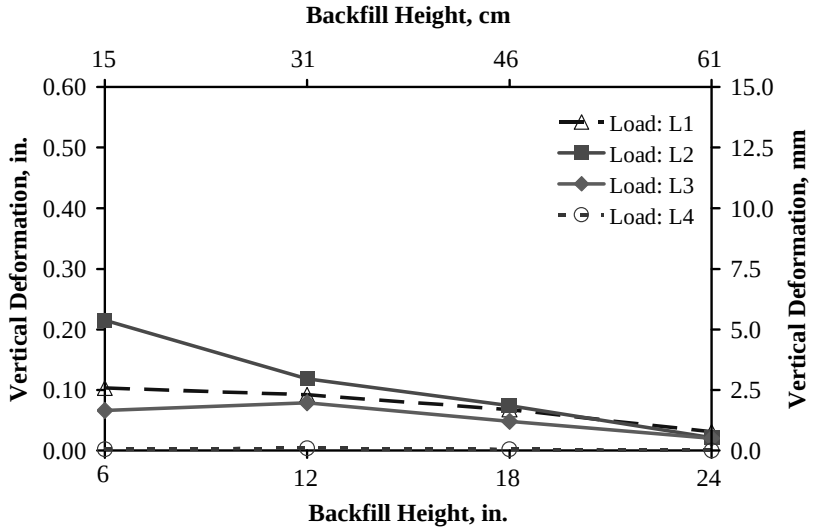

(a)

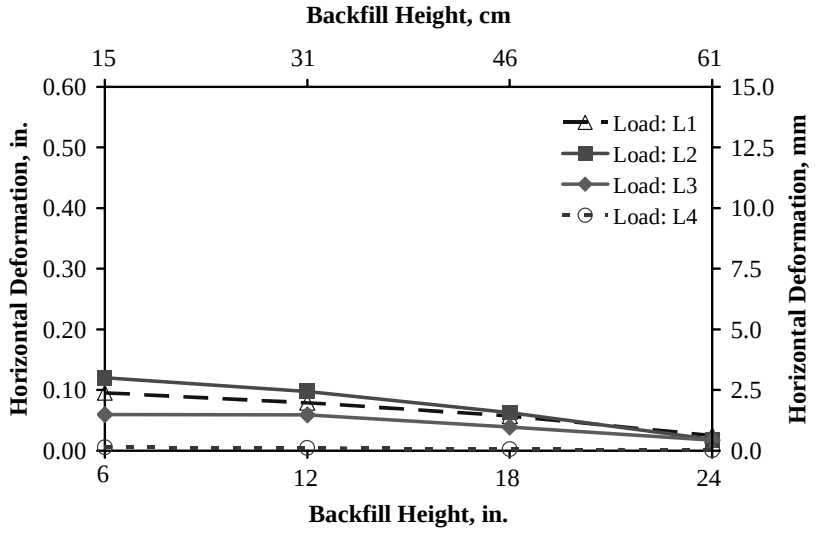

(b)

Figure B.3 Deformation versus backfill height FEM results for P36 under the side-fill Sn90/Sn90; (a) vertical deformation and (b) horizontal deformation.

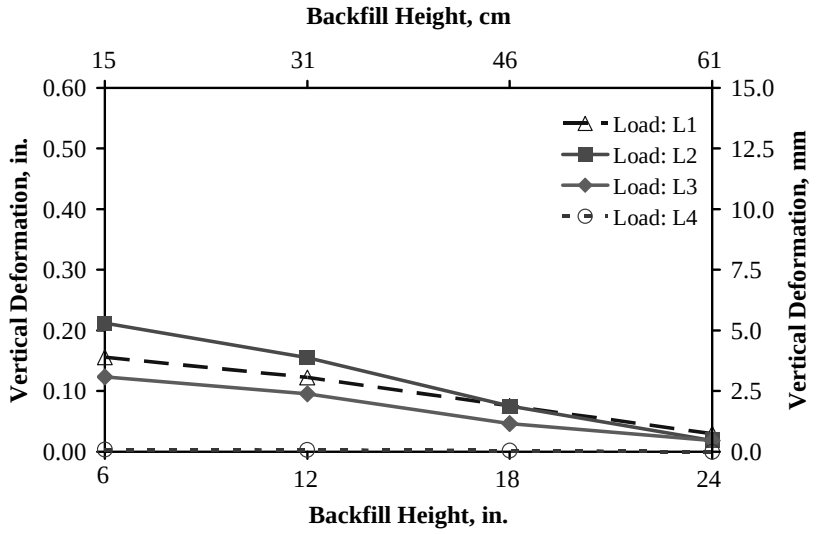

(a)

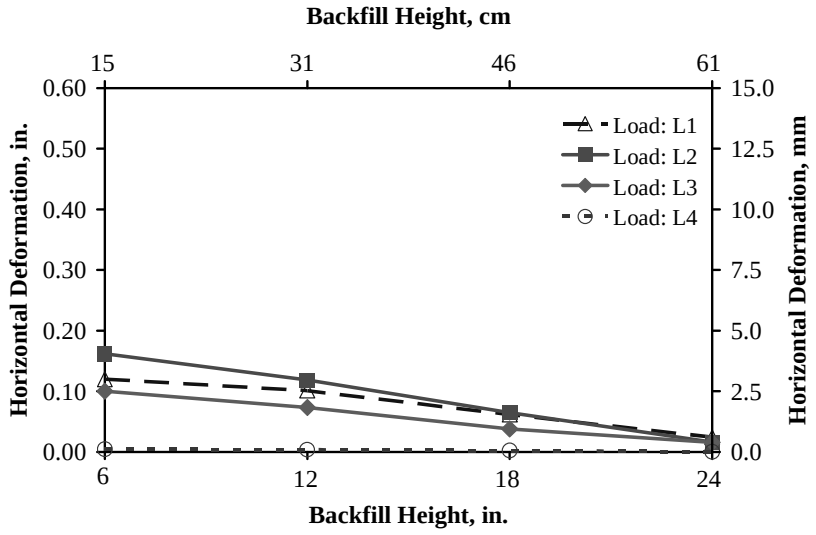

(b)

Figure B.4 Deformation versus backfill height FEM results for P36 under the side-fill Sn90/Si85; (a) vertical deformation and (b) horizontal deformation.

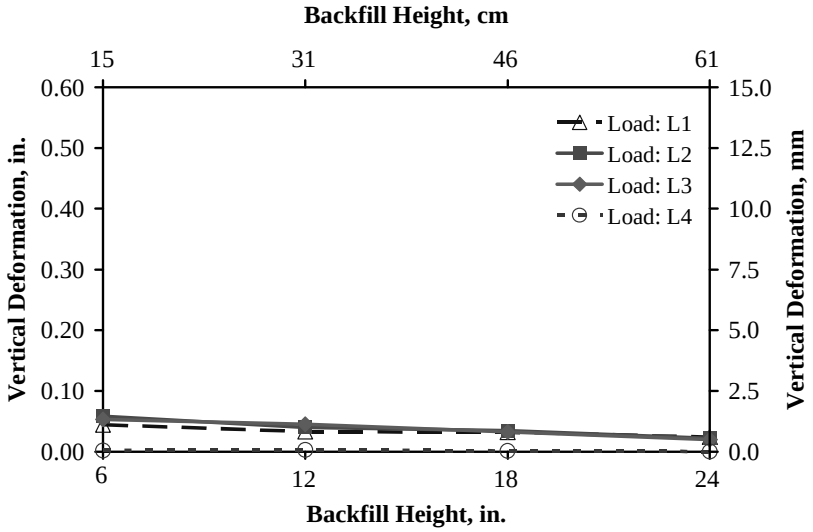

(a)

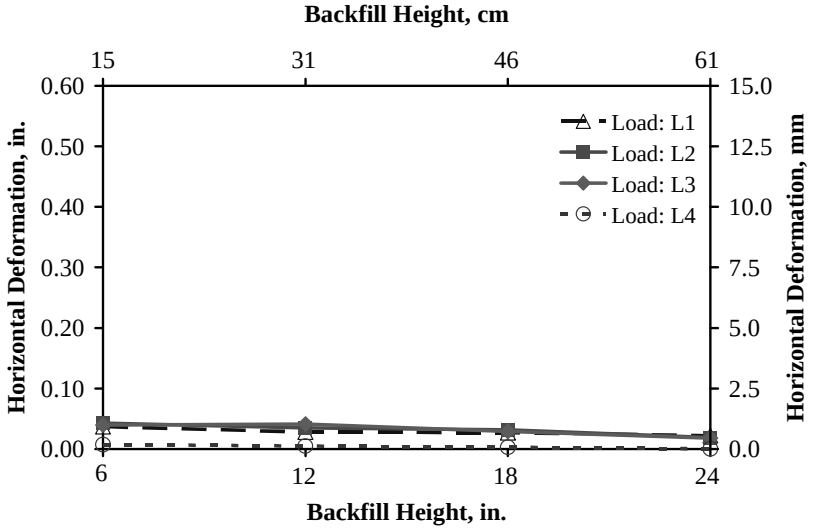

(b)

Figure B.5 Deformation versus backfill height FEM results for P48 under the side-fill Sn90/Sn90; (a) vertical deformation and (b) horizontal deformation.

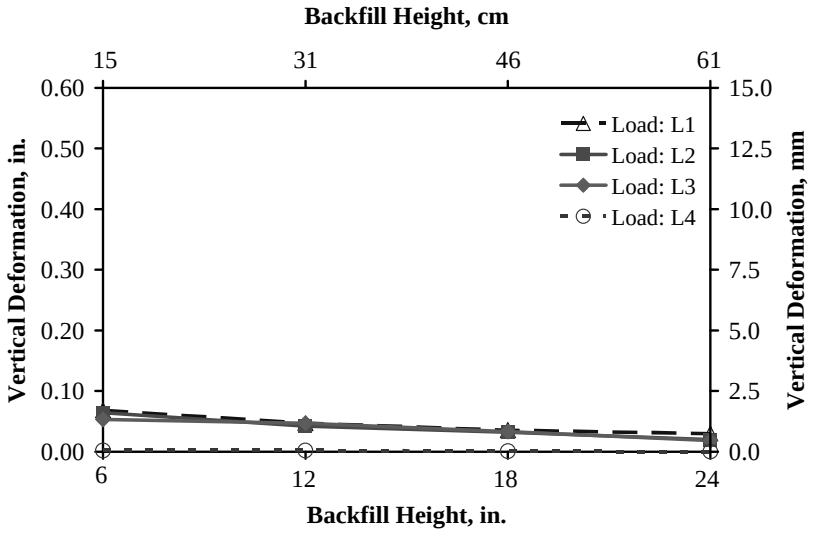

(a)

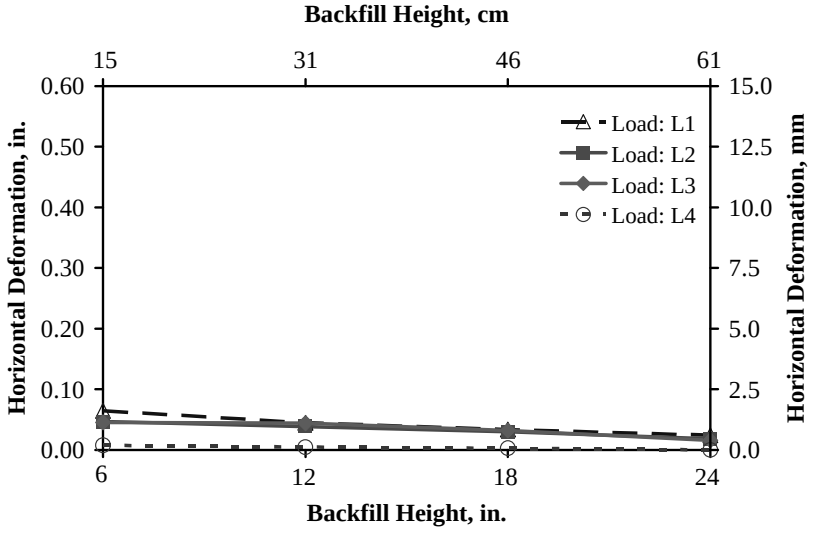

(b)

Figure B.6 Deformation versus backfill height FEM results for P48 under the side-fill Sn90/Si85; (a) vertical deformation and (b) horizontal deformation.

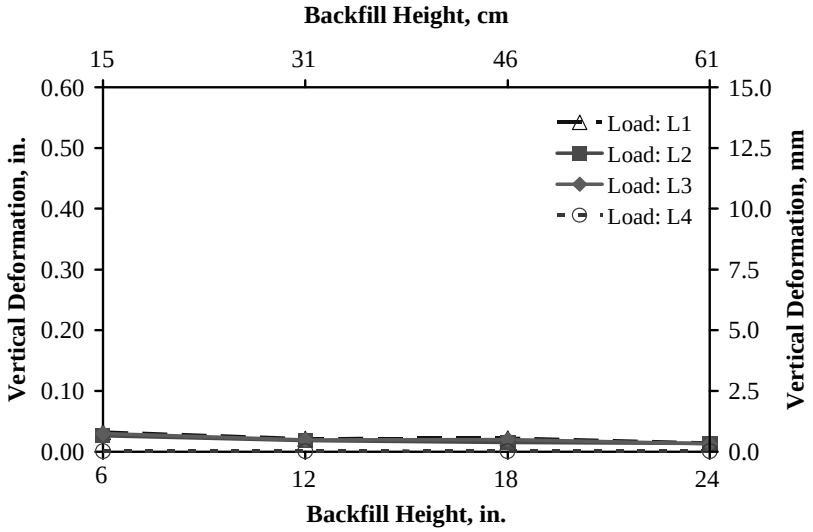

(a)

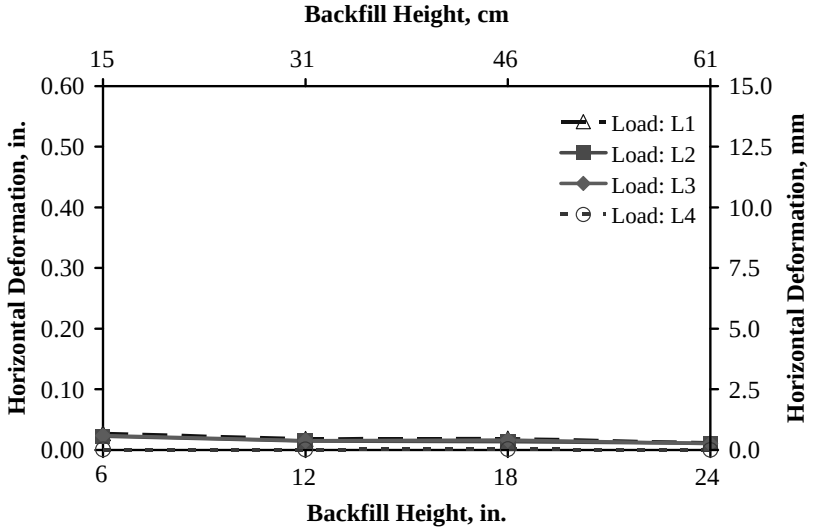

(b)

Figure B.7 Deformation versus backfill height FEM results for P54 under the side-fill Sn90/Sn90; (a) vertical deformation and (b) horizontal deformation.

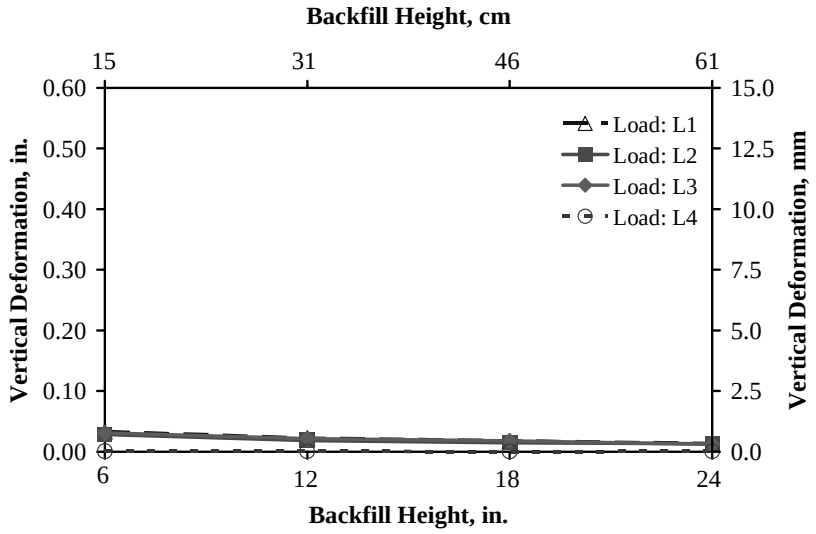

(a)

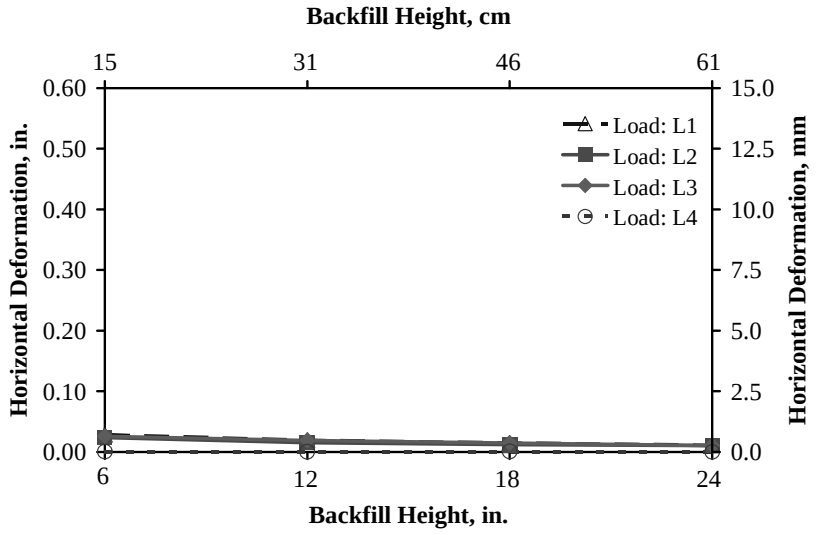

(b)

Figure B.8 Deformation versus backfill height FEM results for P54 under the side-fill Sn90/Si85; (a) vertical deformation and (b) horizontal deformation.

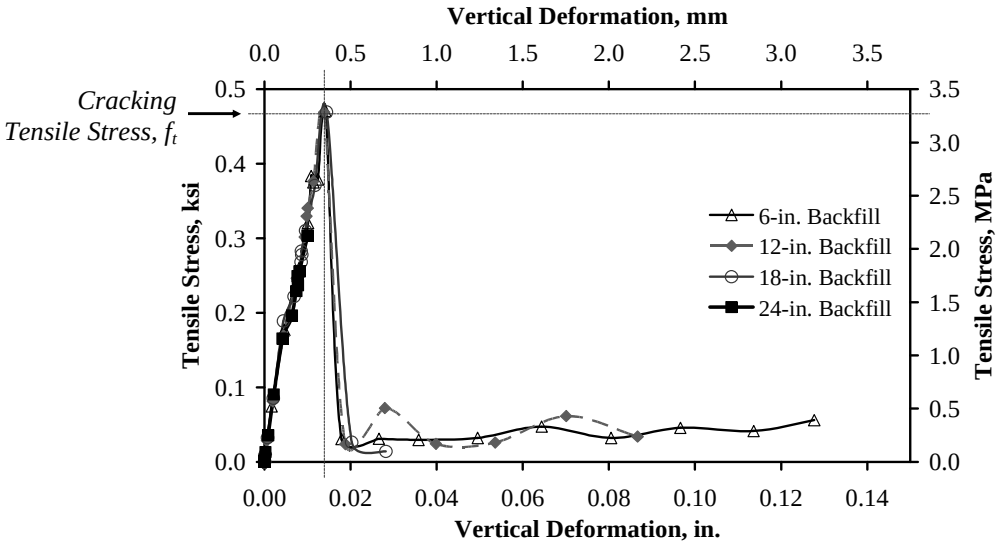

(a)

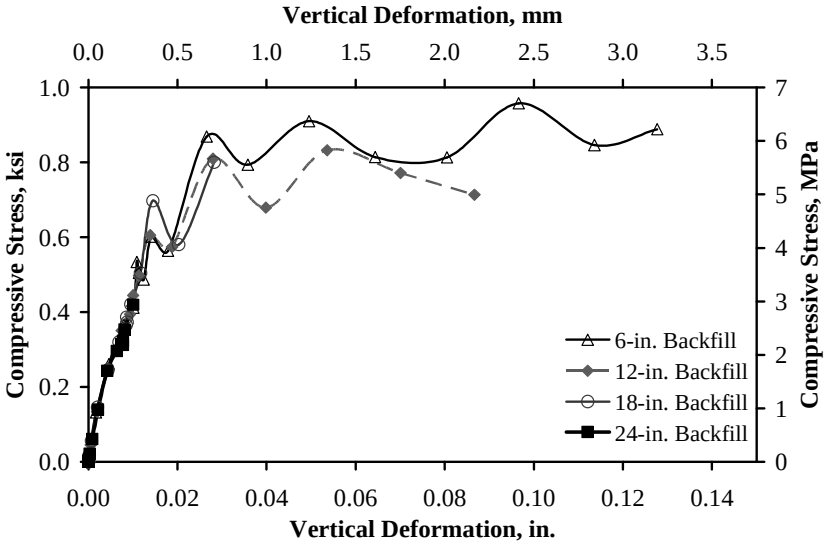

(b)

Figure B.9 Stress-deformation curve FEM results for P24_CRN_JT under the side-fill Sn90/Sn90; (a) tensile stress and (b) compressive stress.

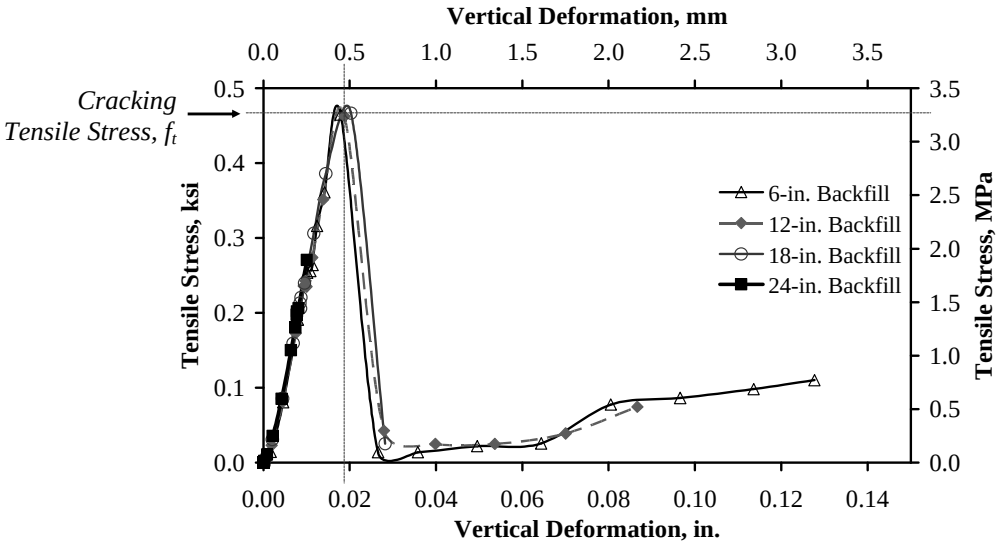

(a)

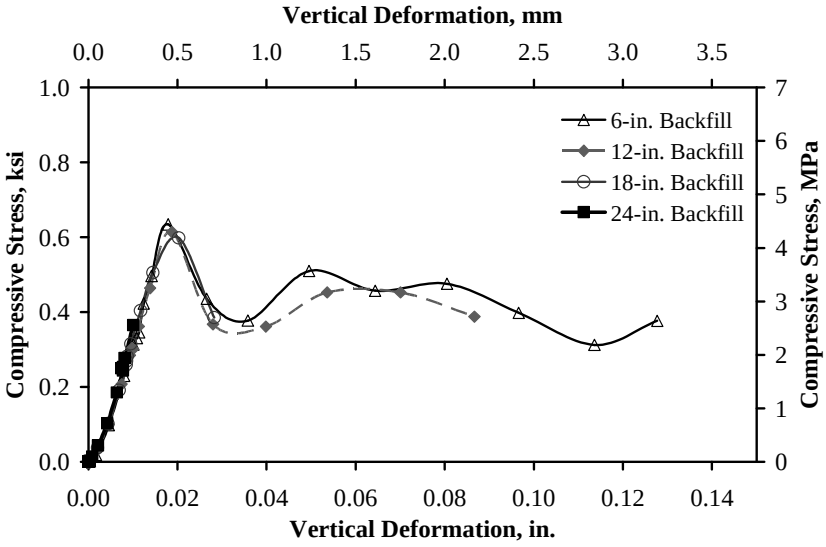

(b)

Figure B.10 Stress-deformation curve FEM results for P24_INV_JT under the side-fill Sn90/Sn90; (a) tensile stress and (b) compressive stress.

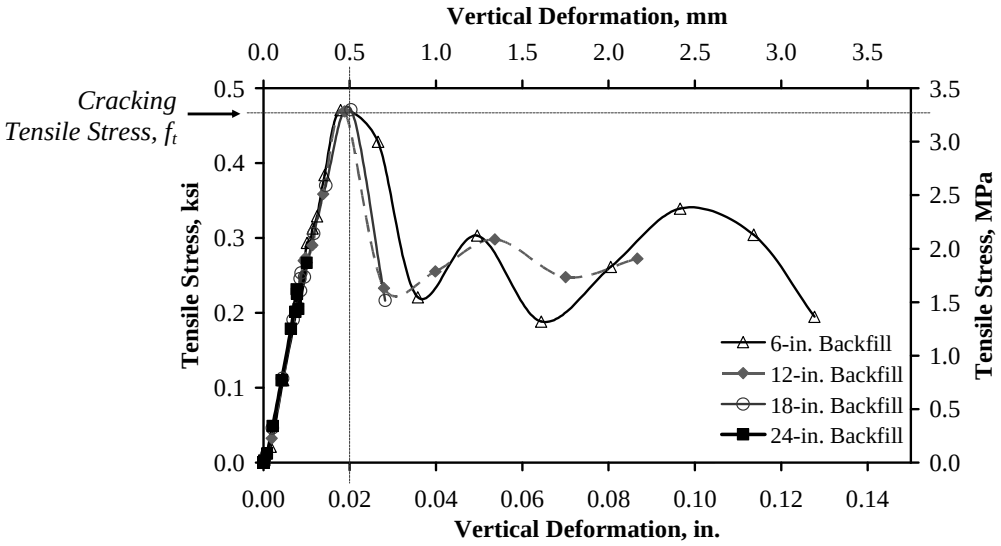

(a)

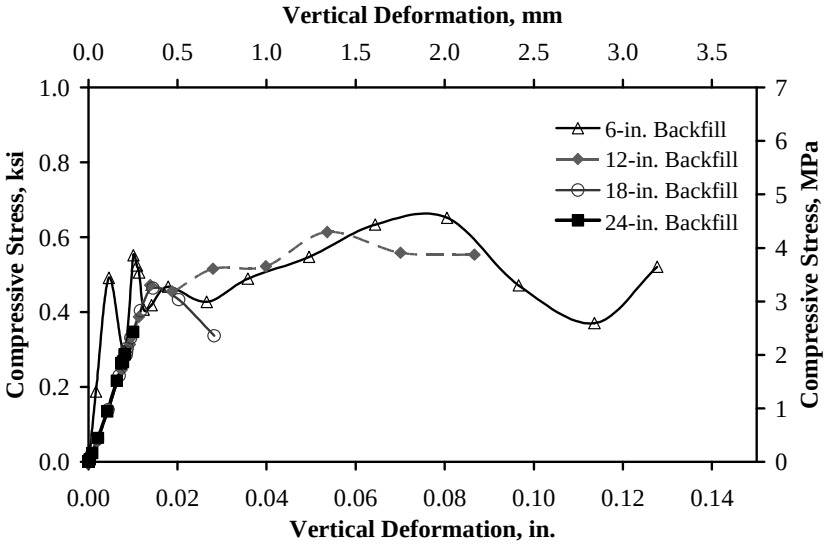

(b)

Figure B.11 Stress-deformation curve FEM results for P24_SPL_JT under the side-fill Sn90/Sn90; (a) tensile stress and (b) compressive stress.

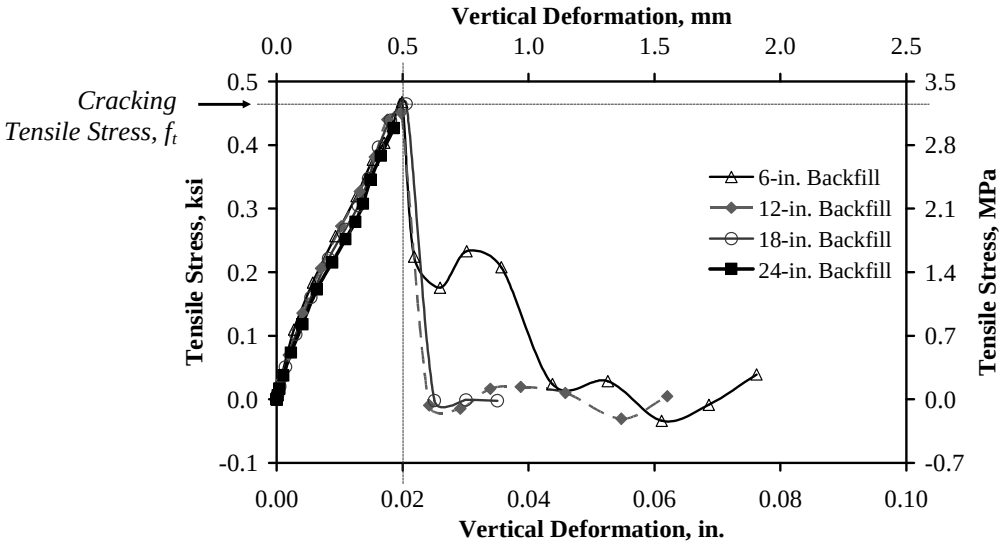

(a)

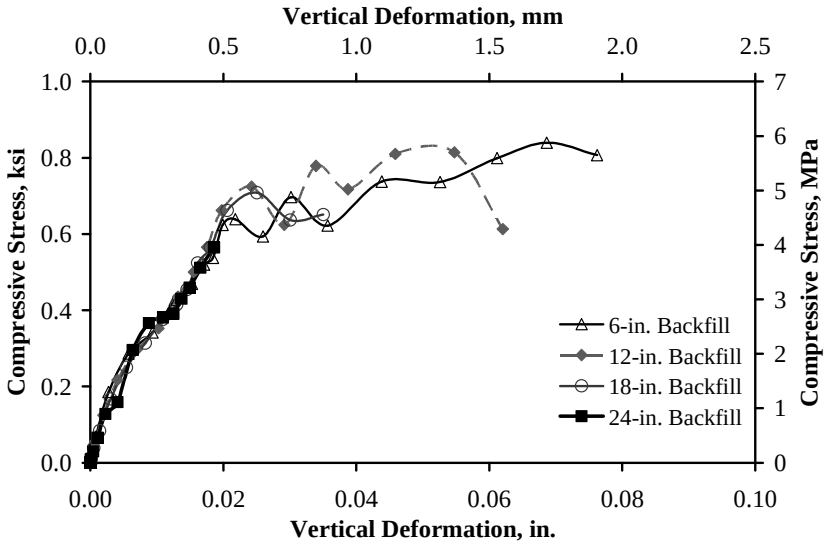

(b)

Figure B.12 Stress-deformation curve FEM results for P36_CRN_JT under the side-fill Sn90/Sn90; (a) tensile stress and (b) compressive stress.

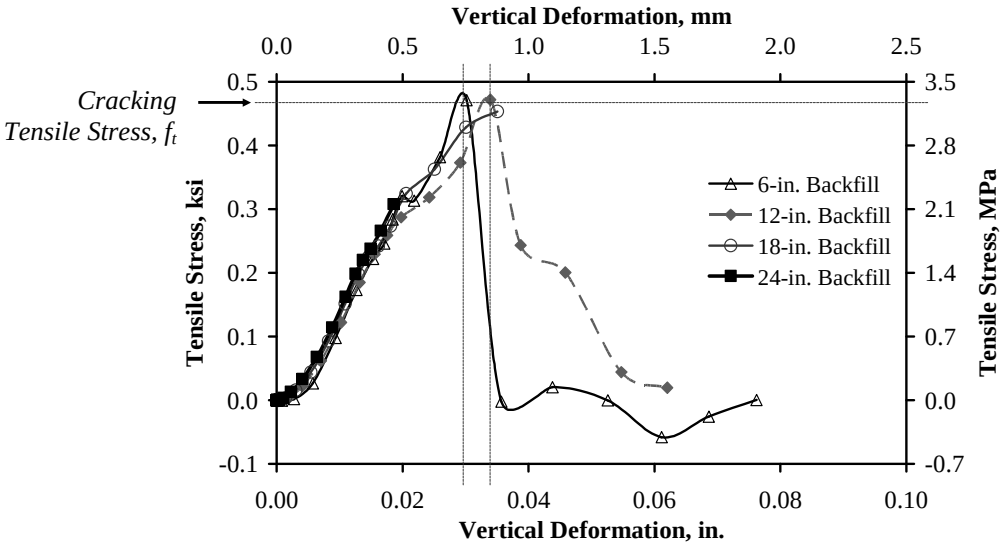

(a)

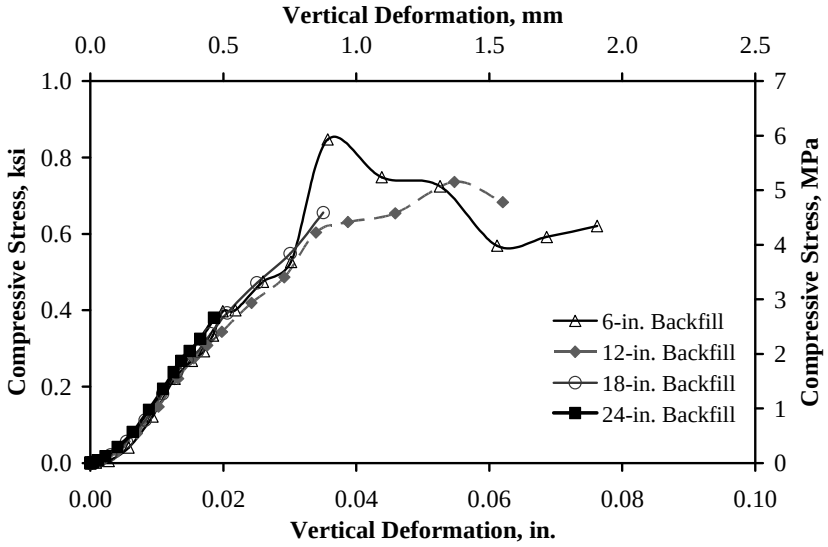

(b)

Figure B.13 Stress-deformation curve FEM results for P36_INV_JT under the side-fill Sn90/Sn90; (a) tensile stress and (b) compressive stress.

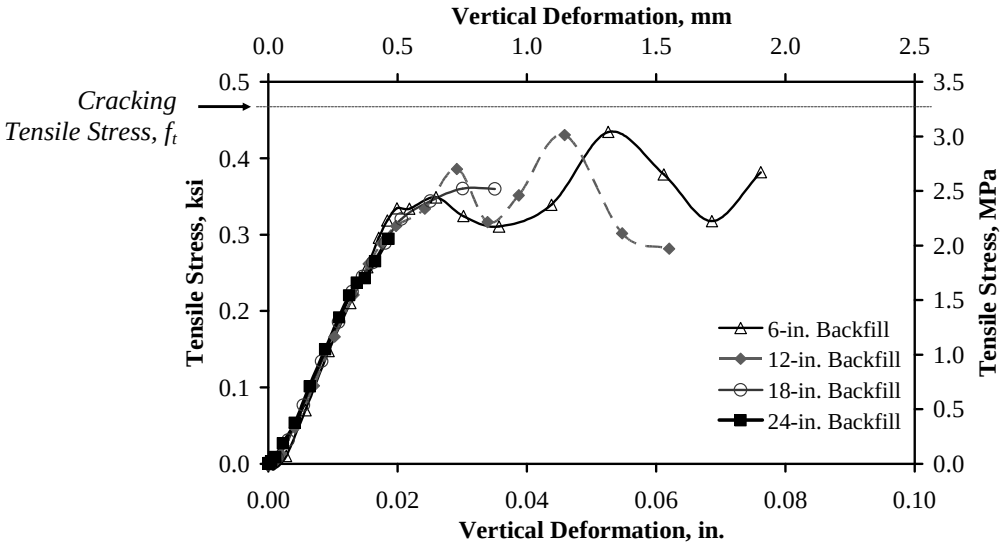

(a)

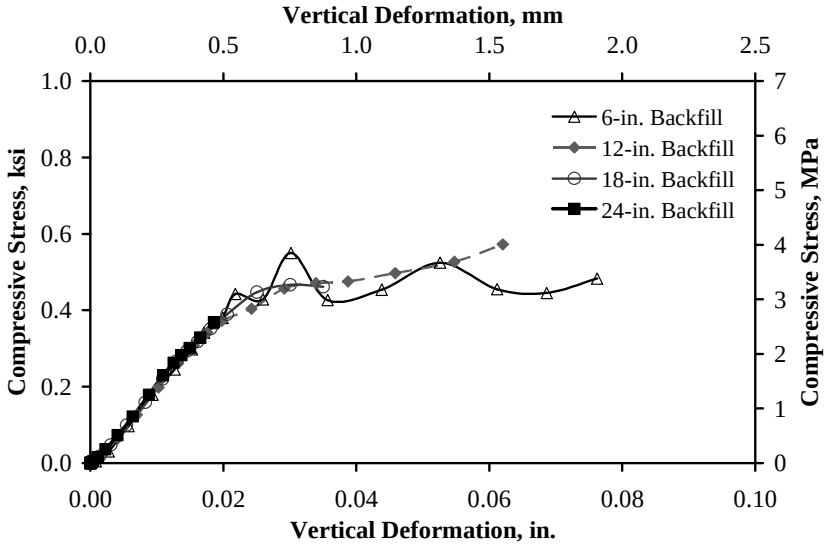

(b)

Figure B.14 Stress-deformation curve FEM results for P36_SPL_JT under the side-fill Sn90/Sn90; (a) tensile stress and (b) compressive stress.

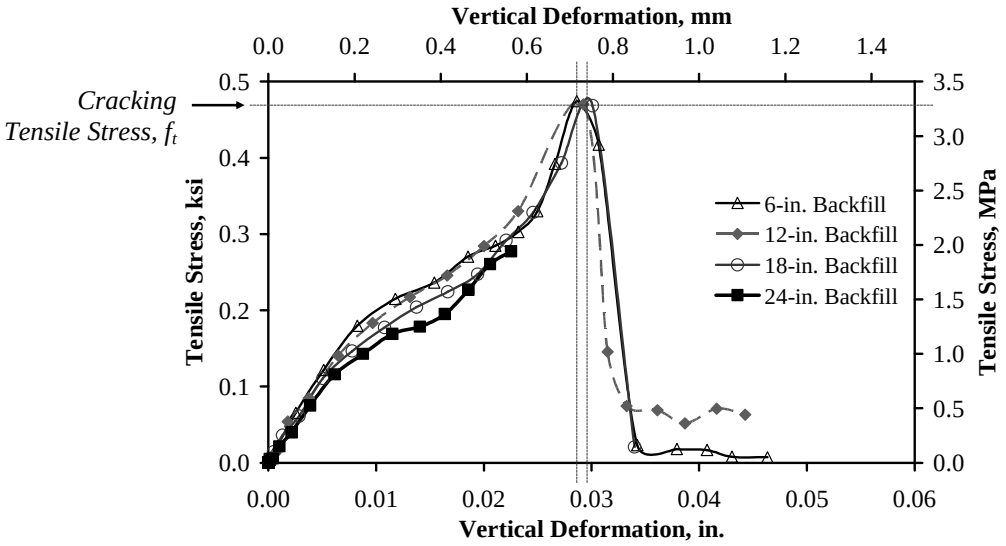

(a)

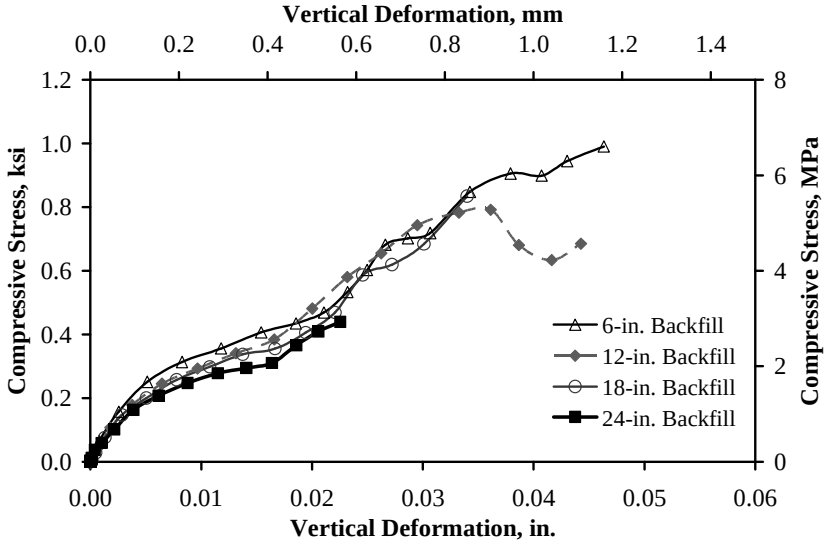

(b)

Figure B.15 Stress-deformation curve FEM results for P48_CRN_JT under the side-fill Sn90/Sn90; (a) tensile stress and (b) compressive stress.

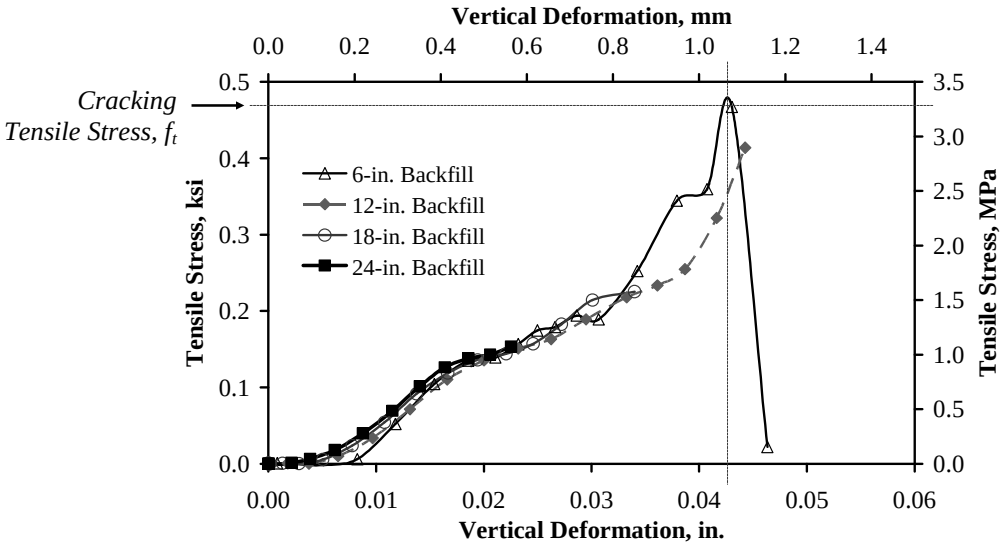

(a)

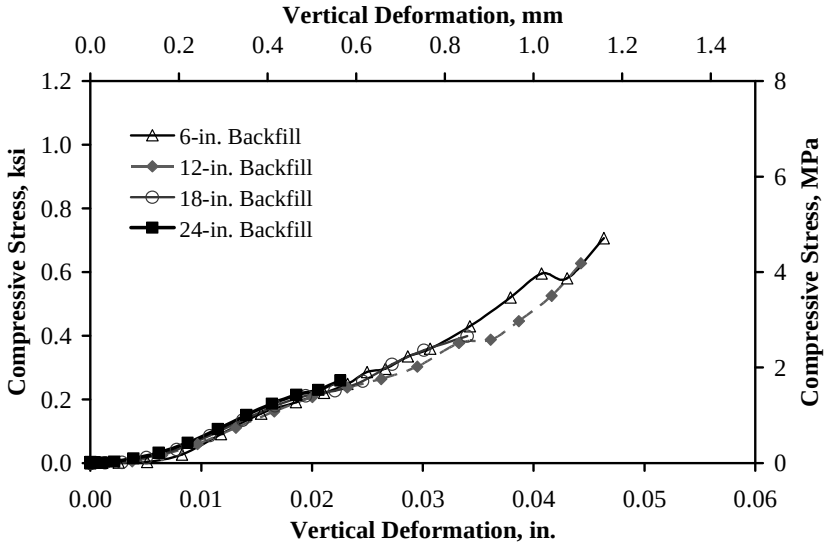

(b)

Figure B.16 Stress-deformation curve FEM results for P48_INV_JT under the side-fill Sn90/Sn90; (a) tensile stress and (b) compressive stress.

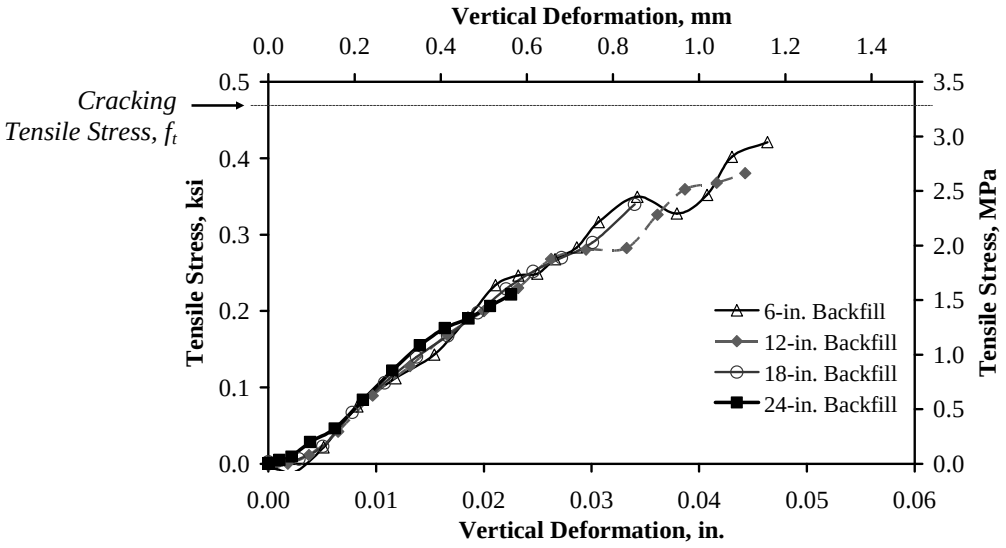

(a)

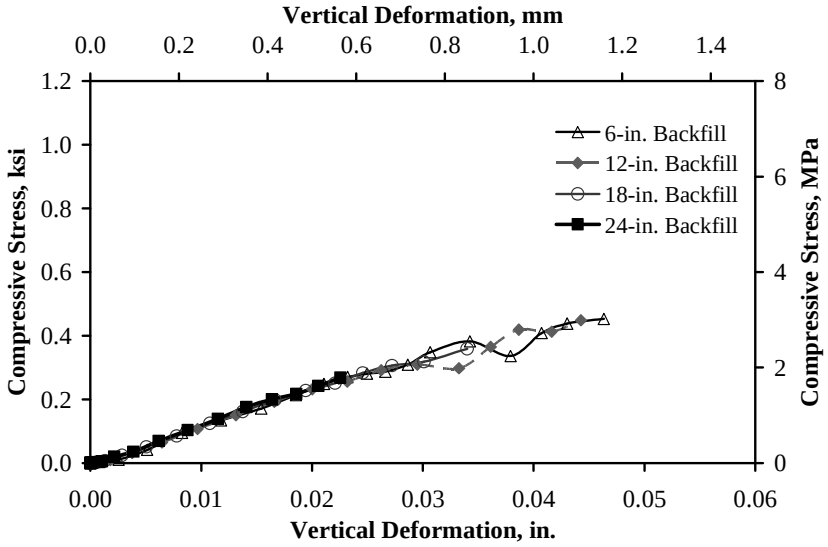

(b)

Figure B.17 Stress-deformation curve FEM results for P48_SPL_JT under the side-fill Sn90/Sn90; (a) tensile stress and (b) compressive stress.

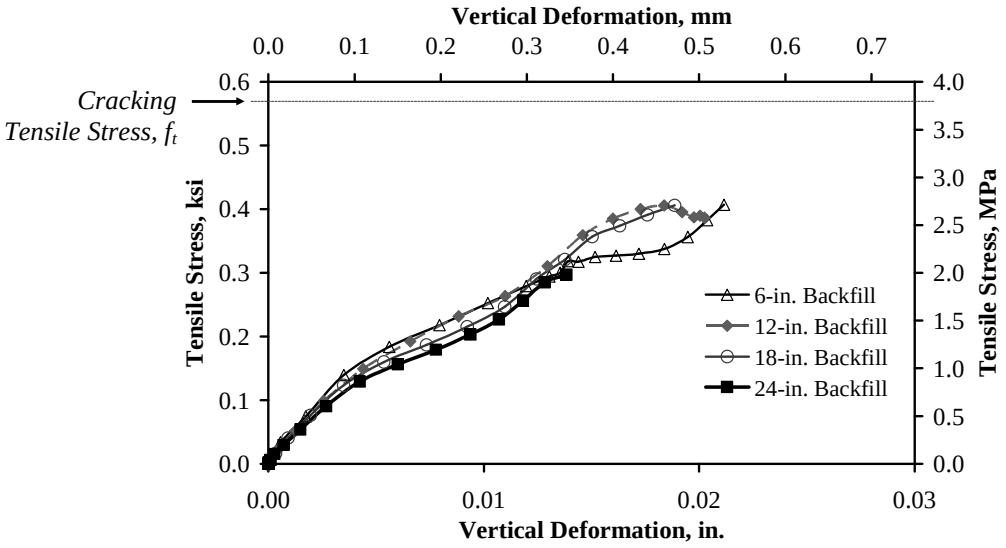

(a)

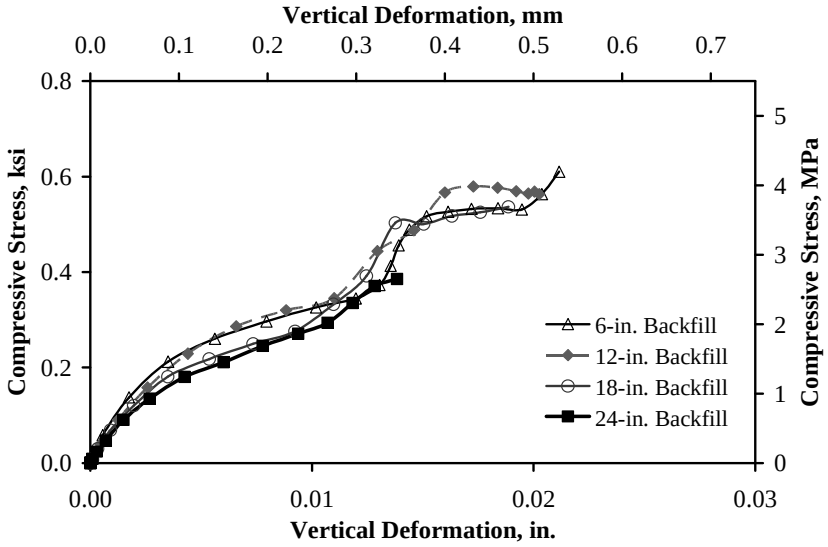

(b)

Figure B.18 Stress-deformation curve FEM results for P54_CRN_JT under the side-fill Sn90/Sn90; (a) tensile stress and (b) compressive stress.

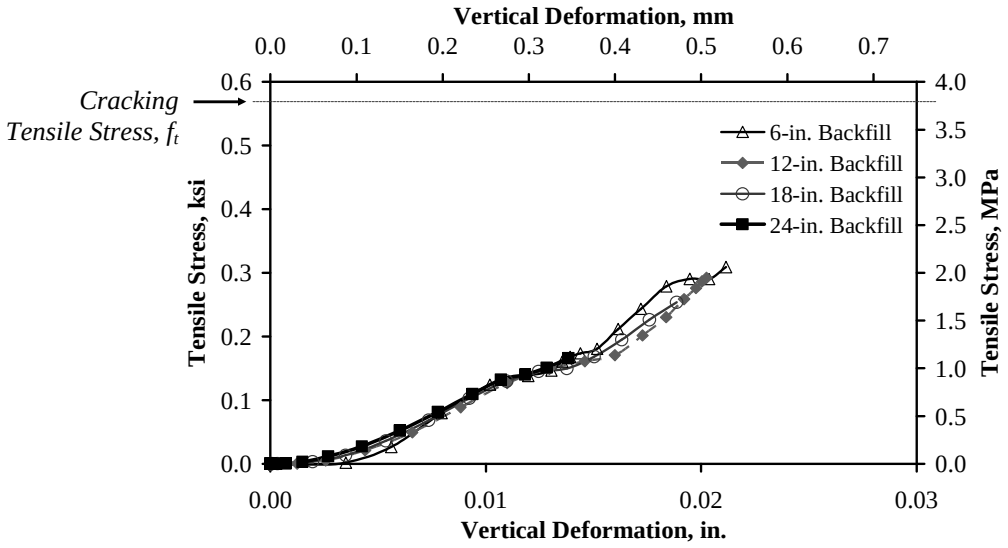

(a)

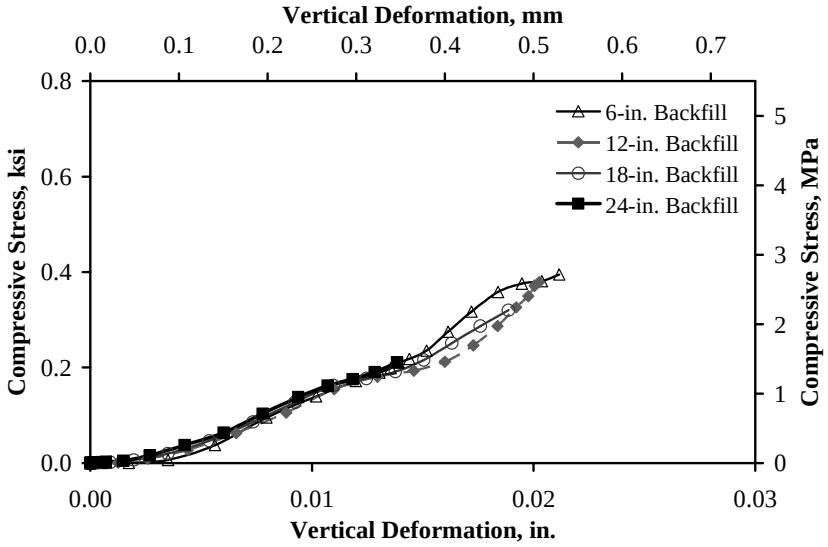

(b)

Figure B.19 Stress-deformation curve FEM results for P54_INV_JT under the side-fill Sn90/Sn90; (a) tensile stress and (b) compressive stress.

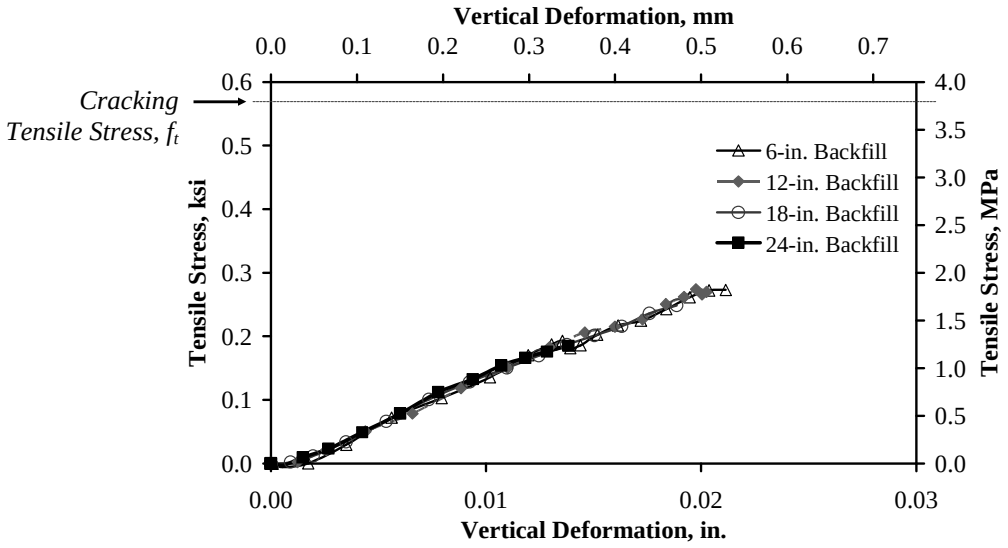

(a)

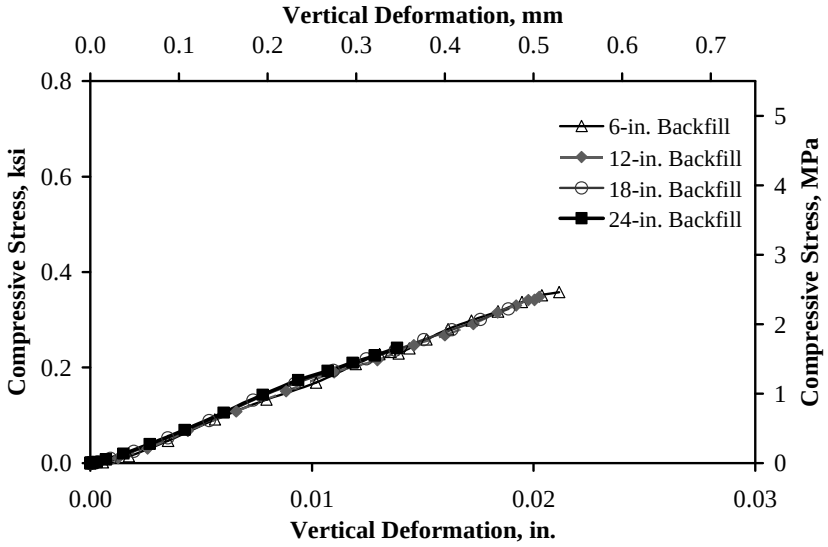

(b)

Figure B.20 Stress-deformation curve FEM results for P54_INV_JT under the side-fill Sn90/Sn90; (a) tensile stress and (b) compressive stress.

REFERENCES

ABAQUS. *ABAQUS manual,* Version 6.8-2, Pawtucket, R.I., 2008.

ACI Committee 318. *Building Code Requirements for Structural Concrete and Commentary,* American Concrete Institute, Detroit, 2008.

American Association of State Highway and Transportation Officials. *AASHTO M 145: Standard Specifications for Classification of Soils and Soil-Aggregate Mixtures for Highway Construction Purposes,* Washington, DC, 2005.

American Association of State Highway and Transportation Officials. *AASHTO M 170: Standard Specification for Reinforced Concrete Culvert, Storm Drain, and Sewer Pipe,* Washington, DC, 2005.

American Association of State Highway and Transportation Officials. *AASHTO M 242: Standard Specification for Reinforced Concrete D-Load Culvert, Storm Drain, and Sewer Pipe,* Washington, DC, 2005.

American Association of State Highway and Transportation Officials. *AASHTO T 99: Standard Methods of Test for The Moisture-Density Relations of Soils and Soil-Aggregate Mixtures Using 5.5-lb (2.5-kg) Rammer and 12-in. (305-mm) Drop,* Washington, DC, 2005.

American Association of State Highway and Transportation Officials. *AASHTO T 180: Standard Methods of Test for The Moisture-Density Relations of Soils and Soil-Aggregate Mixtures Using 10-lb (4.5-kg) Rammer and 18-in. (457-mm) Drop,* Washington, DC, 2005.

American Concrete Pipe Association (ACPA). *Concrete Pipe Installation Manual,* Irving, TX, 2007.

American Concrete Pipe Association (ACPA). *Concrete Pipe Technology Handbook,* 3rd printing, Irving, TX, 2001.

American Society for Testing and Materials Standards. *ASTM C 76: Standard Specification for Reinforced Concrete Culvert, Storm Drain, and Sewer Pipe,* Philadelphia, PA, 2008.

American Society for Testing and Materials Standards. *ASTM C 78: Standard Test Method for Flexural Strength of Concrete (Using Simple Beam with Third-Point Loading),* Philadelphia, PA, 2008.

American Society for Testing and Materials Standards. *ASTM C 293: Standard Test Method for Flexural Strength of Concrete (Using Simple Beam with Center-Point Loading),* Philadelphia, PA, 2008.

American Society for Testing and Materials Standards. *ASTM C 497: Standard Test Methods for Concrete Pipe, Manhole Sections, or Tile,* Philadelphia, PA, 2007.

American Society for Testing and Materials Standards. *ASTM C 655: Standard Specification for Reinforced Concrete D-Load Culvert, Storm Drain, and Sewer Pipe,* Philadelphia, PA, 2007.

American Society for Testing and Materials Standards. *ASTM D 698: Testing Methods for Moisture-Density Relations of Soils and Soil-Aggregate Mixtures Using 5.5-lb (2.5-kg) Rammer and 12-in. (305 mm) Drop,* Philadelphia, PA, 2005.

American Society for Testing and Materials Standards. *ASTM D 1557: Testing Methods for Moisture-Density Relations of Soils and Soil-Aggregate Mixtures Using 10-lb (4.5-kg) Rammer and 18-in. (457 mm) Drop,* Philadelphia, PA, 2005.

American Society for Testing and Materials Standards. *ASTM D 2487: Standard Practice for Classification of Soils for Engineering Purposes (Unified Soil Classification System),* Philadelphia, PA, 2005.

American Society of Civil Engineers (ASCE). *Standard Practice for Direct Design of Buried Precast Concrete Pipe Using Standard Installations (SIDD),* Standard No. 015-93, 50 pp., 1994.

Buttner, R. C. *Reinforcing System for Concrete Pipe,* United States Patent, no. 4494576, 1985.

Concrete Pipe Information. *Effects of Cracks in Reinforced Concrete Culvert Pipe,* The Technical Committee of the California Precast Concrete Pipe Association, 1976.

Dresher. *Plate Type Vibrator Compactor*. United States Patent, no. 3603224, 1971.

Hansen, B., Lee, D., and Demartini, C. *The Cracking of Stormwater Pipes and The Significance of Construction Loads*. Research and Development Section, Brisbane City Council, Queensland, 1997.

Heger, F. J., Leipins, A. A., and Selig, E. T. *SPIDA: An Analysis and Design System for Buried Concrete Pipe*. American Society of Civil Engineers (ASCE), Conference Article, p. 143 – 154, 1985.

Katona, M. G., Smith, J. M., Odello, R.S., and Allgood, J. R. *CANDE – A Modern Approach for the Structural Design and Analysis of Buried Culverts*. Federal Highway Administration, 1976.

Krizek, R. J. and McQuade, P. V. *Behavior of Buried Concrete Pipe.* American Society of Civil Engineers (ASCE) Journal of Geotechnical Engineering Division, Vol. 104, no. 7, p. 815 – 836, 1978.

Maher, M. M., Akl, A. Y., and Metwally, K. G. *Advanced Analysis of Concrete Pipe-Soil Interaction*. Journal of Engineering and Applied Science, Vol. 52, no. 3, p. 437 – 456, 2005.

Marston, A. *The Theory of External Loads on Closed Conduits in the Light of the Latest Experiments*, bulletin 96, Iowa State College, 1930.

Marston, A., Schlick, W. J., and Clemmer, H. F. *The Supporting Strength of Sewer Pipe in Ditches and Methods of Testing Sewer Pipe in Laboratories to Determine Their Ordinary Supporting Strength*, Bulletin 47, Iowa State College, 1917.

McGrath, T. J. *Protocol for 100 Year Service Life of Corrugated HDPE*. Florida Department of Transportation, 2003.

McGrath, T. J. and Kurdziel, J. M. *SPIDA Method for Reinforced Concrete Pipe Design*. American Society of Civil Engineers (ASCE) Journal of Transportation Engineering, Vol. 117, issue 4, pp. 371 – 381, 1991.

McGrath, T. J., Selig, E. T., and Webb, M. C. *Field Tests of Concrete Pipe Performance during Backfilling*. American Society for Testing and Materials (ASTM) Special Technical Publication, no. 1368, p. 73 – 88, 2000.

McGrath, T. J., Selig, E. T., and Webb, M. C. *Instrument for Monitoring Buried Pipe Behavior during Backfilling*. American Society for Testing and Materials (ASTM) Special Technical Publication, no. 1358, p. 101 – 118, 1999.

Olander, H. C. *Stress Analysis of Concrete Pipe*, Engineering Monographs Number 6, United States Department of Interior, Bureau of Declamation, 1950.

Pacific Northwest Concrete Pipe Association. *Concern: Aggressive Compaction Methods*, Technical Bulletin, 1993.

Parmelee, R. A. *Investigation of Soil-Structure Interaction of Buried Concrete Pipe.* Highway Research Board, issue 443, p. 32 – 39, 1973.

Poucher, Novak, and Hindy. *Effective Vibratory Compactors on Buried Concrete Pipe*. The University of Western Ontario, 1976.

Schlick, W. J. *Supporting Strength of Drain Tile and Sewer Pipe Under Different Pipe-Laying Conditions*, Bulletin 57, Iowa State College, 1920.

Selig, E. T. *Soil Properties for Plastic Pipe Installations,* Buried Plastic Pipe Technology, ASTM STP 1093, Philadelphia, 1990.

Spangler, M. G. *The Supporting Strength of Rigid Pipe Culverts*, bulletin 112, Iowa State College, 1933.

St. Louis, P. T. *Backhoe Mounted Vibrating Plate Soil Compactor*. United States Patent, no. 4224003, 1980.

Talesnick, M. *Measuring Soil Contact Pressure on a Solid Boundary and Quantifying Soil Arching*. American Society for Testing and Materials (ASTM), Geotechnical Testing Journal, Vol. 28, no. 2, 2005.

Webb, M. C., McGrath, T. J., and Selig, E. T. *Field Tests of Buried Pipe Installation Procedures*. Transportation Research Record, no. 1541, p. 97 – 106, 1996.

Webb, M. C., McGrath, T. J., and Selig, E. T. *Field Tests of Buried Pipe with CLSM Backfill*. American Society for Testing and Materials (ASTM) Special Technical Publication, no. 1331, p. 237 – 254, 1998.

Zoladz, G. V., McGrath, T. J., and Selig, E. T. *Laboratory Tests of Buried Pipe Installation Procedures*. Transportation Research Record, no. 1541, p. 86 – 96, 1996.

BIOGRAPHICAL INFORMATION

Anupong Kararam was born June 7, 1980 in Bangkok, the capital city in Thailand. He finished his high school level in 1997 with the major courses of mathematics and science. Then, in 2001 he received his bachelor degree in Civil Engineering at the Mahidol University, one of the most famous universities in Thailand. After his graduation, he started working for the company “DKJ construction Co.Ltd.” in the area of civil engineering for one and a half years. He worked as a field engineer for the construction of 8-storey condominium. His main duties were to control the construction processes, and to make the as-built shop drawings using AutoCAD R14. After that, he worked for “Pyramid Development International Co.Ltd.” in the areas of structural analysis and design for one and a half years. He designed reinforced concrete structures for the surveillance tower in Suwannabhumi Airport with his senior structural engineering team. He had abundant of chances to analyze and design structural systems using both hand calculation and computer program, “RISA 3D”. In August 2004, Anupong entered the graduate program in Structural and Applied Mechanics at the University of Texas at Arlington (UTA) and completed Master of Science in Civil Engineering in May 2006. Then, Anupong has been accepted to the Ph.D. program as a graduate research assistant in structural mechanics at UTA, and he is awarded the American Concrete Pipe Association scholarship. He completed Doctor of Philosophy

in Civil Engineering with the minor field of finite element modeling in December 2009. Under the supervision of Dr. Ali Abolmaali, Anupong Kararam has two papers published and two under reviewed.